

Air Force Institute of Technology

AFIT Scholar

Theses and Dissertations

Student Graduate Works

9-12-2007

Hybrid Micro-Electro-Mechanical Tunable Filter

Edward M. Ochoa

Follow this and additional works at: <https://scholar.afit.edu/etd>



Part of the [Electronic Devices and Semiconductor Manufacturing Commons](#)

Recommended Citation

Ochoa, Edward M., "Hybrid Micro-Electro-Mechanical Tunable Filter" (2007). *Theses and Dissertations*. 2894.

<https://scholar.afit.edu/etd/2894>

This Dissertation is brought to you for free and open access by the Student Graduate Works at AFIT Scholar. It has been accepted for inclusion in Theses and Dissertations by an authorized administrator of AFIT Scholar. For more information, please contact richard.mansfield@afit.edu.



HYBRID MICRO-ELECTRO-MECHANICAL TUNABLE FILTER

DISSERTATION

Edward M. Ochoa
Major, USAF

AFIT/DS/ENG/07-23

DEPARTMENT OF THE AIR FORCE
AIR UNIVERSITY

AIR FORCE INSTITUTE OF TECHNOLOGY

Wright-Patterson Air Force Base, Ohio

APPROVED FOR PUBLIC RELEASE; DISTRIBUTION UNLIMITED.

The views expressed in this thesis are those of the author and do not reflect the official policy or position of the United States Air Force, Department of Defense, or the United States Government.

AFIT/DS/ENG/07-23

HYBRID MICRO-ELECTRO-MECHANICAL TUNABLE FILTER

DISSERTATION

Presented to the Faculty
Graduate School of Engineering and Management
Air Force Institute of Technology
Air University
Air Education and Training Command
In Partial Fulfillment of the Requirements for the
Degree of Doctor of Philosophy

Edward M. Ochoa, B.S.E.E., M.S.E.E.
Major, USAF

September 2007

APPROVED FOR PUBLIC RELEASE; DISTRIBUTION UNLIMITED.

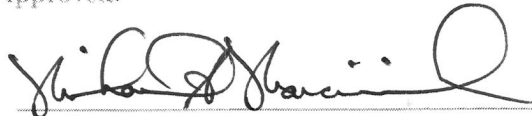
HYBRID MICRO-ELECTRO-MECHANICAL TUNABLE FILTER

DISSERTATION

Edward M. Ochoa, B.S.E.E., M.S.E.E.

Major, USAF

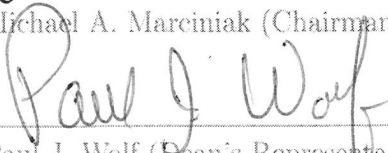
Approved:



Michael A. Marciniak (Chairman)

7 Sep 07

Date



Paul J. Wolf (Dean's Representative)

9/7/07

Date



James A. Fellows (Member)

6 SEP 07

Date



LaVern A. Starman (Member)

6 Sept 07

Date



Thomas R. Nelson (Member)

9/6/07

Date



William D. Cowan (Member)

09/06/07

Date

Accepted:



Marlin U. Thomas

Dean, Graduate School of Engineering and Management

9/12/07

Date

Acknowledgements

I would like to thank my finishing advisor, Dr Mike Marciniak, and my initial advisor, Dr Jim Lott, for mentoring me in my research and facilitating the resources required to accomplish this work. Next, I extend my sincere appreciation and thanks to Lt Col Charles P. Brothers, PhD (deceased July 31, 2001), my VLSI Minor professor and mentor who I was privileged to know during my studies at AFIT. I also extend my sincere appreciation and thanks to all past members in the AFIT MEMS, Photonics, and VLSI programs for their academic advice and friendship. Next, I thank Maj Vern Starman, Maj Jeremy Raley, Maj Mike Harvey, Dr Tom Nelson and Dr Robert Bedford for many hours of stimulating discussions, teamwork, and good will throughout this endeavor. I also thank Dr Olga Blum-Spahn, Dr Bill Cowan, Grant Grossettete, Jen Johnson, Dr Ganesh Subramania, and all the helpful lab researchers and technicians at Sandia National Laboratories, NM. I sincerely appreciate the sponsorship of Dr Fan Ren and Travis Anderson at University of Florida for their support during the final flip-bonding phases of this work. I am also very thankful to all my immediate and extended family, friends, and co-workers for their persistent and supportive encouragement to complete this work.

Words are hard to find to capture the sincere appreciation, love, and thanks I have for my mother. My mother has inspired me throughout my life, and I dedicate this capstone of my professional education to her.

Finally, special thanks go to our five children, who have been patient throughout this work. And, most significantly, my most precious heart-felt thanks and love go to my beautiful, loving, and witty wife, who provided the encouragement and support needed to complete this research!

Edward M. Ochoa

Table of Contents

	Page
Acknowledgements	iv
List of Figures	viii
List of Tables	xv
List of Symbols	xvi
List of Abbreviations	xvii
Abstract	xix
 I. Introduction	 1-1
1.1 MEMS Optoelectronics for National Defense Needs . .	1-1
1.2 MEMS Optoelectronics for WDM	1-3
1.3 MEM-Tunable Optoelectronics	1-5
1.4 Problem Statement	1-6
1.5 Methodology	1-7
1.6 Research Accomplishments	1-7
1.7 Sponsors	1-9
1.8 Organization	1-10
 Bibliography	 1-11
 II. Background	 2-1
2.1 Chapter Overview	2-1
2.2 MEMS	2-1
2.2.1 Micromachining	2-2
2.2.2 Bulk and Surface Micromachining	2-2
2.2.3 MUMPs®	2-2
2.2.4 MEMS Characterization	2-5
2.2.5 MEMS Reliability and Packaging	2-7
2.2.6 MEMS Integration	2-10
2.2.7 MOEMS	2-12
2.3 VCSEL	2-14
2.3.1 VCSEL Advantages	2-14
2.3.2 VCSEL Design and Fabrication	2-15

	Page
2.3.3 VCSEL-CMOS Integration	2-18
2.4 Tunable Filters and Lasers	2-19
2.4.1 DFB and DBR Tuning	2-20
2.4.2 External-Cavity MEM-Tunable Devices	2-22
2.4.3 MEM-TF and MT-VCSEL	2-24
2.5 Chapter Summary	2-26
Bibliography	2-27
III. Impetus for Studying the Hybrid MT-VCSEL	3-1
3.1 Chapter Overview	3-1
3.2 CAD Toolkit	3-2
3.2.1 Electrostatic Piston Deflection	3-2
3.2.2 VCSEL Resonant Wavelength	3-4
3.2.3 Multi-layer, Thin-film Simulation Toolkit . . .	3-7
3.2.4 MT-CAD	3-7
3.3 CAD and Fabrication Investigations	3-11
3.3.1 PolySi prototypes for Hybrid MEM-TF/TVCSEL	3-11
3.3.2 Monolithic versus Hybrid MT-VCSEL	3-19
3.4 Chapter Summary	3-33
Bibliography	3-35
IV. III-V AlGaAs Etch Studies	4-1
4.1 Chapter Overview	4-1
4.2 Multi-Layer Etch Study	4-1
4.3 GaAs Sacrificial Layer Etchant Study	4-2
4.3.1 GaAs Etch Systems	4-2
4.3.2 GaAs Etch Study Methodology	4-5
4.3.3 GaAs Etch Study Results	4-5
4.4 High Al mole fraction AlGaAs HF-based Etch	4-11
4.4.1 HF-based Etch Systems	4-11
4.4.2 HF-based Etch Study Methodology	4-11
4.4.3 HF Undercut Distances and Etch Rates	4-13
4.4.4 HF:IPA:H ₂ O Undercut Distances and Etch Rates	4-16
4.4.5 HF versus HF:IPA:H ₂ O Undercut Comparisons	4-16
4.5 Chapter Summary	4-21
Bibliography	4-22

	Page
V. Flip-Bond Process Development	5-1
5.1 Chapter Overview	5-1
5.2 Hybrid MEM-TF Fabrication	5-1
5.3 Flip-bond Studies	5-3
5.3.1 Methodology	5-3
5.3.2 Au-Au Flip-Bonding	5-3
5.3.3 Au-In Flip-Bonding	5-4
5.3.4 SU-8-SU-8 Flip-Bonding	5-11
5.4 Chapter Summary	5-17
Bibliography	5-18
VI. Hybrid MEM-TF Design, Fabrication, and Demonstration . . .	6-1
6.1 Chapter Overview	6-1
6.2 Design	6-1
6.3 Fabrication	6-9
6.4 Experimental Results	6-9
6.4.1 Measured Tuning versus Actuation Voltage . .	6-9
6.4.2 Calculated versus Measured Results	6-11
6.5 Unstable Resonator Simulation versus Measurement . .	6-19
6.5.1 Fourier Transform Field Propagation	6-22
6.5.2 Field Reflection and Transmission	6-25
6.5.3 Calculated versus Measured Results	6-27
6.6 Discussion	6-31
6.7 Chapter Summary	6-32
Bibliography	6-33
VII. Conclusions, Contributions, and Future Work	7-1
7.1 Contribution and Significance	7-1
7.2 Accomplishments	7-1
7.3 Recommendations for Future Work	7-3
7.4 Author's Publication List	7-4
Bibliography	7-7
Appendix A. Process Flow and Equipment Checklists	A-1
Appendix B. <i>oeng775tools</i>	B-1
Vita	VITA-1

List of Figures

Figure		Page
1.1.	Terrorist CBRN: excerpt from pamphlet summary of typical agents and CBRN devices available to al-Qa'ida and other terrorist groups [1]	1-2
1.2.	Schematic illustrating detection and identification of chemical emission using a tunable EC-QCL source coupled with a mid-infrared camera [3]	1-2
1.3.	Military optoelectronics: a) vertical cavity surface emitting laser [10], b) F-22 fires missile [11], c) holographic memory [12], d) F-35 incorporates fiber optics technology [13]	1-4
1.4.	WDM overview illustration: a) different wavelengths are multiplexed onto fiber optics [14], b) the light is amplified and routed to restoring amplifiers before a demultiplexer separates wavelengths [15]	1-4
2.1.	Relative size of MEMS: a 100- μ m diameter micromachined gear on the head of an ant [2]	2-3
2.2.	Illustration of bulk and surface micromachining [4]	2-4
2.3.	MUMPs [®] micromotor cross section and layer description [5]	2-6
2.4.	Example of polySi structures for material characterization: a) single-layer fixed-fixed beams, b) single-layer comb resonators. [SEM images of Author's devices]	2-7
2.5.	Example of MEMS missile launch shock failure [9]	2-8
2.6.	Wet etch-release structural sticking failure [9]	2-8
2.7.	End view of freely suspended cantilever undercut using a dry (plasma) etch [12]	2-9
2.8.	Illustration of supercritical CO ₂ drying critical point transition [13]	2-10
2.9.	Examples of a) monolithic integration [17] and b) hybrid integration [18]	2-11
2.10.	TI DMD [®] [19]	2-13
2.11.	Micro-optical bench comprised of MEMS structures and an edge emitting semiconductor diode laser [20]	2-13
2.12.	Semiconductor diode laser types and corresponding output beam divergence [21]: a) VCSEL, b) EEL	2-14
2.13.	Schematic illustration of epitaxial VCSEL structure: top and bottom DBR sandwich the MQW active region optical cavity [26]	2-16
2.14.	MBE system [28] and schematic illustration [26]	2-16

Figure		Page
2.15.	Energy bandgap (emission wavelength) dependence on lattice constant [25]	2-17
2.16.	A 64×64 VCSEL array flip-bonded to CMOS [30]	2-19
2.17.	Temperature-tuned DFB laser: a) wavelength versus temperature, b) intensity versus wavelength [33]	2-20
2.18.	Current injection-tuned SG-DBR laser integrated with a semiconductor optical amplifier [34]	2-21
2.19.	ECDL: a) device structure [35], b) a mirror rotating on a MEMS actuator is combined with a laser and a diffraction grating constitute a variable-wavelength filter, which adjusts the output wavelength [34]	2-23
2.20.	MT-VCSEL examples: a) cantilever actuator, electrostatically tuned [37], b) half-symmetric cavity, piston actuator, electrostatically tuned [38], c) cantilever actuator, magnetically tuned [40], d) half-symmetric cavity, ohmic (thermal) actuator, current tuned [43, 44]	2-25
3.1.	Schematic of basic electrostatic piston device [1]	3-2
3.2.	General multi-layer structure used to model E -field intensity on resonance	3-5
3.3.	Tutorial simulation results included with <i>oeng775tools</i> : a) Fabry-Perot etalon (<i>ex1.m</i>), b) VCSEL E-field standing wave (<i>ex2.m</i>)	3-8
3.4.	MT-CAD Flow Diagrams: a) functional block diagram, b) compute resonant wavelength function block elements	3-9
3.5.	MT-CAD MT-VCSEL simulation example: λ_R (* marks) and tunable air-gap (solid line) as a function of actuation voltage; the desirable operating voltages are less than the calculated $V_{pull-in}$ of 13.96 V to avoid device snap-down; resonant wavelength optical mode-hop occurs at approximately 1 μm air-gap	3-11
3.6.	Prototype hybrid MEM-TVCSEL schematic and fabricated MUMPs [®] piston actuator: a) prototype MEM-TVCSEL schematic cross section, b) scanning electron micrograph of four-flexure polySi piston actuator with centrally located, co-planar, Au contact pads for a flip-bonded VCSEL to be vertically displaced above an Au central reflector. This actuator was fabricated as a proof-of-concept, and no VCSEL was flip-bonded to this structure.	3-13
3.7.	Comparison of analytic simulations versus experimental results for seven Poly 1 or Poly 2 MUMPs [®] fabricated prototypes: a) all devices were suspended with four Poly 1 support flexures; analytically simulated and measured pull-in voltages were 12.45V and $11.8 \pm 0.1\text{V}$, respectively, b) all devices were suspended with Poly 2 flexures; analytically simulated and measured pull-in voltages were 8.27V and $7.7 \pm 0.5\text{V}$, respectively	3-15

Figure		Page
3.8.	Au reflector prototypes: a) cross-section schematic, b) scanning electron micrograph of vertically displaced Au mirror (central reflector) prototypes	3-16
3.9.	Simulated E-field intensity at 974-nm resonant wavelength, λ_R , for 0.75- μm -thick air-gap in a flip-bonded 980-nm hybrid MT-VCSEL	3-17
3.10.	Simulated resonant wavelength tuning for flip-bonded 980-nm hybrid MT-VCSEL with 1.5- μm -thick flexures: a) 0.75- μm initial air-gap, b) 2.00- μm initial air-gap	3-18
3.11.	Prototype monolithic MT-VCSEL: a) E-field intensity (a.u., lower blue line) versus index and distance at resonance wavelength, λ_R b) top view schematic of prototype mechanical structure	3-21
3.12.	Prototype hybrid MT-VCSEL: a) E-field intensity (a.u., lower blue line) versus index and distance at resonance wavelength, λ_R b) cross-section schematic of prototype structure	3-23
3.13.	MT-CAD monolithic MT-VCSEL simulation: a) resonant wavelength (* marks) and tunable air gap (solid line) versus actuation voltage, b) three-dimensional visualizations of substrate E-field intensity (over resonant frequency search space)	3-24
3.14.	MT-CAD hybrid MT-VCSEL simulation: a) resonant wavelength (* marks) and tunable air gap (solid line) versus actuation voltage, b) three-dimensional visualizations of substrate E-field intensity (over resonant frequency search space)	3-25
3.15.	Monolithic MT-VCSEL resonant wavelength (* marks) solution space for variation in III-V material growth thickness of: a) -4% , b) -2% ; air-gap simulation space increased from range illustrated in Figure 3.13	3-26
3.16.	Monolithic MT-VCSEL resonant wavelength (* marks) solution space for variation in III-V material growth thickness of 0% ; air-gap simulation space increased from range illustrated in Figure 3.13	3-27
3.17.	Monolithic MT-VCSEL resonant wavelength (* marks) solution space for variation in III-V material growth thickness of: a) $+2\%$, b) $+4\%$; air-gap simulation space increased from range illustrated in Figure 3.13	3-28
3.18.	Hybrid MT-VCSEL resonant wavelength (* marks) solution space for variation in III-V material growth thickness of: a) -4% , b) -2% ; air-gap simulation space increased from range illustrated in Figure 3.14	3-29
3.19.	Hybrid MT-VCSEL resonant wavelength (* marks) solution space for variation in III-V material growth thickness of 0% ; air-gap simulation space increased from range illustrated in Figure 3.14	3-30

Figure		Page
3.20.	Hybrid MT-VCSEL resonant wavelength (* marks) solution space for variation in III-V material growth thickness of: a) +2%, b) +4%; air-gap simulation space increased from range illustrated in Figure 3.14	3-31
4.1.	SEM of stripe-masked multi-layer GaAs/AlGaAs sample; the photoresist mask was removed prior to wet-etch characterization	4-2
4.2.	GaAs crystal planes and directions	4-3
4.3.	Nominal (100)-oriented GaAs anisotropic wet etching characteristics	4-4
4.4.	Nominal, generally inconclusive, multi-layer stripe etch study results: 30-min citric-acid/tripotassium-citrate/hydrogen-peroxide etch at 25 °C, stripe oriented parallel to <110> direction . .	4-6
4.5.	SEM of typical anisotropic GaAs layer etch results in multi-layer stripe etch study: overhead-view of 6-hr citric-acid/tripotassium-citrate/hydrogen-peroxide etch at 25 °C, deep and irregular anisotropic etching of the GaAs substrate was observed as indicated on left side of SEM; the edge of the stripe (indicated by a white vertical line) under study was oriented parallel to the wafer flat (<110> directions)	4-7
4.6.	SEM of 5- μ m wide, multi-layer, stripe mesas that were etched with a citric-acid/tripotassium-citrate/hydrogen-peroxide 5:5:1.5 at 25 °C: a) and b) were etched for 2 hours; c) and d) were etched for 4 hours; in a) and c), stripes were parallel to wafer flat; in b) and d), stripes were 45° from wafer flat	4-8
4.7.	SEM of 100- μ m-wide multi-layer etch study stripes: 2-hr citric-acid/tripotassium-citrate/hydrogen-peroxide 5:5:1.5 etch at 25 °C; stripes oriented 45° from wafer flat; layer composition is illustrated in Figure 4.1	4-9
4.8.	Spiral etch test structure for empirical anisotropy characterization of citric-acid/tripotassium-citrate/hydrogen-peroxide 5:5:1.5 etch at 25 °C: photoresist mask on GaAs substrate; orthogonal etch pits in directions 45° from wafer flats	4-10
4.9.	Example cross section and measurement of stripe etch test structure for undercut characterization of HF/IPA/H ₂ O 1:3:6 1-min etch: Al _{0.7} Ga _{0.3} As undercut is 1.15 μ m; Al _{0.8} Ga _{0.2} As undercut is 5.57- μ m; Al _{0.9} Ga _{0.1} As undercut is 7.27- μ m; when the Al _{0.8} Ga _{0.2} As or other high selectivity layers were etched, the surrounding layers typically collapsed onto each other	4-12
4.10.	HF etch undercut distance as a function of time: a) HF undercut etch of EMC5420, b) HF undercut etch of EMC6844	4-14
4.11.	HF/IPA/H ₂ O 1:3:6 undercut etch distance as a function of time: a) undercut etch measurements for G2-2614, b) undercut etch measurements for EMC5420	4-17
4.12.	HF:IPA:H ₂ O 1:3:6 undercut etch distance as a function of time: undercut etch measurements for EMC6844	4-18

Figure		Page
5.1.	Hybrid MEM-TF three-dimensional design illustrations: a) MUMPs® polySi piston actuator with central Au reflector b) DBR flip-bonded to actuator	5-2
5.2.	Au-Au DBR Si die surrogate flip-bonding: a) donor die DBR mesa sites b) acceptor die Au bond-pad sites, c) SEM photo of cracked DBR, d) microscope photo of a cracked DBR	5-5
5.3.	Au-Au bonding with polySi die after HF release: a) microscope view of polySi platform b) representative example of a cracked DBR after flip-bonding with Au bond-pads	5-6
5.4.	Au-Au bonding with polySi die after dilute-HF release: a) microscope photo overview of polySi die acceptor sites b) microscope photo of a cracked DBR	5-7
5.5.	Au-In bonding: a) evaporated In bond-pads, b) microscope inspection of In bond-pad DBR flip-bonded to Si surrogate die demonstrating crack-free DBR mesas	5-9
5.6.	Au-In bonding: a) crack-free DBR mesas flip-bonded to polySi actuators, b) mottled, damaged Au layer on polySi die	5-10
5.7.	Nominal results for manually-separated, SU-8-to-SU-8-bonded-die; bonding temperature: a) 165 °C, b) 150 °C, c) 135 °C, d) 120 °C, and e) 105 °C.	5-13
5.8.	Hybrid MEM-TF acceptor and donor die pair-wise bond sites: a) electrostatically actuated polySi MEMS platform with centrally located 60- μm^2 Au reflector and photolithographically deposited SU-8 2002 bond-pads, b) $\text{Al}_{0.4}\text{Ga}_{0.6}\text{As}$ -GaAs DBR mesa with bond-pads; the 50 \times 50- μm^2 bond-pads were nominally 2- μm thick	5-15
5.9.	Hybrid MEM-TF: a) $\text{Al}_{0.4}\text{Ga}_{0.6}\text{As}$ -GaAs DBR mesas flip-bonded to polySi MEMS platforms using SU-8 bond pads, b) magnified view of a hybrid MEM-TF.	5-16
6.1.	Hybrid MEM-TF: design cross section of a hybrid MEM-Tunable filter (not to scale)	6-2
6.2.	Hybrid MEM-TF: a) designed DBR layer thickness, b) designed and calculated device layer thickness	6-4
6.3.	Hybrid MEM-TF with designed (980-nm center) DBR: simulated resonant wavelength tuning as a function of applied voltage	6-5
6.4.	DBR reflectivity: designed (solid line), measured (dashed line) using spot reflectance system described in Section 6.4.1 and illustrated in Figure 6.7	6-6
6.5.	DBR growth layer thickness: a) illustration of designed layer thickness and calculated growth layer thickness scale factors, b) designed, measured, and calculated DBR reflectivity as a function of wavelength	6-7

Figure		Page
6.6.	Hybrid MEM-TF with the as-grown DBR growth layer scale factors: calculated resonant wavelength as a function of applied voltage	6-8
6.7.	Diagram and photo of spot reflectance measurement system .	6-10
6.8.	Hybrid MEM-TF: normalized measured reflectivity as a function of actuation voltage; non-catastrophic snapdown voltage was observed at 10.13 V	6-12
6.9.	Hybrid MEM-TF: measured resonant wavelength tuning as a function of applied voltage; non-catastrophic snapdown voltage was observed at 10.13 V	6-13
6.10.	Hybrid MEM-TF: measured versus design resonant wavelength tuning as a function of applied voltage	6-14
6.11.	Hybrid MEM-TF: measured layer thickness data and calculations	6-15
6.12.	Hybrid MEM-TF: a) interferometric image of device at non-catastrophic snap-down voltage of 10.13V, b) interferometrically measured vertical deflection as a function of applied electrostatic actuation voltage	6-16
6.13.	Measured versus calculated hybrid MEM-TF reflectivity as a function of wavelength; 0.0V actuation voltage, calculated via planar-planar cavity assumption	6-17
6.14.	Measured versus calculated hybrid MEM-TF tuning as a function of applied actuation voltage using as-grown DBR growth layer scale factors, measured individual layer thickness, and measured deflection	6-18
6.15.	Hybrid MEM-TF: ZYGO® NewView™ 5000 interferometric image; focus was located near the surface of the flip-bonded, $250 \times 250\text{-}\mu\text{m}^2$, $\text{Al}_{0.4}\text{Ga}_{0.6}\text{As-GaAs}$ DBR	6-19
6.16.	DBR surface: interferometrically measured vertical surface contours; contour level lines are in units of μm ; $50 \times 50\text{-}\mu\text{m}^2$ crop box centered on DBR minima labeled “x”	6-20
6.17.	DBR interferometric data: (Top) row and column data through minimum of DBR surface; (Bottom) average cross section and calculated circle with radius of curvature = 1.19 cm	6-21
6.18.	Optical microcavity bounded by a convex DBR and planar Au mirror	6-23
6.19.	Measured versus calculated hybrid MEM-TF reflectivity as a function of wavelength; 0.0V actuation voltage, calculated via planar-convex cavity assumption	6-28
6.20.	Calculated hybrid MEM-TF reflectivity as a function of wavelength	6-29
6.21.	Measured versus calculated hybrid MEM-TF tuning as a function of applied actuation voltage	6-30
B.1.	<i>oeng775tools</i> : overview slides 1-2	B-2
B.2.	<i>oeng775tools</i> : overview slides 3-4	B-3
B.3.	<i>oeng775tools</i> : overview slides 5-6	B-4

Figure		Page
B.4.	<i>oeng775tools</i> : overview slides 7-8	B-5
B.5.	<i>oeng775tools</i> : overview slides 9-10	B-6
B.6.	<i>oeng775tools</i> : overview slides 11-12	B-7
B.7.	<i>oeng775tools</i> : overview slides 13-14	B-8
B.8.	<i>oeng775tools</i> : overview slides 15-16	B-9
B.9.	<i>oeng775tools</i> : overview slides 17-18	B-10

List of Tables

Table		Page
4.1.	EMC5420 HF etch undercut distances and rates	4-15
4.2.	EMC6844 HF etch undercut distances and rates	4-15
4.3.	G2-2614 HF:IPA:H ₂ O 1:3:6 etch undercut distances and rates	4-19
4.4.	EMC5420 HF:IPA:H ₂ O 1:3:6 etch undercut distances and rates	4-19
4.5.	EMC6844 HF:IPA:H ₂ O 1:3:6 etch undercut distances and rates	4-19
4.6.	EMC5420 HF versus HF:IPA:H ₂ O etch distance	4-20
4.7.	EMC6844 HF versus HF:IPA:H ₂ O etch distance	4-20
A.1.	Quad Level Mask Process Flow (Est. 8-hr)	A-1
A.2.	GaAs Etch Process Flow (Est. 2-hr)	A-2
A.3.	Metal Lift-off Process Flow (Est. 6.5-hr)	A-2
A.4.	Mesa Wet Etch Process Flow (Est. 2.5-hr)	A-2
A.5.	Loomis Scribe Cleaver Checklist (Est. 30-min)	A-2
A.6.	Sublimation Dryer Checklist (Est. 1.5-hr)	A-3
A.7.	PlasmaTherm Downstream Stripper Checklist (Est. 30-min)	A-3
A.8.	LFE Checklist (Est. 20-min)	A-3
A.9.	Ellipsometer Checklist (Est. 5-min)	A-3
A.10.	Nanospec Checklist (Est. 5-min)	A-4
A.11.	HMDS Checklist (Est. 33-min)	A-4
A.12.	790 PECVD Checklist (Est. 2-hr)	A-5
A.13.	790 RIE Checklist (Est. 2-hr)	A-6
A.14.	Temescal Checklist (Est. 3-hr)	A-7
A.15.	Flip Chip Aligner Bonder (FCAB) Checklist (Est. 1-2-hr) . .	A-8
A.16.	Dual Chamber ECR-ICP Checklist (Est. 2-hr)	A-9
A.17.	JEOL SEM 6400 Checklist (Est. 1-2-hr)	A-10
A.18.	WYKO Interferometer Checklist (Est. 30-min)	A-11

List of Symbols

Symbol		Page
λ_D	Bragg design wavelength	2-18
A	electrode area	3-3
ε_0	dielectric constant of air	3-3
M	transfer matrix	3-4
$N(\omega)$	complex refractive index	3-4
D	transfer matrix method dynamical matrix	3-4
P	transfer matrix method propagation matrix	3-4
E^+	incident E-field vector	3-4
E^-	reflected E-field vector	3-4
L	arbitrary layer in transfer matrix method	3-5
N_L	complex index of refraction for layer L	3-5
P_L	propagation matrix for layer L	3-5
d_L	thickness of layer L	3-6
k_{Lx}	x component of the wave vector	3-6
ρ	reflectance coefficient	3-6
κ	imaginary part of the refractive index	3-7
λ_R	resonant wavelength	3-7
E_i	initial electric field profile	6-22
E_R	reflected field profile	6-22

List of Abbreviations

Abbreviation		Page
CBRN	Chemical Biological Radiological Nuclear	1-1
DoD	Department of Defense	1-1
CBDP	Chemical Biological Defense Program	1-1
EC-QCL	external-cavity quantum cascade laser	1-1
Mid-IR	mid-infrared	1-1
MEMS	micro-electro-mechanical systems	1-1
WDM	Wavelength Division Multiplexing	1-3
EEL	edge-emitting laser	1-5
VCSEL	vertical-cavity surface emitting laser	1-5
MEM-TF	MEM-tunable filter	1-5
MT-VCSEL	MEM-tunable VCSEL	1-5
polySi	polysilicon	1-6
AFRL	Air Force Research Laboratory	1-7
AFIT	Air Force Institute of Technology	1-7
SNL	Sandia National Laboratories	1-7
UF	University of Florida	1-7
MOEMS	micro-opto-electro-mechanical systems	2-1
CMOS	complementary metal-oxide semiconductor	2-1
IC	integrated circuit	2-2
MUMPs®	Multi-User MEMS Processes®	2-2
PSG	phosphosilicate glass	2-2
Si	Silicon	2-2
CPD	critical point drying	2-9
TI DMD®	Texas Instruments Digital Multimirror Device®	2-12
DBR	distributed Bragg reflector	2-14
MQW	multiple quantum well	2-15
MBE	molecular beam epitaxy	2-16
DFB	distributed feedback	2-20
DBR _n	distributed Bragg reflection	2-20
SG-DBR _n	sampled-grating DBR _n	2-21
GCSR	grating-assisted coupler and sampled reflector	2-22
AR	anti-reflection	2-22
ECDL	external-cavity diode laser	2-22
EP	electrically pumped	2-24

Abbreviation		Page
CAD	computer-aided design	3-1
MT-CAD	MEM-TF/MT-VCSEL-CAD	3-1
E-field	electric-field	3-4
IPA	isopropanol	4-5
HF	hydrofluoric-acid	4-5
H ₂ O	deionized water	4-5

Abstract

While advantages such as good thermal stability and processing-chemical compatibilities exist for common monolithic-integrated micro-electro-mechanically tunable filters (MEM-TF) and MEM-tunable vertical cavity surface emitting lasers (MT-VCSEL), they often require full processing to determine device characteristics. Alternatively, the MEM actuators and the optical parts may be fabricated separately, then subsequently bonded. This “hybrid approach” potentially increases design flexibility by allowing wafer-level pre-testing and discarding defective parts prior to completing device fabrication. A hybrid MT-VCSEL’s resonant frequency has less sensitivity to growth variations than a monolithic design. Monolithic electrostatically actuated devices are also typically limited to one-third of the original air-gap spacing between the tuning reflector and optically active material. In contrast, a hybrid approach enables electrostatic pull-in voltage to be designed independent of the air-gap between the tuning reflector and optically active or reflective material. Electrostatically actuated monolithic devices suffer catastrophic failure when pull-in occurs. In addition to the use of polySi dimples to prevent stiction, a key advantage of these dimples is they may also be used to eliminate catastrophic failure. Since hybrid techniques allow integration of heterogeneous material systems, “best of breed” compound optoelectronic devices may be customized to enable materials groups to be optimized for tasks for which they are best suited. Thus, as a first step toward a hybrid ($\text{Al}_x\text{Ga}_{1-x}\text{As-polySi}$) MT-VCSEL, this dissertation reports the design, fabrication, and demonstration of an electrostatically actuated hybrid MEM-TF. A $250 \times 250\text{-}\mu\text{m}^2$, $4.92\text{-}\mu\text{m}$ -thick, $\text{Al}_{0.4}\text{Ga}_{0.6}\text{As-GaAs}$ distributed Bragg reflector was successfully flip-bonded to a polySi piston electrostatic actuator using SU-8 photoresist as bonding adhesive. The device demonstrated 53nm ($936.5 - 989.5\text{nm}$) of resonant wavelength tuning over the actuation voltage range of 0 to 10 V.

Hybrid Micro-Electro-Mechanical Tunable Filter

I. Introduction

1.1 MEMS Optoelectronics for National Defense Needs

As shown in Figure 1.1, several Chemical Biological Radiological Nuclear (CBRN) threats known to be available to terrorist groups have been identified [1]. In March 2006, the Department of Defense (DoD) identified CBRN warfare detection as a top national defense priority [2]. As stated in the 2006 Chemical Biological Defense Program (CBDP) Annual Report to Congress [2], “The goal of the DoD’s detection and technology area is to provide a real-time capability to detect, identify, characterize, quantify, locate, and warn against all known or validated CBRN warfare agent hazards, to include toxic and industrial chemical and non-traditional agents.”

As illustrated in Figure 1.2, stand-off chemical detection and identification may be performed using a tunable external-cavity quantum cascade laser (EC-QCL) or light-emitting diode (LED) source coupled with a mid-infrared (Mid-IR) camera [3]. Unfortunately, these (first-generation) remote chemical sensing instruments are bulky and expensive [3,4]. These two characteristics are undesirable; they reduce battlefield portability and limit distribution due to funding limitations. However, since these instruments use optical elements (such as tunable filters) that may be miniaturized using micro-electro-mechanical systems (MEMS) technology, the DoD pursues development and maturity of MEMS optoelectronics to enable chemical sensors development [2].

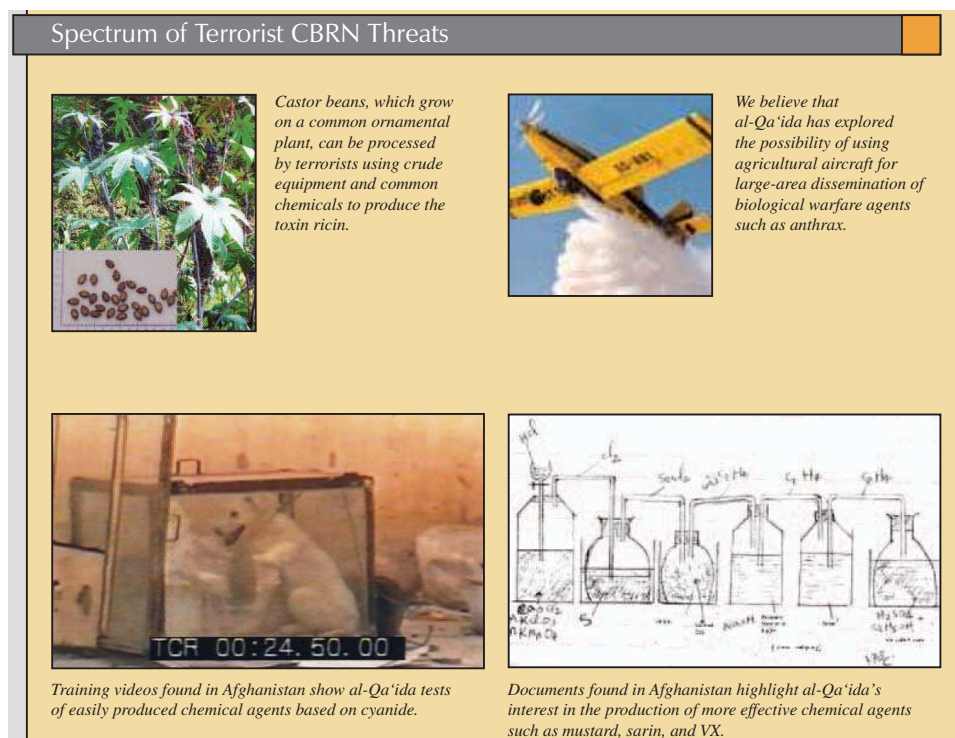


Figure 1.1: Terrorist CBRN: excerpt from pamphlet summary of typical agents and CBRN devices available to al-Qa'ida and other terrorist groups [1]

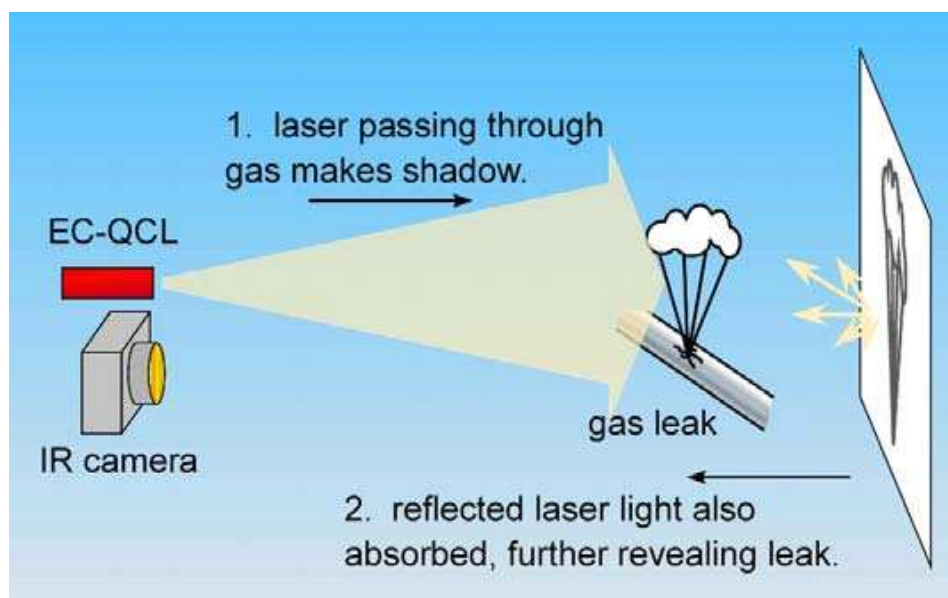


Figure 1.2: Schematic illustrating detection and identification of chemical emission using a tunable EC-QCL source coupled with a mid-infrared camera [3]

The DoD also pursues general research and technology where risk and payoff are both very high, and where success may provide dramatic advances for strategic and tactical military systems [5]. Many military systems require robust, cost-effective, optoelectronic devices for a broad spectrum of data transmission applications. Optoelectronic device applications include missile/decoy interfaces, fiber optic aircraft networks, next-generation holographic memory, fiber optic sensing, signal processing, and communication systems (as shown in Figure 1.3). Other applications pursued by the DoD include IR countermeasures, free-space optical communication, remote sensing, and laser marking applications [6].

1.2 MEMS Optoelectronics for WDM

Optical communication is experiencing an explosive increase in bandwidth demand, fueled by internet growth and ever-increasing microprocessor capabilities [7]. Only ten years ago, it was common for a single fiber optic to carry just one wavelength channel. Fibers have recently been demonstrated capable of handling 1,000 channels, delivering a huge increase in data through-put [8]. As illustrated in Figure 1.4, Wavelength Division Multiplexing (WDM) has emerged as an effective technology to significantly increase bandwidth. Bandwidth is increased by multiplexing several wavelengths through existing fiber optic networks. Thus, the massive investment for new fiber installation is avoided.

However, WDM technology, alone, is not a cure-all. Most implementations cannot consistently operate at the full theoretical capacity, and fail to meet demand fluctuations. Additionally, WDM systems often suffer from wavelength blocking at optical cross-connects, and require a large inventory for spare optical filters and laser sources [7]. Moreover, although WDM networks can carry multiple channels, they cannot carry two signals of the same wavelength simultaneously. In networks using fixed wavelength lasers, each node requires at least one dedicated laser spare, resulting in millions of dollars in spare inventory [7,9].

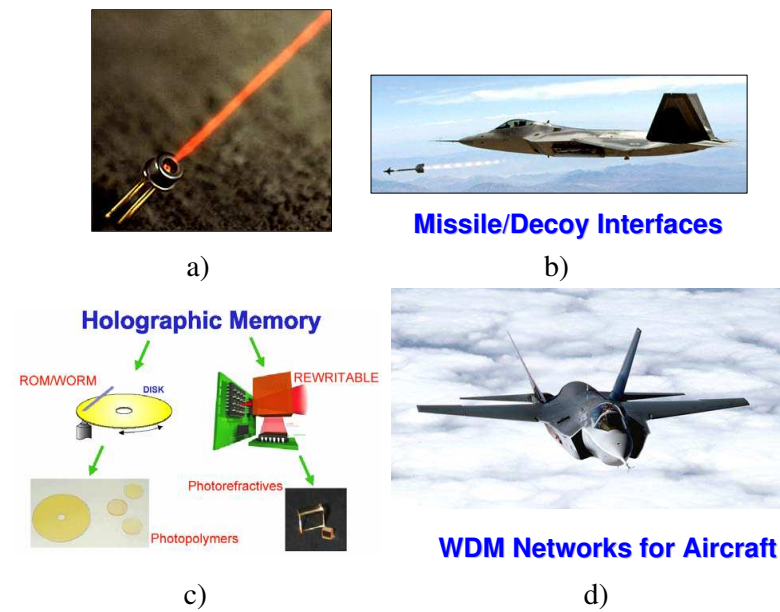


Figure 1.3: Military optoelectronics: a) vertical cavity surface emitting laser [10], b) F-22 fires missile [11], c) holographic memory [12], d) F-35 incorporates fiber optics technology [13]

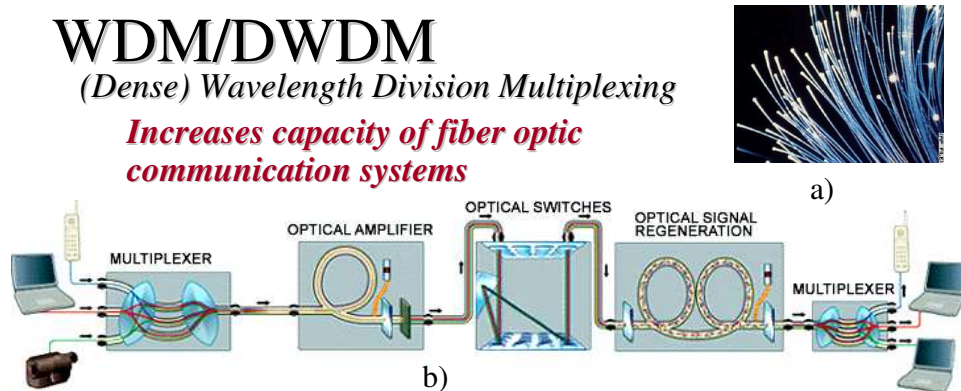


Figure 1.4: WDM overview illustration: a) different wavelengths are multiplexed onto fiber optics [14], b) the light is amplified and routed to restoring amplifiers before a demultiplexer separates wavelengths [15]

1.3 MEM-Tunable Optoelectronics

Unfortunately, standard WDM edge-emitting laser (EEL) sources and optical filters require complex biasing, demand system-specific optical coupling configurations, and are difficult to manufacture [16]. These demands reduce system reliability, yield, and thus, increase unit cost. WDM carriers resolve these WDM limitations by incorporating multi-wavelength diode laser arrays, or widely tunable optoelectronics, into their systems. By using tunable devices, the WDM carriers remove the wavelength-specific limitation and eliminate the need for expensive, idle, spare inventory. In particular, equipment reuse becomes possible because a tunable WDM line-card may be used to cover any of the 80 wavelengths in a WDM system. In contrast, a WDM system using fixed wavelength devices must keep 80 spare line cards, one for each operating wavelength [7]. Tunable optoelectronics also enable WDM carriers to provision light paths promptly, because they reduce reconfiguration complexity [7]. Network fluctuations (in terms of what offers the best system link budget) may be avoided by using preprogrammed software to dynamically reconfigure tunable laser and filter channels [7, 9].

Semiconductor filter, EEL, and vertical-cavity surface emitting laser (VCSEL) tuning has been achieved via monolithically grown MEMS electrostatic- [17], magnetic- [18], and piezoelectric- [19] actuated devices. Typical MEM-tunable filters (MEM-TF) and MEM-tunable VCSEL (MT-VCSEL) operate via electrostatic or magnetic deflection of a monolithically grown multi-layer reflector. A “sacrificial” layer of material is removed via wet or dry etch techniques, leaving behind a suspended reflector element connected to the base substrate via one or more flexures. (Note: The layers that remain are “structural” layers, and those removed are “sacrificial” layers.) As the reflector is displaced vertically, the effective optical path length is modified which tunes the device’s fundamental resonant frequency.

1.4 Problem Statement

Existing MEM-tunable semiconductor diode laser and filter designs impose mechanical and optoelectronic fabrication trade-offs and limits on device performance. For instance, monolithic electrostatically actuated devices are typically limited to one-third of the original air-gap spacing between the tuning reflector and optically active material. This limits tuning range, and thus, device performance [16]. Additionally, while advantages such as good thermal stability and processing-chemical compatibilities exist for common monolithic-integrated MEM-TF and MT-VCSEL, they often require full fabrication (versus testing early in fabrication cycle) in order to determine material and device operation.

Alternatively, as proposed and demonstrated in this dissertation, it is possible for the MEMS actuation and the optical counterparts to be fabricated separately and subsequently bonded to each other during fabrication. This “hybrid approach” potentially avoids some of these undesirable factors and increases design flexibility by allowing wafer-level pre-testing and discarding defective parts prior to completing device fabrication. As reported [20], a monolithically grown MT-VCSEL’s resonant frequency has higher sensitivity to growth variations than a hybrid design.

Additionally, a hybrid approach enables electrostatic pull-in voltage to be designed independent of the air-gap between the tuning reflector and optically active or reflective material [20]. Also, electrostatically actuated monolithic devices suffer catastrophic failure when pull-in occurs. As reported [21], in addition to the use of polysilicon (polySi) MEMS dimples to prevent “stiction”, a key advantage of these dimples is that they may also be used to eliminate catastrophic failure. Thus, since hybrid techniques allow integration of heterogeneous material systems, “best of breed” compound optoelectronic devices may be customized to enable inherent materials groups to be optimized for tasks they are best suited.

1.5 Methodology

As a first step toward hybrid tunable filters and VCSEL, this research investigated, developed, and designed methods to demonstrate a hybrid MEM-TF via flip-bonding an $\text{Al}_x\text{Ga}_{1-x}\text{As}$ -based DBR to a polySi MEMS electrostatically actuated structure (with a built-in Au reflector) [20–22].

All devices were fabricated and tested at the Air Force Research Laboratory (AFRL), the Air Force Institute of Technology (AFIT), Sandia National Laboratories (SNL), and the University of Florida (UF).

1.6 Research Accomplishments

The primary contribution of this research was demonstration of a first-generation MEMS electrostatically tunable Fabry-Perot optical filter with $\text{Al}_x\text{Ga}_{1-x}\text{As}$ -polySi composition. Significant advantages of this methodology included the following:

- Enabled the use of polySi dimples to reduce catastrophic failure due to device stiction and pull-in [23]
- Enabled independent design and optimization of mechanical and optical elements [20–23]
- Enabled ability to pre-screen optical elements prior to full device assembly [23]
- Enabled reduction in device tuning sensitivity to variations in growth of optical elements [20]
- Enabled linear tuning as a function of actuation voltage by designing mechanical actuation independent of initial air-gap between the optical reflector and optical element [21, 23]
- Enabled use of identical polySi mechanical actuators with different AlGaAs material growths [22, 23]

This research demonstrated the following theoretical and/or experimental accomplishments:

- **Theoretical and Experimental Accomplishment:** Implemented and validated the electrostatic piston deflection calculation with polySi prototypes [21]
- **Theoretical Accomplishment:** Designed, implemented, and distributed *oeng775tools* (used by AFIT Photonics students for over four years), a MATLAB[®] modeling toolkit used to design, simulate, and visualize multi-layer thin-film characteristics such as power reflectance, absorption, transmission, reflectivity phase, and E-field intensity [24]
- **Theoretical Accomplishment:** Designed, implemented, and demonstrated MT-CAD, a MATLAB[®] modeling toolkit used to design, simulate, and visualize monolithic or hybrid MT-VCSEL or MEM-TF tuning as a function of applied actuation voltage [20, 25]
- **Theoretical Accomplishment:** Discovered a novel design trade-space via MT-CAD which may enable linear voltage tuning of hybrid MEM-TVCSEL [21]
- **Experimental Accomplishment:** Developed and characterized fabrication techniques to enable flip-bonding intact and crack-free $250 \times 250\text{-}\mu\text{m}^2$ DBRs to actuatable polySi MUMPs[®] devices [22, 23, 26]
- **Experimental Accomplishment:** First report of fabrication and characterization of a hybrid (polySi-AlGaAs) MEM-TF, a first step toward hybrid MEM-TVCSELs [23]
- **Experimental Accomplishment:** Fabrication of a hybrid MEM mirror; as a serendipitous spin-off of this work, this research also demonstrated the feasibility of bonding custom-fabricated, highly reflective (over multiple wavelengths) DBR material to existing MEM actuator designs, adding a new material set to the existing MEM-mirror design space [23]

Additionally, experimental MEM and VCSEL CAD tools were developed, acquired, and integrated to design, simulate, analyze, and optimize III-V and III-IV-V MEM-TF, MT-VCSEL, and MEM-tunable unstable optical resonators. PolySi mechanical structure prototypes successfully validated mechanical simulations. This research contributed toward the development of hybrid MT-VCSEL and, as serendipitous contributions, toward the development of hybrid MEM mirrors and hybrid MEM-tunable unstable optical resonators.

1.7 Sponsors

This dissertation research was sponsored by the following organizations:

- **Air Force Research Laboratory:** Air Force Research Laboratory, Sensors Directorate, Aerospace Components and Subsystems Technology Division, Electro-Optics Components Branch (AFRL/SNDP), Wright-Patterson Air Force Base, Ohio. Sponsor: Dr Tom Nelson; Research Group Members: Dr Robert Bedford, Maj Mike Harvey, Maj Jeremy Raley, and James Ehret.
- **Sandia National Laboratories:** Sandia National Laboratories, Group 1742, Kirtland Air Force Base, NM. Sponsor: Dr Olga Blum-Spahn; Research Group Members: Jen Johnson, Grant Grossetete, and Dr William Cowan. Sandia is a multiprogram laboratory operated by Sandia Corporation, a Lockheed Martin Company, for the United States Department of Energy under contract DE-AC04-94AL85000.
- **University of Florida:** University of Florida, Department of Chemical Engineering, Tallahassee, FL. Sponsor: Dr Fan Ren; Research Group Member: Travis Anderson

1.8 Organization

This dissertation is organized into seven chapters. Chapter II reviews MEMS, VCSEL, and tunable filters and VCSEL. Chapter III presents and reviews the computer-aided design tools developed for monolithic and hybrid MEM-TF and MT-VCSEL simulations. Chapter IV reviews the sacrificial layer experiments used to characterize candidate III-V etchants for MEM-TF and MT-VCSEL micromachining. Chapter V reviews flip-bonding materials and methods investigated to enable hybrid MEM-TF fabrication. Chapter VI describes the fabrication and characterization of a first-generation hybrid MEM-TF. Chapter VII concludes this dissertation with a summary of research accomplishments, contributions, and recommendations for future work.

Bibliography

1. Central Intelligence Agency, "Terrorist CBRN: Materials and Effects," Internet, May 2003, www.cia.gov/cia/reports/terrorist_cbrn/CBRN_threat.pdf.
2. Office of the Under Secretary of Defense (Acquisition, Technology and Logistics) and the Assistant Secretary of Defense, "Annual Report of the Department of Defense (DoD) Chemical and Biological Defense Program (CBDP)," Department of Defense, Internet, Tech. Rep., March 2006, www.acq.osd.mil/cp/2006_cbdp-annual_report_final.pdf.
3. M. J. Weida, D. Arnone, and T. Day, "Tunable QC laser opens up mid-IR sensing applications," Internet, July 2006, lfw.pennnet.com/articles/article_display.cfm?article_id=259939.
4. P. Li, K. Lee, W. Wang, and J. Peters, "Novel MEMS technology based silicon and polymer hybrid actuator and applications as a tunable filter in telecom and in IR chemical detector," in *Micromachining and Microfabrication Process Technology VIII*, ser. Proceedings of SPIE, J. A. Yasaitis, M. A. Perez-Maher, and J. M. Karam, Eds., vol. 4979. SPIE, 2003, pp. 207–216.
5. Defense Advanced Research Projects Agency, "DARPA Home Page," Internet, January 2007, www.darpa.mil.
6. A. P. Ongstad, G. C. Dente, M. L. Tilton, J. C. Chavez, and D. M. Gianardi, "High Brightness from an Unstable Resonator Mid-IR Semiconductor Laser," Air Force Research Laboratory Directed Energy Directorate, 3550 Aberdeen Ave SE, Kirtland AFB NM 87117, Technical Paper, June 2006.
7. R. Rubenstein, "Competition heightens in the tunable laser market," Internet, September 2006, fibers.org/articles/fs/10/9/3.
8. PhysOrg.com, "First time 1,000 channel WDM transmission demonstration in an installed optical fiber," Internet, March 2005, www.physorg.com/news3316.html.
9. A. Martin, "By itself, DWDM does not spell success," Laser Focus World, May 2001.
10. Honeywell, "Honeywell VCSEL Homepage," Internet, 2001, content.honeywell.com/sensing/components/graphics.
11. US Air Force, "F-22 successfully fires AIM-9 missile," Internet, July 2000, www.af.mil/photos/Jul2000/001120a.jpg.
12. D. Psaltis, "Rewritable Holographic Memory," in *NASA Goddard Conference on Mass Storage Systems and Technologies*, NASA. Internet, Mar 2000, esdis-it.gsfc.nasa.gov/MSST/conf2000/VG/D04VG.PDF.

13. Lockheed Martin, "F-35 Joint Strike Fighter Media Kit Photos," Internet, January 2007, www.lockheedmartin.com/data/assets/7763.zip.
14. CNN.com, "Fiber Optics," Internet, 2004, cnn.com/specials/2004/explorers/interactive/profiles/fiber.optics/content.html.
15. G. Stix, "The Triumph of the Light," *Scientific American*, vol. 284, no. 1, Jan 2001.
16. C. J. Chang-Hasnain, *Micromechanical Tunable VCSEL*, ser. Optoelectronic Properties of Semiconductors and Superlattices. Gordon and Breach Science Publishers, 2000, ch. 6, pp. 279–318.
17. C. Chang-Hasnain, "Tunable VCSEL," *IEEE Journal On Selected Topics in Quantum Electronics*, vol. 6, no. 6, pp. 978–987, November/December 2000.
18. H.-K. Lee, K.-S. Kim, and E. Yoon, "A Wide-range Linearly Tunable Optical Filter using Lorentz Force," *IEEE Photon. Technol. Lett.*, vol. 16, pp. 2087–2089, Sept 2004.
19. M. C. Y. Huang, K. B. Cheng, Y. Zhou, B. Pesala, and C. J. Chang-Hasnain, "Demonstration of Piezoelectric Actuated GaAs-Based MEMS-Tunable VCSEL," *IEEE Photon. Technol. Lett.*, vol. 18, pp. 1197–1199, May 2006.
20. E. M. Ochoa, T. R. Nelson, O. Blum-Spahn, and J. A. Lott, "Computer-Aided Design Comparisons of Monolithic and Hybrid MEM-Tunable VCSELs," in *Physics and Simulation of Optoelectronic Devices XI, Proceedings of SPIE*, vol. 4986, San Jose, CA, Jan 2003, pp. 293–303.
21. E. Ochoa, L. Starman, W. Cowan, T. Nelson, O. Blum-Spahn, and J. Lott, "Polysilicon Prototypes for Flip-bonded Hybrid MEM-tunable Filters and VCSELs," in *Technical Proceedings of the 2002 International Conference on Modeling and Simulation of Microsystems*, San Juan, Puerto Rico, Apr 2002.
22. M. Harvey, E. Ochoa, J. Lott, and T. R. Nelson, "Toward the Development of Hybrid MEMS Tunable Optical Filters and Lasers," in *Proceedings of the 2004 International Conference on Compound Semiconductor Manufacturing Technology*, Miami Beach, FL, May 2004.
23. E. Ochoa, T. Nelson, R. Bedford, J. Ehret, L. Starman, M. Harvey, T. Anderson, and F. Ren, "Demonstration of Hybrid $\text{Al}_x\text{Ga}_{1-x}\text{As}$ -Polysilicon Microelectromechanical Tunable Filter," *IEEE Photon. Technol. Lett.*, vol. 19, no. 6, pp. 381–383, Mar. 2007.
24. E. M. Ochoa, "oeng775tools: A MATLAB[®] toolbox," AFIT/ENG, Wright-Patterson AFB, OH, unpublished, February 2001.
25. E. M. Ochoa, J. A. Lott, T. R. N. Jr., M. C. Harvey, J. A. Raley, A. Stintz, and K. J. Malloy, "Monolithic III-V and Hybrid Polysilicon-III-V Microelec-

tromechanical Tunable Multilayer Filters and Vertical Cavity Surface Emitting Lasers,” in *Proceedings of SPIE*, vol. 5116, April 2003, pp. 465–472.

26. E. Ochoa, L. Starman, R. Bedford, T. Nelson, J. Ehret, M. Harvey, T. Anderson, and F. Ren, “Flip bonding with SU-8 for hybrid $\text{Al}_x\text{Ga}_{1-x}\text{As}$ -polysilicon MEMS-tunable filter,” *J. Micro/Nanolith. MEMS MOEMS*, vol. 6, no. 3, Jul-Sep 2007.

II. Background

2.1 Chapter Overview

This chapter introduces and reviews the following topics and sub-topics:

- **MEMS:** bulk and surface micromachining, the MUMPs® foundry, MEMS characterization, MEMS reliability and packaging, MEMS integration, and micro-opto-electro-mechanical systems (MOEMS)
- **VCSEL:** advantages, design and fabrication, and VCSEL-complementary metal-oxide semiconductor (VCSEL-CMOS) hybrid integration

For the sake of clarity and brevity, this is not an exhaustive review of the vast literature in these fields. Instead, the focus is predominantly on fundamentals required for this research. For more detailed descriptions, please consult references contained within the cited literature.

2.2 MEMS

This section reviews fundamentals in the field of micromachined sensors and actuators, referred to as MEMS [1]. Specifically, this section reviews the following topics:

- Micromachining and its associated advantages
- Bulk and surface micromachining
- The MUMPs® foundry used to fabricate MEM-prototypes
- MEMS reliability, packaging, and integration issues
- MOEMS

2.2.1 Micromachining. Micromachining is the integration of transducers and electronics on a common substrate via microfabrication technology. MEMS augment microelectronics computational abilities with the perception and control capabilities of microsensors and microactuators. MEMS is a surface technology that may be used to sense, control, and influence phenomena on both the microscale and macroscale. Tools originally developed for the integrated circuit (IC) industry are used to manufacture MEMS (Figure 2.1) [2]. Thus, MEMS leverage existing IC mass-production fabrication tools and systems [2, 3].

2.2.2 Bulk and Surface Micromachining. As shown in Figure 2.2, MEMS devices are fabricated using bulk and/or surface micromachining. Bulk micromachining is a process that removes “bulk” substrate material to form micromechanical structures [1, 4]. In contrast, surface micromachining is processing “above” the substrate, where the substrate is used as a base to build upon [1]. Surface micromachining consists of depositing, patterning, and selectively removing one or more material layers. The layers that remain are structural layers, and those removed are sacrificial layers.

2.2.3 MUMPs®. The Multi-User MEMS Processes® (MUMPs®) is a commercial micromachining foundry used to prototype MEMS. The MUMPs® consists of two structural polySi layers, two phosphosilicate glass (PSG) sacrificial layers, and one metal (Au) layer as listed (with corresponding thicknesses) in Figure 2.3 [2, 5, 6]. The seven MUMPs® layers are deposited conformally on a silicon (Si) substrate in the following order: Nitride, Poly 0, Oxide 1, Poly 1, Oxide 2, Poly 2, and Metal. The following eight masks are used to pattern the structural layers: Poly 0, Dimples, Anchor 1, Poly 1, Poly 1 - Poly 2 Via, Anchor 2, Poly 2, and Metal.

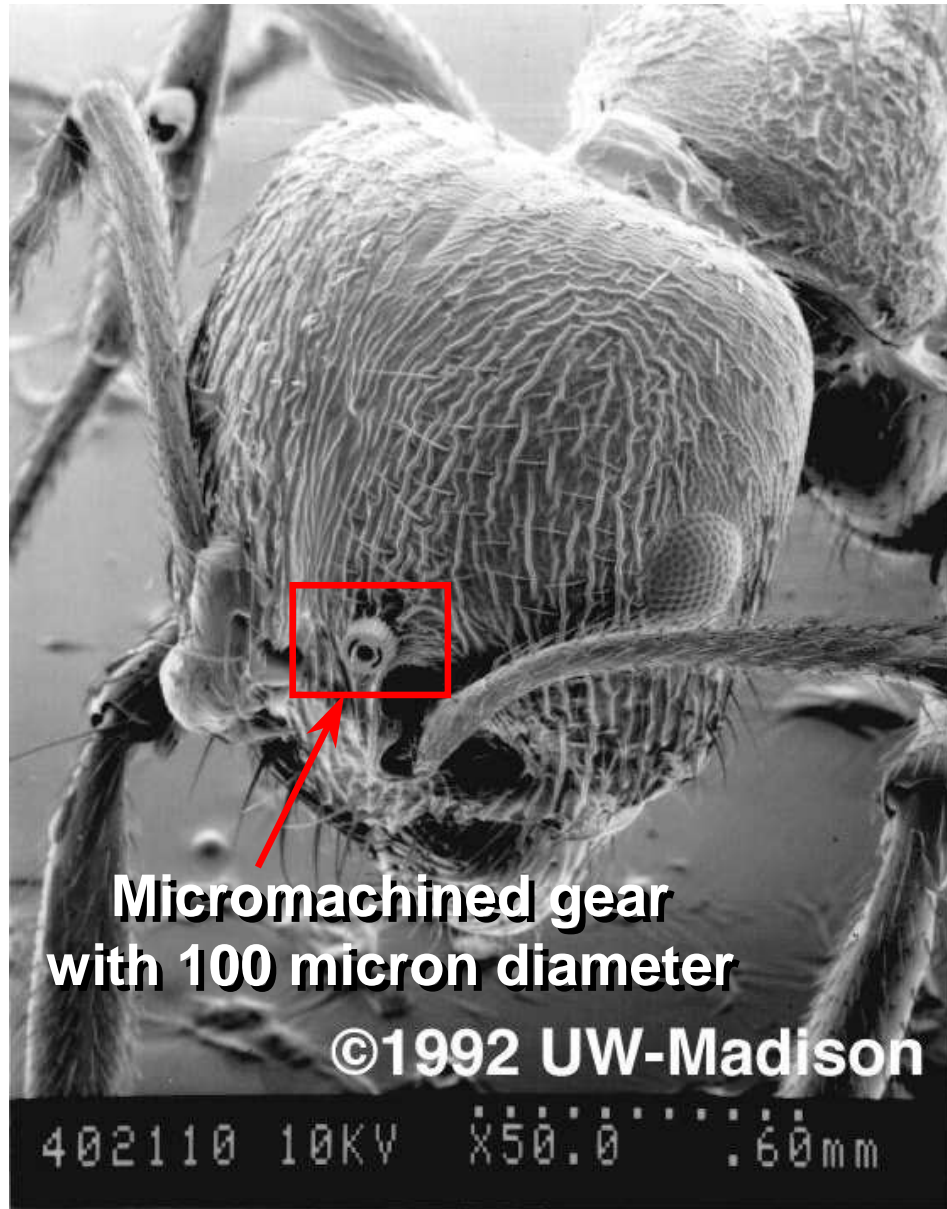


Figure 2.1: Relative size of MEMS: a 100- μm diameter micromachined gear on the head of an ant [2]

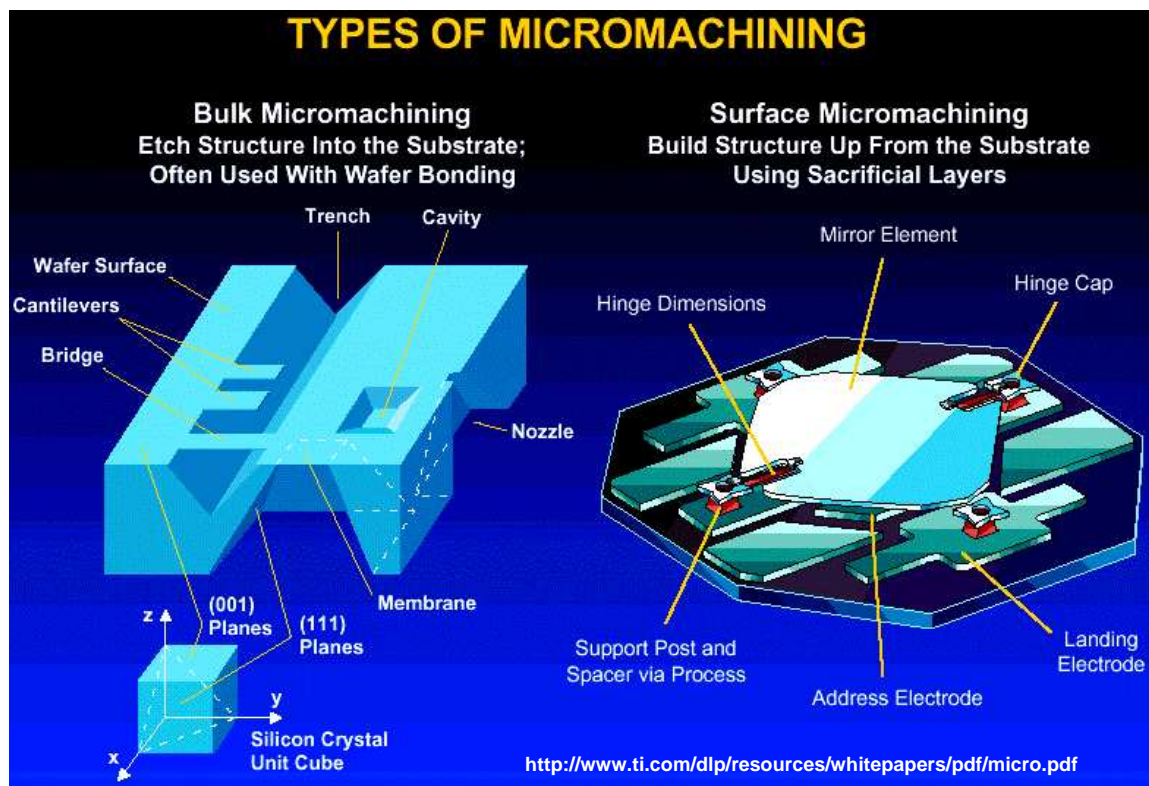


Figure 2.2: Illustration of bulk and surface micromachining [4]

The MUMPs® Design Handbook [5] describes fabrication steps in detail. For purposes of brevity and clarity, an example simplified MUMPs® micromotor (Figure 2.3) fabrication process follows [5, 7]:

- **Step 1:** First, deposit an Si nitride layer for dielectric isolation. Next, deposit then etch the first polySi layer (Poly 0) which typically serves as a structural base and/or electrical ground.
- **Step 2:** Deposit the first an Si dioxide (referred to as *oxide*) sacrificial layer (Oxide 1) to define the shape of future layers.
- **Step 3:** Etch “dimples” in the Oxide 1 layer. (Dimples are often used to increase MEMS yield by preventing sticking between released structural layers.) Deposit then etch the second polySi layer (Poly 1), which serves as the first structural layer.
- **Step 4:** Deposit the second oxide sacrificial layer (Oxide 2). This layer is often used to isolate the two polySi structural layers.
- **Step 5:** Deposit, then etch the final polySi structural layer (Poly 2). In addition, deposit, then etch the Au layer (Metal) atop Poly 2.
- **Step 6:** Deposit a photoresist layer to protect structures during shipping.
- **Step 7:** Upon receipt, remove the protective photoresist layer, then dissolve the sacrificial layers to release the MEMS structures. Finally, rinse, then dry via a hot plate bake or super-critical drying (discussed below).

2.2.4 MEMS Characterization. MEMS characterization is performed using both qualitative and quantitative techniques. Qualitative characterization of structural characteristics is often performed using a scanning electron beam microscope, an interferometer, and an optical microscope.

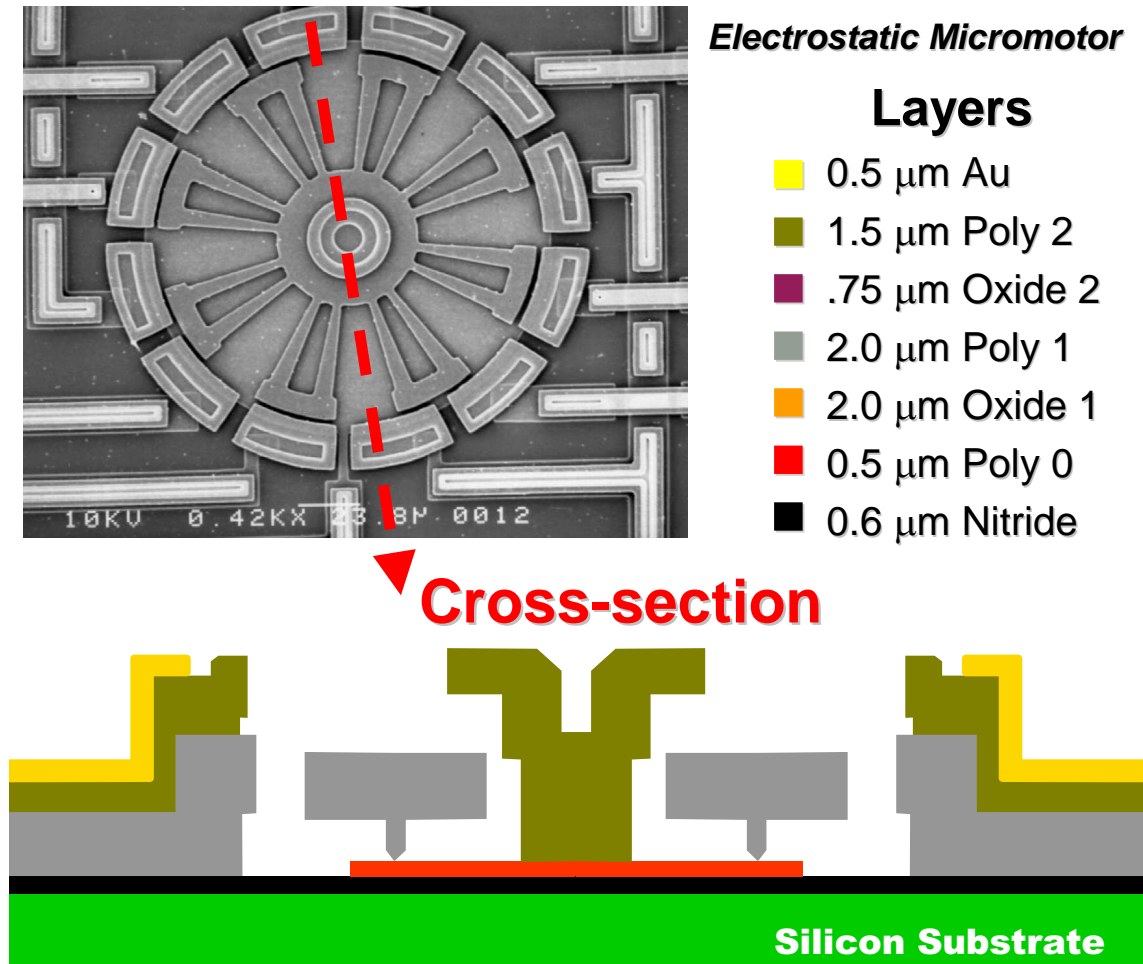


Figure 2.3: MUMPs[®] micromotor cross section and layer description [5]

As shown in Figure 2.4, quantitative measurements of material properties (such as Young's Modulus and stress) are typically performed on standard MEMS test structures (*i.e.*, comb-resonators or fixed-fixed-beams). These measurements (of comb-resonator frequency and fixed-fixed beam-buckling length) are straight-forward and generally only require a simple set of standard electrical characterization equipment such as an oscilloscope and digital multi-meter.

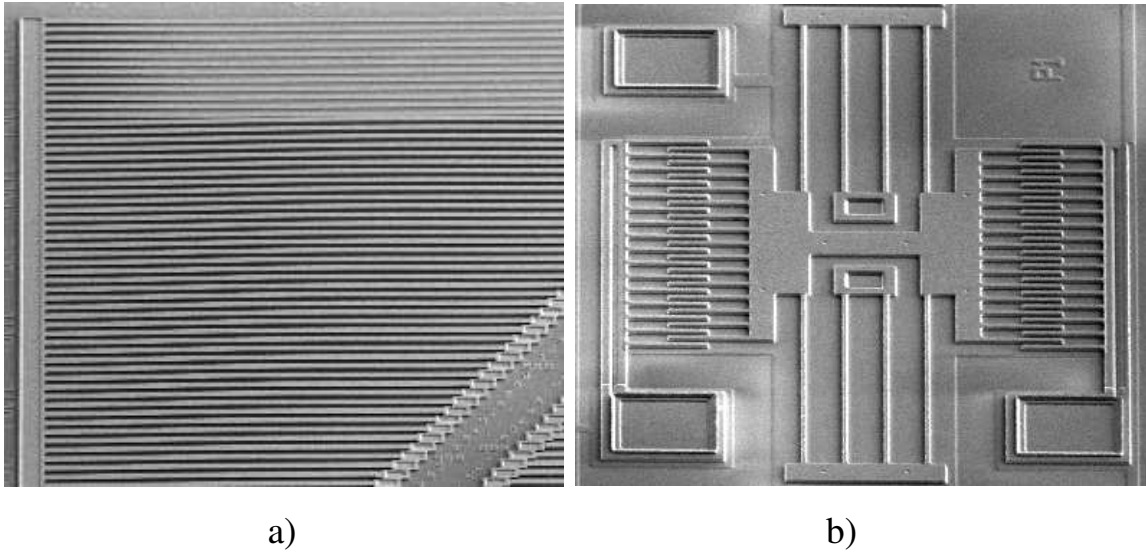


Figure 2.4: Example of polySi structures for material characterization: a) single-layer fixed-fixed beams, b) single-layer comb resonators. [SEM images of Author's devices]

2.2.5 MEMS Reliability and Packaging. The field of polySi MEMS is still maturing and several problems remain, such as industrial challenges (lack of MEMS standards), launch-shock resistance issues (Figure 2.5), friction, and adhesion at the molecular level [8,9]. Also, since MEMS are transducers (convert one form of energy to another), a lack of expertise exists in device optimization across and between multiple-energy domains. It is still rare to identify an individual who possesses expertise in both their field of study *and* MEMS.

The structural release process prior to packaging is typically performed via the sacrificial layer wet chemical etch. This is followed by a rinse to stop the etch, and

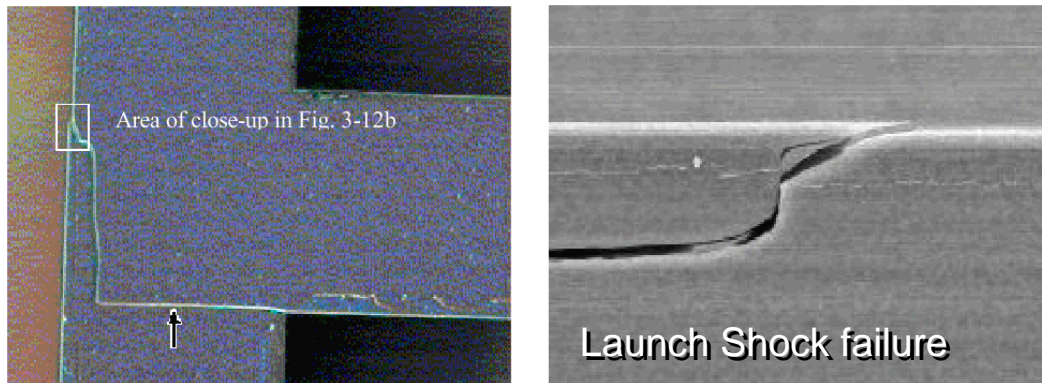


Figure 2.5: Example of MEMS missile launch shock failure [9]

then (rapid) evaporation via hot plate (or oven) bake. As the liquid evaporates, negative capillary forces induce surface tension on released structures. This often causes released structures to collapse and stick to underlying (or adjacent) structures as shown in Figure 2.6 [9].

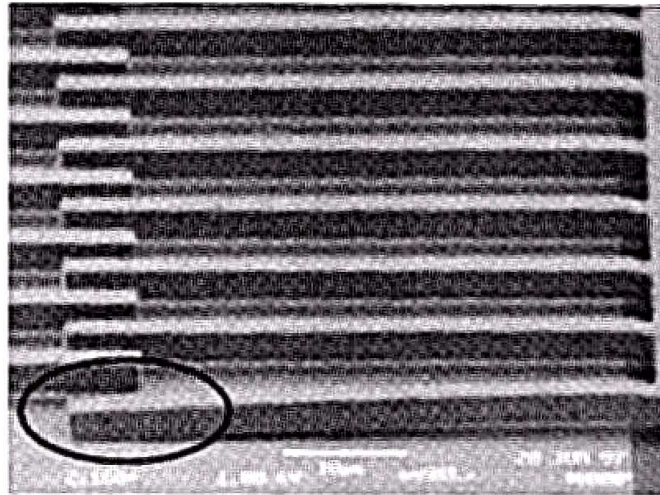


Figure 2.6: Wet etch-release structural sticking failure [9]

Alternatively, a dry (plasma) etch may be performed (Figure 2.7). However, toxic byproducts are often produced [10], and in some cases, a thin (wet) film may be left behind [11]. This film must then be wet-etched, and dried. Again, as the liquid evaporates, sticking problems may arise.

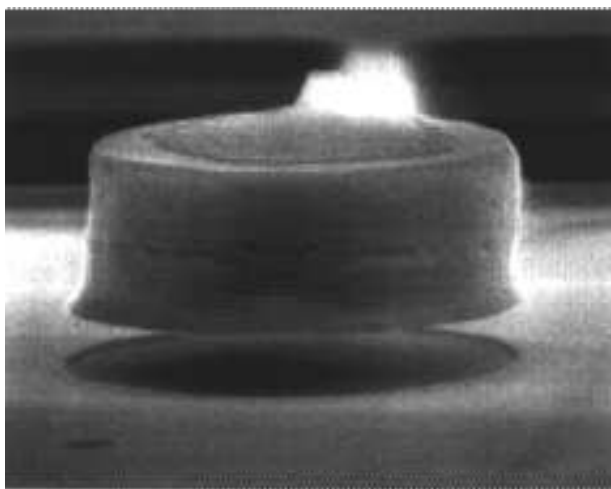


Figure 2.7: End view of freely suspended cantilever undercut using a dry (plasma) etch [12]

These sticking problems are referred to as stiction. Stiction may be caused by Van Der Waals forces, electrostatic forces, hydrogen bonding, chemical bonding, etch residues, and many other mechanisms [13]. To avoid stiction due to wet-release processing, MEMS developers may perform CO₂ critical point drying (CPD) [13]. Supercritical CO₂ has zero surface tension, thus, eliminating the capillary force [13]. In the CO₂ CPD process, liquid CO₂ enters the (typically) methanol-soaked chamber, which contains the sample. After the CO₂ completely replaces the methanol, the chamber temperature is increased until the critical point transition is achieved. As illustrated in Figure 2.8, this transition occurs when the CO₂ sublimates into gaseous carbon dioxide (at 1055 psi and 33.1 °C [11, 13]).

In addition to stiction-related yield problems, packaging-related process steps may be required, which are typically detrimental to MEMS-CMOS electronics. This added level of fabrication complexity makes the job of MEMS-CMOS integration extremely difficult. In particular, some etchants used in microfabrication attack exposed CMOS metallization, contaminate CMOS with impurities, are hazardous to use, and often present disposal problems [1, 14]. Additionally, in the case of surface micromachining, layer deposition temperatures near 600 °C and stress/resistivity-

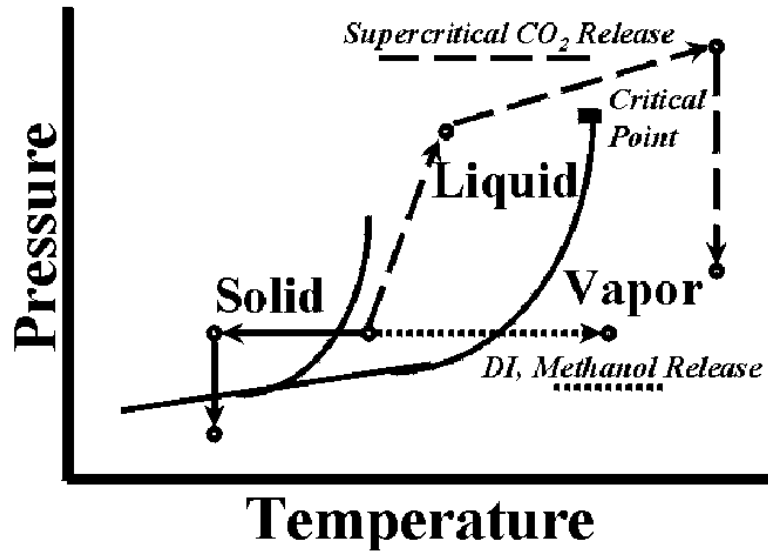


Figure 2.8: Illustration of supercritical CO₂ drying critical point transition [13]

reducing annealing temperatures near 900 °C are used. These high temperatures lead to degradation of metals and junctions and are generally not compatible with conventional CMOS metallization schemes [15]. Thus, over the last few decades, a tremendous investment has been made in developing practical MEMS-CMOS integration strategies to overcome these challenges and other problems due to the microfabrication process.

2.2.6 MEMS Integration. Many existing MEMS contain a transducer in one housing and electronics in a second housing connected to the transducer by wires [1]. There are several reasons for having the transducer and electronics in one housing, and the potential to allow this type of integration is considered one of the principal advantages of MEMS technology. In addition to improved performance and reduced cost, CMOS-MEMS integration is motivated by several of the following objectives [16]:

- The need for shielding is reduced because signals between transducer and microelectronics are often weak

- A method for system calibration is provided early in the design process
- Active control (by the microelectronics) is better done locally
- External interconnects make mounting complex and increase cost

Two basic strategies for microsystems integration are used: monolithic integration and hybrid integration [16]. In monolithic integration, the transducer and electronics are located on the same substrate. In hybrid integration, several components, each on an individual substrate, are put together into one system. As shown in Figure 2.9a, a monolithic solution has been achieved, which contains a MEMS transducer (3-axis accelerometer) in the center, surrounded by microelectronic circuitry co-located on the same chip [17]. The photograph in Figure 2.9b contains a commercially available hybrid solution to transducer and electronics integration [18]. In this case, the transducer and electronics were assembled into a single housing.

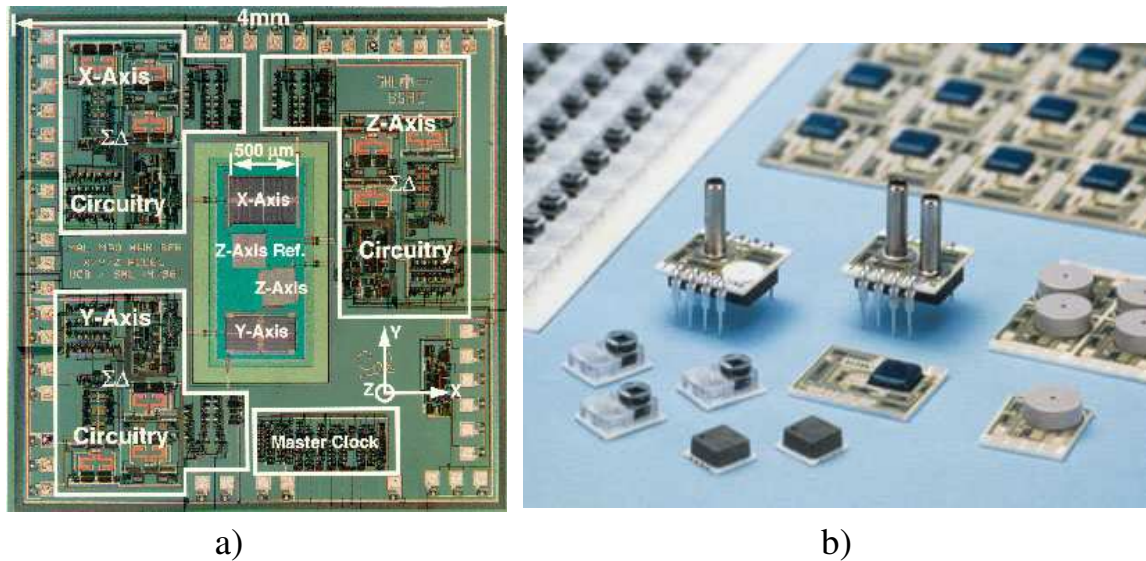


Figure 2.9: Examples of a) monolithic integration [17] and b) hybrid integration [18]

During the early stages of microsystems technology development, much time, money, and effort were focused on the development of monolithic systems [16]. Over

time, many researchers and commercial laboratories have found the hybrid approach more desirable due to several of the following factors [16]:

- Transducer development cycles are much slower than those for CMOS
- When yield problems occur, the hybrid approach allows discarding defective parts
- In microelectronics, a tendency now exists toward multi-chip modules
- Development of monolithic systems is difficult and expensive

Due to the tremendous cost, monolithic integration is typically feasible only for the case of products that are sold in large quantities, or for systems that must be monolithically integrated due to a large number of interconnects [16]. A commercially available example of a monolithically integrated device is the Texas Instruments Digital Multimirror Device[®] (TI DMD[®]) shown in Figure 2.10 [19]. Unfortunately, but understandably, the developers do not identify the fabrication process sequence [1]. However, upon inspection of the TI DMD[®] (Figure 2.10), one can see the developers have used surface micromachining techniques to build the micromirror structure over the CMOS addressing circuitry [1].

2.2.7 MOEMS. The TI DMD[®] is an example of the integration of MEMS and optics, referred to as Optical MEMS (OMEMS), Micro-Optical MEMS (MOMS), or MOEMS. MOEMS enable light-beam micro-manipulation such as diffraction, reflection, refraction, spatial deflection (Figure 2.10), and amplitude or wavelength modulation. MOEMS configurations span the range from arrays of integrated devices (TI DMD[®]) to integrated MOEMS such as the Free Space Micro-Optical Bench in Figure 2.11. As shown in Figure 2.11, in addition to micro-optical elements, MOEMS may include semiconductor diode lasers [20].

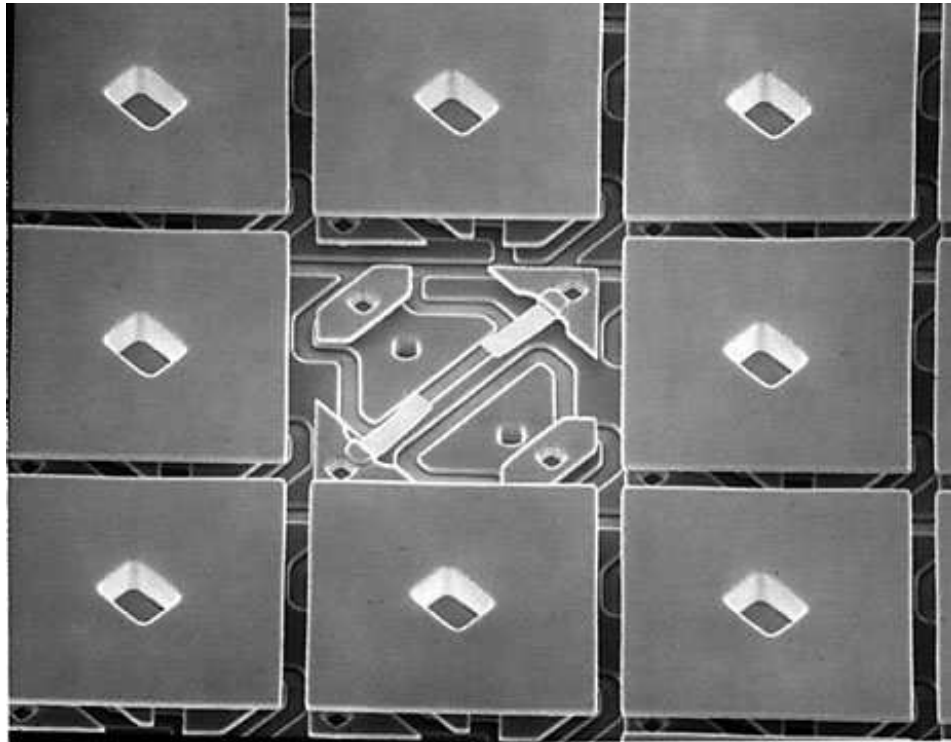


Figure 2.10: TI DMD® [19]

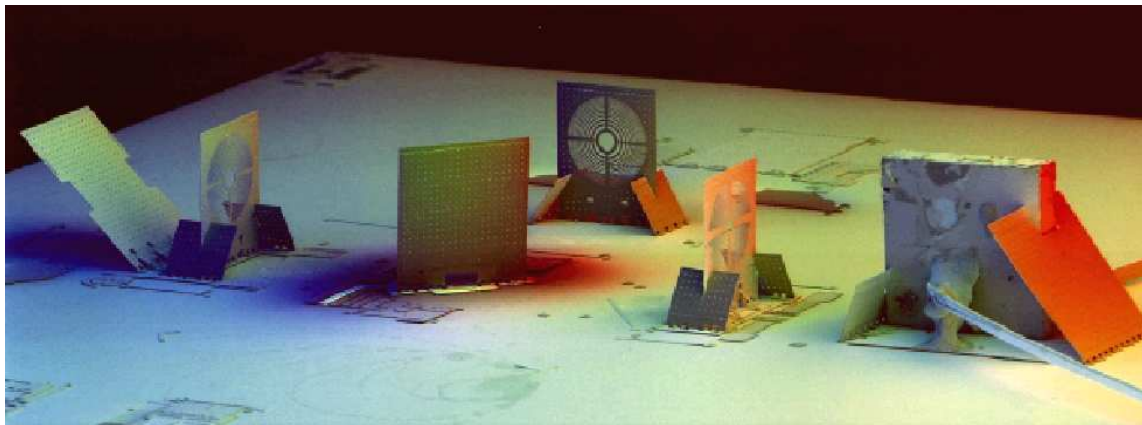


Figure 2.11: Micro-optical bench comprised of MEMS structures and an edge emitting semiconductor diode laser [20]

2.3 VCSEL

This section reviews VCSEL fundamentals. First, several advantages of VCSEL over EEL are presented. Next, the design and fabrication of VCSEL structures are discussed. Finally, recent work on VCSEL-CMOS integration is reviewed.

2.3.1 VCSEL Advantages. Semiconductor diode lasers are categorized by their emission direction with respect to the substrate. As shown in Figure 2.12b, an EEL emits light from a cleaved (mirror) edge, parallel to the substrate. In contrast, a VCSEL emits light perpendicular to the substrate (Figure 2.12a) [21].

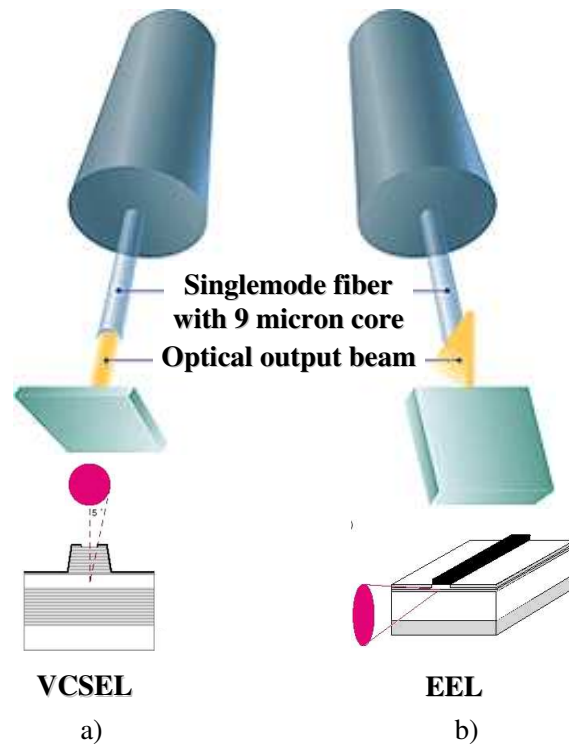


Figure 2.12: Semiconductor diode laser types and corresponding output beam divergence [21]: a) VCSEL, b) EEL

A VCSEL's vertical emission is enabled through the use of distributed Bragg reflector (DBR) mirrors for longitudinal optical confinement. Thus, a fundamental difference between VCSEL and EEL is elimination of facet mirrors fabricated by cleaving or dry etching. VCSEL have several advantages over EEL including: a

low divergence circular beam (Figure 2.12b), wafer-level testing capability *prior* to packaging, ease of making two-dimensional arrays, and single-mode operation (due to short optical cavity) [22–24]. The following list summarizes key advantages of VCSEL over EEL [25]:

- **Performance Advantages:** surface normal output, circular output beams, low beam divergence, small active volumes, low threshold currents, single longitudinal frequency, thermally stable operation, high-speed modulation, two-dimensional arrays
- **Manufacturing Advantages:** on-wafer testing, ease of integration, amenable to mass production high volume/high density, fabrication based on inexpensive microelectronics technology

2.3.2 VCSEL Design and Fabrication. As shown in Figure 2.13, a VCSEL consists of two highly reflecting DBR separated by an optical cavity [26]. Since the distance between the two DBR is on the order of a wavelength, the optical cavity is often referred to as a *microcavity* [27]. The DBR and optical cavity are comprised of multiple (possibly hundreds) semiconductor layers with stringent growth tolerances. As with any laser, the optical cavity contains a gain region in which the internal optical field is amplified. The gain region is typically made of multiple quantum wells (MQW), where the thickness of each QW is on the order of 100 Angstroms thick [11, 23].

The first reported VCSEL were not all-epitaxial structures (as shown in Figure 2.13). Early VCSEL included dielectric mirror stacks on either side of epitaxial active regions. This required complex post-growth processing and ultimately motivated the refinement of epitaxial growth techniques [26].

Precise epitaxial growth was, and in some cases remains, the limiting factor in VCSEL development. Since a VCSEL’s wavelength is directly related to layer thicknesses (discussed later), overall system growth stability on the order of 1% or

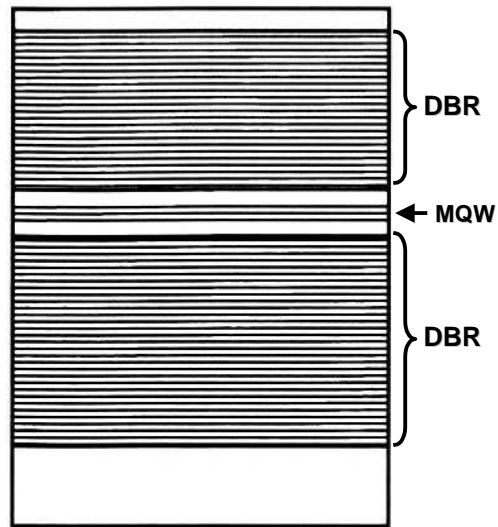


Figure 2.13: Schematic illustration of epitaxial VCSEL structure: top and bottom DBR sandwich the MQW active region optical cavity [26]

so is required to match the gain wavelength with the Fabry-Perot mode [26]. In practice, high precision and control of epitaxial VCSEL growth may be achieved via molecular beam epitaxy (MBE) (see Figure 2.14 [28]).

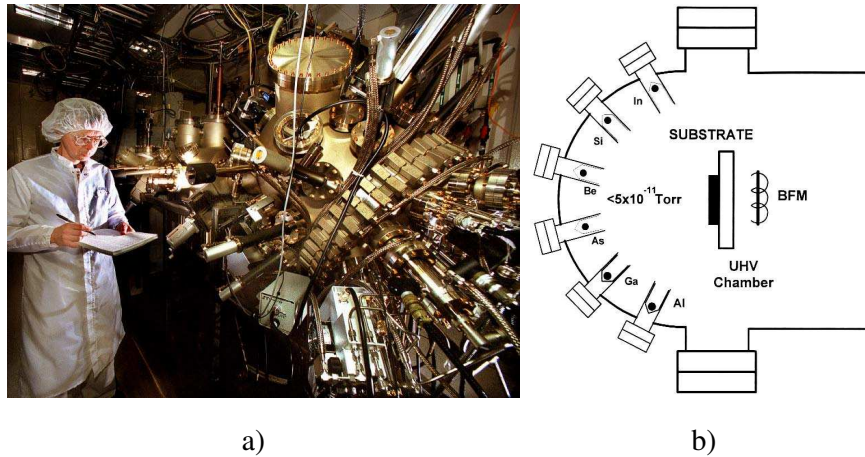


Figure 2.14: MBE system [28] and schematic illustration [26]

As illustrated in Figure 2.14, MBE growth is performed in an ultra-high vacuum; the required pressure prior to layer deposition is typically less than 10^{-10} Torr [26]. Layer deposition on a heated (single crystal) substrate is achieved through the reaction of multiple molecular beams of differing flux density and chemistry. The temperature of each source is stringently controlled to obtain desired layer composition. Each source is arranged around the (typically rotated) substrate to ensure film composition and thickness uniformity during growth. Additional compositional control is obtained via mechanical shutters between each source and substrate [26].

A wide variety of III-V alloys may be grown on GaAs and InP substrates. Moreover, many alloys offer advantages in performance and wavelength accessibility [25,26]. Figure 2.15 illustrates the energy bandgap (and corresponding emission wavelength) dependence on lattice constant.

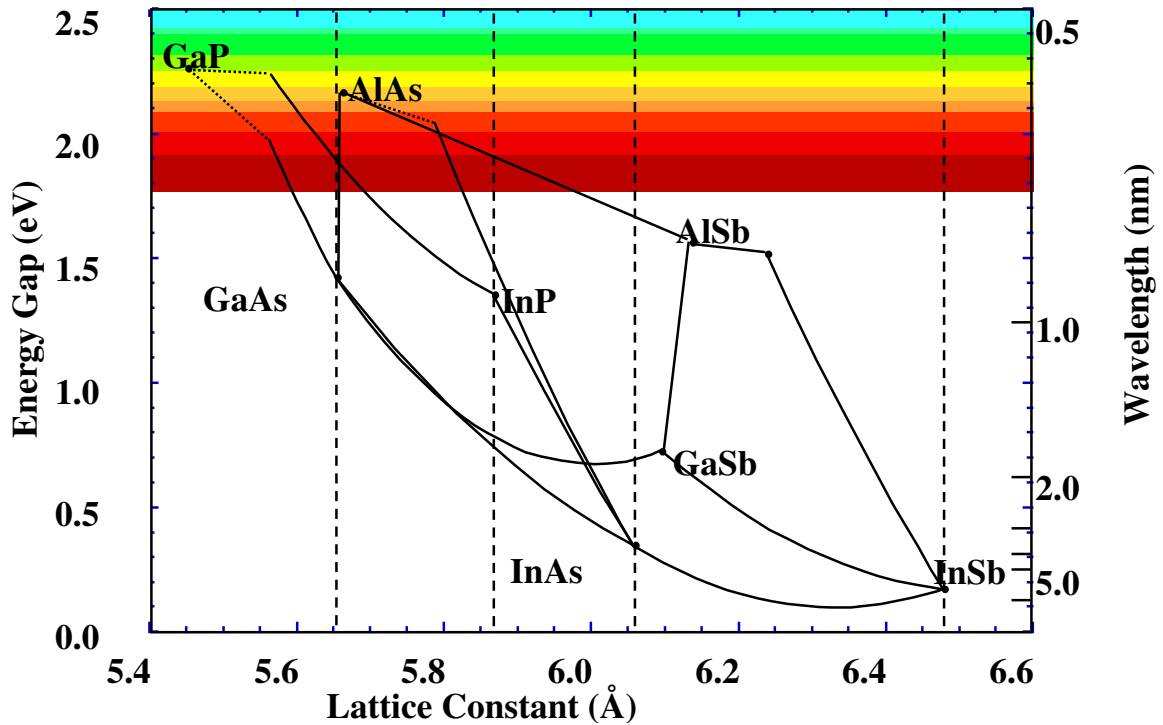


Figure 2.15: Energy bandgap (emission wavelength) dependence on lattice constant [25]

In practice, a VCSEL's emission wavelength is designed using Fabry-Perot fundamentals by sandwiching a precisely grown (composition and thickness) MQW optical cavity with coplanar DBR. DBR display a narrow band of high reflectivity known as the *stop-band*. A DBR typically consists of m -pairs of quarter-wave layers. Multiple reflections at DBR layer interfaces, and constructive interference of multiple reflected waves increase reflectivity with increasing m -pairs, reaching a maximum at the Bragg design wavelength (λ_D) [27].

2.3.3 VCSEL-CMOS Integration. As optoelectronics performance improves, the greater is the demand on the associated controlling CMOS circuits. Thus, it should be no surprise that efforts are ongoing to realize monolithic and hybrid optoelectronic-CMOS integration. As with MEMS-CMOS integration, there is no simple answer to the question of monolithic versus hybrid integration [29]. The following outline summarizes some of the advantages and disadvantages of hybrid and monolithically integrated optoelectronics-CMOS:

- **Monolithic Optoelectronic-CMOS Integration**

Advantages: single chip, few packaging interfaces

Disadvantages: high development cost, high production/equipment cost, non-planar interconnects, lower performance

- **Hybrid Optoelectronic-CMOS Integration**

Advantages: lower cost, shorter development time, can use standard chip technology, optimized component performance

Disadvantages: many packaging interfaces, poorer mechanical reliability, non-planar interconnects

Additionally, hybrid integration usually offers more flexibility in the choice of components and materials, because the components do not need to be lattice matched to the substrate [29].

As shown in Figure 2.16, arrays of flip-bonded VCSEL have been successfully demonstrated. As many as 64×64 VCSEL/CMOS arrays have been reported and 128×128 arrays are reported in development [30]. However, these chips require special handling after VCSEL bonding. Improvements in packaging processes may increase their robustness and make this technique suitable for very large arrays.

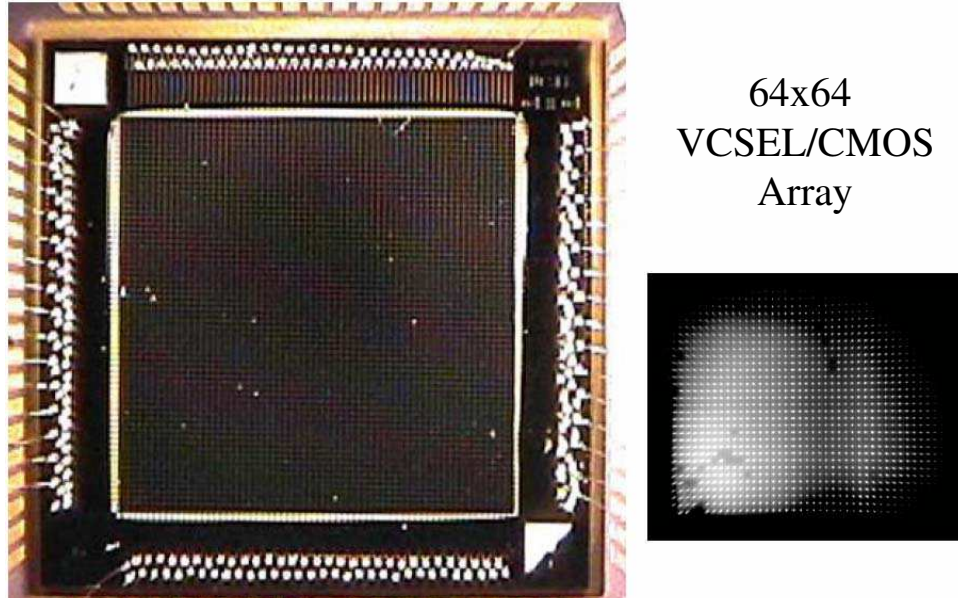


Figure 2.16: A 64×64 VCSEL array flip-bonded to CMOS [30]

2.4 Tunable Filters and Lasers

The huge demand for increased bandwidth and the potential for WDM have driven the quest for the “ideal” tunable laser. The ideal tunable laser is able to:

- 1) generate constant output power across a broad range of wavelengths;
- 2) maintain stable, narrow line-width emission in its operating environment;
- 3) has reasonable manufacturing requirements; and
- 4) cost-effective (price versus performance) [31].

Both semiconductor diode lasers and erbium-doped fiber lasers provide broad gain bandwidths. However, it is difficult to fabricate tunable erbium-fiber lasers because the laser cavity normally contains at least a meter of fiber [31]. Thus, this section reviews the following examples of tunable semiconductor diode lasers:

- tuning via distributed feedback (DFB), distributed Bragg-*reflection* (DBR_n) (denoted with n subscript to avoid confusion with the DBR abbreviation also used for distributed Bragg *reflectors*), and related DBR_n structures:
- “tunable” arrays of fixed-wavelength microlasers
- external-cavity tunable EEL
- MT-VCSEL designs and properties

2.4.1 DFB and DBR Tuning. DFB and DBR_n lasers are fundamentally similar to EEL; however, the cavity is typically defined by one or more virtual reflectors formed by a series of corrugations, known as a Bragg grating [32]. Single-wavelength output is selected by adjusting the spacing and refractive index of the grating. Tuning is typically achieved by varying the refractive index via thermal tuning as shown in Figure 2.17. Drawbacks to thermal tuning are high power consumption and slow response time.

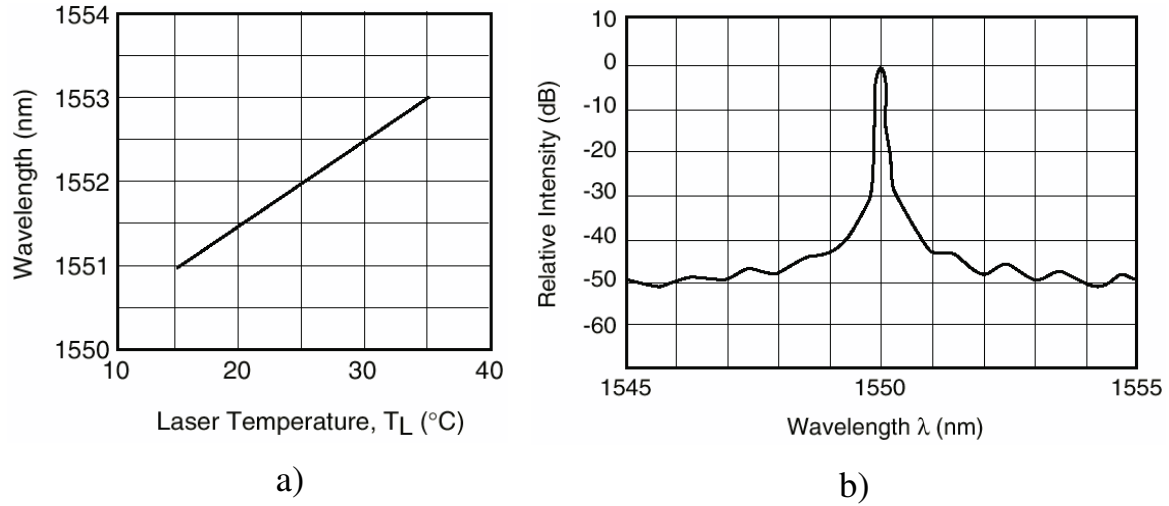


Figure 2.17: Temperature-tuned DFB laser: a) wavelength versus temperature, b) intensity versus wavelength [33]

DFB gratings are located in the laser’s active section; DBR laser gratings are typically electrically isolated from the active area. Tuning ranges for DFB are

typically on the order of a few nanometers, while tuning ranges more than 10-nm are possible for DBR_n structures. Tuning ranges have been extended to tens of nanometers by using a different type of DBR_n structure, known as a sampled-grating DBR_n (SG- DBR_n), as shown in Figure 2.18.

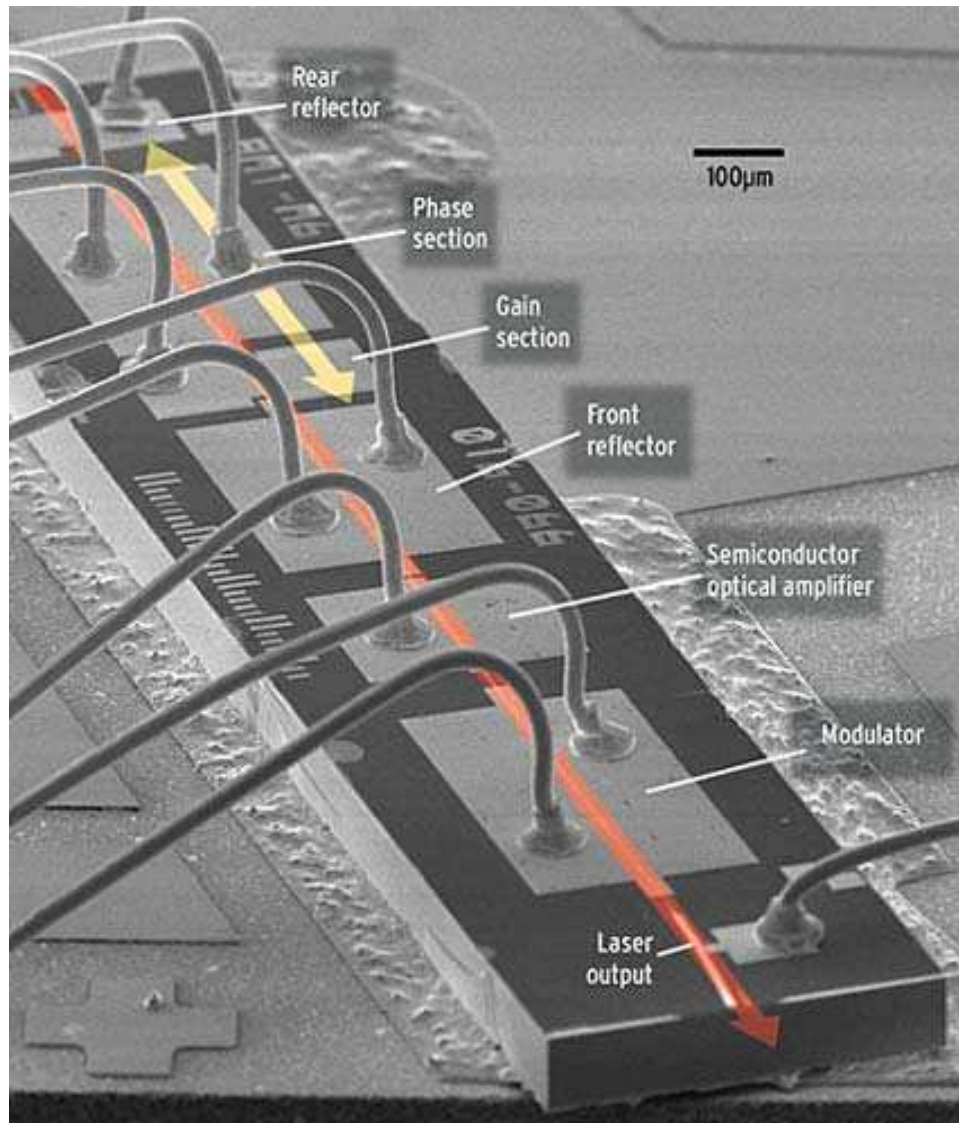


Figure 2.18: Current injection-tuned SG-DBR laser integrated with a semiconductor optical amplifier [34]

Each DBR_n region in the SG-DBR_n has sets of gratings with different spacings, which effectively reflect a comb-like series of wavelengths. Laser oscillation occurs when both SG-DBR_n gratings overlap wavelengths [31]. A related DBR_n approach is the grating-assisted coupler and sampled reflector (GCSR), which consists of four stages with distinct functions. The GCSR laser oscillation wavelength is current-controlled by the three stages as follows: the coupler section is used for coarse-tuning, the reflector section is used for moderate-tuning, and the phase section for fine-tuning [31].

2.4.2 External-Cavity MEM-Tunable Devices. The external-cavity configuration typically consists of an EEL with an anti-reflection (AR) coating (on one facet), a dispersive element, and a mirror. The dispersive element is used to spread out a range of wavelengths. Adjusting the dispersive element and the mirror provides feedback for tuning the laser to the desired wavelength [31].

In a *Littrow* external-cavity configuration, a reflective diffraction grating serves both as mirror and dispersive element. Pivoting the mirror changes both the length of the cavity and selects the resonant wavelength fed back to the EEL; light reflected from the grating becomes the laser output. In practice, Littrow cavities have been assembled using EEL and bulk optics for instrumentation and fiber optics [31].

As shown in Figure 2.19a and illustrated in Figure 2.19b, a Littrow external-cavity diode laser (ECDL) has been implemented via MEMS-microlaser hybrid integration. The mirror element is attached via flexural rotary suspensions to an electrostatic comb-drive MEMS actuator. Mirror rotation is achieved by applying up to 140V to the comb-drive actuators [35]. The movable reflector gives this laser both its great advantage and its main weakness - a wide tuning range and a low tuning rate, respectively [34].

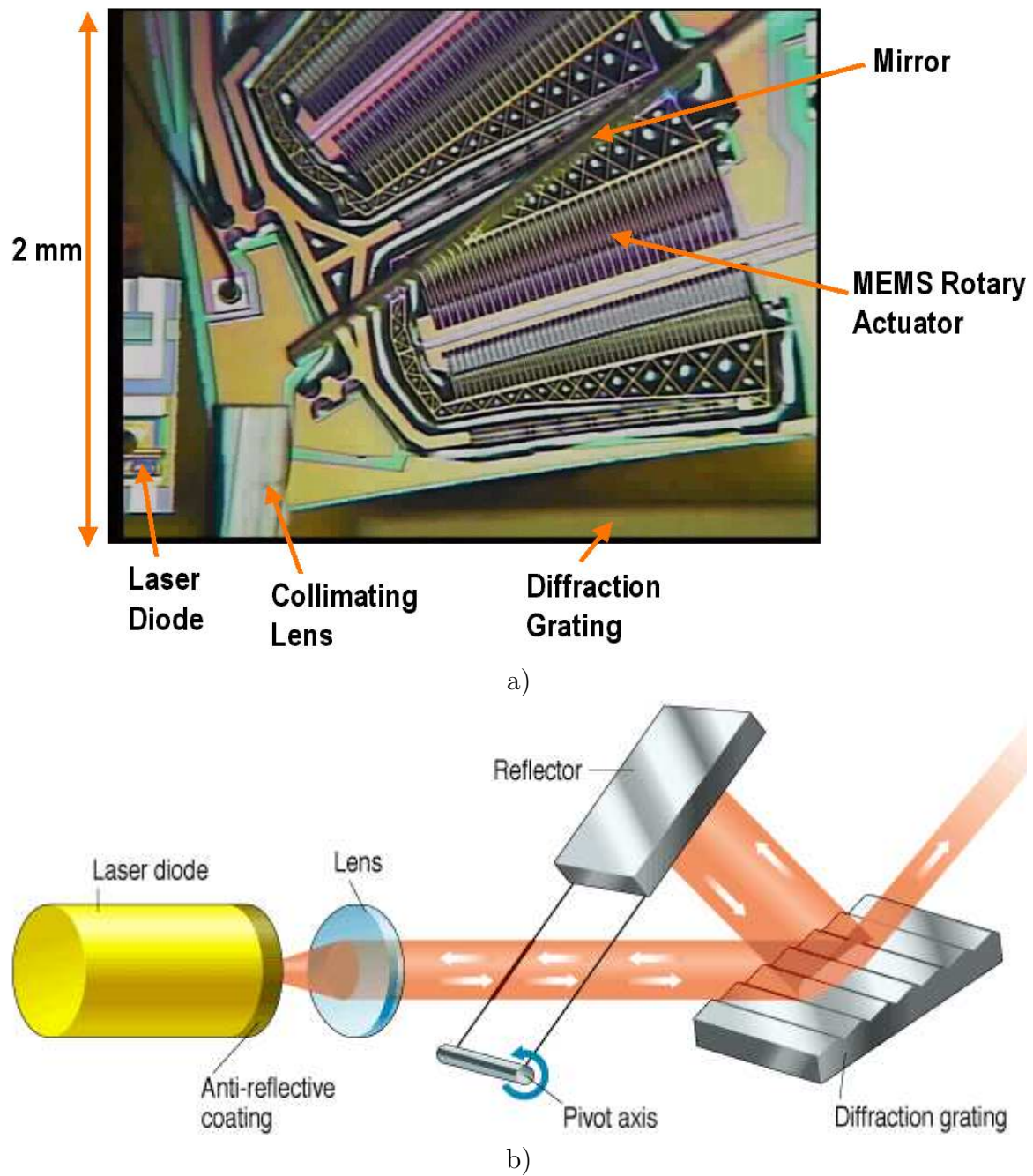


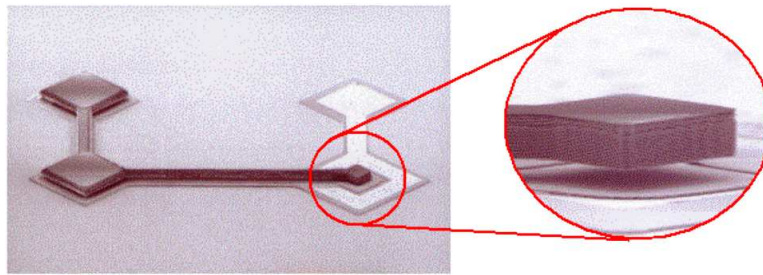
Figure 2.19: ECDL: a) device structure [35], b) a mirror rotating on a MEMS actuator is combined with a laser and a diffraction grating constitute a variable-wavelength filter, which adjusts the output wavelength [34]

2.4.3 MEM-TF and MT-VCSEL. MEMS actuation has been used to tune filters and VCSEL, referred to here as MEM-TF and MT-VCSEL, respectively. MT-VCSEL were developed to take advantage of several VCSEL properties mentioned earlier: simpler fiber coupling, easier (on-wafer) testing prior to packaging, the ability to be fabricated in arrays, and an inherent single-wavelength structure well suited for wavelength tuning [25,36]. In general, the first step toward MT-VCSEL development is the demonstration of a MEM-TF compatible with a proposed MT-VCSEL design [37].

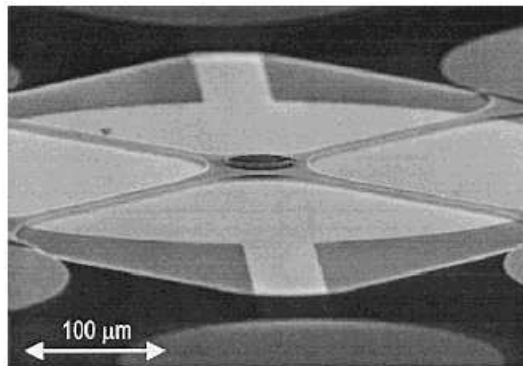
Reported MT-VCSEL are electrically pumped (EP) [36] (Figure 2.20a)) and optically pumped [38] (Figure 2.20b)). Electrostatic [37, 38] (Figure 2.20a) and b)), magnetic [39, 40] (Figure 2.20c)), and piezoelectric [41, 42] MEM-TF and MT-VCSEL actuation methods have been reported. The device's effective cavity length is adjusted by moving a MEM-actuated DBR mirror with respect to the laser gain medium, thus tuning the laser's output wavelength.

Most MT-VCSEL consist of a bottom DBR, active region, and a movable top DBR, which contains an adjustable air-gap layer [38, 40, 45]. Moving the top DBR toward the substrate reduces the air-gap, and thus tunes (blue-shifts) the Fabry-Perot's resonant frequency toward shorter wavelengths [45]. Since MT-VCSEL incorporate MEM-TF designs to enable tunability, several key factors in the design of MEM-TF and MT-VCSEL include (but are not limited to) the following:

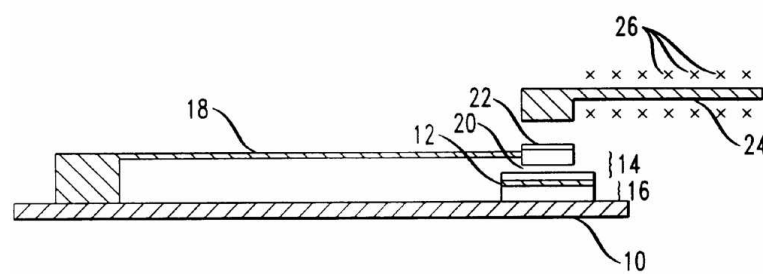
- For the same air-gap size, the farther the air-gap is from the center of the cavity, the less tuning may be obtained [45].
- To maximize tuning range, the air-gap size should be increased; however, this leads to a longer cavity (smaller free spectral range) and thus limits the tuning range [45].



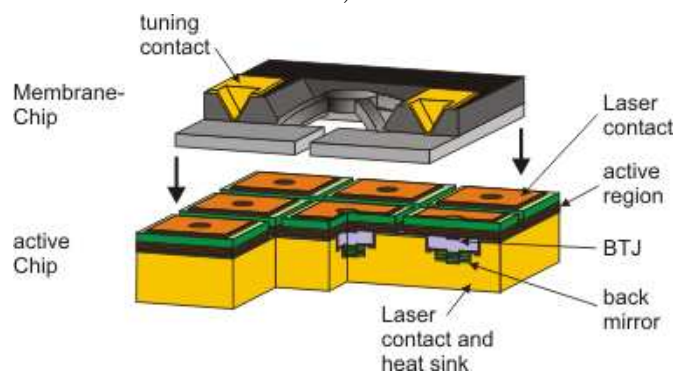
a)



b)



c)



d)

Figure 2.20: MT-VCSEL examples: a) cantilever actuator, electrostatically tuned [37], b) half-symmetric cavity, piston actuator, electrostatically tuned [38], c) cantilever actuator, magnetically tuned [40], d) half-symmetric cavity, ohmic (thermal) actuator, current tuned [43, 44]

- The maximum deflection is typically limited to one-third the initial air-gap for electrostatically actuated MT-VCSEL [45]. (As the deflection of the upper DBR approaches approximately one-third the initial air-gap, the electrostatic force is increasing more rapidly than the DBR's supporting flexure force; the system becomes unstable, and the DBR snaps down [6].) This mechanically limits tuning range. As a work-around, the air-gap thickness may be increased; however, this leads to higher actuation voltages.
- Reducing the thickness of the p-doped DBR (located between the air-gap and active region) increases tuning range. However, this leads to less uniform current injection [45].

Thus, MEM-TF/TVCSEL design and performance optimization requires a balance between several design trade-offs. These considerations add many challenges and opportunities to optimize MEM-TF/TVCSEL design and fabrication [45].

2.5 Chapter Summary

This chapter reviewed MEMS, semiconductor diode lasers, and tunable semiconductor lasers. MEM-TF and MT-VCSEL designs have performance limitations typically attributed to the monolithic design approaches used to fabricate these devices. Hybrid integration introduces new design options and may enable new performance attributes for MEM-TF and MT-VCSEL. Thus, a new design trade space for hybrid MEM-TF and MT-VCSEL exists which is investigated in the latter portion of the following chapter.

Bibliography

1. G. T. A. Kovacs, *Micromachined Transducers Sourcebook*. WCB/McGraw-Hill, 1998.
2. W. D. Cowan, "Introduction to Micro-Electro-Mechanical Systems (MEMS)," *Defense Manufacturing Conference*, 2001.
3. MEMS Exchange, "What is MEMS Technology?" Internet, www.mems-exchange.org/MEMS/what-is.html, last accessed January 2007.
4. G. A. Magel, "Tutorial: Micromachining in optics," OSA Annual Meeting, October 1996, www.dlp.com/dlp/resources/whitepapers/pdf/micro.pdf.
5. D. A. Koester, R. Mahadevan, B. Hardy, and K. W. Markus, *MUMPs® Design Handbook, Revision 6.0*. Cronos Integrated Microsystems, 2001, www.memsrus.com/cronos/mumps.pdf.
6. W. D. Cowan, "Foundry Microfabrication of Deformable Mirrors for Adaptive Optics," Ph.D. dissertation, Air Force Institute of Technology, Department of Electrical and Computer Engineering, Wright Patterson AFB, OH, 1998, AFIT/DS/ENG/98-07.
7. D. Miller, "Microelectromechanical systems design using the MUMPs® foundry process," Online Article, March 2000, mems.colorado.edu/c1.res.ppt/ppt/g.design/slide001.htm.
8. Potomac Institute for Policy Studies, "Out of the Box and Into the Future: A National Security Forecast," Internet, June 2000, www.potomacinstitute.org/research/outoftheboxstudy.htm.
9. B. Stark, "MEMS Reliability Assurance Guidelines for Space Applications," Internet, January 1999, parts.jpl.nasa.gov/docs/JPL%20PUB%2099-1A.pdf.
10. T. R. Nelson, "Personal interviews," Electro-Optical Team Lead, Air Force Research Laboratory, Sensors Directorate, Wright-Patterson AFB, OH. August 2000 - January 2007.
11. M. Y.-Y. Li, "Wavelength-Tunable Micromechanical Vertical Cavity Surface Emitting Lasers," Ph.D. dissertation, University of California, Berkeley, Berkeley, CA, 1999.
12. C. J. Chang-Hasnain, E. Vail, and M. Wu, "Isotropic Selective Dry Etching of GaAs/AlGaAs for Micromachining Optoelectronic Tunable Devices," Department of Electrical Engineering, Stanford University, www-snf.stanford.edu/Projects/Hasnain-Wu/Isotropic.gif.

13. I. Jafri, H. Moritz, H. Busta, and S. Walsh, "Critical point drying and cleaning for MEMS technology," in *MEMS Reliability for Critical and Space Applications*, ser. Proceedings of SPIE, R. A. Lawton, W. M. Miller, G. Lin, and R. Ramesham, Eds., vol. 3880. SPIE, 1999, pp. 51–58.
14. N. H. Tea, V. Milanovic, C. A. Zincke, J. S. Suehle, M. Gaitan, M. E. Zaghloul, and J. Geist, "Hybrid Postprocessing Etching for CMOS-Compatible MEMS," *Journal of Microelectromechanical Systems*, vol. 6, no. 4, pp. 363–367, December 1997.
15. A. Franke, "Micro-electromechanical systems technology," Internet, diva.eecs.berkeley.edu/~tking/mems.html, last accessed January 2007.
16. W. Lang, "Reflections on the Future of Microsystems," *Sensors and Actuators: A (Physical)*, vol. 72, pp. 1–15, 1999.
17. M. Lemkin, M. Ortiz, N. Wongkomet, B. Boser, and J. Smith, "A 3-axis surface micromachined sigma-delta accelerometer," in *Proc. ISSCC '97*, Feb. 1997, pp. 202–203.
18. TRW NovaSensor Online Catalog, "NPC Series Silicon Pressure Sensors in Ceramic Packages," Internet, www.novasensor.com/catalog/NPCSeries.html.
19. Texas Instruments, "Texas Instruments Digital Multimirror device," Internet, Jan 1999, www.ti.com/dlp/docs/developer/resources/library/pixels_micro.shtml.
20. Department of Defense, "Special technology area review on microoptoelectromechanical systems (MOEMS)," Department of Defense Advisory Group on Electron Devices Working Group C (Electro-Optics), Office of the Under Secretary of Defense Acquisition and Technology, Washington, DC 20301-3140, Tech. Rep., December 1997.
21. VERTILAS GmbH, "VCSELs for Data/Telecommunication Applications," Internet, www.vertilas.com/produkte_daten_.php, last accessed January 2007.
22. K. D. Choquette, *The Technology of Selectively Oxidized Vertical-Cavity Lasers*, ser. Optoelectronic Properties of Semiconductors and Superlattices. Gordon and Breach Science Publishers, 2000, ch. 2, pp. 279–318.
23. K. D. Choquette and K. M. Geib, *Vertical-Cavity Surface Emitting Lasers*. Cambridge University Press, 1999, ch. 5, pp. 193–232.
24. R. C. Williamson, *Vertical-Cavity Surface Emitting Lasers*. Cambridge University Press, 1999, ch. 9, pp. 334–347.
25. C. Sullivan and K. Choquette, "Research at Sandia National Laboratories in Optical Interconnects," in *Optical Interconnects for High Performance Computing Workshop*, Oak Ridge National Laboratory. Internet, Nov 1999, www.ornl.gov/sci/optical/docs/SullivanSNL19991108.ppt.

26. R. P. Schneider and Y. H. Houn, *Vertical-Cavity Surface Emitting Lasers*. Cambridge University Press, 1999, ch. 4, pp. 108–192.
27. E. F. Schubert and N. E. J. Hunt, *Vertical-Cavity Surface Emitting Lasers*. Cambridge University Press, 1999, ch. 5, pp. 68–107.
28. Sandia National Laboratories, “CRADA with Cielo Communications makes development possible,” Internet, June 2000, <http://www.sandia.gov/media/NewsRel/NR2000/laser.htm>.
29. C. W. Wilmsen, *Vertical-Cavity Surface Emitting Lasers*. Cambridge University Press, 1999, ch. 12, pp. 417–448.
30. BAE Systems, “VLSI Photonics Common Optical Module,” Internet, July 2001, www.darpa.mil/MTO/VLSI/Presentations/Ciemiewicz.pdf.
31. J. Hect, “Tuning in to tunable lasers,” Internet, March 2001, lfw.pennnet.com/Articles/Article_Display.cfm?Article_ID=95878.
32. P. Heywood, “Tune In!” Light Reading, April 2000.
33. Fujitsu Compound Semiconductor, Inc., “1,550nm MQW-DFB DWDM Direct Modulation Laser,” Internet, www.fcsi.fujitsu.com/products/LWpdf/FLD5F6CX-E.pdf, last accessed January 1999.
34. E. Bruce, “Tunable Lasers,” *IEEE Spectrum*, Feb 2002, www.spectrum.ieee.org/WEBONLY/publicfeature/feb02/tunaf3.html.
35. J. Berger, Y. Zhang, J. Grade, H. Lee, S. Hrinya, H. Jerman, A. Fennema, and A. Tselikov, “Micro External Cavity Laser (ECL) Presentation,” Internet, March 2001, www.iolon.com/ppt/ofc_jberger.pps.
36. C. Chang-Hasnain, “Tunable VCSEL,” *IEEE Journal On Selected Topics in Quantum Electronics*, vol. 6, no. 6, pp. 978–987, November/December 2000.
37. C. J. Chang-Hasnain, “The Optical Awakening,” Internet, July 2000, www.nacsa.com/slides/connie_slides_index.html.
38. P. Tayebati, “Half-Symmetric Cavity Tunable Microelectromechanical VCSEL with Single Spatial Mode,” *IEEE Photon. Technol. Lett.*, vol. 10, no. 12, pp. 1679–1681, December 1998.
39. H.-K. Lee, K.-S. Kim, and E. Yoon, “A Wide-range Linearly Tunable Optical Filter using Lorentz Force,” *IEEE Photon. Technol. Lett.*, vol. 16, pp. 2087–2089, Sept 2004.
40. S. Jin and H. Mavoori, “Magnetically Tunable And Latchable Broad Range Semiconductor Laser,” U.S. Patent and Trademark Office, November 2000, patent Number: 6,154,471.

41. S. Eliahou-Niv, R. Dahan, and G. Golan, "Design and analysis of a novel tunable optical filter," *Microelectronics Journal*, vol. 37, pp. 302–307, 2006.
42. M. C. Y. Huang, K. B. Cheng, Y. Zhou, B. Pesala, and C. J. Chang-Hasnain, "Demonstration of Piezoelectric Actuated GaAs-Based MEMS-Tunable VCSEL," *IEEE Photon. Technol. Lett.*, vol. 18, pp. 1197–1199, May 2006.
43. Walter Schottky Institute, "Tunable VCSELs: Device structure," Internet, 2007, www.wsi.tum.de/E26/en/research/tunvcsel/index.htm.
44. M. Maute, B. Kogel, G. Bohm, P. Meissner, and M.-C. Amann, "MEMS-Tunable 1.55- μ m VCSEL With Extended Tuning Range Incorporating a Buried Tunnel Junction," *IEEE Photon. Technol. Lett.*, vol. 18, pp. 688–690, 2006.
45. C. J. Chang-Hasnain, *Micromechanical Tunable VCSEL*, ser. Optoelectronic Properties of Semiconductors and Superlattices. Gordon and Breach Science Publishers, 2000, ch. 6, pp. 279–318.

III. Impetus for Studying the Hybrid MT-VCSEL

3.1 Chapter Overview

This chapter reviews the custom-developed modeling tools and the design studies performed in the course of this research to simulate the performance of hybrid MEM-TF/TVCSSEL devices. Specifically the following sections are reviewed:

- **Computer-aided design (CAD) Toolkit:** In this section, the following CAD tools are reviewed: electrostatic piston deflection calculation, VCSEL resonant wavelength modeling, DBR modeling toolkit, and MEM-TF/MT-VCSEL-CAD (MT-CAD).
- **PolySi prototypes for flip-bonded hybrid MEM-TF and MT-VCSEL:** In this section, two polySi mechanical structures for flip-bonded hybrid MEM-TF and MT-VCSEL were characterized by comparing simulations with foundry fabricated actuators.
- **CAD comparisons of monolithic and hybrid MT-VCSEL:** In this section, the MT-CAD methodology was used to investigate the resonant frequency design space for monolithic and hybrid MT-VCSEL.

The CAD investigations demonstrated key advantages of a hybrid MT-VCSEL over monolithic devices. Some of the hybrid advantages demonstrated in this chapter include the following: enabled the use of MUMPs® dimples to reduce stiction, enabled independent design and optimization of mechanical and optical elements, enabled use of identical mechanical prototypes in different wavelength-tunable applications, and simulations indicated a performance trade space which includes MEM-TF or MT-VCSEL linear wavelength-tuning as a function of applied actuation voltage. The simulations also demonstrated the monolithic MT-VCSEL resonant wavelength was more sensitive to variations in III-V growth than hybrid MT-VCSEL. Finally, since the hybrid design was comprised of a MUMPs® polySi mechanical actuator,

pull-in voltage remained independent of the initial optical air-gap between the tuning reflector and the III-V material.

3.2 CAD Toolkit

3.2.1 Electrostatic Piston Deflection. In this research, the basic electrostatic piston deflection calculation described by Cowan [1] is used to analytically model MT-VCSEL deflection dependence on actuation voltage. As shown in Figure 3.1, the basic electrostatic piston device consists of two parallel-plate electrodes separated by a dielectric gap with thickness, g . In this research, the dielectric gap is assumed to consist of air.

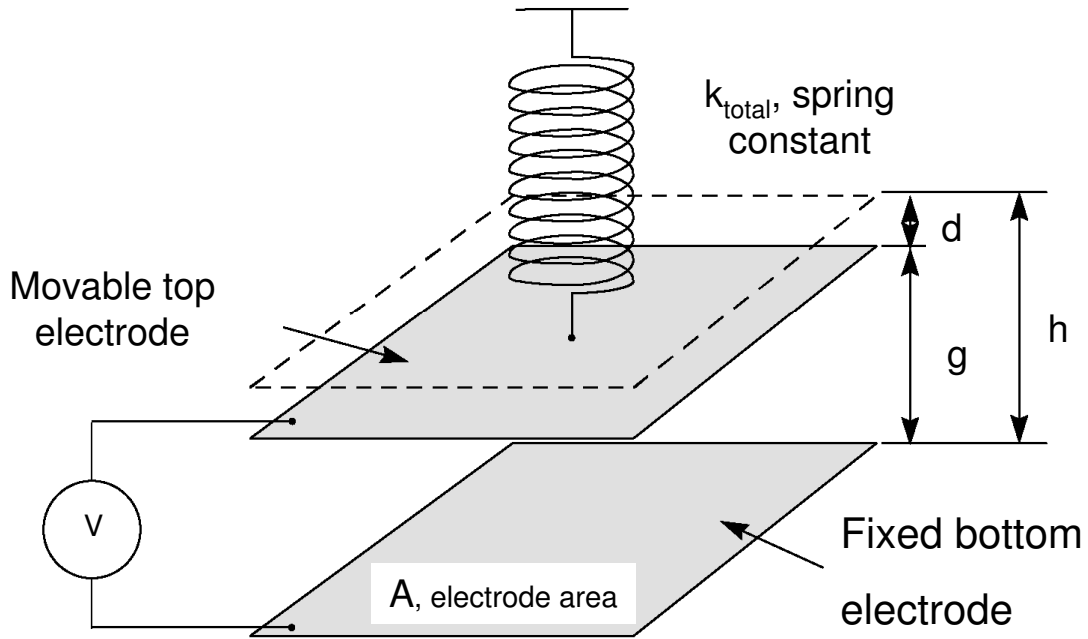


Figure 3.1: Schematic of basic electrostatic piston device [1]

The movable upper electrode is supported by $i = [1, 2, \dots, n]$ spring flexures with total spring constant k_{total} , given by

$$k_{total} = \sum_{i=1}^n k_i \quad (3.1)$$

where

$$k_i = \left[\frac{Y_i w_i t_i^3}{l_i^3} + \frac{S_i(1 - \sigma_i) w_i t_i}{2l_i} \right] \quad (3.2)$$

where Y_i is Young's Modulus of flexure i , S_i is residual stress of flexure i , σ_i is Poisson Ratio of flexure i , and w_i , l_i , and t_i are flexure i 's width, length, and thickness, respectively.

The lower electrode is fixed. If a voltage potential is applied across the overlapping electrode areas, the electrostatic force is given by

$$F = \frac{A \varepsilon_0 V^2}{2g^2} \quad (3.3)$$

where A is the overlapping electrode area, ε_0 is the dielectric constant of air, 8.854×10^{-12} F/m, and V is the voltage across the electrodes. For small deflections, the counter force applied by the spring flexures is $F = k_{total}d$. Thus, the force balance equation for the system is given by

$$k_{total}d = \frac{A \varepsilon_0 V^2}{2(h - d)^2} \quad (3.4)$$

where $g = (h - d)$, h is the initial air-gap thickness, and d is the deflection of the upper electrode toward the lower electrode. Solving Equation (3.4) for V gives

$$V = (h - d) \sqrt{\frac{2k_{total}d}{\varepsilon_0 A}} \quad (3.5)$$

where V is the actuation voltage and d is the corresponding deflection of the upper electrode. When V increases, d decreases. As d approaches $h/3$, the electrostatic attractive force overwhelms the restoring force of k , and the result is the top plate slamming down onto the bottom electrode, often with catastrophic results. This

“pull-in” instability is well-known in the MEMS community, and the corresponding voltage is known as the “pull-in” voltage, $V_{pull-in}$.

3.2.2 VCSEL Resonant Wavelength. The transfer matrix- (M -) method of Yeh [2] is used to model MT-VCSEL resonant wavelength dependence on air-gap thickness. The M -method relies on the following assumptions [3]:

- nonmagnetic films
- isotropic and homogeneous materials
- smooth interfaces without scatter
- plane parallel films of infinite lateral extent
- semi-infinite incident and substrate media
- linear wave equation

The general multi-layer structure used to model MEM-TF or MT-VCSEL resonant wavelength dependence on air-gap thickness is shown in Figure 3.2. This method is used to model various multi-layer designs, examine the overlap of electric-field (E-field) intensity with gain layers, and model phase penetration depth into DBR mirrors. This method has been implemented via computer programs to serve as design tools [4]. The refractive index, $N(\omega) = n(\omega) - i\kappa(\omega)$, is complex in each layer to model absorption.

The M -method [2] uses 2×2 “dynamical” (D) and “propagation” (P) matrices to relate the incident (E^+) and reflected (E^-) E-field vectors to the same quantities at either side of an interface. Matrix multiplication is performed to find an overall M . The amplitudes of the incident and reflected E-field plane waves at $x = 0$ are related to those at $x = t$ by

$$\begin{pmatrix} E_o^+ \\ E_o^- \end{pmatrix} = \begin{pmatrix} M_{11} & M_{12} \\ M_{21} & M_{22} \end{pmatrix} \begin{pmatrix} E_s^+ \\ E_s^- \end{pmatrix} \quad (3.6)$$

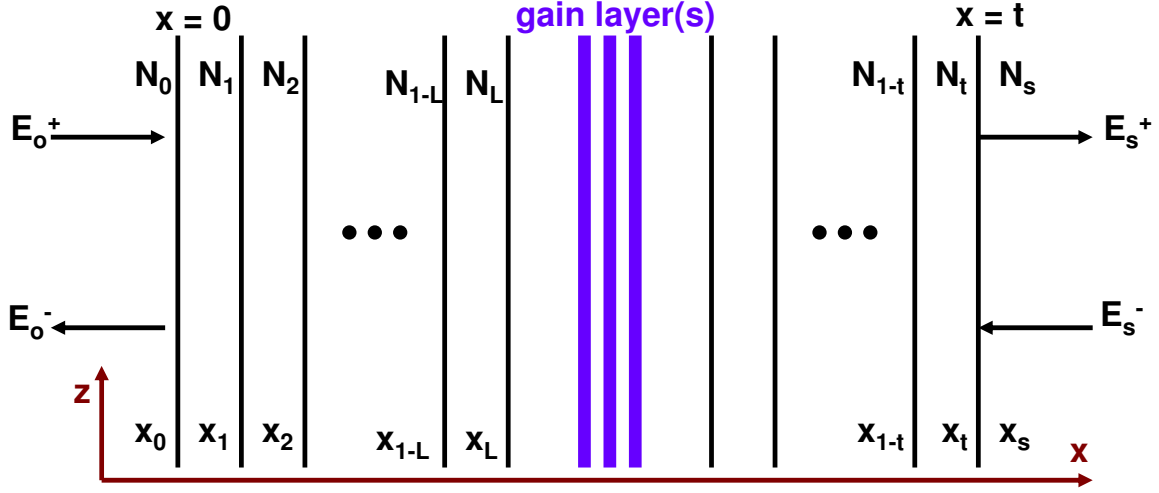


Figure 3.2: General multi-layer structure used to model E -field intensity on resonance

where M is given by

$$M = \begin{pmatrix} M_{11} & M_{12} \\ M_{21} & M_{22} \end{pmatrix} = D_o^{-1} \left[\prod_{L=1}^t D_L P_L D_L^{-1} \right] D_s \quad (3.7)$$

and $L = 0, 1, 2, \dots, t, s$. At normal incidence, the dynamical matrices for arbitrary layer L , are given by

$$D_L = \begin{pmatrix} 1 & 1 \\ N_L & -N_L \end{pmatrix} \quad (3.8)$$

and

$$D_L^{-1} = \frac{1}{2} \begin{pmatrix} 1 & \frac{1}{N_L} \\ 1 & -\frac{1}{N_L} \end{pmatrix} \quad (3.9)$$

where N_L is the complex index of refraction for layer L . The propagation matrix for layer P_L , is given by

$$P_L = \begin{pmatrix} e^{i\varphi_L} & 0 \\ 0 & e^{-i\varphi_L} \end{pmatrix} \quad (3.10)$$

where

$$\varphi_L = k_{Lx}d_L \quad (3.11)$$

and

$$k_{Lx} = N_L \frac{\omega}{c_o} = N_L \frac{2\pi}{\lambda_o} \quad (3.12)$$

and where d_L is the thickness of layer L , and k_{Lx} is the x component of the wave vector. The E-field amplitude through the structure is given by

$$E(x) = \begin{cases} E_o^+ e^{-ik_{ox}(x-x_o)} + E_o^- e^{ik_{ox}(x-x_o)} & : x < x_o \\ E_L^+ e^{-ik_{Lx}(x-x_L)} + E_L^- e^{ik_{Lx}(x-x_L)} & : x_{L-1} < x < x_L \\ E_s^+ e^{-ik_{sx}(x-x_t)} + E_s^- e^{ik_{sx}(x-x_t)} & : x_t < x \end{cases} \quad (3.13)$$

From Equation (3.6), the reflectance coefficient (ρ) with $E_s^- = 0$ is given by

$$\rho = \frac{M_{21}}{M_{11}} \quad (3.14)$$

The numerical method used to find the resonant wavelength relies on the following assumptions [3]:

- The reflectance of the bottom DBR is 1.0 (within numerical precision) as seen from the optical cavity
- The gain layers provide uniform and equal gain

To solve for the resonant wavelength, the imaginary part of the refractive index (κ) for the gain layers in Figure 3.2 is made negative (providing gain) to minimize the E-field intensity at the substrate over a range of wavelengths slightly above and below λ_D . The minimum E-field intensity at the substrate is found numerically, and the corresponding wavelength is the resonant wavelength (λ_R).

3.2.3 Multi-layer, Thin-film Simulation Toolkit. As shown in Figure 3.3, in the course of this research, *oeng775tools* [4] was developed. This custom MATLAB® “toolbox” is a set of functions to design, simulate, and visualize multi-layer thin-film characteristics such as power reflectance, absorption, transmission, reflectivity phase, and E-field intensity.

The *oeng775tools* MATLAB® toolbox is available to members of AFRL, and has been used for several years by AFIT to support the course, OENG 775, Introduction to Photonics Devices [4]. (Note: this MATLAB® toolkit is compatible with student and professional versions of MATLAB® .) Unless otherwise noted, all research prototype simulations are performed using *oeng775tools*.

3.2.4 MT-CAD. As illustrated in Figure 3.4, a MT-CAD methodology was custom-developed for this research and includes the following characteristics:

- Able to incorporate analytic or (Finite Element Model) MEM-TF or MT-VCSEL CAD simulations
- Able to automatically simulate and calculate the resonant frequency of a MEM-TF or MT-VCSEL for an arbitrary air-gap
- Able to automatically generate a two-dimensional visualization of MEM-TF or MT-VCSEL resonant frequency and deflection as a function of actuation voltage

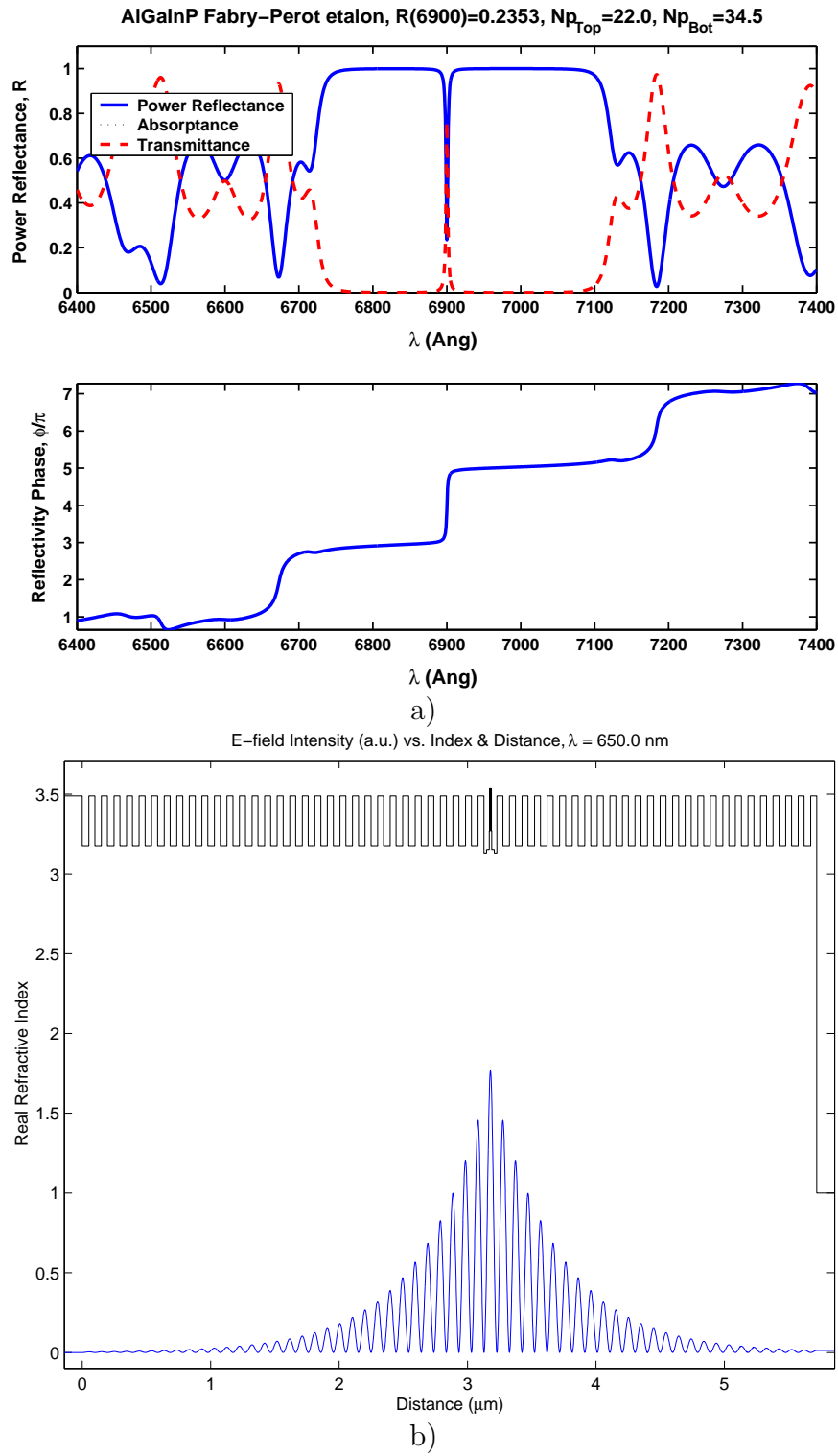


Figure 3.3: Tutorial simulation results included with *oeng775tools*: a) Fabry-Perot etalon (*ex1.m*), b) VCSEL E-field standing wave (*ex2.m*)

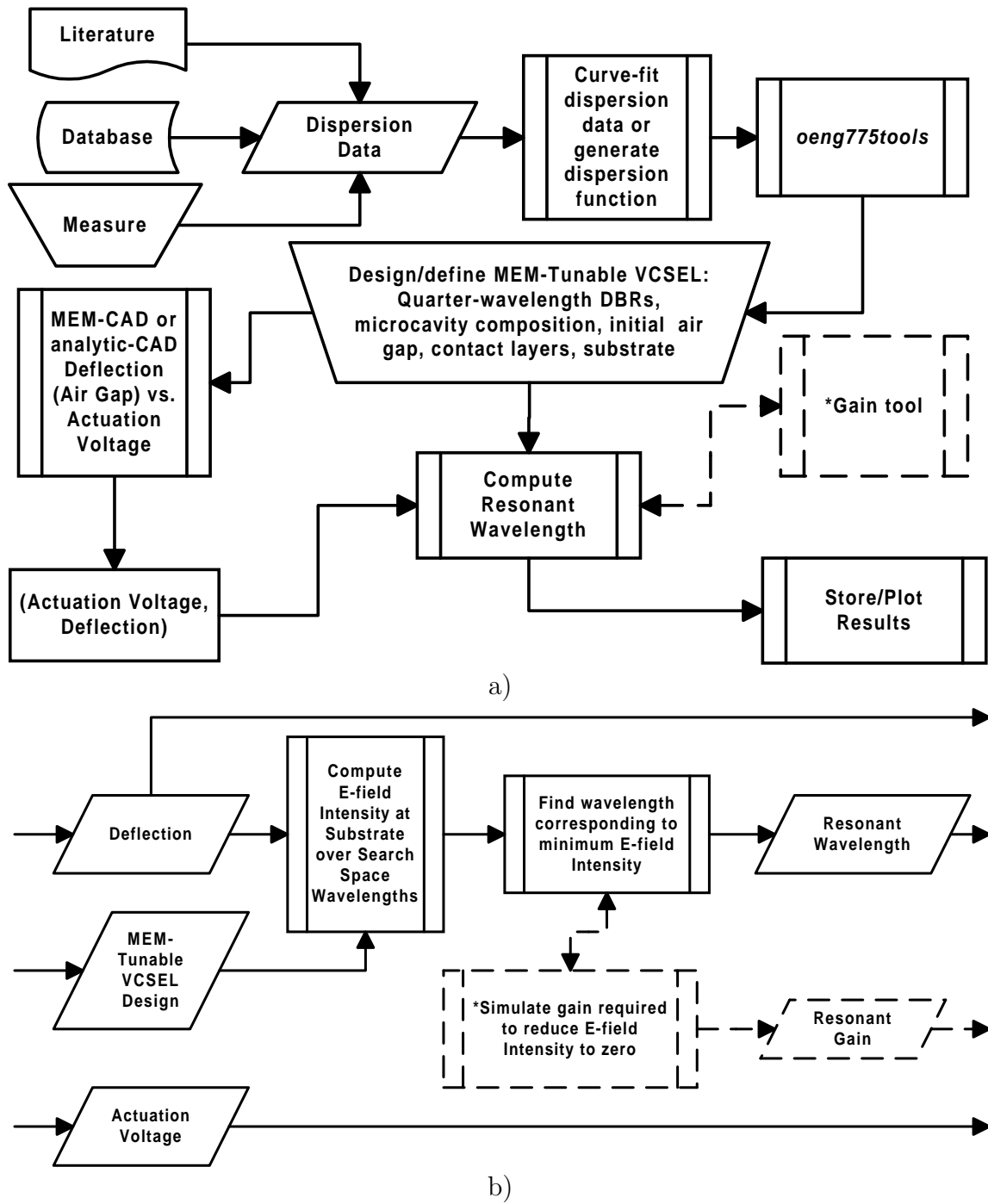


Figure 3.4: MT-CAD Flow Diagrams: a) functional block diagram, b) compute resonant wavelength function block elements

- Able to automatically generate a three-dimensional visualization of MEM-TF or MT-VCSEL substrate E-field intensity (over a given resonant frequency search space)

A first-generation implementation of this methodology was designed by using MATLAB[®] as the computational engine, the *oeng775tools* design kit discussed earlier, and additional MATLAB[®] functions. The MT-CAD methodology (Figure 3.4) proceeds as follows:

- Acquire dispersion data for each material in the optical path for the MEM-TF/TVCSSEL. Data sources may include, but are not limited to the literature, local database, or new measurements
- Curve-fit the dispersion data or generate a continuous, wavelength-dependent, representation of material dispersion
- Manually design the MEM-TF/TVCSSEL, including but not limited to quarter-wavelength DBR, micro-cavity with active region (composition, thickness, and placement of associated layers), initial air-gap, contact layers, and substrate
- Use MEM-CAD or analytic-CAD to simulate deflection (vary air-gap) as a function of actuation voltage
- Use MEM/analytic-CAD results and MEM-TF/TVCSSEL design parameters to compute resonant wavelength as illustrated in Figure 3.4b
- Store and visualize MT-CAD simulation results as shown in Figure 3.5

The “Gain tool” block in Figure 3.4a and in (slightly expanded form) Figure 3.4b is currently simulated by assuming constant gain over the search space wavelengths. As shown in Figure 3.5, MT-CAD may be used to characterize a MT-VCSEL’s resonant frequency and air-gap dependance as a function of actuation voltage. However, an accurate gain model is still desirable to help the MT-CAD discriminate between (expected) multiple resonant wavelength solutions that exist for a given air-gap thickness as shown in Figure 3.5.

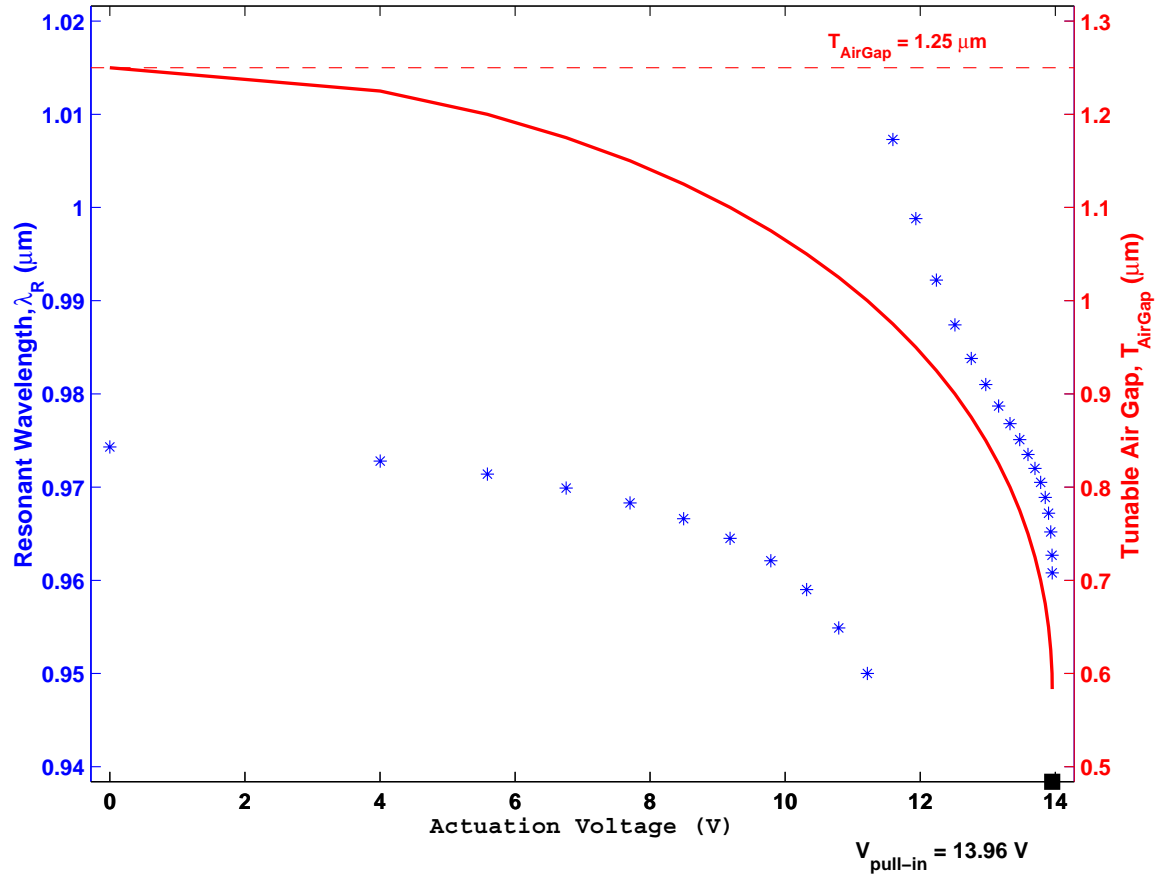


Figure 3.5: MT-CAD MT-VCSEL simulation example: λ_R (* marks) and tunable air-gap (solid line) as a function of actuation voltage; the desirable operating voltages are less than the calculated $V_{pull-in}$ of 13.96 V to avoid device snap-down; resonant wavelength optical mode-hop occurs at approximately 1 μm air-gap

3.3 CAD and Fabrication Investigations

3.3.1 PolySi prototypes for Hybrid MEM-TF/TVCSSEL. In this section, two polySi mechanical structures for flip-bonded hybrid MEM-TF and MT-VCSEL were characterized by comparing simulations with foundry fabricated actuators. The two prototypes, each with different flexure thicknesses (MUMPs® Poly 1 or Poly 2), had analytically simulated and measured pull-in voltages of (11.6V, 11.8 \pm 0.1V) and (8.4V, 7.7 \pm 0.5V), respectively. As a result of this investigation, the hybrid approach was anticipated to reduce cost, shorten development time, enable use of

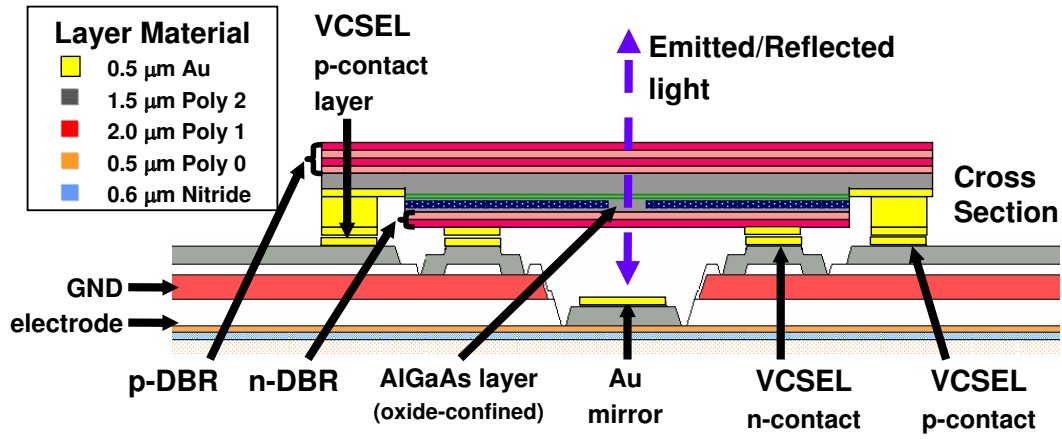
standard flip-chip technology and IC/MEMS foundries, and offer material flexibility, because the components do not need to be lattice matched.

3.3.1.1 Design. As shown in Figure 3.6, the prototype design consisted of a flip-bonded filter or VCSEL with co-planar contacts in an alternate instantiation of the Wilmsen *et al.* [5] approach. Ring contacts were proposed to ensure planar-to-substrate placement and mechanical symmetry. Also, the MUMPs® [6] Au layer was proposed as a fixed reflector and the filter or VCSEL as the vertically actuated element. This was the first proposed prototype design to vertically displace the active region of a tunable diode laser rather than displacing the tuning element [7].

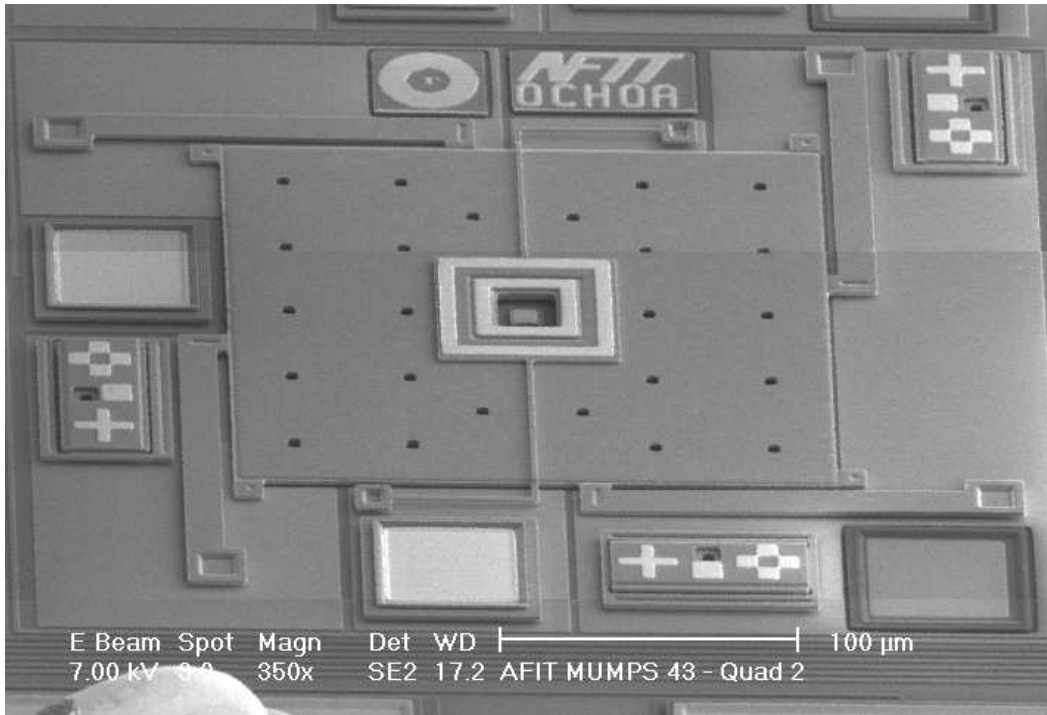
Decoupling the optical and mechanical elements prior to flip-bonding enabled simulated independent optimization of resonant wavelength tuning and actuation. The proposed fixed, lower reflector was MUMPs® Au, which is highly reflective for typical WDM wavelengths. Since shorter wavelengths are not as highly reflected by Au, depositing alternate materials with higher reflectivity was also considered. Moreover, if the central Au reflector was raised to be coplanar to the flip-bond plane, a highly reflective DBR was considered for bonding.

However, as discussed later in Chapter V, and noted in Chapter VII, the processing methods developed in this research to flip-bond a DBR to a polySi actuator, and then release the DBR from the donor GaAs substrate required significant process development. This was the most challenging impediment to demonstrating a hybrid MEM-TF, and may likely be the most challenging impediment to demonstrating a hybrid MEM-TVCSEL.

3.3.1.2 Simulation Method. The MT-CAD methodology described earlier was used to simulate a hybrid MT-VCSEL device with λ_D of 980nm. The basic electrostatic piston deflection calculation (described earlier) was used to analytically model deflection dependence on actuation voltage. Also, as described earlier, the *M*-



a)



b)

Figure 3.6: Prototype hybrid MEM-TVCSEL schematic and fabricated MUMPS[®] piston actuator: a) prototype MEM-TVCSEL schematic cross section, b) scanning electron micrograph of four-flexure polySi piston actuator with centrally located, coplanar, Au contact pads for a flip-bonded VCSEL to be vertically displaced above an Au central reflector. This actuator was fabricated as a proof-of-concept, and no VCSEL was flip-bonded to this structure.

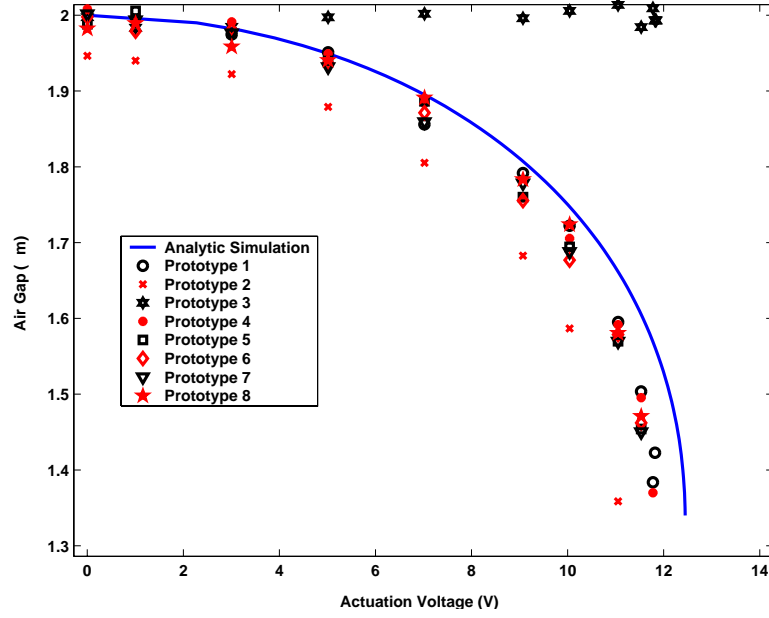
method was used to model hybrid or monolithic MT-VCSEL resonant wavelength dependence on air-gap thickness.

3.3.1.3 Prototype Actuator Fabrication and Simulation. As illustrated in Figure 3.6a, fabrication was performed, but is not limited to, the MUMPs® foundry [6]. On each die, material properties test structures (fixed-fixed beam arrays and comb-resonators) were co-located to enable characterization of each mechanical layer. The structures were released with HF, rinsed with methanol, then underwent supercritical CO₂ drying to prevent stiction. Next, the released die were packaged and the material properties test structures and our mechanical prototypes were characterized. Finally, hybrid MT-VCSEL simulations were performed using these prototype mechanical structures as design prototypes.

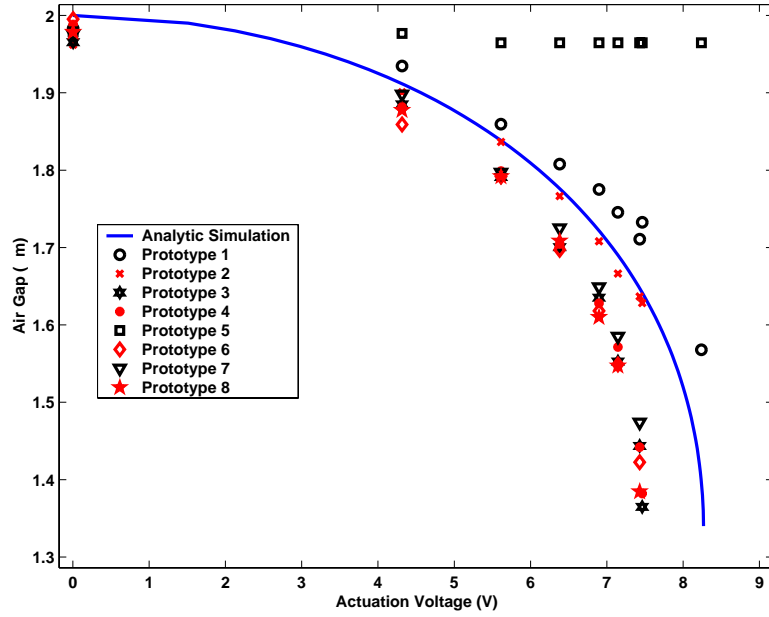
3.3.1.4 Results. The reported MUMPs® 43 Run Poly 1 and Poly 2 thickness was $1.9717 \pm 0.0145\mu\text{m}$ and $1.5088 \pm 0.0075\mu\text{m}$, respectively [8]. For the experimental die containing the prototypes and co-located material properties test structures, Youngs modulus and stress of Poly 1 and Poly 2 were measured as $(125 \pm 13\text{GPa}, -4.9 \pm 0.5\text{MPa})$ and $(162 \pm 4\text{GPa}, -9.4 \pm 0.2\text{MPa})$, respectively.

This material data was used to calculate the total spring constant, k , for two sets of prototypes. The computed k for the first set of prototypes with four Poly 1 support flexures and two Poly 2 central flexures was 19.60N/m. The computed k for the second set of prototypes with all Poly 2 flexures was 10.43N/m. The overlapping electrode area, A , for all prototypes was $39,216\mu\text{m}^2$. The initial electrode air-gap, h , was $2\mu\text{m}$. Next, a ZYGO® NewView™ 5000 interferometer was used to measure deflection versus actuation voltage.

As shown in Figure 3.7, the prototypes with Poly 1 or Poly 2 flexures had analytically simulated and measured pull-in voltages of (12.45V, $11.8 \pm 0.1\text{V}$) and (8.27V, $7.7 \pm 0.5\text{V}$), respectively. As shown in Figure 3.7, the pull-in voltage of the Poly 2 design was approximately 4-V less than the Poly 1 design.



a)



b)

Figure 3.7: Comparison of analytic simulations versus experimental results for seven Poly 1 or Poly 2 MUMPs[®] fabricated prototypes: a) all devices were suspended with four Poly 1 support flexures; analytically simulated and measured pull-in voltages were 12.45V and $11.8 \pm 0.1V$, respectively, b) all devices were suspended with Poly 2 flexures; analytically simulated and measured pull-in voltages were 8.27V and $7.7 \pm 0.5V$, respectively

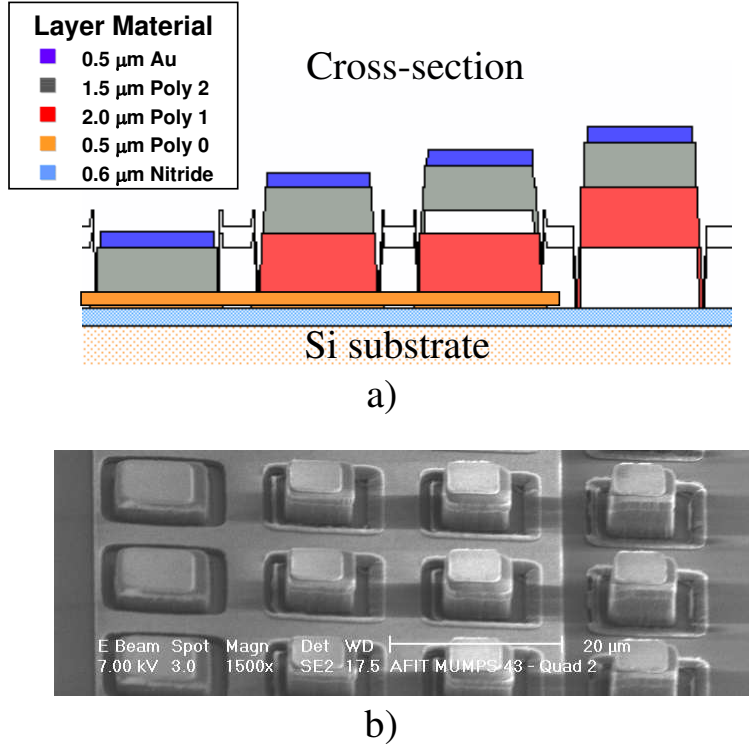


Figure 3.8: Au reflector prototypes: a) cross-section schematic, b) scanning electron micrograph of vertically displaced Au mirror (central reflector) prototypes

As shown in Figure 3.8, several prototype Au central reflectors were fabricated in MUMPs®. Height variations were constructed by layering and/or encapsulating one or both MUMPs® oxide layers prior to Au deposition on Poly 2. The heights photographed here corresponded to one of the following tunable air-gap initial thicknesses, $T_{AirGap-i}$: $0.75\mu\text{m}$, $1.25\mu\text{m}$, $2.0\mu\text{m}$, or $3.25\mu\text{m}$.

Since the second set of prototypes with Poly 2 flexures had lower actuation voltage characteristics, a 980-nm flip-bonded MT-VCSEL was simulated to investigate the design trade-offs associated with a device's initial air-gap thickness. A flip-bonded hybrid MT-VCSEL device was simulated with a 980-nm resonant wavelength. As shown in Figure 3.9, DBR_0 was 16.5 pairs of $\text{Al}_{0.1}\text{Ga}_{0.9}\text{As}/\text{Al}_{0.9}\text{Ga}_{0.1}\text{As}$, and DBR_1 was 1.5 pairs of $\text{Al}_{0.1}\text{Ga}_{0.9}\text{As}/\text{Al}_{0.9}\text{Ga}_{0.1}\text{As}$. For each air-gap thickness,

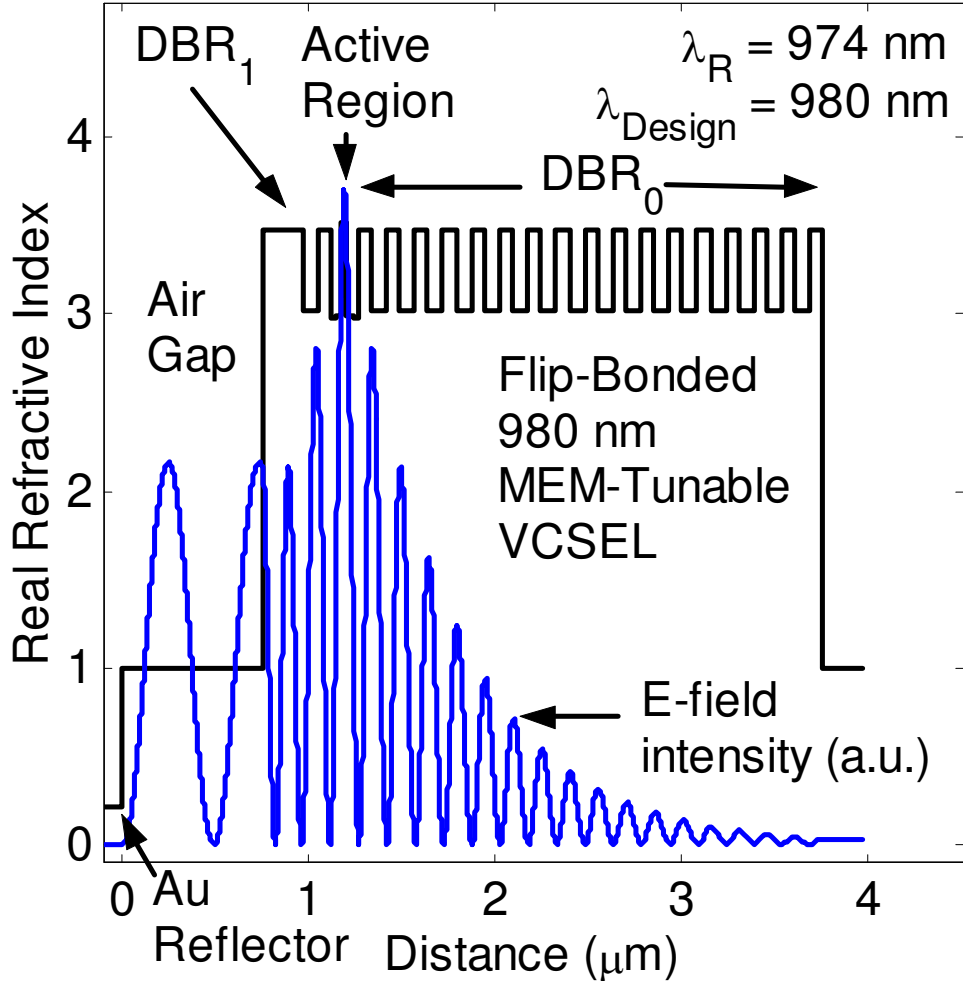
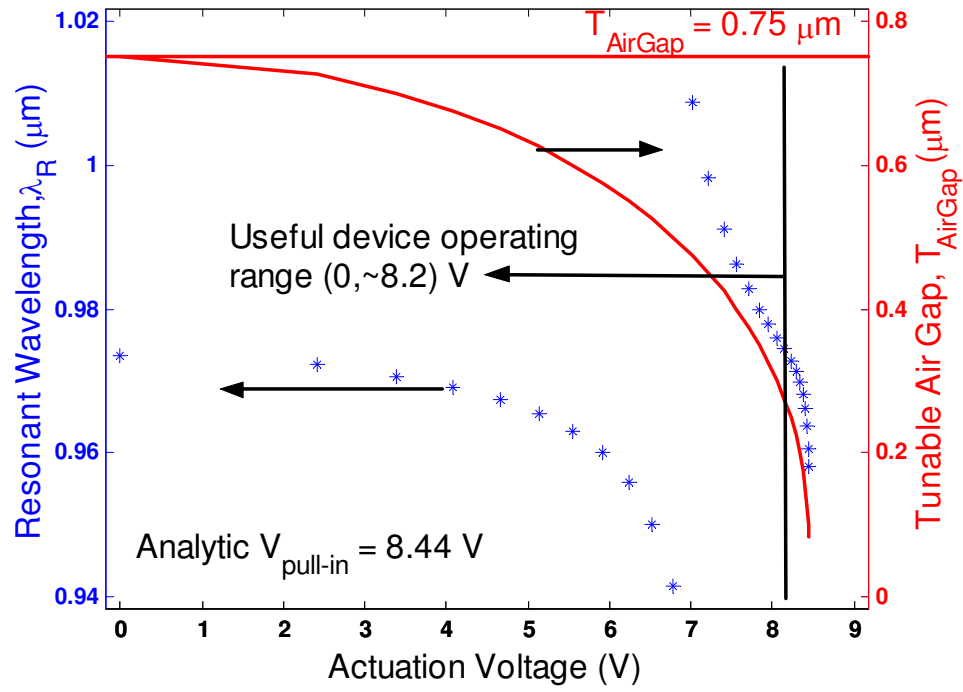


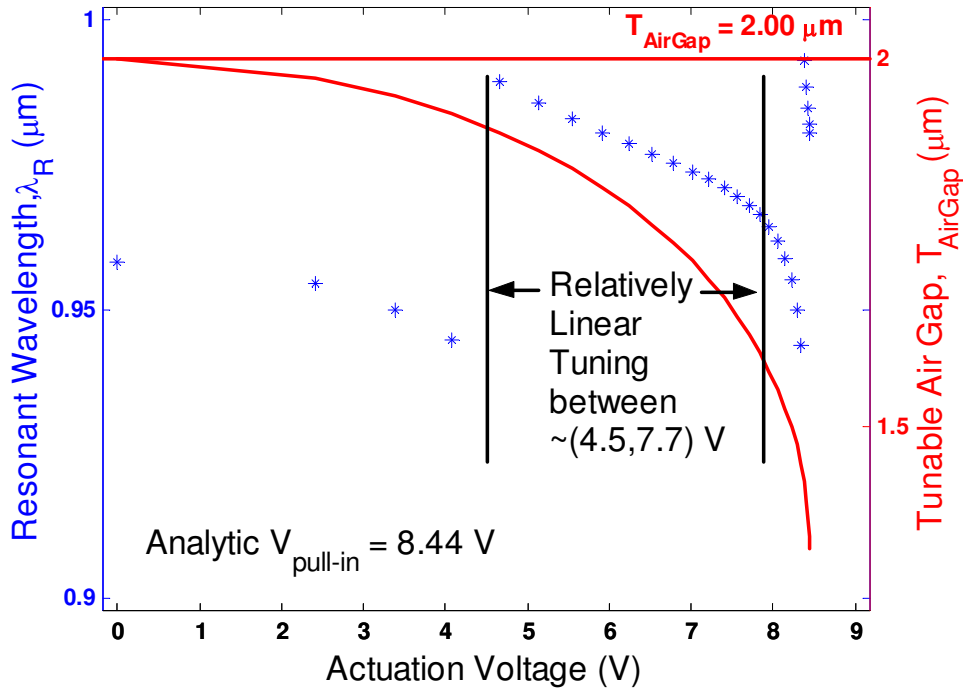
Figure 3.9: Simulated E-field intensity at 974-nm resonant wavelength, λ_R , for 0.75- μm -thick air-gap in a flip-bonded 980-nm hybrid MT-VCSEL

the corresponding resonant wavelength and E-field intensity through the device was calculated via the MT-CAD methodology described earlier.

As shown in Figure 3.10, the simulations indicated the choice of $T_{air-gap}$ significantly influenced tuning characteristics, which led to a relatively linear tuning response to actuation voltage. This was more apparent in Figure 3.10b, which demonstrated resonant wavelength tuning from 989 to 964nm corresponded to control voltages of 4.5 to 7.7V with less than 1.3-nm deviation from linearity (as measured by line of best fit).



a)



b)

Figure 3.10: Simulated resonant wavelength tuning for flip-bonded 980-nm hybrid MT-VCSEL with 1.5-μm-thick flexures: a) 0.75-μm initial air-gap, b) 2.00-μm initial air-gap

3.3.1.5 Conclusions. The polySi mechanical prototypes were first-generation candidates for flip-bonded hybrid MEM-TF and MT-VCSEL. Resonance wavelength tuning was accomplished by vertically reducing air-gap thickness. Key advantages included the following: enabled the use of MUMPs® dimples to reduce stiction, enabled independent design and optimization of mechanical and optical elements, enabled use of identical mechanical prototypes in different wavelength-tunable applications, and simulations indicated a performance trade space which includes MEM-TF or MT-VCSEL linear wavelength-tuning as a function of applied actuation voltage.

3.3.2 Monolithic versus Hybrid MT-VCSEL. In this section, the MT-CAD methodology was used to investigate the resonant frequency design space for monolithic and hybrid MT-VCSEL. For various initial optical air-gap thicknesses, the sensitivity of monolithic or hybrid MT-VCSEL resonant frequency was characterized by simulating $\pm 0\%$, $\pm 2\%$, and $\pm 4\%$ variations in III-V material growth thickness. As expected, as initial optical air-gap increased, tuning range decreased due to less coupling between the active region and the tuning mirror. However, each design had different resonant frequency sensitivity to variations in III-V growth parameters. In particular, since the monolithic design was comprised of III-V material, the shift in all growth thicknesses significantly shifted the resonant frequency response. However, for the hybrid MT-VCSEL, less shift resulted, because the lower reflector was an Au mirror with reflectivity independent of III-V growth variations. Finally, since the hybrid design was comprised of a MUMPs® polySi mechanical actuator, pull-in voltage remained independent of the initial optical air-gap between the tuning reflector and the III-V material. Conversely, as the initial air-gap increased in the monolithic design, the pull-in voltage significantly increased.

3.3.2.1 Simulation Methodology. The MT-CAD methodology described earlier was used to simulate and visualize simulation results for a tunable

hybrid and monolithic MT-VCSEL device with design wavelength (λ_D) of 980nm. The basic electrostatic piston deflection calculation was used to analytically model deflection dependence on actuation voltage. The M method of Yeh [2] was used to model MT-VCSEL resonant wavelength dependence on air-gap thickness. First, the device structure was optically and mechanically simulated assuming there was no variation in III-V material growth layers. Next, for various initial optical air-gap thicknesses, the sensitivity of monolithic or hybrid MT-VCSEL resonant frequency was characterized by simulating $\pm 0\%$, $\pm 2\%$, and $\pm 4\%$ variations in III-V material growth thickness.

3.3.2.2 Monolithic MT-VCSEL. As illustrated in Figure 3.11a, the prototype monolithic MT-VCSEL consisted of a top DBR (DBR₀) comprised of 33.5 pairs of quarter- λ_D layers of GaAs/Al_{0.04}Ga_{0.96}As, with total thickness of 4.8075 μ m. The top DBR was followed by a sacrificial layer, which acted as the tunable air-gap for the device. A coupling DBR (DBR₁) followed, which consisted of a half- λ_D (0.2084- μ m) thick GaAs contact layer followed by one pair of GaAs/Al_{0.04}Ga_{0.96}As. Next followed a half- λ_D cavity consisting of four quantum wells surrounded by high Al mole-fraction cladding layers for oxide-aperture current confinement. Finally, the bottom DBR (DBR₂) was 55 pairs of quarter- λ_D layers of GaAs/Al_{0.04}Ga_{0.96}As.

The device fabrication was assumed to consist of a sacrificial-layer removal step, such as an HF-based etch of a high Al mole-fraction or oxidized sacrificial layer. Due to the oxide-aperture current-confinement, the oxide-aperture layers were assumed to be protected (using photoresist) during the HF-based etch. Finally, as illustrated in Figure 3.11b, the mechanical structure of the monolithic MT-VCSEL was assumed to be a 40- μ m square electrostatically actuated piston device supported by four 100- μ m long flexures, each with a width of 4 μ m.

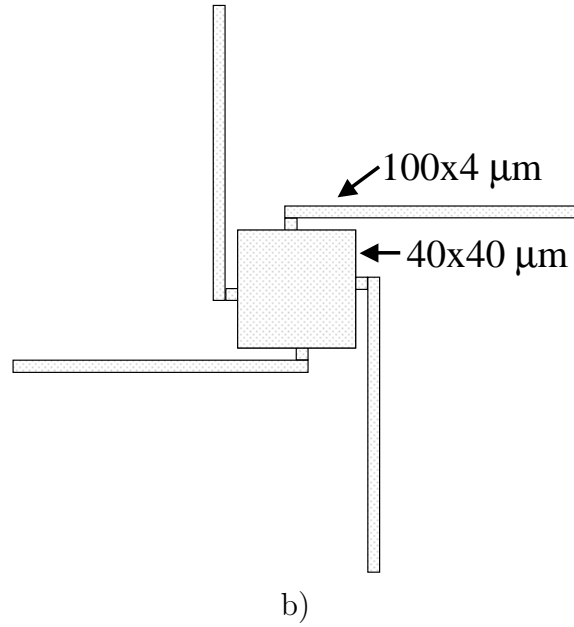
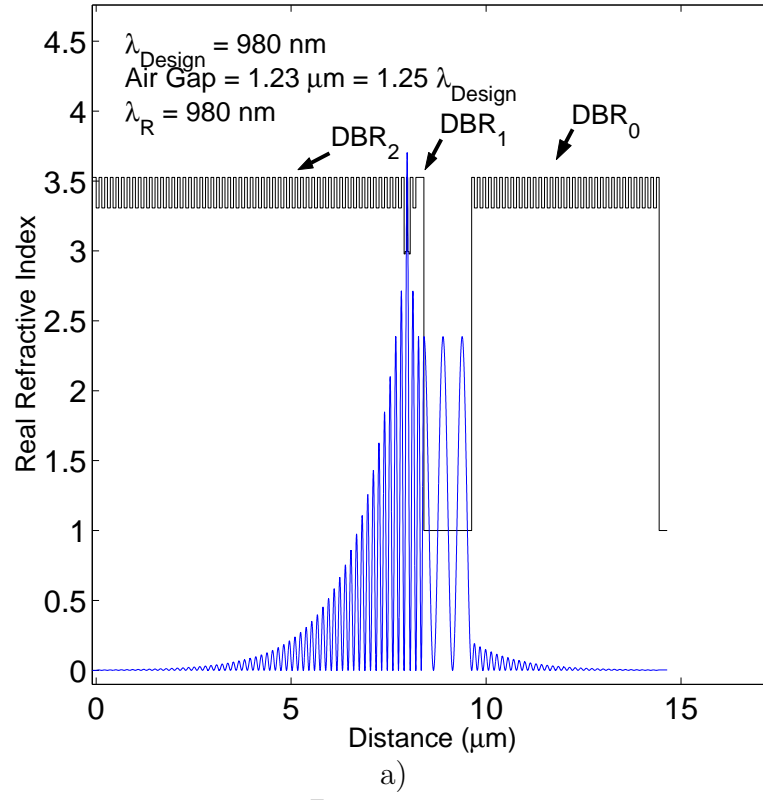


Figure 3.11: Prototype monolithic MT-VCSEL: a) E-field intensity (a.u., lower blue line) versus index and distance at resonance wavelength, λ_R b) top view schematic of prototype mechanical structure

3.3.2.3 Hybrid MT-VCSEL. As illustrated in Figure 3.12a, the prototype hybrid MT-VCSEL consisted of a top DBR (DBR₂) comprised of 16.5 pairs of quarter- λ_D layers of GaAs/Al_{0.04}Ga_{0.96}As, with a total thickness of 2.4957 μ m. Next followed a half- λ_D cavity consisting of four quantum wells surrounded by high Al mole-fraction cladding layers for oxide-aperture current confinement. A coupling DBR (DBR₁) followed, which consisted of one pair of GaAs/Al_{0.04}Ga_{0.96}As followed by a half- λ_D (0.2084- μ m) thick GaAs contact layer. This ended the III-V portion of the device. Next, the tunable optical air-gap with variable initial thickness was defined by the distance between the GaAs contact layer and bottom Au reflector.

The device fabrication was assumed to consist of a sacrificial-layer removal step, such as an HF-based etch of a sacrificial layer to detach the III-V material from the source substrate, and to release the MUMPs® polySi mechanical structure. Due to the oxide-aperture current-confinement, the oxide-aperture layers were assumed to be protected during the HF-based etch. Finally, as illustrated in Figure 3.12b, the mechanical structure of the hybrid MT-VCSEL was assumed to be a MUMPs® polySi electrostatically actuated piston structure supported by four 125- μ m long flexures with width of 13 μ m and thickness of 2 μ m.

3.3.2.4 Results. Each monolithic and hybrid device structure was optically and mechanically simulated via MT-CAD, assuming no variation in III-V material growth layers as shown in Figures 3.13 and 3.14. Next, the MT-CAD was used to simulate the influence of III-V layer growth variations on the resonant frequency of monolithic and hybrid MT-VCSEL.

As shown in Figures 3.15 - 3.20, for both the monolithic and hybrid MT-VCSEL prototype designs described earlier, the MT-CAD was used to vary the thicknesses of all III-V layers by $\pm 0\%$, $\pm 2\%$, and $\pm 4\%$, and solve for the resultant resonant frequency for each actuation voltage. As shown in both Figures 3.16 and 3.19, as

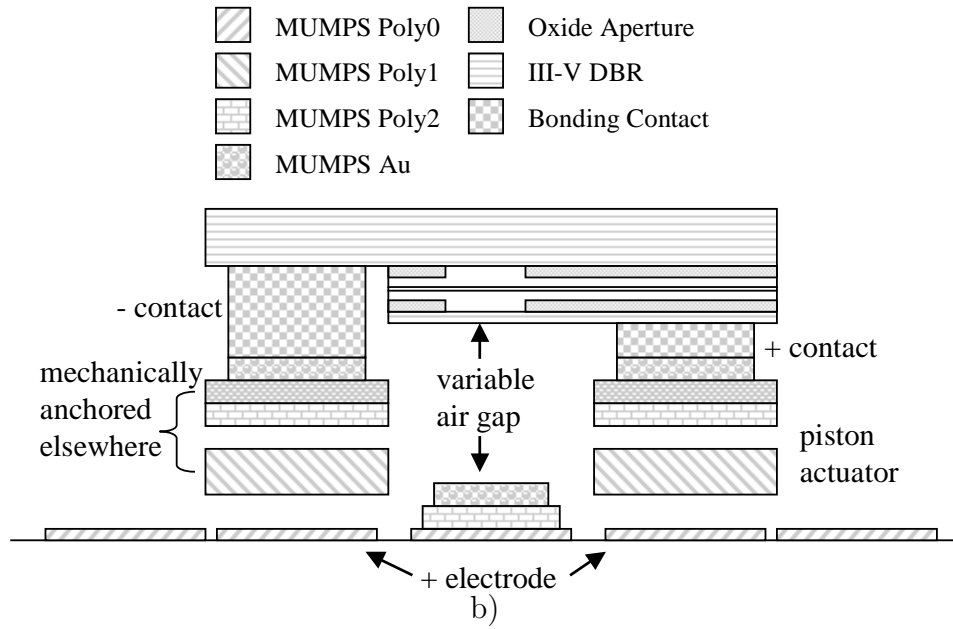
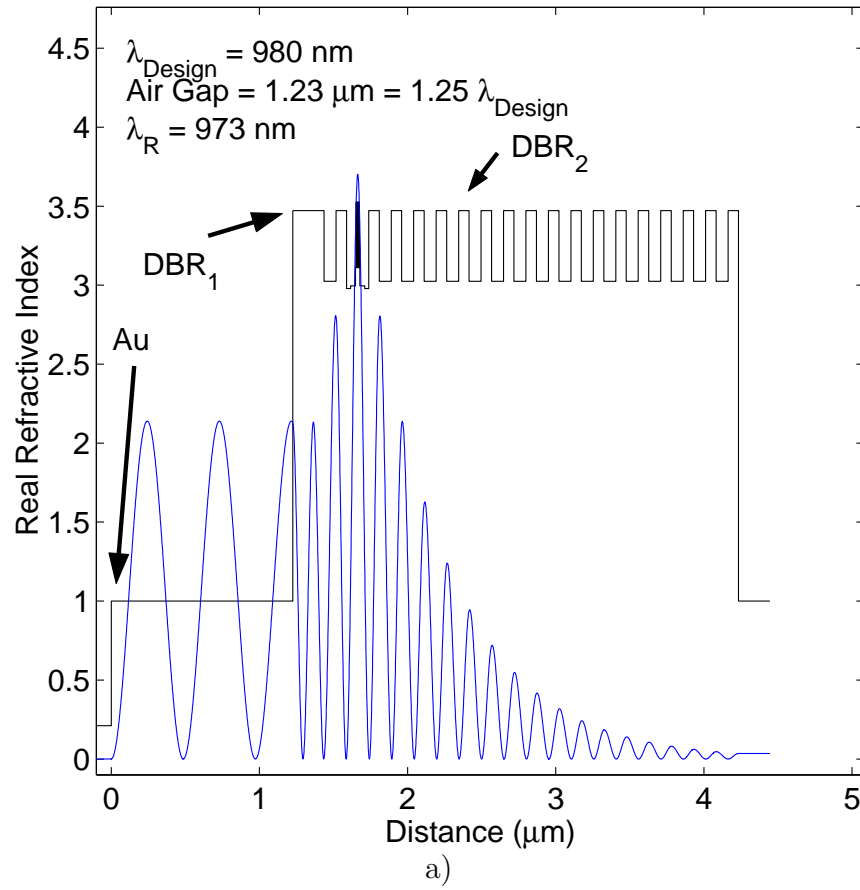
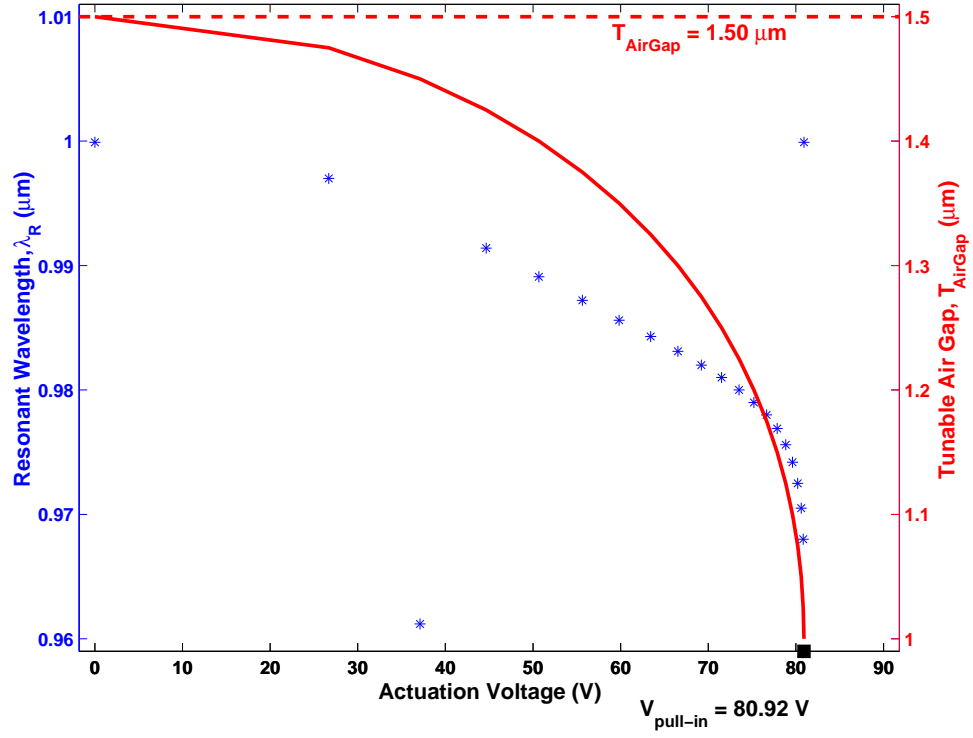
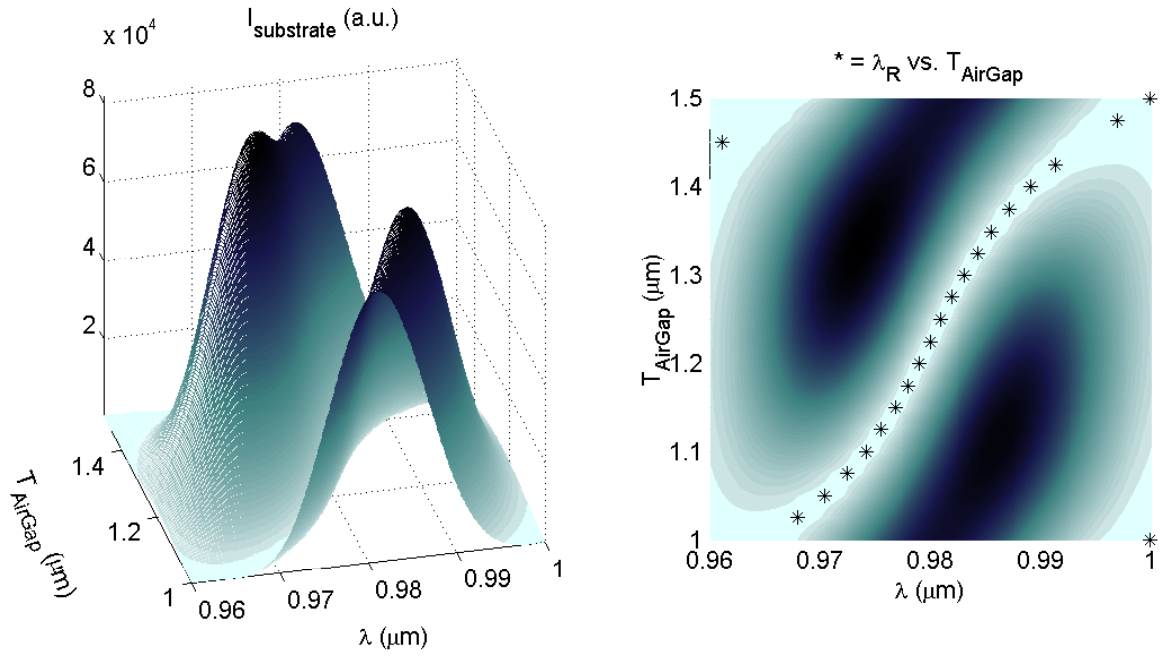


Figure 3.12: Prototype hybrid MT-VCSEL: a) E-field intensity (a.u., lower blue line) versus index and distance at resonance wavelength, λ_{R} b) cross-section schematic of prototype structure



a)



b)

Figure 3.13: MT-CAD monolithic MT-VCSEL simulation: a) resonant wavelength (* marks) and tunable air gap (solid line) versus actuation voltage, b) three-dimensional visualizations of substrate E-field intensity (over resonant frequency search space)

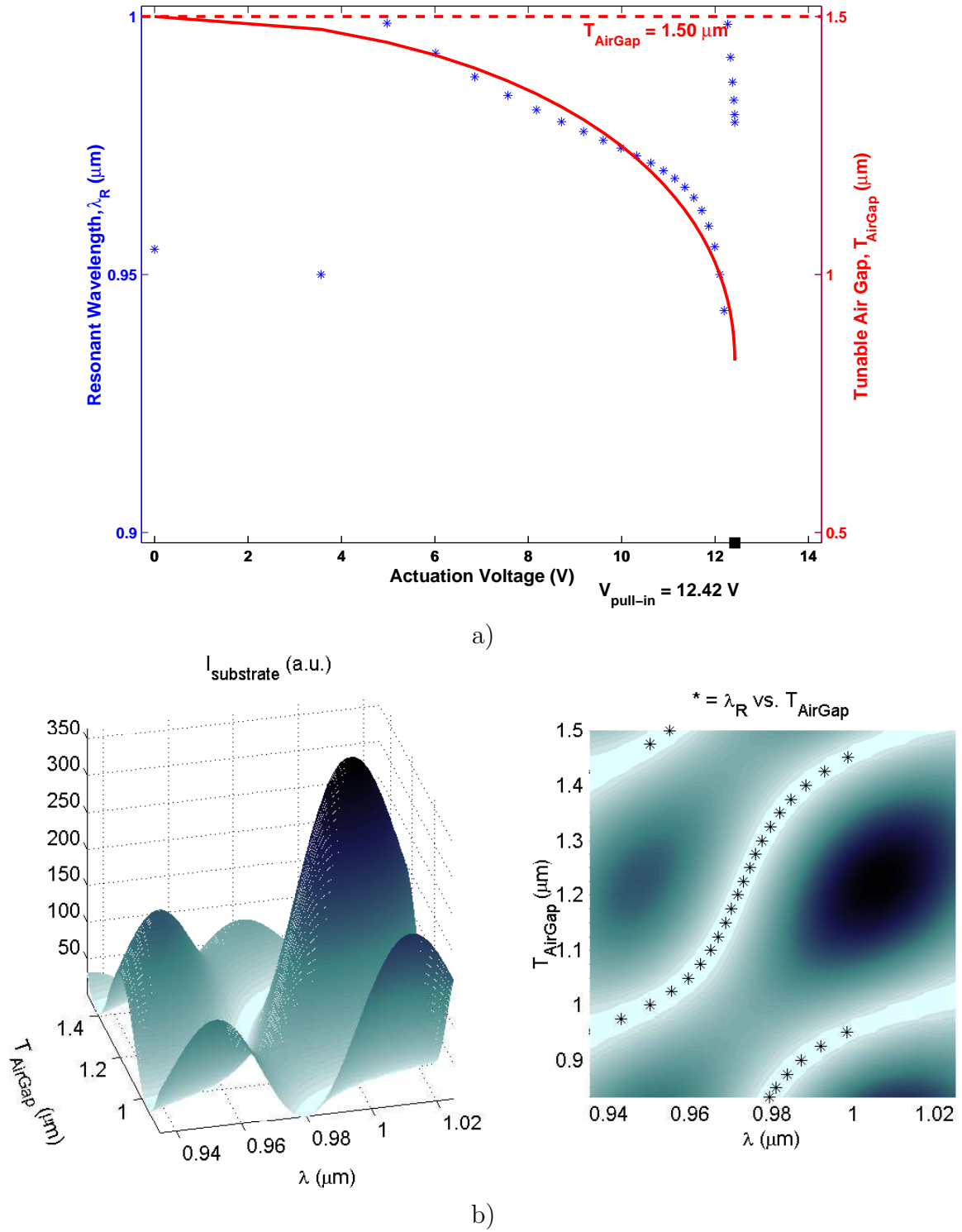
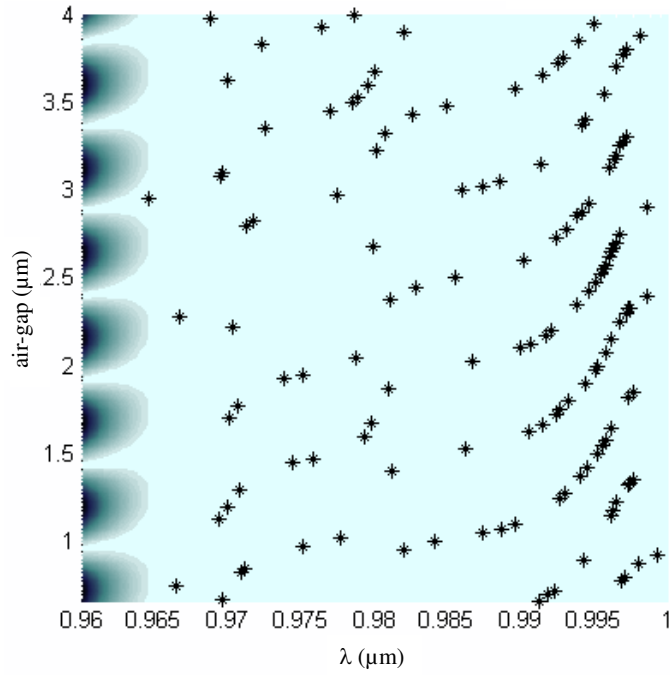
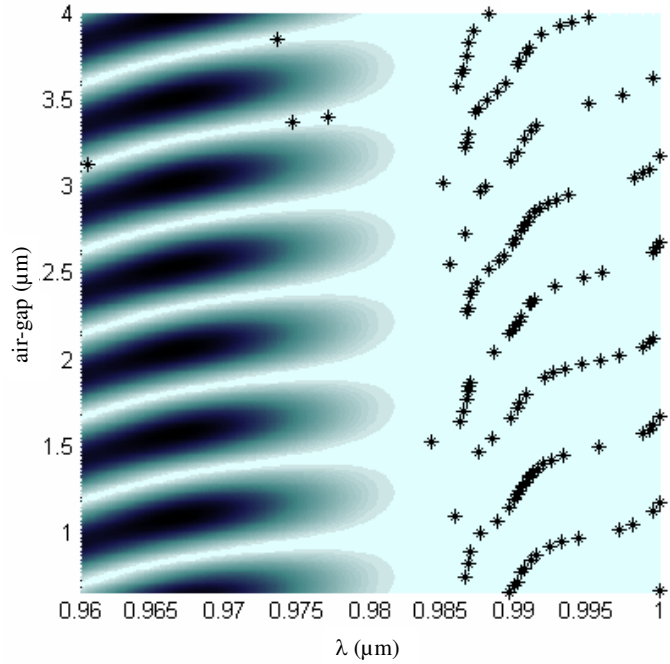


Figure 3.14: MT-CAD hybrid MT-VCSEL simulation: a) resonant wavelength (* marks) and tunable air gap (solid line) versus actuation voltage, b) three-dimensional visualizations of substrate E-field intensity (over resonant frequency search space)



a)



b)

Figure 3.15: Monolithic MT-VCSEL resonant wavelength (* marks) solution space for variation in III-V material growth thickness of: a) -4% , b) -2% ; air-gap simulation space increased from range illustrated in Figure 3.13

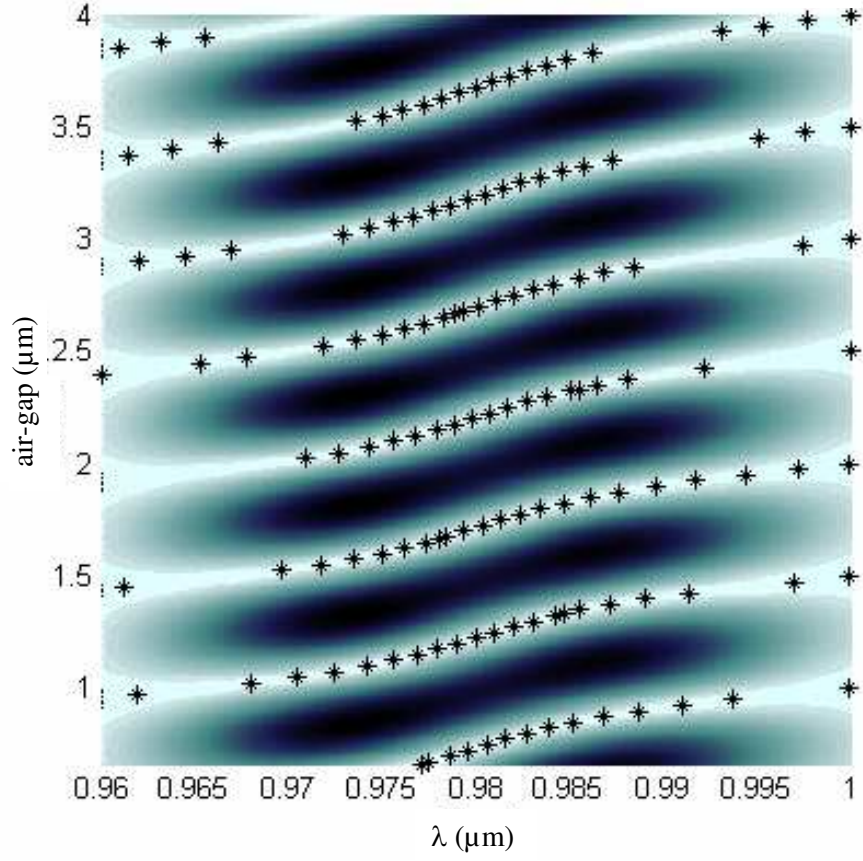
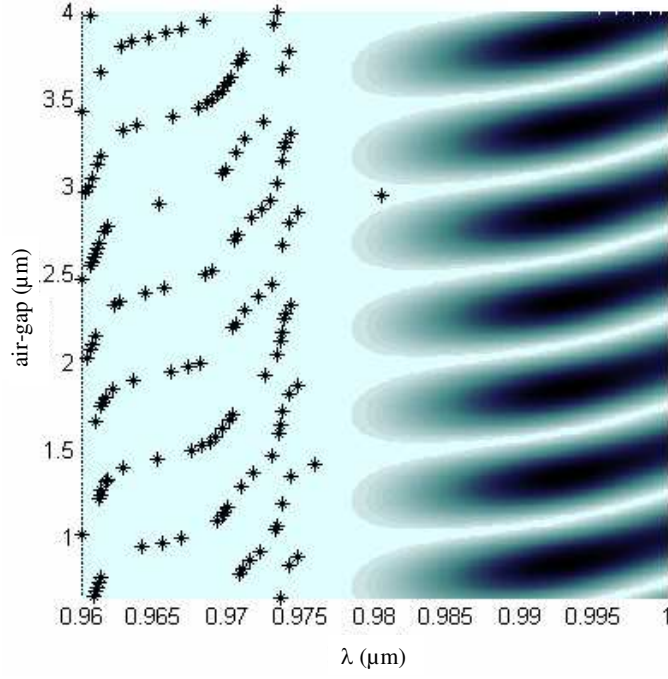
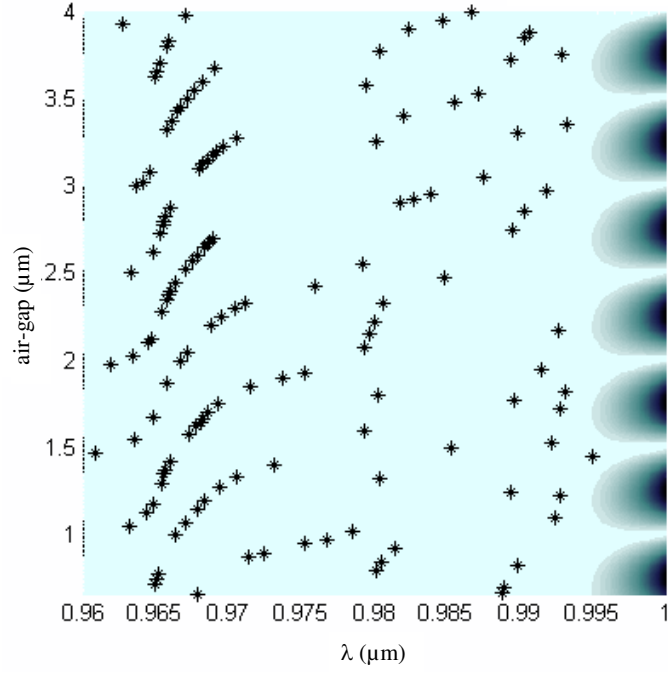


Figure 3.16: Monolithic MT-VCSEL resonant wavelength (* marks) solution space for variation in III-V material growth thickness of 0%; air-gap simulation space increased from range illustrated in Figure 3.13

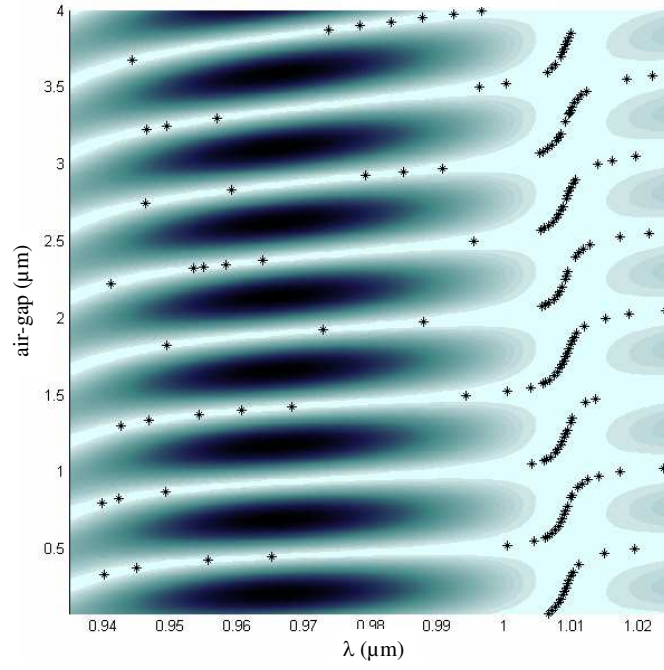


a)

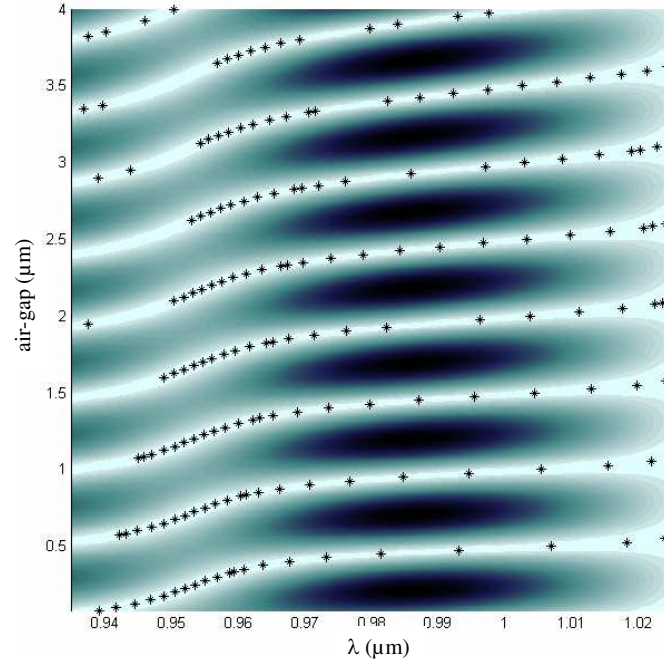


b)

Figure 3.17: Monolithic MT-VCSEL resonant wavelength (* marks) solution space for variation in III-V material growth thickness of: a) +2%, b) +4%; air-gap simulation space increased from range illustrated in Figure 3.13



a)



b)

Figure 3.18: Hybrid MT-VCSEL resonant wavelength (* marks) solution space for variation in III-V material growth thickness of: a) -4% , b) -2% ; air-gap simulation space increased from range illustrated in Figure 3.14

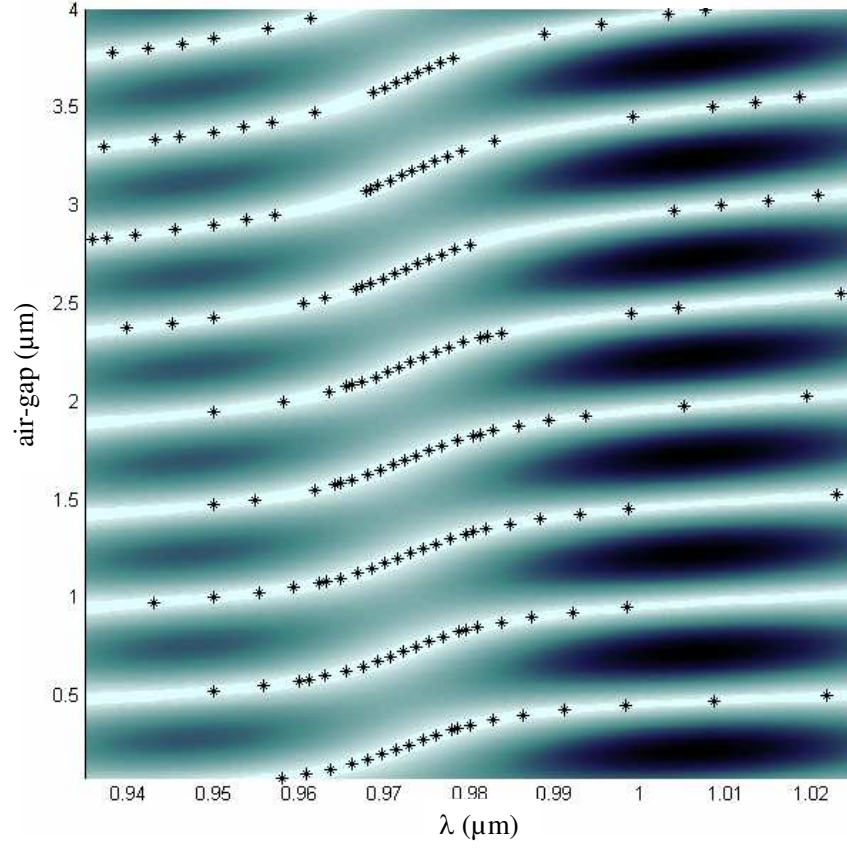
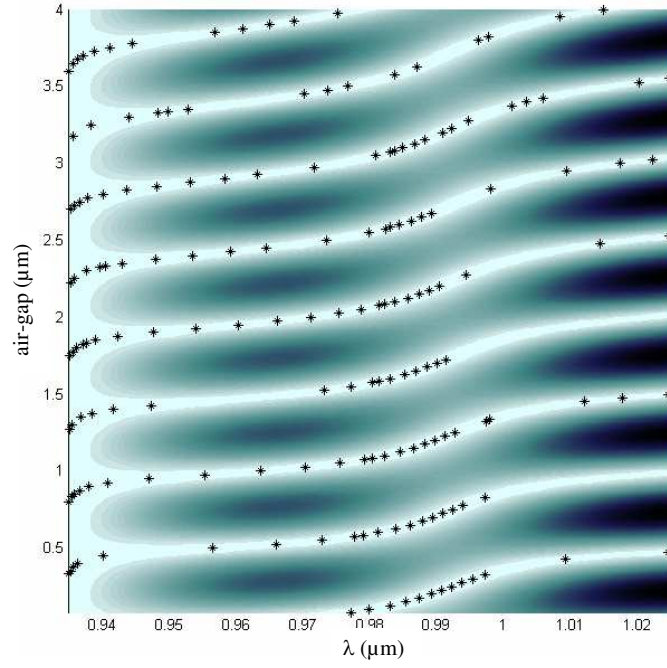
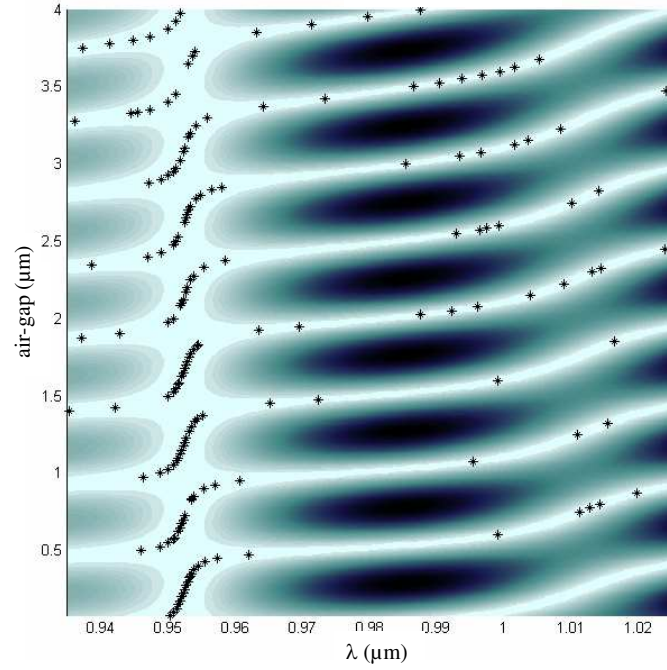


Figure 3.19: Hybrid MT-VCSEL resonant wavelength (* marks) solution space for variation in III-V material growth thickness of 0%; air-gap simulation space increased from range illustrated in Figure 3.14



a)



b)

Figure 3.20: Hybrid MT-VCSEL resonant wavelength (* marks) solution space for variation in III-V material growth thickness of: a) +2%, b) +4%; air-gap simulation space increased from range illustrated in Figure 3.14

optical air-gap increased, the slope of the resonant frequency centered on the design wavelength increased. As slope increased, the tuning range decreased. In coupled-cavity designs, this occurred as a result of the larger air-gap which reduced the coupling between the active region and tuning reflector. Thus, to maximize tuning range, it was found desirable to operate in a region of the curve with minimum slope.

3.3.2.5 Discussion. Each design had a significant influence on sensitivity to variations in III-V growth parameters. In particular, since the monolithic design was entirely comprised of III-V material, the shift in all growth thicknesses significantly shifts the resonant frequency characteristics. This would make recovery of mis-grown devices difficult and likely impractical. The shifted thickness of all layers in each reflector for the coupled cavity design shifted the resonant frequency space almost completely outside the designed region of 980nm. However, as shown in Figures 3.18 - 3.20, for hybrid MT-VCSEL, the shift was significantly less, since the lower reflector was a Au mirror with reflectivity independent of III-V growth variations.

Finally, since the hybrid design was comprised of a MUMPs® polySi mechanical actuator fabricated independently of the III-V material, $V_{pull-in}$ was consistently the calculated value of 12.42V, independent of the initial optical air-gap between the tuning reflector and the III-V material. Conversely, as the initial air-gap increased in the monolithic design, $V_{pull-in}$ significantly increased. For example, in the monolithic design with an air-gap of $1.5\mu\text{m}$, the calculated $V_{pull-in}$ was 81V. When the initial monolithic air-gap increased to $3.0\mu\text{m}$, the calculated $V_{pull-in}$ was 229V.

3.3.2.6 Conclusions. The MT-CAD methodology was useful for investigating the resonant frequency design space for monolithic and hybrid MT-VCSEL. As expected, as initial optical air-gap increased, tuning range decreased due to less coupling between the active region and tuning mirror. However, the simulations indicated the monolithic MT-VCSEL resonant wavelength was more sensitive

to variations in III-V growth than hybrid MT-VCSEL. The reduction in hybrid MT-VCSEL sensitivity was attributed to the Au mirror reflector whose reflectivity was independent of III-V material growth variations. Finally, since the hybrid design was comprised of a MUMPs[®] polySi mechanical actuator, pull-in voltage remained independent of the initial optical air-gap between the tuning reflector and the III-V material.

3.4 Chapter Summary

This chapter reviewed the simulation tools custom-developed for design and simulation studies of hybrid MEM-TF/TVCEL devices. The electrostatic piston deflection calculation was implemented and validated with MUMPs[®] fabricated prototype devices. The MT-CAD toolkit was implemented to simulate hybrid MEM-TF and hybrid MT-VCSEL tuning as a function of actuation voltage. This toolkit was also used to investigate the resonant frequency design space for monolithic and hybrid MT-VCSEL.

The CAD investigations demonstrated key advantages of a hybrid MT-VCSEL over monolithic devices. Some of the hybrid advantages demonstrated in this chapter include the following: enabled the use of MUMPs[®] dimples to reduce stiction, enabled independent design and optimization of mechanical and optical elements, enabled use of identical mechanical prototypes in different wavelength-tunable applications, and simulations indicated a performance trade space which includes MEM-TF or MT-VCSEL linear wavelength-tuning as a function of applied actuation voltage.

The MT-CAD simulations identified several design trades previously unreported in monolithic MT-VCSEL designs. Specifically, in comparison to a monolithic design, the hybrid MT-VCSEL design space introduces less wavelength tuning sensitivity to III-V material growth variations and pull-in voltage independent of initial optical air gap between the tuning reflector and III-V material. The simulations also demonstrated the monolithic MT-VCSEL resonant wavelength was more sensitive to

variations in III-V growth than hybrid MT-VCSEL. Finally, since the hybrid design was comprised of a MUMPs® polySi mechanical actuator, pull-in voltage remained independent of the initial optical air-gap between the tuning reflector and the III-V material.

Bibliography

1. W. D. Cowan, “Foundry Microfabrication of Deformable Mirrors for Adaptive Optics,” Ph.D. dissertation, Air Force Institute of Technology, Department of Electrical and Computer Engineering, Wright Patterson AFB, OH, 1998, AFIT/DS/ENG/98-07.
2. P. Yeh, *Optical Waves in Layered Media*. Wiley: New York, 1988.
3. J. A. Lott, “Visible Vertical Cavity Surface Emitting Lasers,” Ph.D. dissertation, University of New Mexico, Albuquerque, New Mexico, December 1993.
4. E. M. Ochoa, “*oeng775tools*: A MATLAB® toolbox,” AFIT/ENG, Wright-Patterson AFB, OH, unpublished, February 2001.
5. C. W. Wilmsen, *Vertical-Cavity Surface Emitting Lasers*. Cambridge University Press, 1999, ch. 12, pp. 417–448.
6. D. A. Koester, R. Mahadevan, B. Hardy, and K. W. Markus, *MUMPs® Design Handbook, Revision 6.0*. Cronos Integrated Microsystems, 2001, www.memsrus.com/cronos/mumps.pdf.
7. E. Ochoa, L. Starman, W. Cowan, T. Nelson, O. Blum-Spahn, and J. Lott, “Polysilicon Prototypes for Flip-bonded Hybrid MEM-tunable Filters and VC-SELs,” in *Technical Proceedings of the 2002 International Conference on Modeling and Simulation of Microsystems*, San Juan, Puerto Rico, Apr 2002.
8. Cronos Integrated Microsystems, “MUMPs® run #43 run data,” Internet, 2007, www.memscap.com/mumps/documents/PolyMUMPs.rundata.xls.

IV. III-V AlGaAs Etch Studies

4.1 Chapter Overview

In this chapter, studies are performed to investigate and characterize candidate III-V AlGaAs material etchants to enable fabrication of a hybrid MEM-TF (as a first step toward fabrication of a hybrid MT-VCSEL). These studies seek to identify a candidate etch chemistry compatible (non-destructive) with sacrificial layer release of an AlGaAs DBR.

Sacrificial etching for III-V MEMS is feasible when the etch selectivity and rate of underetch are high. To obtain both high selectivity and underetch rates, III-V MEMS designers use dry and wet-etch approaches [1,2]. Two wet-etch approaches compatible with the III-V materials and hybrid MEM-TF designs developed in this research are characterized in this chapter. Specifically, the following itemized sections are described and reported:

- **Multi-layer Etch Study**
- **GaAs Sacrificial Layer Etchant Study**
- **High Al mole fraction AlGaAs HF-based Etch**

4.2 Multi-Layer Etch Study

A multi-layer, AlGaAs MOVPE (RunID: EMC6844) sample was grown to obtain undercut etch rate data over a range of available Al mole fraction AlGaAs. As shown and annotated in Figure 4.1, the growth consisted of a 0.1- μm -thick $\text{Al}_{0.2}\text{Ga}_{0.8}\text{As}$ substrate cap layer, then alternating/decreasing Al mole fraction AlGaAs 0.1- μm -thick layers paired with $\text{Al}_{0.2}\text{Ga}_{0.8}\text{As}$ 0.1- μm -thick layers. The methodology for using this sample follows:

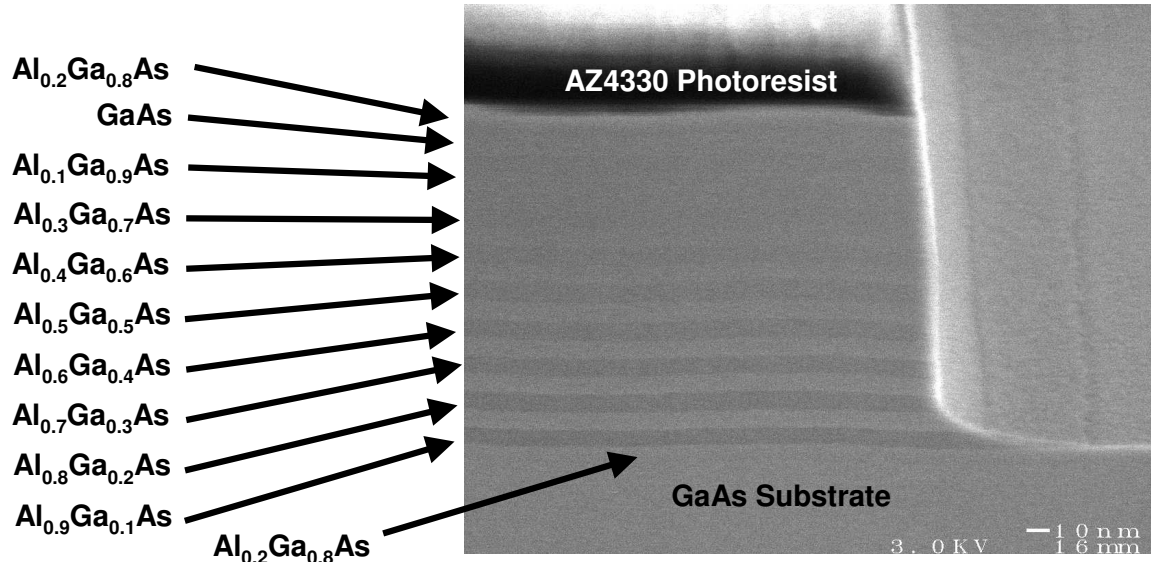


Figure 4.1: SEM of stripe-masked multi-layer GaAs/AlGaAs sample; the photoresist mask was removed prior to wet-etch characterization

1. Vertical mesa dry-etch stripe mask test patterns
2. Laterally wet-etch via a candidate etch system
3. Stop and record the length of time for the (lateral) wet-etch
4. Dice the test samples perpendicular to the mesa etch stripes to obtain cross-sections for SEM lateral etch distance measurements
5. Characterize, measure, record, and calculate undercut etch rates (lateral distance as a function of time)

4.3 GaAs Sacrificial Layer Etchant Study

4.3.1 GaAs Etch Systems. Most GaAs etchants operate by first oxidizing the surface, then dissolving the oxide. In general, the etchant contains one component which acts as the oxidizer and the other which acts as the dissolving agent. The oxidation is an electrochemical process in which localized anodic and cathodic sites exist at the semiconductor interface; oxidation occurs at anodic sites and the oxidant is reduced at cathodic sites. Since it is an electrochemical process, it is sensitive to

illumination and electrical currents which can supply/restrict electrons/holes at the surface [3].

The zinc-blende crystal structure of GaAs leads to etch characteristics which are significantly different than those of Si. In particular, the crystalline structure of GaAs (Figure 4.2) leads to anisotropic etching in almost all cases in which masks are used to pattern the wafer for etching [3].

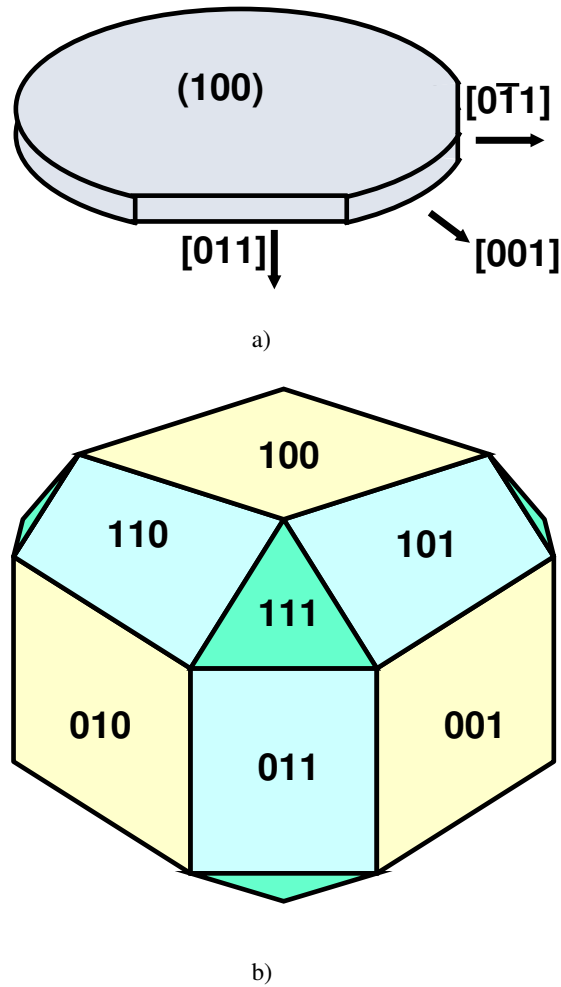


Figure 4.2: GaAs crystal planes and directions

As shown in Figure 4.3a, the photoresist mesa is oriented with edges parallel to a $\langle 110 \rangle$ direction. In this case, two of the edges will yield profiles with outward slopes; the other two edges will have inward sloping or undercut profiles. In Fig-

ure 4.3b, the photoresist mesa is oriented with edges 45° to a $\langle 110 \rangle$ direction. In this case, the resulting edge profiles will yield essentially vertical walls (since it is midway between the two cases above) [3].

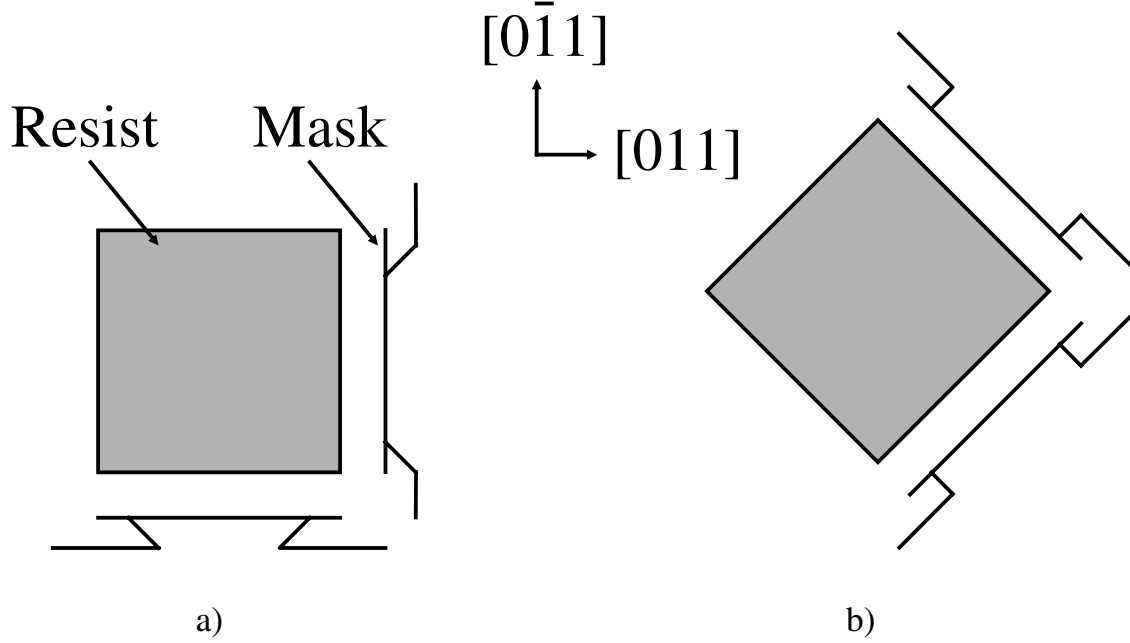


Figure 4.3: Nominal (100)-oriented GaAs anisotropic wet etching characteristics

Although many wet-etch systems have been reported for GaAs, few have been reported with both high undercut and selectivity for GaAs over $\text{Al}_x\text{Ga}_{1-x}\text{As}$ [4]. Until relatively recently, successful development of AlGaAs/GaAs HFETs has been hampered by the absence of a highly selective etch for removing GaAs over $\text{Al}_x\text{Ga}_{1-x}\text{As}$. However, the possibility of increasing selectivity to greater than 1000 has been obtained by buffering the citric-acid based etch with potassium-citrate [5–7].

In particular, as reported [7], a selectivity of 3400:1 for GaAs/ $\text{Al}_{0.2}\text{Ga}_{0.8}\text{As}$ using citric-acid/tripotassium citrate/hydrogen-peroxide. This was the highest selectivity reported at the time of this study for the GaAs/ $\text{Al}_x\text{Ga}_{1-x}\text{As}$ material system. Unfortunately, the corresponding undercut of GaAs over other Al-mole-fractions and the characterization of the corresponding undercut etch rates were not within the

scope of their research [6, 7]. Thus, the next section summarizes the effort to determine if this etch system was a candidate for GaAs sacrificial layer etching over $\text{Al}_x\text{Ga}_{1-x}\text{As}$.

The selectivity of the citric-acid-based solution is low, less than 200:1. However, the addition of tripotassium-citrate greatly increases selectivity. It is believed the hydrolysis of tripotassium-citrate produces hydroxyls which contribute to oxide formation on the $\text{Al}_x\text{Ga}_{1-x}\text{As}$ surface, forming a layer protecting the surface from etching. Chang *et al.* obtained a selectivity of 3400:1 for GaAs/ $\text{Al}_{0.2}\text{Ga}_{0.8}\text{As}$ when using a citric-acid/tripotassium-citrate/hydrogen-peroxide composition of 5:5:1.5 [7].

4.3.2 GaAs Etch Study Methodology. After removing the photoresist mask with acetone, the test samples were cleaned with methanol and isopropanol (IPA) to remove impurities. Next, the samples were placed in an LFE barrel stripper to remove organic impurities from the surface. The etch solution was prepared, and placed on an automatic hot-cold plate set to maintain a constant temperature of 25 °C. Just prior to etching, the test samples were dipped in a hydrofluoric-acid (HF)-based solution to remove the surface oxide. The test samples were placed in the solution, then the solution was covered to prevent illumination from interfering with the etching process as discussed above [3]. The solution was not agitated. The etch was stopped via a deionized water (H_2O) dip or methanol rinse. Finally, the test samples were cleaved perpendicular to the stripe mesas, then the etch profile was investigated using a scanning electron microscope.

4.3.3 GaAs Etch Study Results. Unfortunately, as illustrated in Figure 4.4, the stripe-mask approach initially led to inconclusive results. The edge of the stripe was typically not well defined after the etch. This was most likely due to etching of the intermediate $\text{Al}_{0.2}\text{Ga}_{0.8}\text{As}$ layers, since the top $\text{Al}_{0.2}\text{Ga}_{0.8}\text{As}$ layer was etched. Although there was generally an indication of undercutting in the GaAs layer near

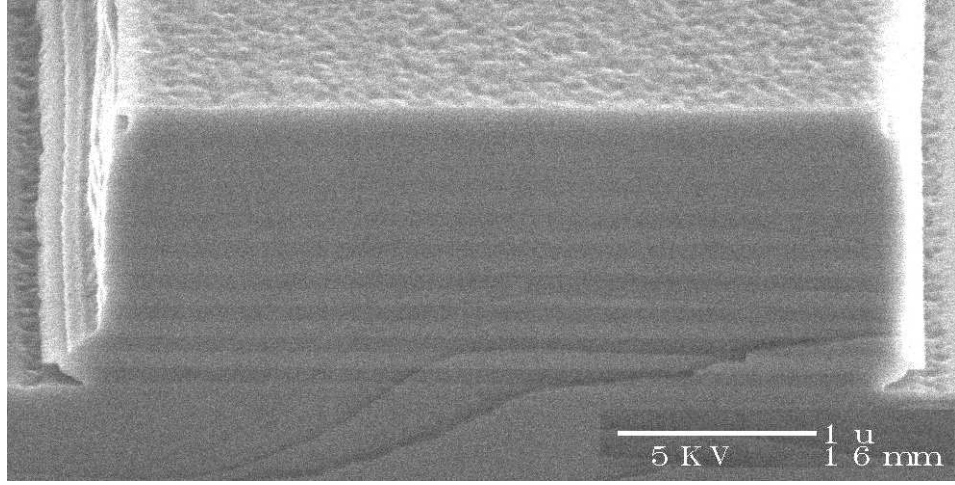


Figure 4.4: Nominal, generally inconclusive, multi-layer stripe etch study results: 30-min citric-acid/tripotassium-citrate/hydrogen-peroxide etch at 25 °C, stripe oriented parallel to $\langle 110 \rangle$ direction

the top of the multi-layer stripe, characterization of the GaAs undercut etch rate was difficult to estimate since the adjacent layers were also etched.

In parallel with the multi-layer stripe etch study, an MBE growth was obtained which consisted of a 1.5- μm -thick GaAs candidate sacrificial layer surrounded by $\text{Al}_{0.1}\text{Ga}_{0.9}\text{As}/\text{Al}_{0.9}\text{Ga}_{0.1}\text{As}$ DBR. The layers adjacent to the GaAs sacrificial were composed of $\text{Al}_{0.9}\text{Ga}_{0.1}\text{As}$. The material was lithographically patterned then mesa-etched. Test die were then etched and inspected via the GaAs etch system described above. In spite of etching 4 hours, the GaAs undercut distance only measured $0.64 \pm 0.39\mu\text{m}$, corresponding to an etch rate of $0.16 \pm 0.10\mu\text{m}/\text{min}$ in the $\langle 110 \rangle$ directions. Also, the etch rate of the $\text{Al}_{0.1}\text{Ga}_{0.9}\text{As}$ layers in the upper DBR was $0.12 \pm 0.01\mu\text{m}/\text{min}$, while the $\text{Al}_{0.1}\text{Ga}_{0.9}\text{As}$ etch rate in the lower DBR was $0.32 \pm 0.16\mu\text{m}/\text{min}$.

As shown Figure 4.5, significant anisotropic etching was detected in a section of a 6-hr multi-layer stripe mask study corresponding to punch-through of the $\text{Al}_{0.2}\text{Ga}_{0.8}\text{As}$ substrate cap. The edge of the stripe corresponds to the vertically oriented white linear feature on the right third of the SEM image. The dominant etch

planes were oriented 45° from the stripe mask, in the $\langle 001 \rangle$ directions. Aligning the stripe mask parallel to wafer flats assumed isotropic etch rates along crystal planes. Thus, to detect whether there is significant anisotropic etching between stripes parallel to or 45° from wafer flats, a new stripe test structure set was fabricated.

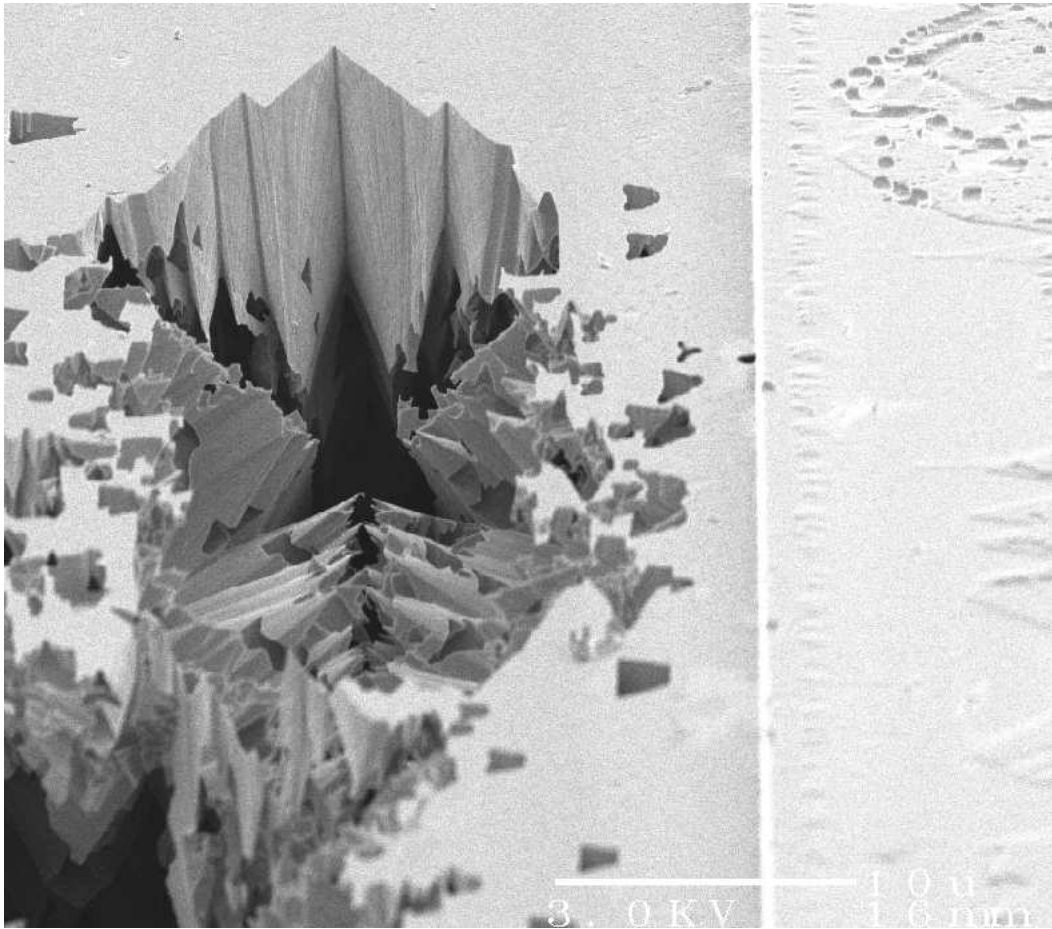


Figure 4.5: SEM of typical anisotropic GaAs layer etch results in multi-layer stripe etch study: overhead-view of 6-hr citric-acid/tripotassium-citrate/hydrogen-peroxide etch at 25°C , deep and irregular anisotropic etching of the GaAs substrate was observed as indicated on left side of SEM; the edge of the stripe (indicated by a white vertical line) under study was oriented parallel to the wafer flat ($\langle 110 \rangle$ directions)

The new stripe test structures were rotated 45° from the wafer flat, corresponding to the $\langle 110 \rangle$ directions. Next, the etch study described above was repeated for 2 and 4 hours with both sets of stripe test structures. To remove etch debris which tends to accumulate after longer etch times, the test structures were rinsed with agitation in methanol. In all cases during the methanol rinse, a cloud of etch debris was observed separating from the test die.

The $5\text{-}\mu\text{m}$ -wide stripes in Figure 4.6 illustrate typical results. The upper layers consisting of low Al mole fraction AlGaAs were slowly etched after 2 hours. However, as shown in Figures 4.6b and d, during the 4-hr etch, the upper $\text{Al}_{0.2}\text{Ga}_{0.8}\text{As}$ layer was eventually penetrated, leading to exposure of the underlying lower Al mole fraction layers, which were then etched, leading to a rugged surface.

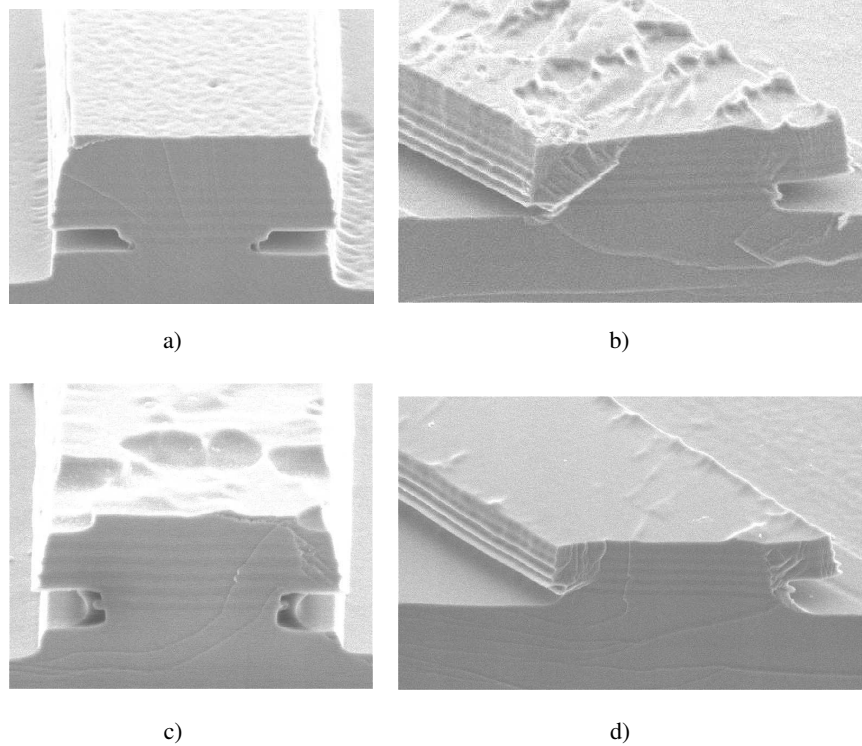


Figure 4.6: SEM of $5\text{-}\mu\text{m}$ wide, multi-layer, stripe mesas that were etched with a citric-acid/tripotassium-citrate/hydrogen-peroxide 5:5:1.5 at 25°C : a) and b) were etched for 2 hours; c) and d) were etched for 4 hours; in a) and c), stripes were parallel to wafer flat; in b) and d), stripes were 45° from wafer flat

In both the 2- and 4-hr cases, the lower $\text{Al}_{0.2}\text{Ga}_{0.8}\text{As}$ layers surrounding the $\text{Al}_{0.9}\text{Ga}_{0.1}\text{As}$ layer undercut $0.72 \pm 0.30\mu\text{m}$. The $\text{Al}_{0.9}\text{Ga}_{0.1}\text{As}$ layer was most likely broken off during the methanol rinse (agitated to remove etch debris). Some etch debris is still present, as shown in the lower right corner of Figure 4.6b.

Upon further inspection of the 2-hr 45° stripe test die, most of the $\text{Al}_{0.2}\text{Ga}_{0.8}\text{As}$ cap layers were undercut and broken off, most likely during the methanol agitation and rinse. As shown in Figure 4.7, the GaAs undercut distance measured $35.40 \pm 0.57\mu\text{m}$, corresponding to an etch rate of $0.295 \pm 0.004\mu\text{m}/\text{min}$. The undercut etch front is not clearly demarcated. This is likely due to the sensitivity of this anisotropic etch to dislocations or defects in the GaAs sacrificial layer [3]. Although undercut is possible when etch planes are parallel to $\langle 110 \rangle$, the anisotropic nature of this etchant leads to small-scale roughness (microfaceting) on the surface layer immediately adjacent to the removed GaAs layer.

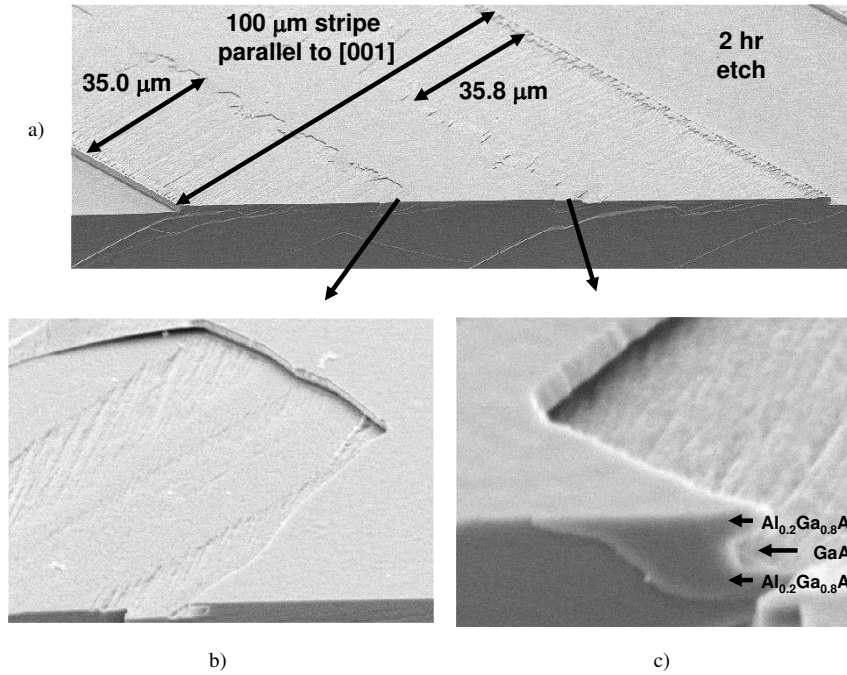


Figure 4.7: SEM of 100- μm -wide multi-layer etch study stripes: 2-hr citric-acid/tripotassium-citrate/hydrogen-peroxide 5:5:1.5 etch at 25°C ; stripes oriented 45° from wafer flat; layer composition is illustrated in Figure 4.1

Next, an empirical confirmation of the relative anisotropy of this GaAs etchant, a (100) GaAs wafer was lithographically patterned with a photoresist mask including structures designed to characterize etchant anisotropy. The GaAs wafer was diced into test die, then the GaAs etch study described earlier was performed. To avoid removing the photoresist mask, the rinse was performed with deionized water. As shown in Figure 4.8, anisotropy is clearly present, as shown by the orthogonal etch pits directed along the $\langle 001 \rangle$ directions. Thus, the citric-acid/tripotassium-citrate/hydrogen-peroxide 5:5:1.5 anisotropic GaAs wet-etch is not a good candidate

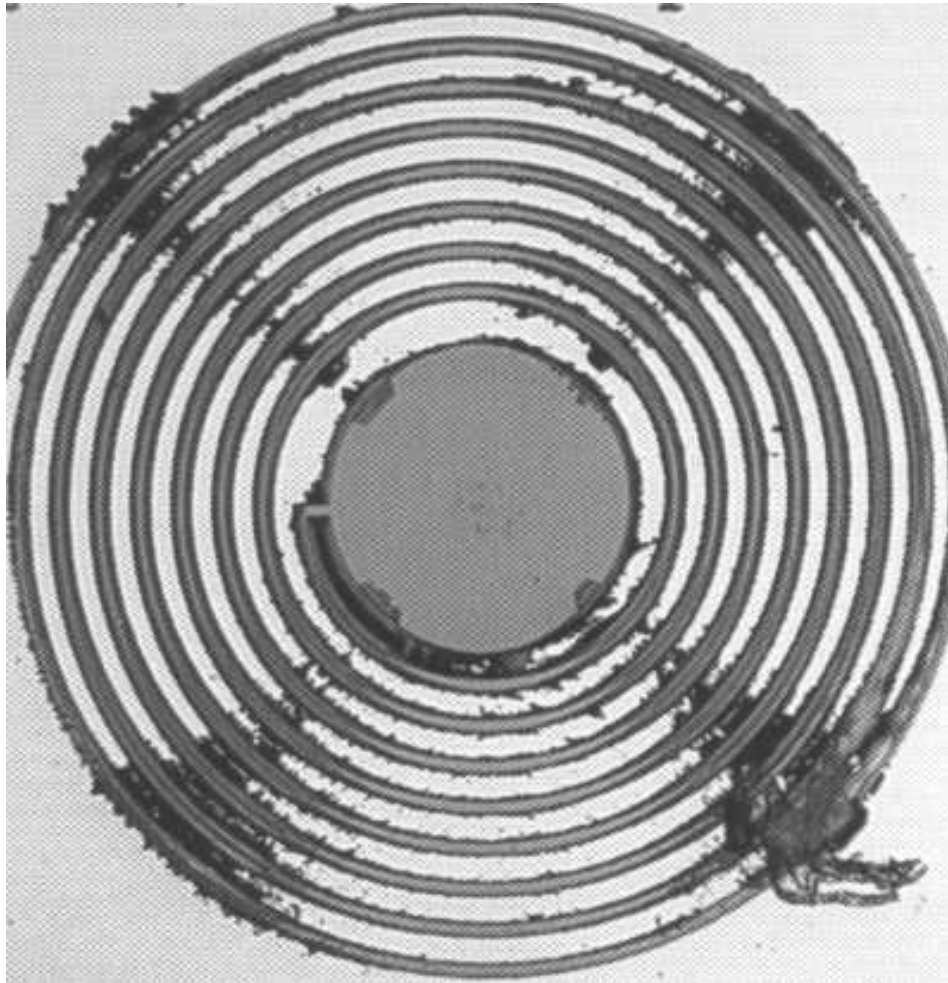


Figure 4.8: Spiral etch test structure for empirical anisotropy characterization of citric-acid/tripotassium-citrate/hydrogen-peroxide 5:5:1.5 etch at 25 °C: photoresist mask on GaAs substrate; orthogonal etch pits in directions 45° from wafer flats

for this hybrid MEM-tunable device research due to the following undesirable properties:

- Microfaceting of layers adjacent to the GaAs sacrificial layer
- Sensitivity to growth dislocations or defects in the GaAs sacrificial layer
- Relatively slow GaAs etch rates: $0.295 \pm 0.004 \mu\text{m}/\text{min}$ and $0.16 \pm 0.10 \mu\text{m}/\text{min}$ in the $\langle 001 \rangle$ and $\langle 011 \rangle$ directions, respectively
- Etch debris being difficult to remove; rinsing with agitation may damage MEMS devices

4.4 High Al mole fraction AlGaAs HF-based Etch

4.4.1 HF-based Etch Systems. Since the MUMPs[®] process incorporates HF as the sacrificial layer release etchant, the HF and dilute-HF etchants were identified as potentially compatible candidates for fabrication of a hybrid MEM-TF. Although we have reported HF-based isotropic etch systems for high Al mole fraction AlGaAs [2], at the time of this study, few studies of undercut etch distances and rates versus Al mole fraction of AlGaAs had been reported [4]. Thus, the next section is a summary of undercut rates to characterize this etch system as a candidate for sacrificial layer etching of high Al mole fraction, x , $\text{Al}_x\text{Ga}_{1-x}\text{As}$ over low or zero Al mole fraction.

4.4.2 HF-based Etch Study Methodology. The following is an overview of the HF-based etch study methodology. The samples are lithographically patterned then etched with a mesa mask consisting of stripe or square mesa patterns aligned parallel to the wafer flat. After removing the photoresist mask with acetone, the test samples were cleaned with methanol and IPA to remove impurities.

Next, the samples were placed in an LFE barrel stripper to remove organic impurities from the surface. The etch solution is prepared and placed in a plastic

petri dish at room temperature (nominally 25 °C). The test samples are placed in the solution without agitation. The etch is stopped via a deionized water dip or methanol rinse. Finally, the test samples are cleaved perpendicular to the stripe mesas, then, the etch profile is investigated using a scanning electron microscope. As shown in Figure 4.9, the high selectivity and well-defined undercut of high Al mole fraction sacrificial layers make measurements straight forward to perform. At least three measurements for each layer on different cross sections were used to calculate the mean and standard deviation for each undercut distance data point.

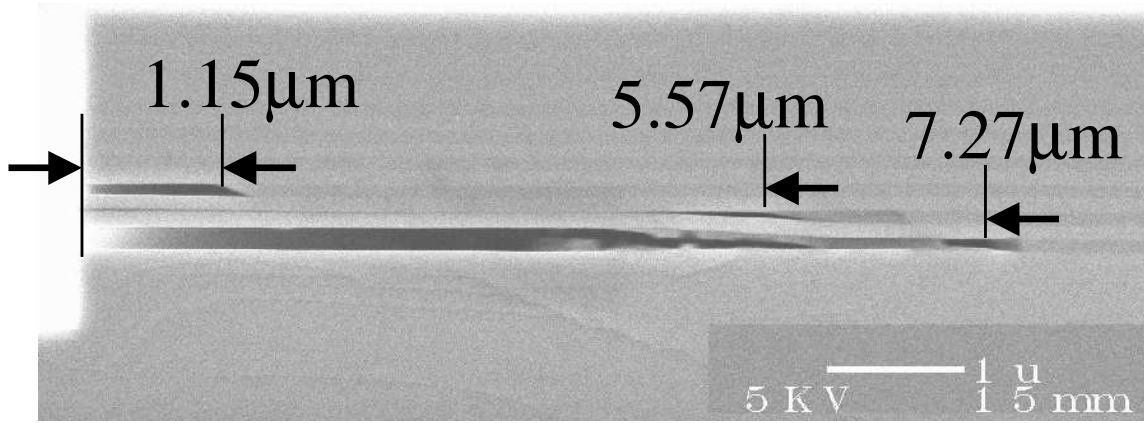


Figure 4.9: Example cross section and measurement of stripe etch test structure for undercut characterization of HF/IPA/H₂O 1:3:6 1-min etch: Al_{0.7}Ga_{0.3}As undercut is 1.15 μm; Al_{0.8}Ga_{0.2}As undercut is 5.57-μm; Al_{0.9}Ga_{0.1}As undercut is 7.27-μm; when the Al_{0.8}Ga_{0.2}As or other high selectivity layers were etched, the surrounding layers typically collapsed onto each other

The above HF-based etch study was performed using two etch solutions. The first was pure HF, and the second was HF:IPA:H₂O 1:3:6. The addition of IPA was to mitigate hydrogen bubbles which may adhere to the surface being etched and cause nonuniform etching [3]. The H₂O was added to further dilute the HF concentration. (Note: an alternative method reported to avoid hydrogen bubbles is to use 0 °C HF etch solution [8].)

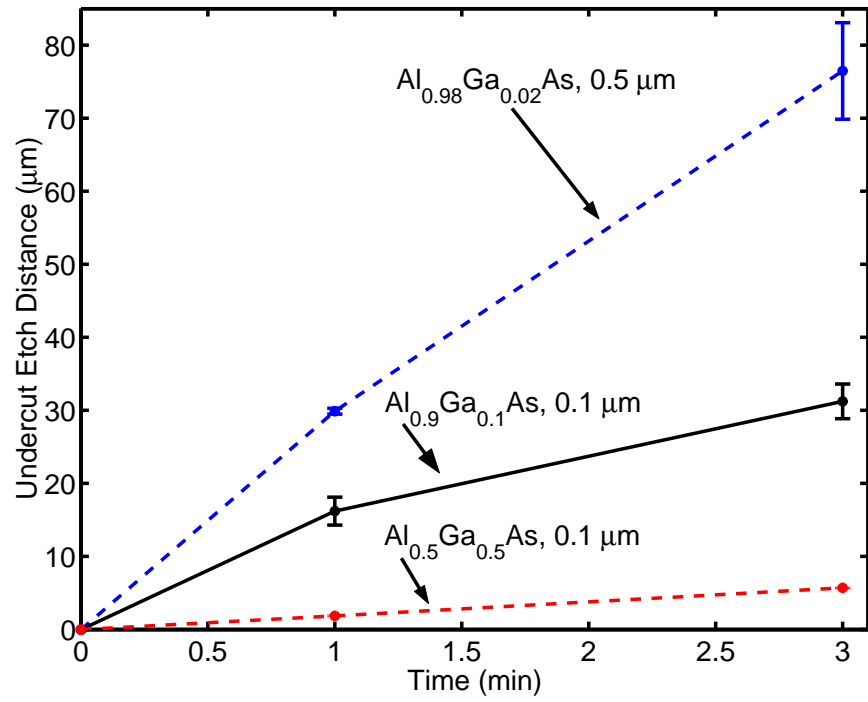
The material used in this etch study consisted of three material growths. The first two samples of materials were obtained from unrelated, salvaged wafer growths.

The first sample, MBE-grown G2-2614, contained a 0.5- μm AlAs sacrificial layer between an upper GaAs/AlAs 10.5-period DBR and a lower GaAs/AlAs 12-period DBR. This sample was patterned with square mesas. The objective of using the first sample was to measure the undercut etch rate for AlAs.

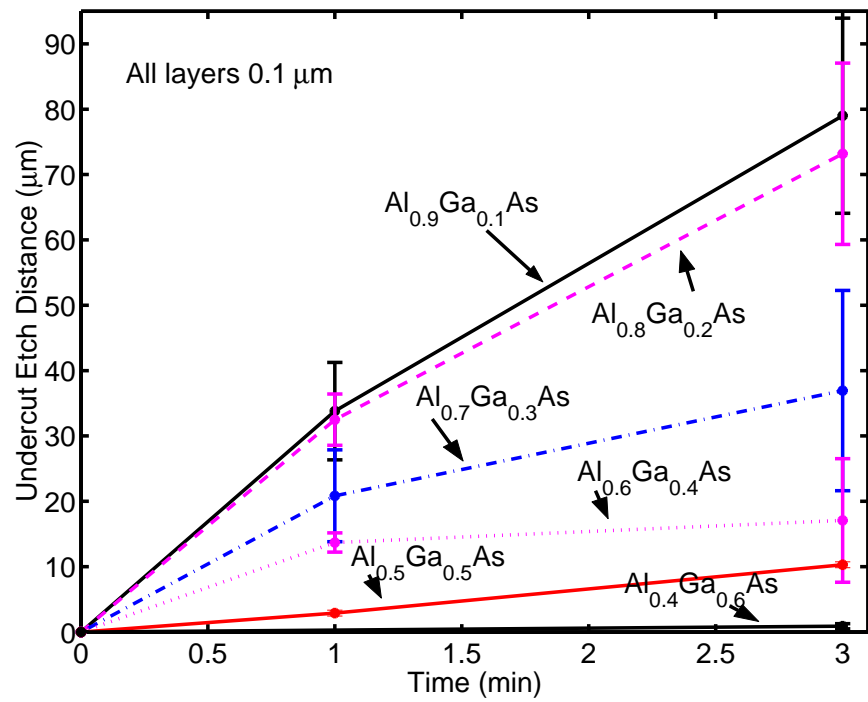
The second sample, MOVPE-grown EMC5420, consisted of the following layers, listed from substrate to top: 0.2- μm GaAs substrate cap, 0.5- μm $\text{Al}_{0.98}\text{Ga}_{0.02}\text{As}$, 0.097- μm GaAs, 0.105- μm $\text{Al}_{0.5}\text{Ga}_{0.5}\text{As}$, 0.097- μm GaAs, 0.105- μm $\text{Al}_{0.9}\text{Ga}_{0.1}\text{As}$, and a 0.097- μm GaAs cap. This sample was patterned with stripe mesas. The objective of using the second sample was to measure the undercut etch rates for $\text{Al}_{0.98}\text{Ga}_{0.02}\text{As}$, $\text{Al}_{0.9}\text{Ga}_{0.1}\text{As}$, and $\text{Al}_{0.5}\text{Ga}_{0.5}\text{As}$.

Finally, the third sample is the MOVPE EMC6844 material previously illustrated and annotated in Figure 4.1. The third sample consisted of a 0.1- μm -thick $\text{Al}_{0.2}\text{Ga}_{0.8}\text{As}$ substrate cap layer, then alternating/decreasing Al mole fraction Al-GaAs 0.1- μm -thick layers paired with $\text{Al}_{0.2}\text{Ga}_{0.8}\text{As}$, 0.1- μm -thick layers. This sample was also patterned with stripe mesas. The objective of using the third sample was to measure undercut etch rates for all layers etched by the test solutions studied.

4.4.3 HF Undercut Distances and Etch Rates. As illustrated in Figure 4.10 and listed in Tables 4.1 and 4.2, the HF etch system was characterized using the EMC5420 and EMC6844 stripe samples. In general, the undercut etch rates fell as time progressed. This was expected since the HF etch system is a diffusion-limited reaction, controlled by the rate at which reactant species can reach the surface [3]. As shown earlier in Figure 4.9, a major contributing factor to the relatively high standard deviation among undercut distances and rates listed in Tables 4.1 and 4.2 is the tendency for layers to collapse as they are undercut, pinching-off HF etchant access to sacrificial layers below.



a)



b)

Figure 4.10: HF etch undercut distance as a function of time: a) HF undercut etch of EMC5420, b) HF undercut etch of EMC6844

Table 4.1: EMC5420 HF etch undercut distances and rates

Al mole fraction	Thickness	Etch Time	Undercut distance (μm)		Undercut Rate ($\mu\text{m}/\text{min}$)	
(x)	(μm)	(min)	MEAN	STD DEV	MEAN	STD DEV
0.50	0.105	1	1.86	0.12	1.86	0.12
0.90	0.105	1	16.20	1.91	16.20	1.91
0.98	0.500	1	29.88	0.40	29.88	0.40
0.50	0.105	3	5.70	0.10	1.90	0.03
0.90	0.105	3	31.23	2.38	10.41	0.79
0.98	0.500	3	76.47	6.60	25.49	2.20

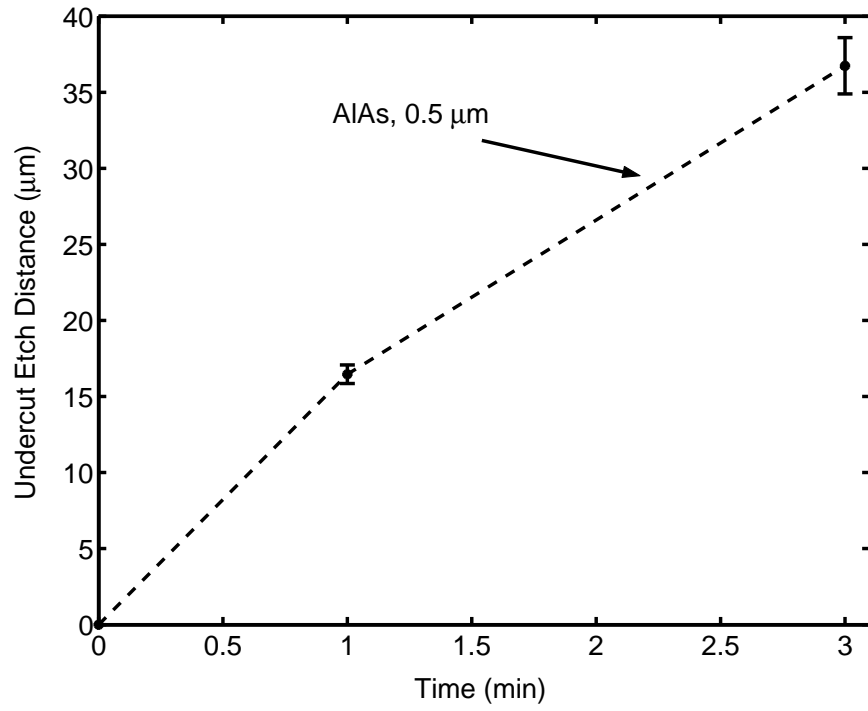
Table 4.2: EMC6844 HF etch undercut distances and rates

Al mole fraction	Thickness	Etch Time	Undercut distance (μm)		Undercut Rate ($\mu\text{m}/\text{min}$)	
(x)	(μm)	(min)	MEAN	STD DEV	MEAN	STD DEV
0.5	0.100	1	2.89	0.46	2.89	0.46
0.6	0.100	1	13.69	1.48	13.69	1.48
0.7	0.100	1	20.84	7.03	20.84	7.03
0.8	0.100	1	32.49	3.92	32.49	3.92
0.9	0.100	1	33.80	7.45	33.80	7.45
0.4	0.100	3	0.88	0.40	0.29	0.13
0.5	0.100	3	10.29	0.45	3.43	0.15
0.6	0.100	3	17.07	9.45	5.69	3.15
0.7	0.100	3	36.94	15.32	12.31	5.11
0.8	0.100	3	73.18	13.87	24.39	4.62
0.9	0.100	3	79.01	14.93	26.34	4.98

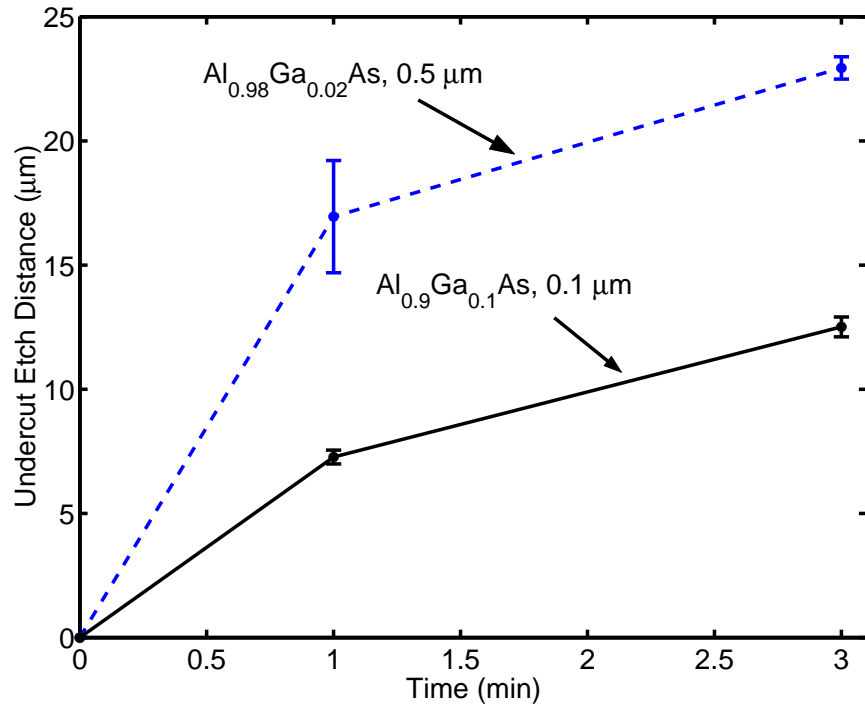
Undercut distances and rates for the AlAs layer in the G2-2614 samples were not measurable due to top DBR lift-off in all samples confirmed via SEM inspection. However, during SEM inspection of the 1- and 3-min HF-etched samples, the 1-min samples had trace amounts of the AlAs sacrificial layer remaining in the center of each mesa. Inspection of the 3-min samples revealed all had total removal of the top DBR, AlAs sacrificial layer, and bottom DBR. As a final note, while the G2-2614 samples were being HF-etched, the behavior of the bubbles which formed on the mesa test structures was closely observed. At about the 1.5-min point, the bubbles began to rise. This may have been when the AlAs sacrificial layer was completely removed, considering the top DBR had already detached (based on SEM inspection results mentioned above).

4.4.4 HF:IPA:H₂O Undercut Distances and Etch Rates. As listed and illustrated in Figures 4.11 and 4.12, and Tables 4.3-4.5, the HF:IPA:H₂O 1:3:6 etch system was characterized using the G2-2614, EMC5420, and EMC6844 samples. As with pure HF, the undercut etch rates fell as time progressed due to the diffusion-limited reaction rates for this etch system. Again, a major contributing factor to the relatively high standard deviation among undercut distances and rates is the tendency for layers to fall as they are undercut, pinching-off etchant access to sacrificial layers.

4.4.5 HF versus HF:IPA:H₂O Undercut Comparisons. As listed in the right column of Tables 4.6 and 4.7, the dilution of HF with IPA and H₂O led to undercut reduction between 46 and 95%. In general, when comparing percent reduction for identical layers in the same material growth, the percent reduction was fairly consistent. However, when comparing the percent reduction for Al_{0.9}Ga_{0.1}As layers between the two material growths, the percentage reduction was inconsistent. The major contributing factor to this inconsistency is the difference in material growths



a)



b)

Figure 4.11: HF/IPA/H₂O 1:3:6 undercut etch distance as a function of time: a) undercut etch measurements for G2-2614, b) undercut etch measurements for EMC5420

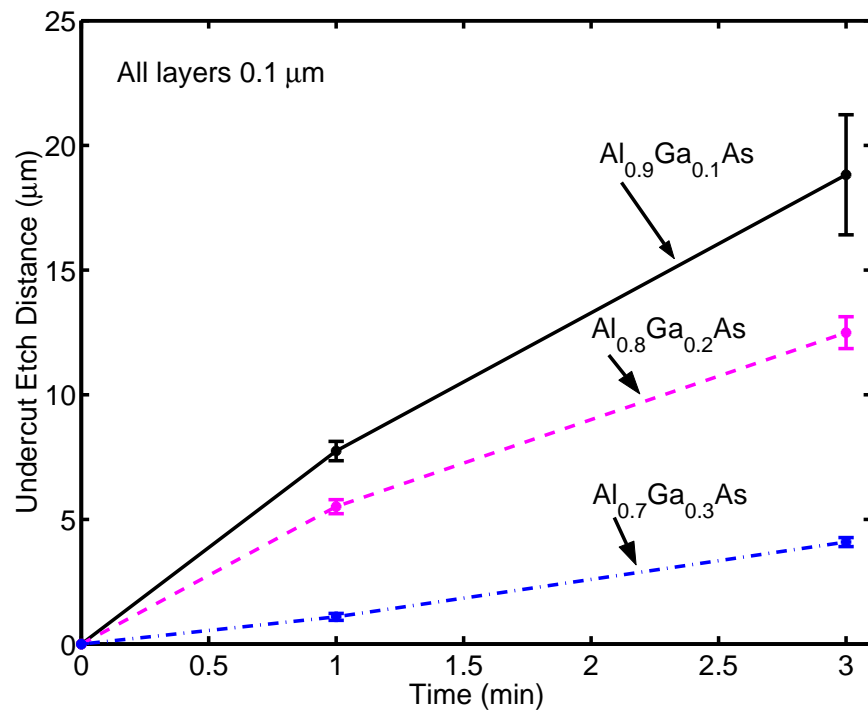


Figure 4.12: HF:IPA:H₂O 1:3:6 undercut etch distance as a function of time: undercut etch measurements for EMC6844

Table 4.3: G2-2614 HF:IPA:H₂O 1:3:6 etch undercut distances and rates

Al mole fraction	Thickness	Etch Time	Undercut distance (μm)		Undercut Rate ($\mu\text{m}/\text{min}$)	
(x)	(μm)	(min)	MEAN	STD DEV	MEAN	STD DEV
1.00	0.500	1	16.46	0.61	16.46	0.61
1.00	0.500	3	36.74	1.85	12.25	0.62

Table 4.4: EMC5420 HF:IPA:H₂O 1:3:6 etch undercut distances and rates

Al mole fraction	Thickness	Etch Time	Undercut distance (μm)		Undercut Rate ($\mu\text{m}/\text{min}$)	
(x)	(μm)	(min)	MEAN	STD DEV	MEAN	STD DEV
0.90	0.105	1	7.27	0.28	7.27	0.28
0.98	0.500	1	12.51	0.40	12.51	0.40
0.90	0.105	3	16.95	2.26	5.65	0.75
0.98	0.500	3	22.94	0.45	7.65	0.15

Table 4.5: EMC6844 HF:IPA:H₂O 1:3:6 etch undercut distances and rates

Al mole fraction	Thickness	Etch Time	Undercut distance (μm)		Undercut Rate ($\mu\text{m}/\text{min}$)	
(x)	(μm)	(min)	MEAN	STD DEV	MEAN	STD DEV
0.70	0.100	1	1.09	0.14	1.09	0.14
0.80	0.100	1	5.51	0.28	5.51	0.28
0.90	0.100	1	7.74	0.39	7.74	0.39
0.70	0.100	3	4.09	0.18	1.36	0.06
0.80	0.100	3	12.49	0.64	4.16	0.21
0.90	0.100	3	18.82	2.41	6.27	0.80

Table 4.6: EMC5420 HF versus HF:IPA:H₂O etch distance

Material:	EMC5420	Etch System:	HF	HF:IPA:H ₂ O	Percent reduction (%)
Al mole fraction (x)	Thickness (μm)	Etch Time (min)	Undercut (μm)	Undercut (μm)	
0.90	0.105	1	16.20	7.27	55
0.98	0.500	1	29.88	12.51	58
0.90	0.105	3	31.23	16.95	46
0.98	0.500	3	76.47	22.94	70

Table 4.7: EMC6844 HF versus HF:IPA:H₂O etch distance

Material:	EMC6844	Etch System:	HF	HF:IPA:H ₂ O	Percent reduction (%)
Al mole fraction (x)	Thickness (μm)	Etch Time (min)	Undercut (μm)	Undercut (μm)	
0.70	0.10	1.00	20.84	1.09	95
0.80	0.10	1.00	32.49	5.51	83
0.90	0.10	1.00	33.80	7.74	77
0.70	0.10	3.00	36.94	4.09	89
0.80	0.10	3.00	73.18	12.49	83
0.90	0.10	3.00	79.01	18.82	76

and the corresponding exposure of more/less high Al mole fraction AlGaAs layers available to react with each etch system. Thus, although these tables provide a means to estimate anticipated undercut rates, the fundamentally more accurate approach is to characterize rates using the actual growth samples and structures under consideration.

4.5 Chapter Summary

The objective of this chapter was to investigate and characterize candidate III-V AlGaAs materials etchants to enable fabrication of a hybrid MEM-TF. Studies were performed to identify a candidate etch chemistry compatible (non-destructive) with both an AlGaAs DBR and a MUMPs® polySi actuator. Three III-V sacrificial layer etchants were examined, one for GaAs and the other two for high Al mole fraction AlGaAs.

First, characterization of a citric-acid/tripotassium-citrate/hydrogen-peroxide etchant for GaAs sacrificial layers was attempted. Unfortunately, due to micro-faceting, sensitivity to growth dislocations, and significant etch debris, this etchant was determined to not be a candidate for a GaAs sacrificial layer etch. Thus, this etchant and GaAs sacrificial layer etching was no longer pursued.

Next, two HF-based high Al mole fraction etch studies were performed, one with HF and the other with dilute HF. In both cases, this etchant was successfully characterized and etch rates were reported. Additionally, the multi-layer HF and dilute HF studies identified the Al mole-fraction of $x = 0.4$ as a consistent etch-stop for both HF and dilute-HF. Finally, since the MUMPs® process incorporates HF as the sacrificial layer release etchant, the HF and dilute-HF etchants were identified as potentially compatible candidates for fabrication of a hybrid MEM-TF.

Bibliography

1. C. J. Chang-Hasnain, *Micromechanical Tunable VCSEL*, ser. Optoelectronic Properties of Semiconducors and Superlattices. Gordon and Breach Science Publishers, 2000, ch. 6, pp. 279–318.
2. O. Blum-Spahn, T. Bakke, C. P. Tigges, J. Johnson, G. Grossetete, F. R. Gass, E. M. Ochoa, J. L. Reno, J. F. Klem, G. M. Peake, and C. T. Sullivan, “GaAs-based Waveguide MOEMS,” in *Modeling and Simulation of Microsystems 2002*, San Juan, Puerto Rico, April 2002.
3. R. Williams, *Modern GaAs Processing Methods*. Artech House: Boston, 1990.
4. A. R. Clawson, “Guide to references on III-V semiconductor chemical etching,” *Materials Science and Engineering*, vol. 31, pp. 1–438, 2001.
5. N. L. Rimmer, C. Pillote, and J. H. Huang, “Selective Etching GaAs/AlGaAs Using Buffered Citric Acid Etch,” in *State-Of-The-Art Program on Compound Semiconductors XXI*, Miami Beach, FL, Oct 1994, pp. 141–146.
6. E. Y. Chang, Y.-L. Lai, Y. S. Lee, and S. H. Chen, “A GaAs/AlAs Wet Selective Etch Process for the Gate Recess of GaAs Power Metal-Semiconductor Field Effect Transistors,” *Journal of the Electrochemical Society*, vol. 148, no. 6, pp. G4–G9, 2001.
7. H. C. Chang, E. Y. Chang, C.-C. Chung, and C. T. Kuo, “Highly Selective GaAs/Al(0.2)Ga(0.8)As Wet Etch Process for the Gate Recess of Low-Voltage-Power Pseudomorphic High-Electron-Mobility Transistor,” *Jpn. J. Appl. Phys.*, vol. 39, no. 8, pp. 4699–4703, 2000.
8. A. Riedel, E. Wiebicke, H. Kostial, R. Hey, and K.-J. Friedland, “High mobility electron gas wafer-fused on LiNbO₃,” in *International Symposium on Carrier Interactions in Mesoscopic Systems 2001 (CIM 2001)*, Atsugi, Kanagawa, Japan, Feb 2001.

V. Flip-Bond Process Development

5.1 Chapter Overview

This chapter reports the hybrid MEM-TF process methods developed to flip-bond a 4.92- μm -thick, $250 \times 250\text{-}\mu\text{m}^2$, $\text{Al}_{0.4}\text{Ga}_{0.6}\text{As}$ -GaAs DBR to a polySi actuator, and then release the DBR from the donor GaAs substrate. These steps required significant process development and were the most challenging impediments to demonstrating a hybrid MEM-TF.

Specifically, material processing methods were developed to ensure hybrid MEM-TF devices could withstand subsequent polySi sacrificial layer etch and release processing. Both HF and dilute-HF etchants were used to release the DBR mesa on AlAs sacrificial layer from the GaAs donor substrate. Also, metallic (Au-Au, Au-In) and epoxy (SU-8-SU-8) flip-bonding material combinations were investigated.

5.2 Hybrid MEM-TF Fabrication

The hybrid MEM-TF device consisted of a fixed central Au reflector encircled by a MUMPs[®] polySi platform actuator (Figure 5.1a) with a flip-bonded DBR (Figure 5.1b). Eight, $50 \times 50\text{-}\mu\text{m}^2$ bond-pads were photolithographically patterned onto each RIE-etched DBR mesa and corresponding polySi actuator. To increase potential device yield during process development, a 5×6 array of hybrid MEM-TF devices and DBR mesas was patterned on both the GaAs (donor) and 0.5-cm MUMPs[®] (acceptor) die. The donor and acceptor die were flip-bonded using an RD Automation M9A Flip Chip Aligner Bonder. After flip-bonding the donor and acceptor die, the GaAs substrate was released via an HF-based AlAs sacrificial layer etch. Next, the MUMPs[®] actuators were released with a 5-min HF soak, rinsed in methanol for 5 min, and then underwent supercritical CO_2 drying. Finally, device die were packaged at room temperature and prepared for tuning characterization.

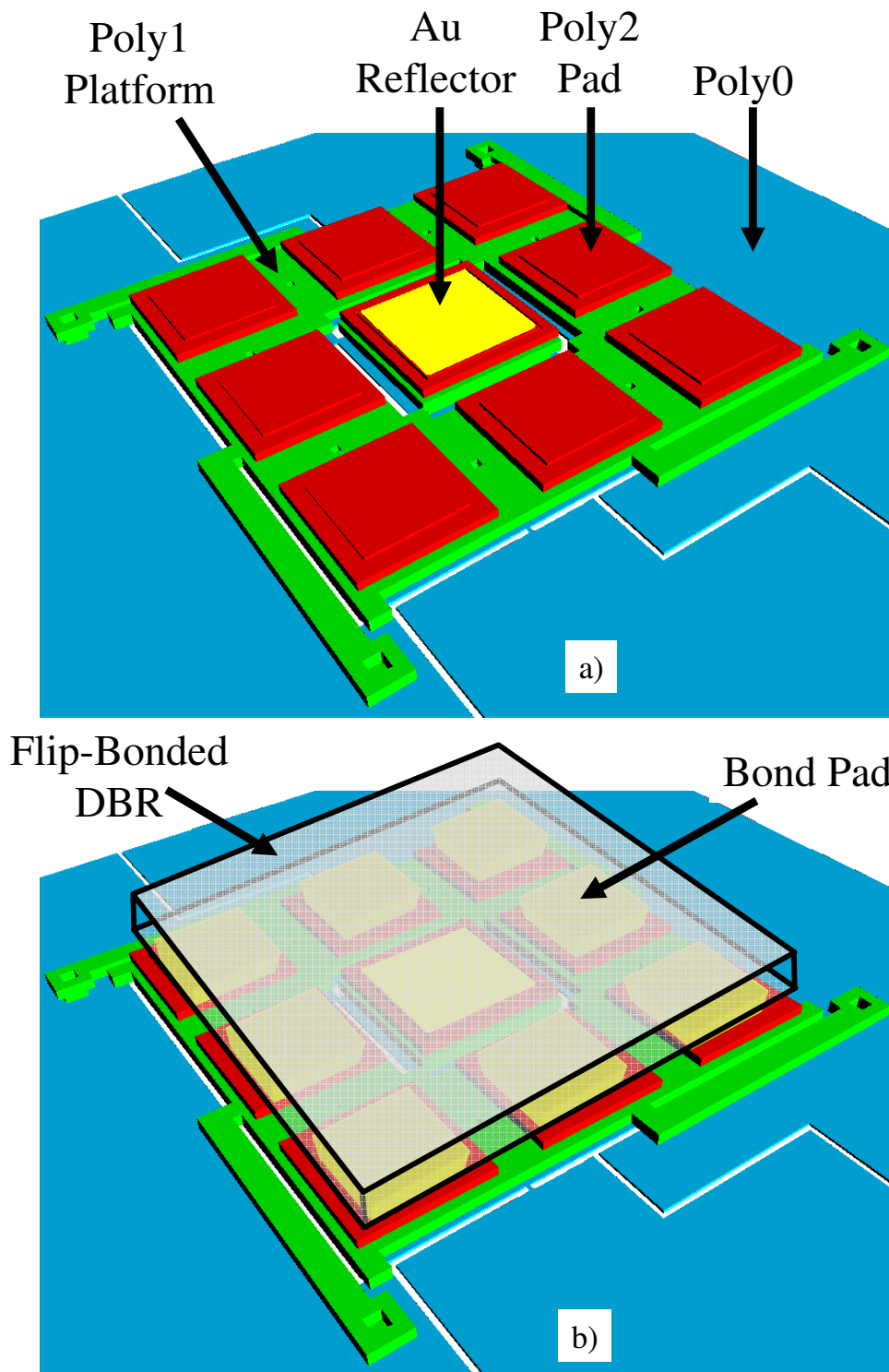


Figure 5.1: Hybrid MEM-TF three-dimensional design illustrations: a) MUMPs® polySi piston actuator with central Au reflector b) DBR flip-bonded to actuator

5.3 *Flip-bond Studies*

5.3.1 Methodology. In order to preserve the limited DBR and polySi material, each bond-pad candidate material was photolithographically patterned/deposited onto donor and acceptor 0.5-cm Si die, corresponding to DBR donor die and MUMPs® acceptor die surrogates, respectively. Next, the bond-pad material, and the flip-bonding temperature, time, and pressure settings were experimentally determined post-bonding via manual separation and visual inspection of pair-wise bond-sites. If the bonds were resistant to manual separation, the material under study was considered a viable bond-pad candidate material.

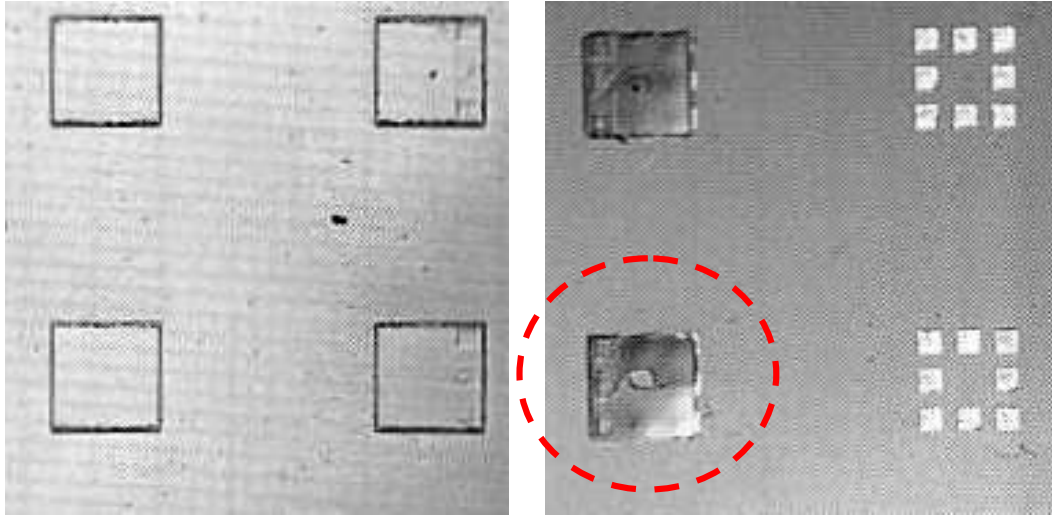
Next, to further preserve the limited polySi material, the DBR donor and 0.5-cm Si die (MUMPs® surrogate) were bonded using the candidate material, then underwent DBR release processing. The DBR release was considered successful if the DBR mesas appeared intact post-release. At this point, if the polySi material supply was sufficient, the bond-pad candidate material was then used to flip-bond the DBR and polySi die. The bond-pad material and fabrication process was considered viable if the DBR appeared intact (crack-free) post-bonding and the hybrid MEM-TF device was electrostatically actuatable after undergoing the MUMPs® polySi release steps described earlier.

5.3.2 Au-Au Flip-Bonding. As discussed in Chapter II, the MUMPs® foundry process provides a design option to deposit a chrome adhesion layer followed by a 0.5- μm Au layer. Thus, Au-Au bond-pads were selected as the first candidate material for both the DBR donor and MUMPs® acceptor die. As a result, the MUMPs® actuators were designed with $50 \times 50\text{-}\mu\text{m}^2$ 0.5- μm -thick Au bond-pads. Au bond-pads were photolithographically patterned (deposited) onto donor and acceptor 0.5-cm Si die (DBR and MUMPs® surrogates). The Au-Au bond-pad flip-bonding temperature, time, and pressure settings were experimentally determined as 375 °C, 1hr, and 1333kg/cm², respectively [1].

Next, the DBR donor die were patterned with $50 \times 50\text{-}\mu\text{m}^2$ $0.5\text{-}\mu\text{m}$ Au bond-pads, defined by lift-off resist photolithography. The 0.5-cm Si die (MUMPs® surrogate) were patterned with $50 \times 50\text{-}\mu\text{m}^2$ $0.5\text{-}\mu\text{m}$ Au bond-pads. The donor and acceptor die were flip-bonded, then underwent a 5-min HF DBR release with nominal results shown in Figure 5.2. Although several DBR were flip-bonded to the surrogate 0.5-cm Si die, the DBR were consistently damaged/cracked. In spite of repeated attempts to optimize the flip-bonding process step (*i.e.*, flip-bonder calibration, attention to flip-bonder donor-acceptor die planarity, *etc.*), the DBR cracking persisted.

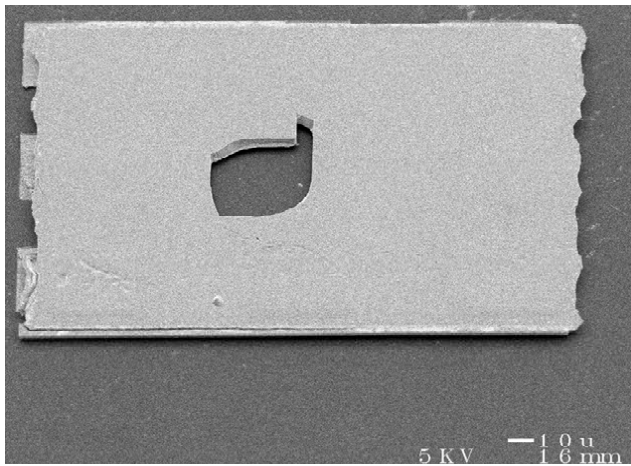
Although these results were not optimal, to confirm whether Au-Au bond-pad processing may be compatible with the MUMPs® polySi actuators, several attempts were made to Au-Au bond using DBR and polySi die with results similar to Figure 5.3. Since these results were not optimal, several dilute-HF etch solution (HF:IPA:DIW with 1:3:6 ratio) attempts were performed next with similar results as shown in Figure 5.4. As we reported, the DBR damage was finally attributed to the high bonding pressure required to flip-bond with Au-Au bond-pads [1].

5.3.3 Au-In Flip-Bonding. Since the DBR damage was attributed to the high pressure required for Au-Au bonding, and in an effort to maximize use of the remaining MUMPs® die with $0.5\text{-}\mu\text{m}$ -thick Au bond-pads, an alternate DBR bond-pad material was sought which was compatible with the prototype MEM-TF HF release chemistry and also able to bond to the MUMPs® Au bond-pads. Since In forms a strong bond with Au and is a much softer metal, flip-bonding with Au-In bond-pads was investigated next. In bond-pads were electroplated or evaporated onto donor and acceptor 0.5-cm Si die (DBR and MUMPs® surrogates). The Au-In bond-pad flip-bonding temperature, time, and pressure settings were experimentally determined as $275\text{ }^\circ\text{C}$, 1hr, and 333kg/cm^2 , respectively [1].

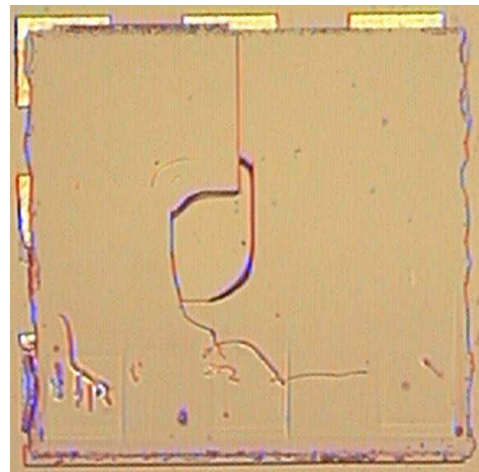


a)

b)

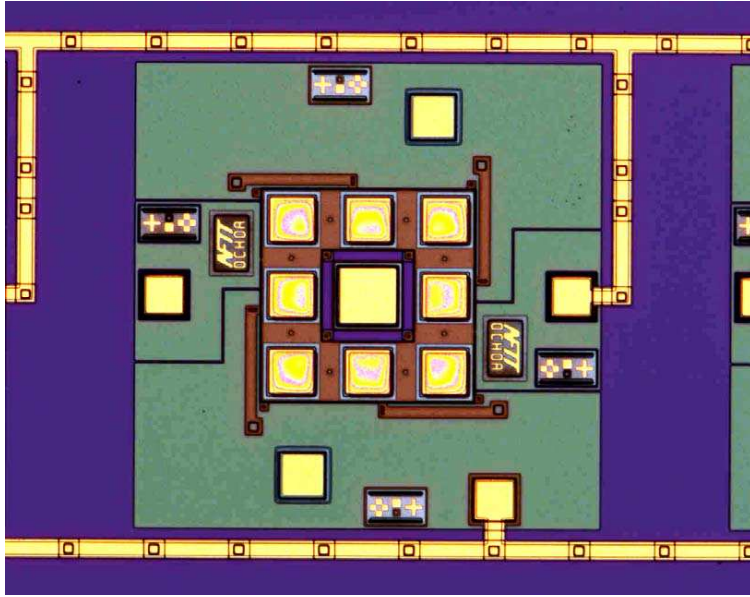


c)

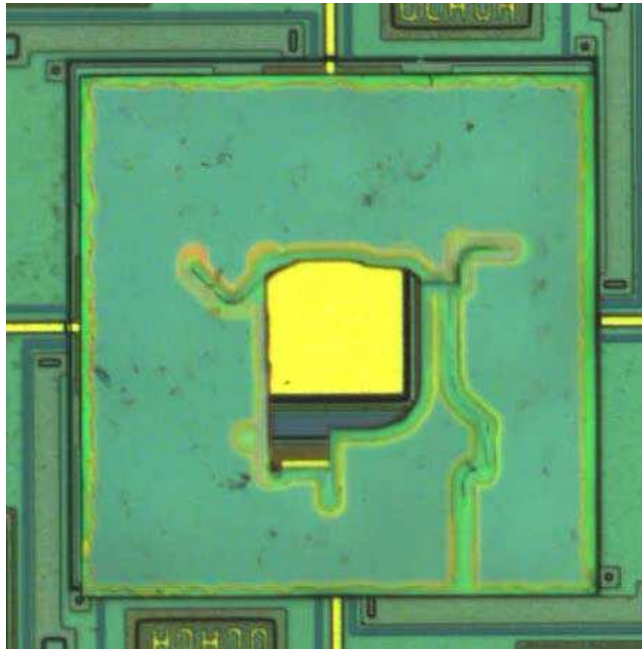


d)

Figure 5.2: Au-Au DBR Si die surrogate flip-bonding: a) donor die DBR mesa sites b) acceptor die Au bond-pad sites, c) SEM photo of cracked DBR, d) microscope photo of a cracked DBR

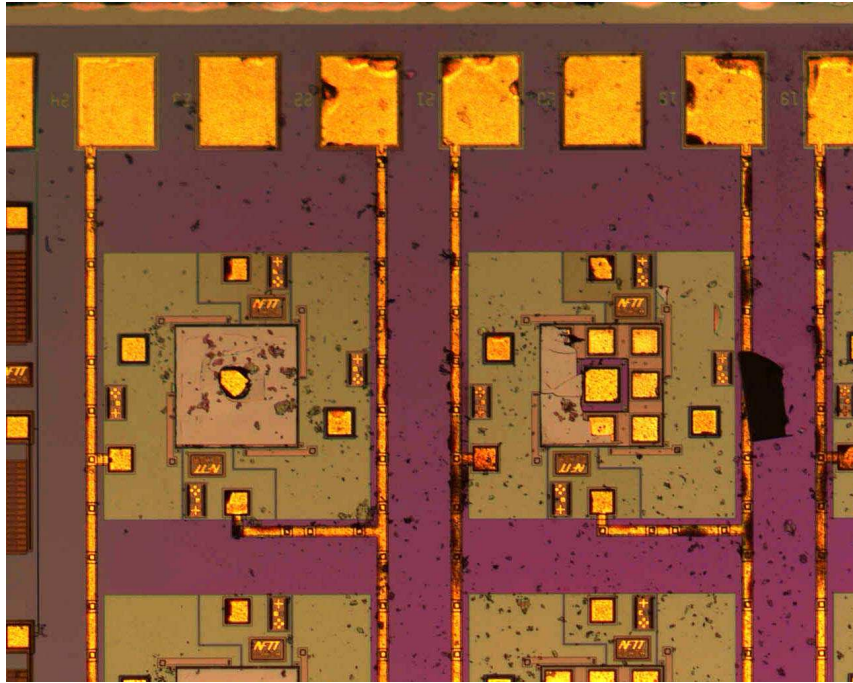


a)

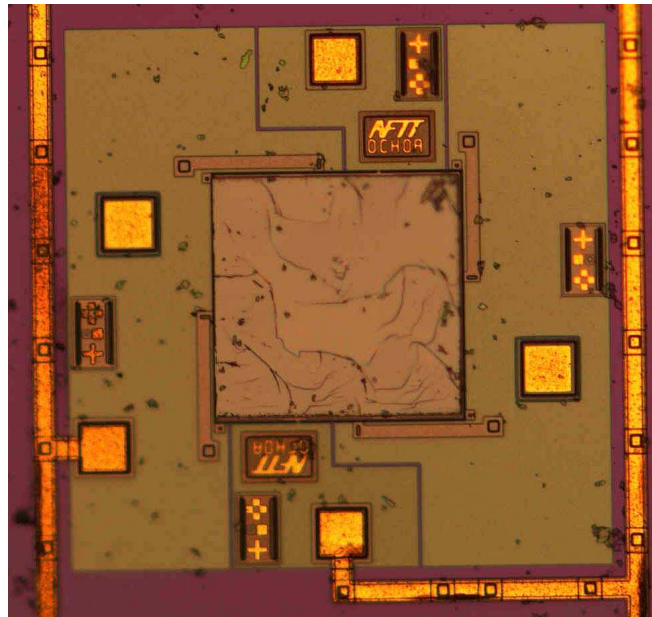


b)

Figure 5.3: Au-Au bonding with polySi die after HF release: a) microscope view of polySi platform b) representative example of a cracked DBR after flip-bonding with Au bond-pads



a)



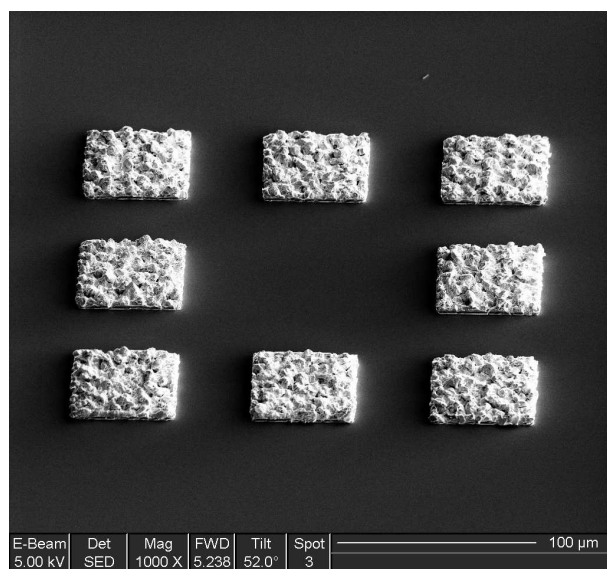
b)

Figure 5.4: Au-Au bonding with polySi die after dilute-HF release: a) microscope photo overview of polySi die acceptor sites b) microscope photo of a cracked DBR

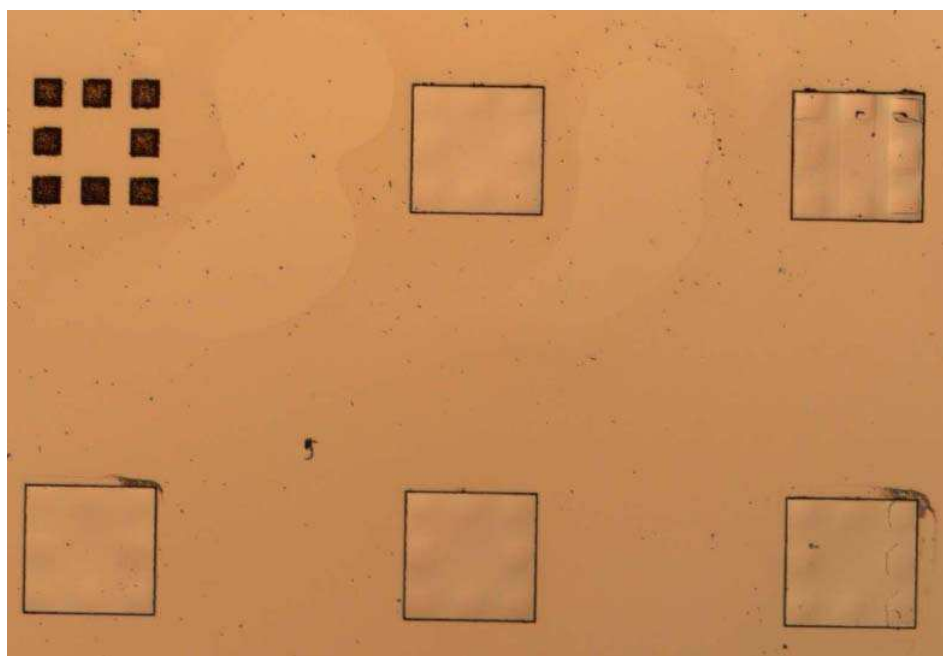
Next, the DBR donor die were patterned with $50 \times 50\text{-}\mu\text{m}^2$ $1.5\text{-}\mu\text{m}$ In bond-pads. Again, 0.5-cm Si die (MUMPs[®] surrogate) were patterned with $50 \times 50\text{-}\mu\text{m}^2$ $0.5\text{-}\mu\text{m}$ Au bond-pads. The donor and acceptor die were flip-bonded, then underwent a 5-min HF DBR release with results similar to Figure 5.2. Although several DBR mesas were flip-bonded to the surrogate 0.5-cm Si die, the all were consistently damaged and/or cracked. Again, after additional process optimization investigations, the DBR cracking was consistent in all HF release attempts. Next, the 75-min dilute-HF etch (HF:IPA:DIW with 1:3:6 ratio) was performed with promising results; several crack-free DBR survived the release process as shown in Figure 5.5. Although the Au-In bonds were not as strong as the Au-Au bonds, 21 of the 30 possible bond attempts sites resulted with crack-free, attached DBR.

Since the dilute-HF etch yielded promising results, the dilute-HF release was investigated next. As shown in Figure 5.6a, DBR donor die with In bond-pads were flip-bonded to the MUMPs[®] polySi die, then underwent dilute HF DBR release, followed by full-strength HF polySi actuator release with CO_2 dry. Although the bond-pad material and fabrication process was initially considered viable since the DBR appeared intact (crack-free), all hybrid MEM-TF devices were not electrostatically actuatable.

Upon further investigation, significant damage to the MUMPs[®] Au-layer was observed as shown in Figure 5.6b. The Au layer physical damage characteristics included a mottled appearance, small bumps, and peeling. This loss of Au planarity was undesirable since it damaged the Au reflector, a key element in the device design. The primary sources of Au layer damage were attributed to two fabrication process steps. The first source of Au layer damage was the high $375\text{ }^\circ\text{C}$ Au-Au or $275\text{ }^\circ\text{C}$ Au-In bonding temperatures, which led to small bumps observed in the Au layer [1]. Both of these temperatures exceeded $225\text{ }^\circ\text{C}$, a previously reported threshold temperature, beyond which Au damage and reduction in reflectivity has been reported [2].

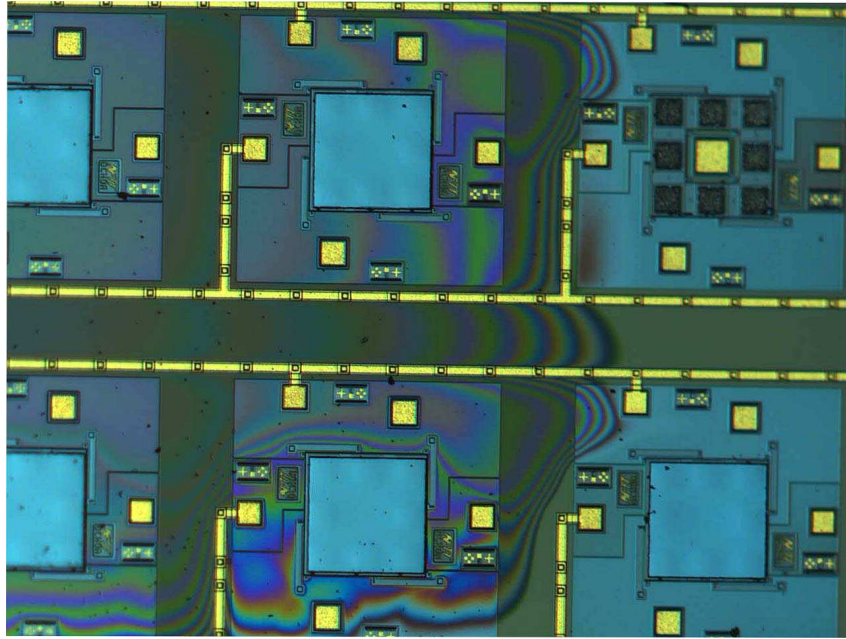


a)

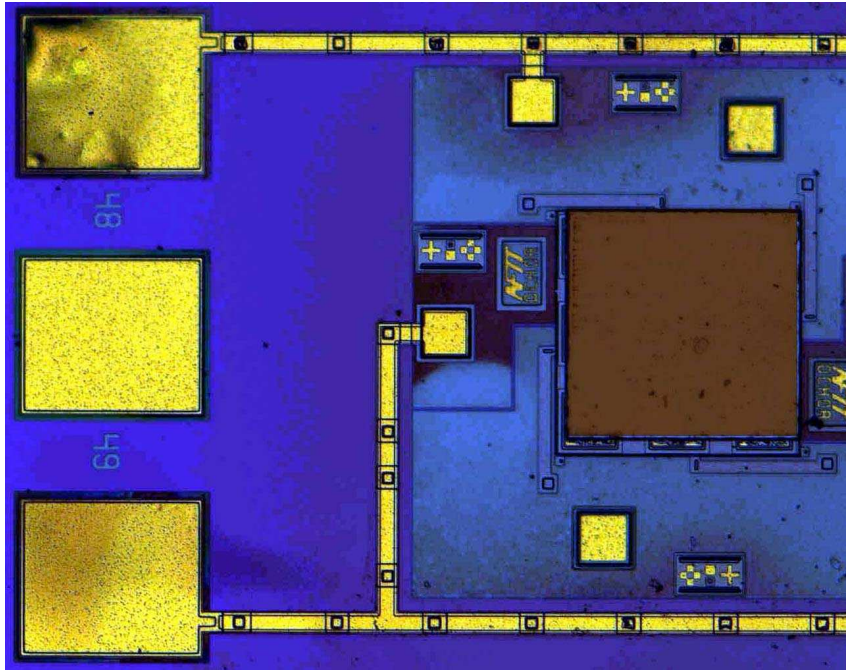


b)

Figure 5.5: Au-In bonding: a) evaporated In bond-pads, b) microscope inspection of In bond-pad DBR flip-bonded to Si surrogate die demonstrating crack-free DBR mesas



a)



b)

Figure 5.6: Au-In bonding: a) crack-free DBR mesas flip-bonded to polySi actuators, b) mottled, damaged Au layer on polySi die

The second source of Au layer damage was the 1.5-hr DBR mesa release via dilute HF solution (1:3:6 HF:IPA:H₂O) electrochemical interaction with the polySi on the acceptor die and the (unintentional) significant amount of Au on the MUMPs® die [3]. Thus, the fabrication sequence, which included Au-In flip-bonding then dilute-HF release, was found unsatisfactory for hybrid MEM-TF fabrication.

However, since the dilute-HF etch enabled crack-free DBR flip-bonding, the dilute-HF step remained a candidate process step. Additionally, although the electrochemical interaction was due to the relatively lengthy (time) dilute-HF etch, the use of the softer/lower-bond-pressure In was identified as a contributing factor toward crack-free DBR mesas. Since the most significant amount of Au on the MUMPs® die was associated with wiring for electrostatic actuation, this Au wiring and several unused Au bond-pads were either replaced or substituted with Poly 2 to mitigate the electrochemical interaction identified earlier.

Although In-In bonding was not investigated in this research, this bonding material may be compatible (low bond pressure and temperature) for fabricating flip-bonded, active (emitting or sensing) optoelectronic devices. Since the MEM-TF is not an active optoelectronic device, the bond-pad material search space was increased to find an alternate material which does not require high pressure or temperature during flip-bonding, and is compatible with dilute-HF.

5.3.4 SU-8-SU-8 Flip-Bonding. As we reported [1], SU-8 2002 was demonstrated to have both low-temperature and low-pressure bonding characteristics, and a well-known resistance to HF (and dilute-HF). In this study, the influence of bonding temperature on SU-8 to SU-8 bond strength was characterized. As a result of this investigation, SU-8 was identified as a viable hybrid MEM-TF material candidate and enabled successful flip-bonding of Al_{0.4}Ga_{0.6}As-GaAs crack-free DBR to MUMPs® polySi MEMS platforms [4].

In preparation for flip-bonding the DBR mesa structures to polySi MEMS devices, the effect of bond temperature on SU-8 to SU-8 bond strength was investigated. In order to preserve the limited DBR and polySi material, the donor and acceptor die were simulated by substituting two 0.5-cm die diced from a quarter wafer of Si.

The Si quarter wafer was photolithographically patterned with multiple 5×6 arrays of SU-8 bond-pad sets. Each bond-pad set consisted of eight, $50 \times 50\text{-}\mu\text{m}^2$ bond-pads. The SU-8 photolithography included the following steps: 1) 30-s, 2000-r/min SU-8 spin, 2) 3-min, $65\text{ }^\circ\text{C}$ bake, 3) 3-min, $110\text{ }^\circ\text{C}$ bake, 4) 9-s, $7\text{-mW}/\text{cm}^2$, 365-nm exposure, 5) 3-min, $65\text{ }^\circ\text{C}$ bake, 6) 3-min, $110\text{ }^\circ\text{C}$ bake, 7) 90-s SU-8 bucket develop, and 8) 15-s IPA rinse. This process resulted with nominally $2\text{-}\mu\text{m}$ thick SU-8 bond-pads.

For each bonding temperature (identified below), two 0.5-cm die with SU-8 bond-pads were flip-bonded using a RD Automation M9A Flip-Chip Aligner Bonder set to 1-kg applied weight ($\sim 167\text{-kg}/\text{cm}^2$) and 10-min bond time. In order to further characterize the low temperature bonding characteristics of SU-8, the temperatures investigated were lower and included the $165\text{ }^\circ\text{C}$ bonding temperature demonstrated in our prior work [1]. The bond temperatures characterized were $105\text{ }^\circ\text{C}$, $120\text{ }^\circ\text{C}$, $135\text{ }^\circ\text{C}$, $150\text{ }^\circ\text{C}$, and $165\text{ }^\circ\text{C}$. After flip-bonding, each pair of SU-8 bonded die was manually separated then visually inspected.

As described earlier, low-temperature processing was desired to preserve Au layer reflectivity. As shown in Figure 5.7, when the bond temperature was set to $135\text{ }^\circ\text{C}$ or higher, the bond-pads nominally separated from one die to the other. Each image pair is a representative set of bond-pads which illustrate nominal results of each labeled flip-bonder temperature setting. At $135\text{ }^\circ\text{C}$, the bonding strength appeared significantly stronger between the SU-8 pads than between the SU-8 pad and Si die. Thus, $135\text{ }^\circ\text{C}$, the lowest temperature with significant bond strength, was selected for hybrid MEM-TF fabrication.

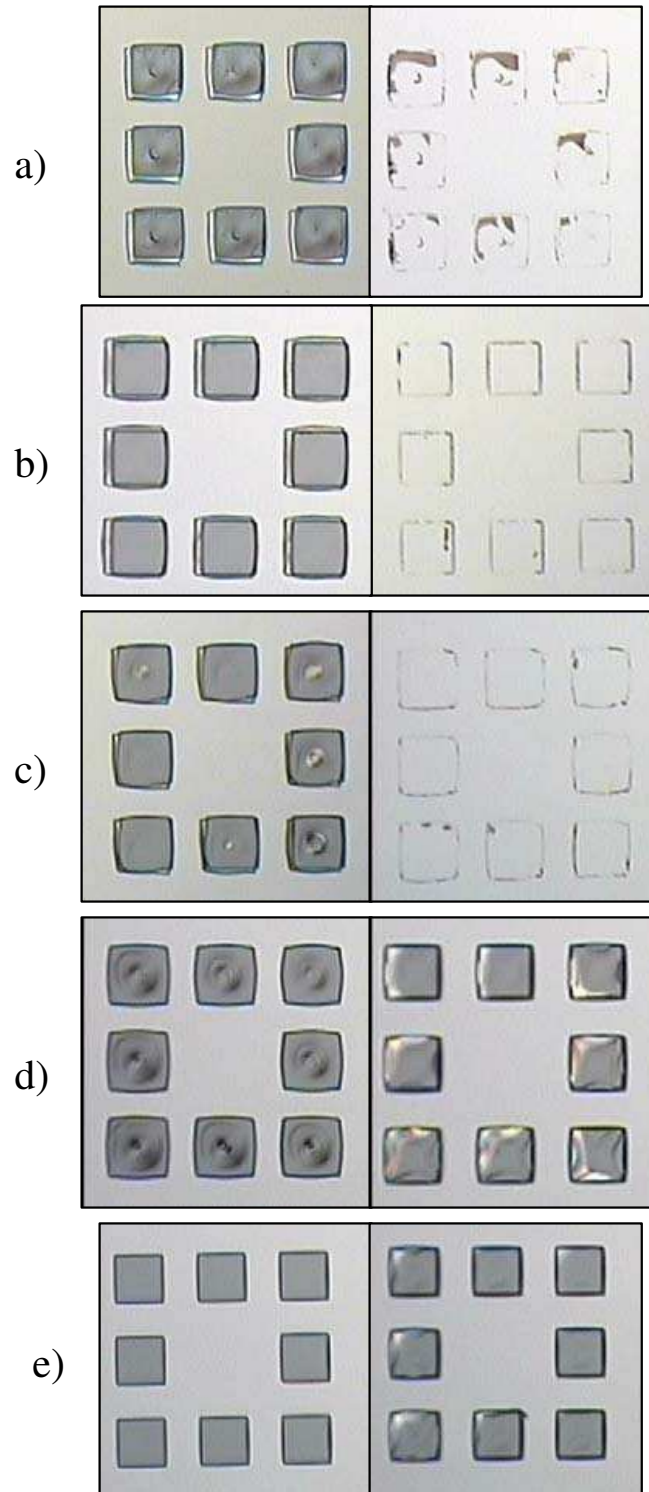
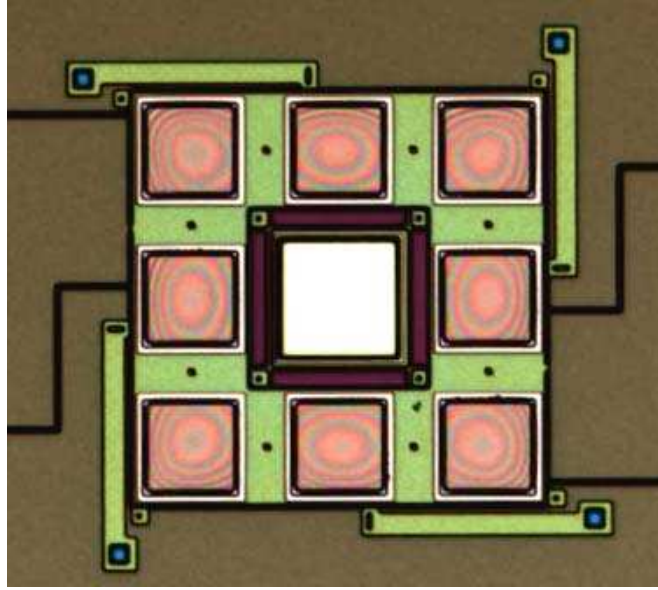


Figure 5.7: Nominal results for manually-separated, SU-8-to-SU-8-bonded-die; bonding temperature: a) 165 °C, b) 150 °C, c) 135 °C, d) 120 °C, and e) 105 °C.

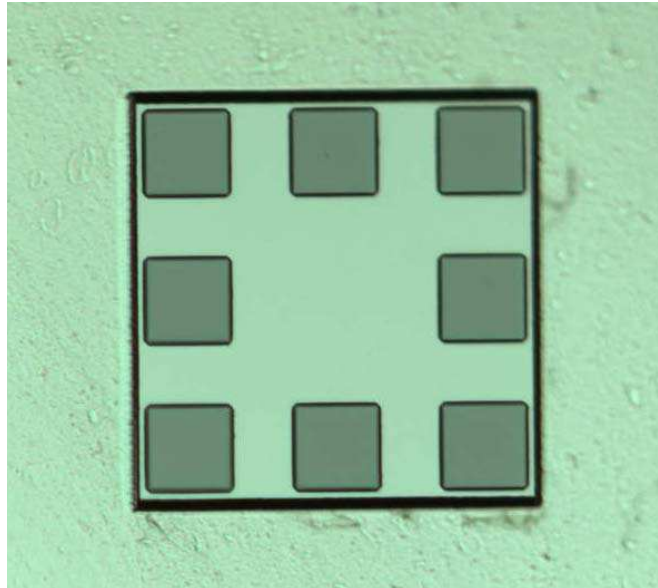
As shown in Figure 5.8, the DBR donor and MUMPS acceptor die were prepared by photolithographically depositing 2- μm SU-8 2002 bond pads. The SU-8 photolithography resulted in very good uniformity, and there was little issue with the slight non-uniformity of the bumps due to the relatively close mesa edge. This non-uniformity was observed in the white-light interference fringes as shown in Figure 5.8a.

The $\text{Al}_{0.4}\text{Ga}_{0.6}\text{As}$ -GaAs DBR mesa structures were flip-bonded to the MUMPS® die as described earlier. The DBR mesa structures were released by etching the donor die AlAs sacrificial layer via a 1.5-hr soak in the dilute-HF solution. Next, the underlying polySi actuators were released with a 5-min HF soak, rinsed in methanol for 5 min, and then underwent supercritical CO_2 drying. Finally, device die were packaged at room temperature and prepared for tuning characterization.

As shown in Figure 5.9, the SU-8 process reported above led to bonding of several intact (attached and crack-free) DBR mesas. Three sets of die were flip bonded with a mixed yield of DBR-attached-to-polySi-MEMS platforms which responded to voltage actuation. The first set, *Die135a*, had 11 intact DBR and eight demonstrated voltage actuation. The second set, *Die135b*, had 25 intact DBR and 15 demonstrated voltage actuation. The third set, *Die135c*, had 15 intact DBR and four demonstrated voltage actuation. Of the 90 attempted bonds, the 51 crack-free successfully attached DBR corresponded to a 57% yield, and the 27 devices which demonstrated voltage actuation represented a total device yield of 30%. Candidate sources of yield problems potentially included, but were not limited to, the following: poor planarity during flip-bonding, mis-handling during pre- or post-processing, insufficient surface preparation (cleaning, adhesive promoters) prior to SU-8 photolithography, insufficient SU-8 surface preparation prior to flip-bonding, and environmental exposure during clean-room processing or packaging. Follow-up procedural refinement research should explore optimization of these processes to improve device yield.

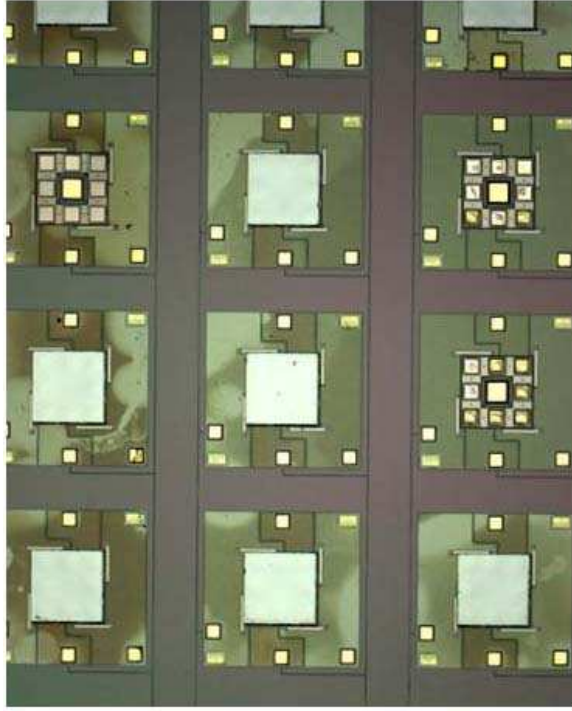


a)

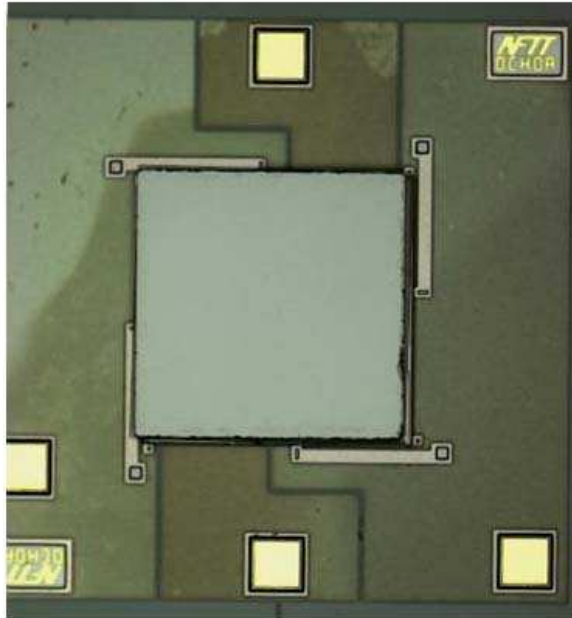


b)

Figure 5.8: Hybrid MEM-TF acceptor and donor die pair-wise bond sites: a) electrostatically actuated polySi MEMS platform with centrally located $60\text{-}\mu\text{m}^2$ Au reflector and photolithographically deposited SU-8 2002 bond-pads, b) $\text{Al}_{0.4}\text{Ga}_{0.6}\text{As}$ -GaAs DBR mesa with bond-pads; the $50\times 50\text{-}\mu\text{m}^2$ bond-pads were nominally $2\text{-}\mu\text{m}$ thick



a)



b)

Figure 5.9: Hybrid MEM-TF: a) $\text{Al}_{0.4}\text{Ga}_{0.6}\text{As}$ -GaAs DBR mesas flip-bonded to polySi MEMS platforms using SU-8 bond pads, b) magnified view of a hybrid MEM-TF.

5.4 Chapter Summary

A low-temperature, low-pressure flip-chip bonding procedure for the purpose of heterogeneously integrated MEMS-TF was successfully demonstrated. A temperature-dependent investigation identified 135 °C as the lowest characterized temperature where bonding of SU-8 bumps was consistently achieved. At this temperature, SU8-SU-8 bonding withstood subsequent processing steps, resulting in a 57% bond yield and an overall 30% operating device yield.

Bibliography

1. M. Harvey, E. Ochoa, J. Lott, and T. R. Nelson, "Toward the Development of Hybrid MEMS Tunable Optical Filters and Lasers," in *Proceedings of the 2004 International Conference on Compound Semiconductor Manufacturing Technology*, Miami Beach, FL, May 2004.
2. D. M. Burns and V. M. Bright, "Investigation of the Maximum Optical Power Rating for a Micro-Electro-Mechanical Device," in *1997 International Conference on Solid-State Sensors and Actuators (Transducers '97)*, Chicago, IL, 1997, pp. 335–338.
3. L. Torcheux, A. Mayeux, and M. Chemla, "Electrochemical Coupling Effects on the Corrosion of Silicon Samples in HF Solutions," *Journal of the Electrochemical Society*, vol. 142, pp. 2037–2046, June 1995.
4. E. Ochoa, L. Starman, R. Bedford, T. Nelson, J. Ehret, M. Harvey, T. Anderson, and F. Ren, "Flip bonding with SU-8 for hybrid $\text{Al}_x\text{Ga}_{1-x}\text{As}$ -polysilicon MEMS-tunable filter," *J. Micro/Nanolith. MEMS MOEMS*, vol. 6, no. 3, Jul-Sep 2007.

VI. Hybrid MEM-TF Design, Fabrication, and Demonstration

6.1 Chapter Overview

As a first step towards a hybrid (AlGaAs-polySi) MT-VCSEL, designs and methods were developed to demonstrate a hybrid MEM-TF via flip-bonding an $\text{Al}_x\text{Ga}_{1-x}\text{As}$ DBR to a polySi MEMS electrostatically actuated structure (with a built-in Au reflector) [1–3]. The following sections report the design, fabrication, and the demonstration of a hybrid $\text{Al}_x\text{Ga}_{1-x}\text{As}$ -polySi electrostatically actuated MEM-TF. A $250 \times 250\text{-}\mu\text{m}^2$, $4.92\text{-}\mu\text{m}$ -thick, $\text{Al}_{0.4}\text{Ga}_{0.6}\text{As}$ -GaAs DBR was successfully flip-bonded to a polySi piston electrostatic actuator using SU-8 photoresist as bonding adhesive. The device demonstrated 53nm ($936.5\text{--}989.5\text{ nm}$) of resonant wavelength tuning over the actuation voltage range of 0 to 10 V.

6.2 Design

As shown in Figure 6.1, the hybrid MEM-TF consisted of an $\text{Al}_x\text{Ga}_{1-x}\text{As}$ DBR flip-bonded to a MUMPs® Run #68 polySi piston actuator. Eight, $50 \times 50\text{-}\mu\text{m}^2$, $2\text{-}\mu\text{m}$ thick, SU-8 2002 bond-pads were used to bond the DBR to the actuator. The piston actuator incorporated structural features (flexures, dimples, and quarter-symmetry) of the mirror piston actuator described by Cowan [4]. The piston actuator was designed to be vertically displaced via electrostatic attraction between the upper piston platform and the lower electrode which encircled a fixed, Au-capped, reflector platform. As shown in Figure 5.1, the piston actuator included a large opening in the center to encircle the Au reflector platform, eight Poly 2 mesas with encapsulated Oxide 2 for SU-8 bond-pad lithography/alignment, and quarter-symmetrically distributed dimples to mitigate stiction in the device's center.

After flip-bonding and device release to enable electrostatic actuation, the DBR was designed to be suspended directly above the Au reflector platform. This DBR, air-gap, and Au reflector comprised a Fabry-Perot filter when optically viewed from

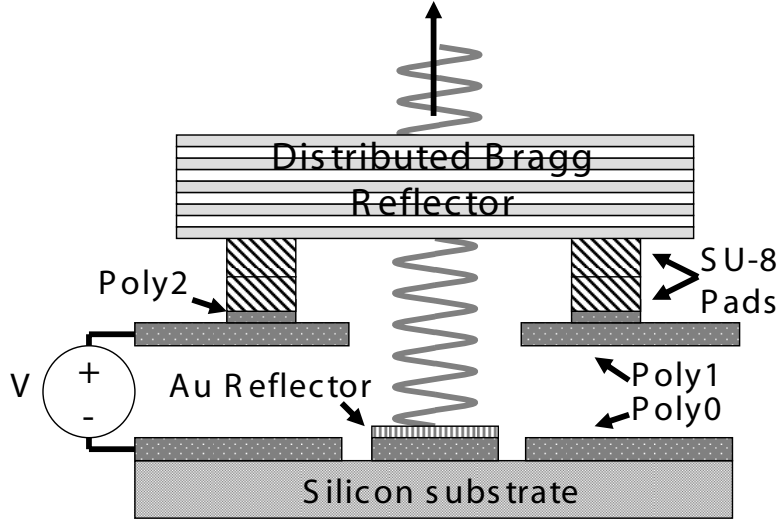


Figure 6.1: Hybrid MEM-TF: design cross section of a hybrid MEM-Tunable filter (not to scale)

directly above the DBR over the center of the underlying Au mirror. Since the DBR was mechanically attached to the polySi piston actuator, electrostatic displacement of the actuator displaced the DBR toward the Au mirror. This displacement reduced the air-gap which blue-shifted the filter's resonant wavelength.

As discussed in Chapter V, previously reported attempts to flip-bond using Au-Au (Figure 5.4) and Au-In (Figure 5.5) bump bonds experienced significantly cracked DBR structures and significant damage to the Au material on acceptor die. Since both the DBR and MUMPs[®] polySi actuator release chemistries were HF-based, bond material compatibility with HF was desired. Also, as discussed in Chapter V and reported by Harvey *et al.* [3], SU-8 performed well as a bump bond and was known to be highly resistant to most chemicals, including HF.

To mitigate DBR cracking, SU-8 was selected as the bond material due to its high elasticity and lower bonding temperature (versus Au-Au or Au-In bonding) as discussed in Chapter V. To mitigate the Au damage due to the electrochemical interaction of Au on the MUMPs[®] polySi die with the 1.5-hr DBR-release in dilute HF (1:3:6 HF:isopropyl alcohol:de-ionized water) [5], all previously used Au (as shown in

Figure 5.4) on the MUMPs® polySi die was minimized or eliminated, except the Au for the bottom mirror platform (with 98% reflectivity) and the Au wire-bond pads (for packaging). In order to improve prototype device yield during process development, a 5×6 array of 30 polySi actuators was designed on the 0.5-cm^2 MUMPs® (acceptor) die and a 5×6 array of 30 $250 \times 250\text{-}\mu\text{m}^2$ DBR mesas was designed on the GaAs (donor) die.

As shown in Figure 6.2, the designed DBR growth consisted of a GaAs donor die, a $1\text{-}\mu\text{m}$ AlAs sacrificial layer for dilute-HF release, and a 25-period, $\text{Al}_{0.4}\text{Ga}_{0.6}\text{As}$ -GaAs, $980\text{-nm-}\lambda_D$ DBR with a $1\text{-}\mu\text{m}$ GaAs cap layer. The piston-actuator-to-underlying-electrode initial air-gap was $2\mu\text{m}$, and the DBR-to-Au-reflector initial air-gap was $3.5\mu\text{m}$. The overlapping electrode area, A , for all prototypes was $48,288\mu\text{m}^2$. As shown in Figure 6.3, the MT-CAD methodology and piston deflection calculation described in Chapter II were used to simulate and visualize results for this tunable hybrid filter with the designed DBR described above. For the purpose of this simulation, the Poly 1 Young's modulus and stress of Poly 1 were assumed to be 125GPa and -6.6MPa , respectively. This value for Young's modulus was based on the Poly 1 study data reported in Chapter III. The value for Poly 1 stress was the average of MUMPs® Run #65-67.

As shown in Figure 6.4, the as-grown DBR had low and high stop-band minima at 930.5 and 1003.5nm , respectively, and a maximum reflectivity of 97% at 965.5nm . Since the maximum reflectivity blue-shifted approximately 15nm from the 980-nm designed center wavelength, an iterative, best-fit (minimized sum squared error over all measured wavelengths) calculation was performed to analyze individual DBR growth layer scale factors. As listed in Figure 6.5, the $\text{Al}_{0.4}\text{Ga}_{0.6}\text{As}$ DBR layer may have been the most significant growth rate error influence, since the 0.97 scaling factor associated with this layer corresponded to a 3% reduction in layer thickness from design.

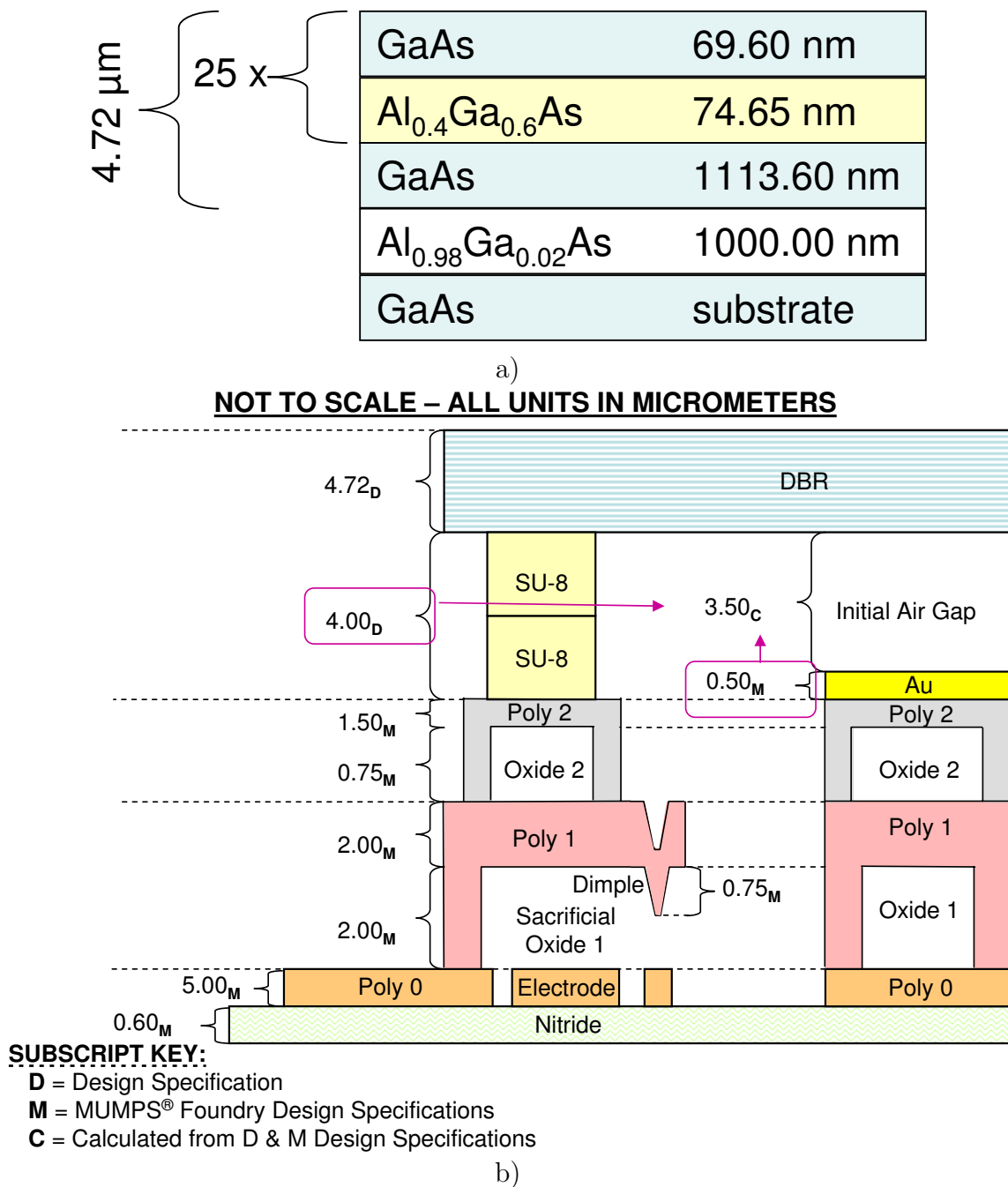


Figure 6.2: Hybrid MEM-TF: a) designed DBR layer thickness, b) designed and calculated device layer thickness

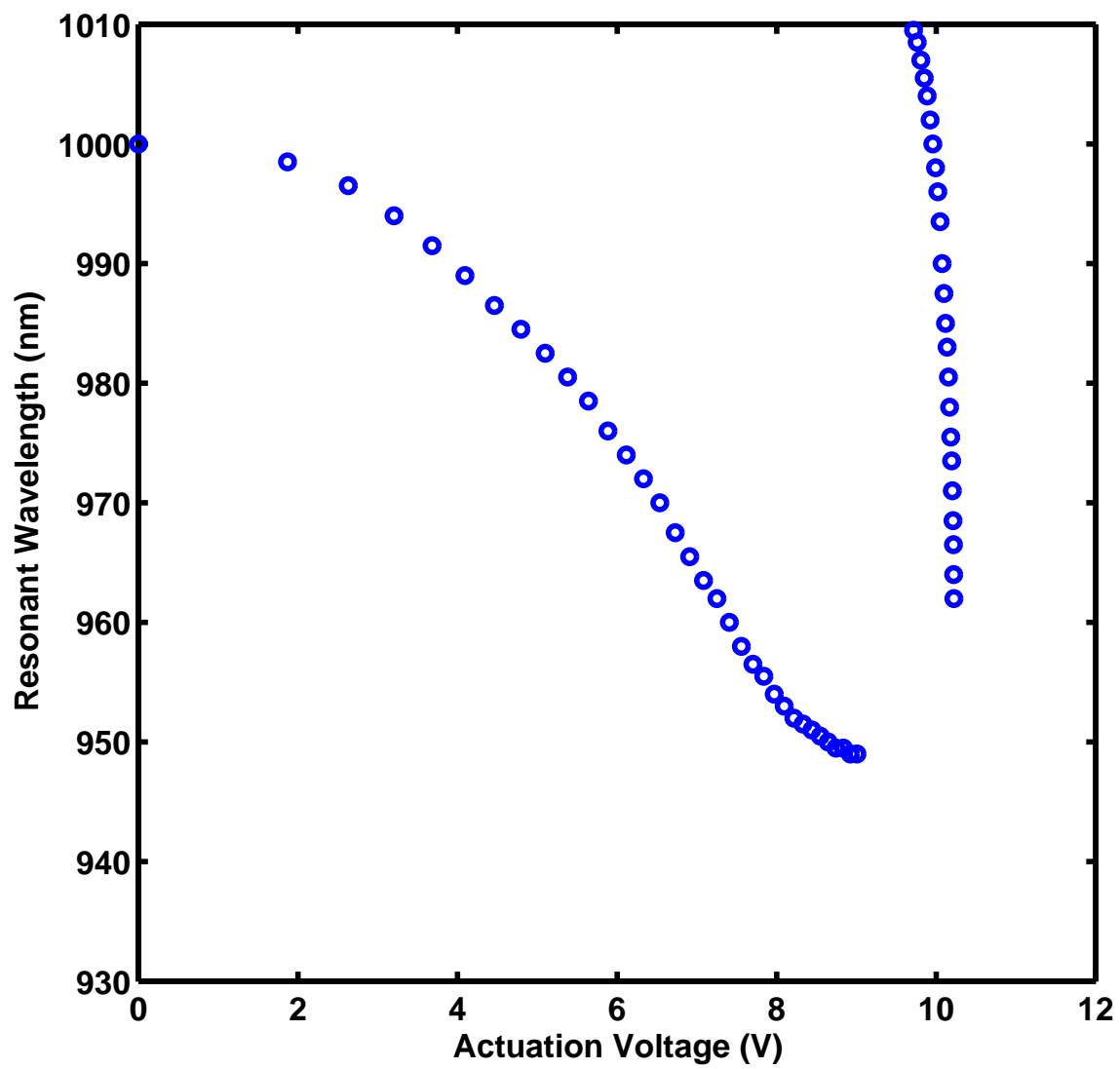


Figure 6.3: Hybrid MEM-TF with designed (980-nm center) DBR: simulated resonant wavelength tuning as a function of applied voltage

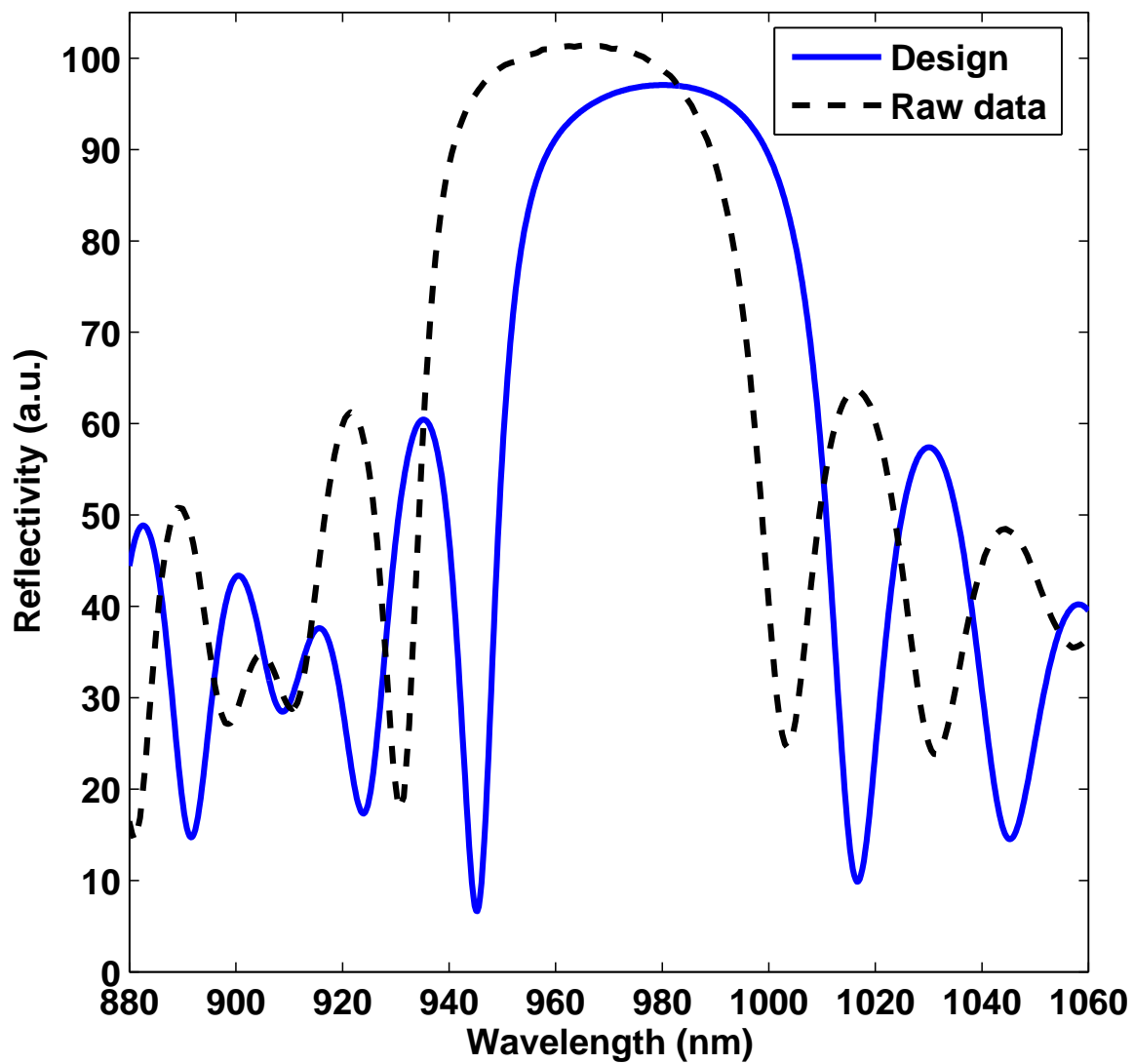


Figure 6.4: DBR reflectivity: designed (solid line), measured (dashed line) using spot reflectance system described in Section 6.4.1 and illustrated in Figure 6.7

Designed			Calculated	
4.72 μm	25 x	GaAs	69.60 nm	Layer _{FIT} = 1.0009
		Al _{0.4} Ga _{0.6} As	74.65 nm	Layer _{FIT} = 0.9666
		GaAs	1113.60 nm	Layer _{FIT} = 0.9812
		Al _{0.98} Ga _{0.02} As	1000.00 nm	Layer _{FIT} = 1.0012
		GaAs	substrate	

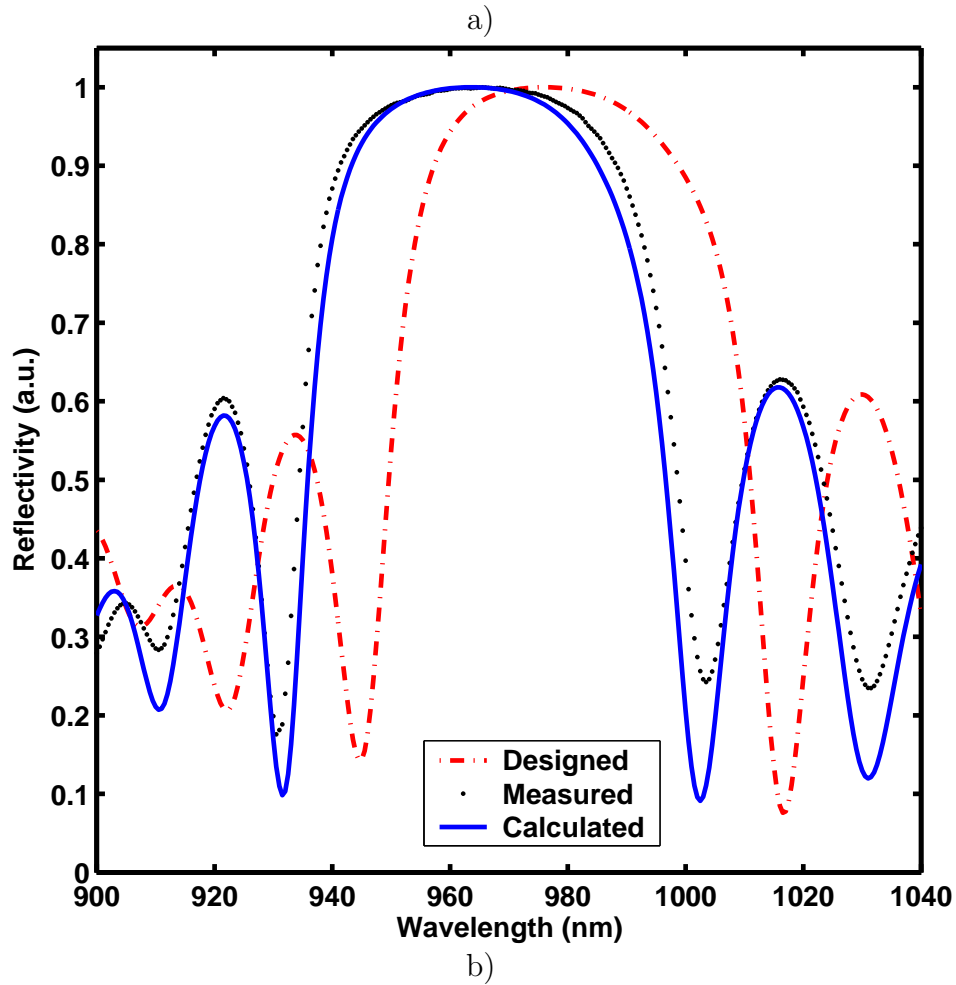


Figure 6.5: DBR growth layer thickness: a) illustration of designed layer thickness and calculated growth layer thickness scale factors, b) designed, measured, and calculated DBR reflectivity as a function of wavelength

In order to determine the influence of the DBR growth on device performance, the MT-CAD was used to simulate the hybrid MEM-TF with the as-grown DBR growth layer scale factors. As shown in Figure 6.6, although growth rate inaccuracies caused the as-grown DBR reflectance to drift from the 980-nm center DBR design wavelength, this material was considered useful for MEM-TF demonstration purposes. This was considered an unplanned but early demonstration of the benefit of the hybrid MEM-TF design. Specifically, the use of independently grown optical and mechanical elements enabled process assembly trades to be performed prior to full device fabrication. Instead of discarding the entire device, this methodology enabled the option of optical element (DBR) regrowth.

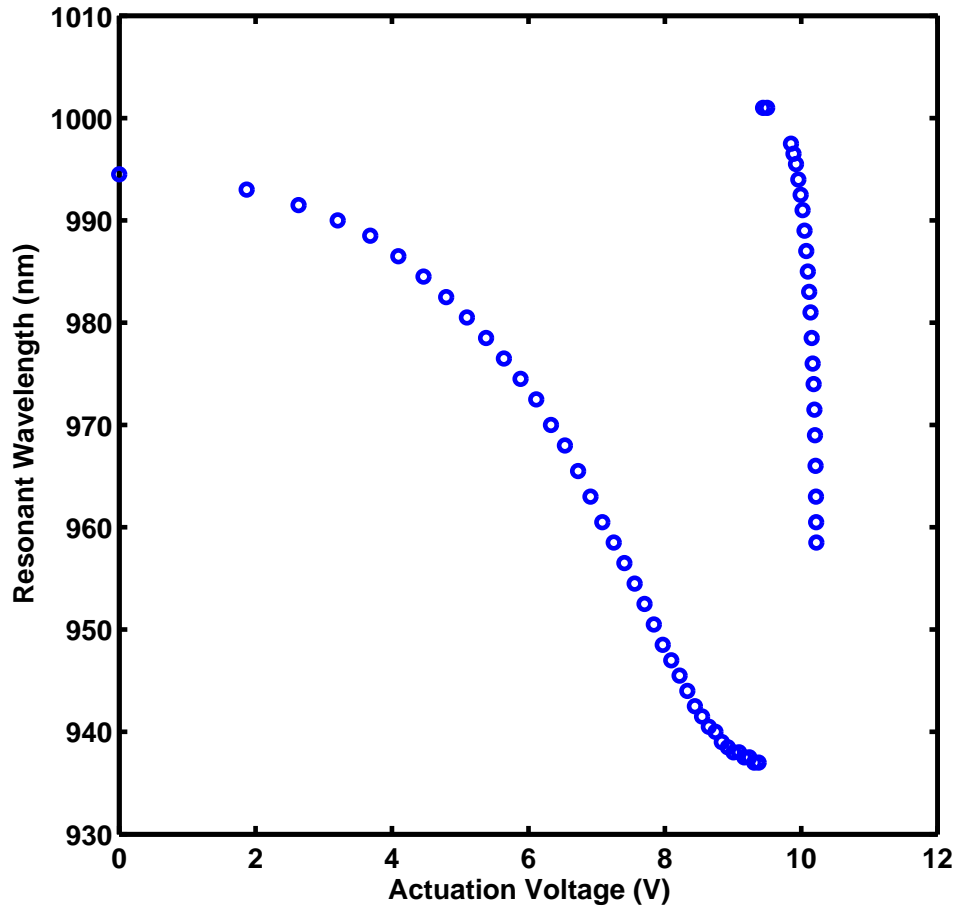


Figure 6.6: Hybrid MEM-TF with the as-grown DBR growth layer scale factors: calculated resonant wavelength as a function of applied voltage

6.3 Fabrication

A 5×6 array of $250 \times 250\text{-}\mu\text{m}^2$ mesas was wet-etched into the $\text{Al}_{0.4}\text{Ga}_{0.6}\text{As}$ -GaAs DBR donor die. As shown in Figure 5.8, SU-8 2002 $2\text{-}\mu\text{m}$ bond pads were photolithographically deposited onto both the donor and acceptor die, measuring $50 \times 50\text{-}\mu\text{m}^2$ each, eight per device. The SU-8 photolithography resulted in very good uniformity and there was little issue with the slight non-uniformity of the bumps due to the relatively close mesa edge. This non-uniformity was observed in the white-light interference fringes as shown in Figure 5.8a.

The donor die were then flip-bonded to the acceptor die using a RD Automation M9A Flip Chip Aligner Bonder set to the following parameters: 1-kg applied weight, 135°C bonding temperature, and 10-min bond time. The DBR were next released from the GaAs donor substrate by etching the AlAs sacrificial layer via a 1.5-hr soak in the aforementioned dilute HF solution, leaving a $4.92\text{-}\mu\text{m}$ thick DBR structure attached to the underlying polySi actuators. Next, the polySi actuators were released with a 5-min HF soak, rinsed in methanol for 5-min, and then underwent supercritical CO_2 drying. Finally, device die were packaged (crystal-bonded onto chip carrier and wire-bonded for electrostatic actuation) then prepared (aligned for optical measurements) for tuning characterization.

6.4 Experimental Results

6.4.1 Measured Tuning versus Actuation Voltage. As shown in Figure 5.9 and described in Section 5.3.4, the SU-8 process led to bonding of several intact (attached and crack-free) DBR mesas to polySi MEMS platforms. Hybrid MEM-TF reflectance and tuning curve characterization was next performed via the custom spot reflectance measurement system. As shown in Figure 6.7, a multi-mode ($62.5\text{-}\mu\text{m}$ core) fiber-coupled white light source was imaged to a nominally $45\text{-}\mu\text{m}$ spot size, less than the $60\text{-}\mu\text{m}^2$ Au post mirror.

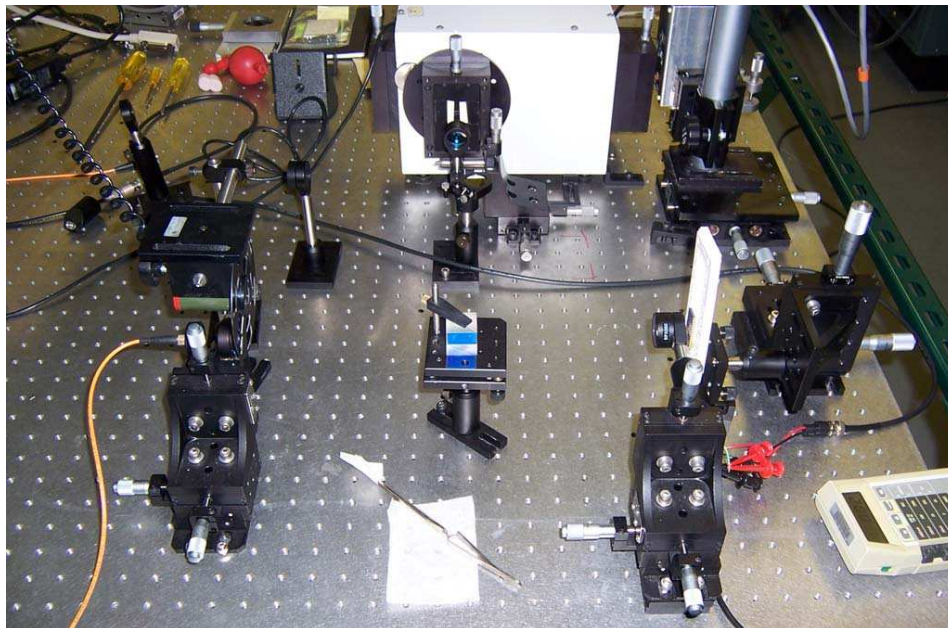
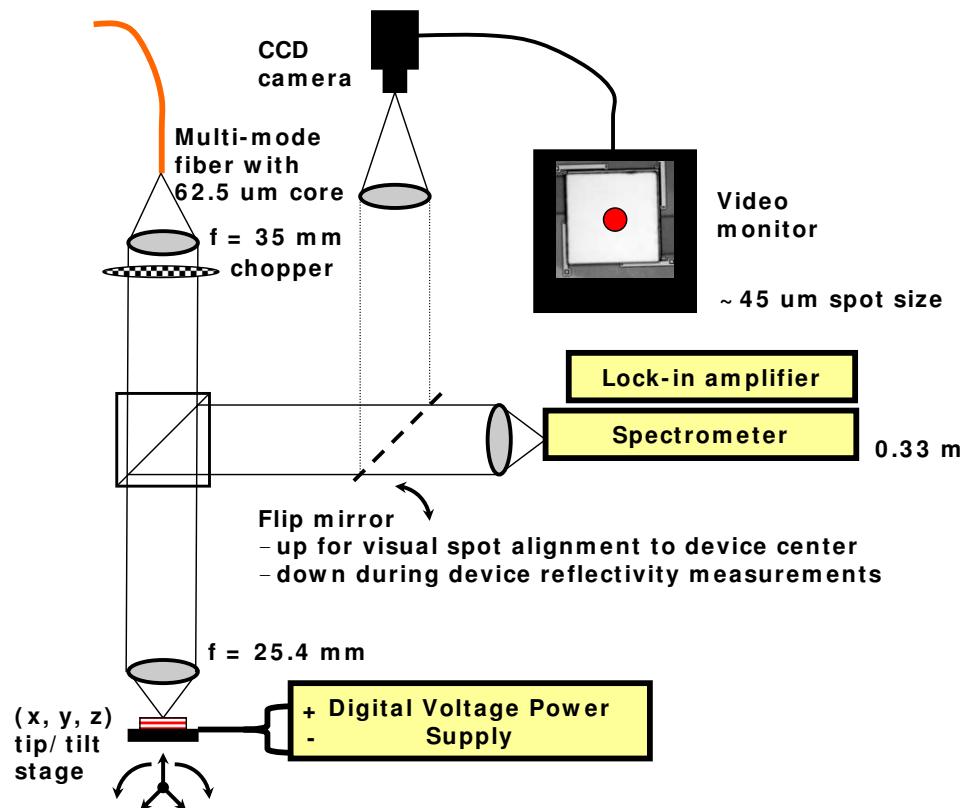


Figure 6.7: Diagram and photo of spot reflectance measurement system

The packaged die were mounted to a six-axis (x-y-z, tip/tilt) stage to facilitate alignment. Reflection was measured by incorporating a nominally 50/50 non-polarizing beam-splitter cube to send the reflected light into a 0.33-m grating spectrometer. The input signal was chopped, and signal-to-noise ratio was increased via lock-in detection.

Additionally, a flip-up mirror in the reflected signal path was directed into a CCD camera using imaging optics to allow visual confirmation for when the MEM-TF was aligned with the optical spot. Prior to each set of reflectance measurements, the measurement system was calibrated using a Si wafer with evaporated Au as the normalization standard.

All reflectance measurements ranged from 920 to 1020nm in 0.5-nm steps. As shown in Figures 6.8 and 6.9, the device demonstrated 53nm (936.5-989.5nm) of resonant wavelength tuning over the electrostatic actuation voltage range of 0 to 10V.

6.4.2 Calculated versus Measured Results. The designed and measured tuning curves are plotted in Figure 6.10 for comparison purposes. In order to characterize potential sources of discrepancy between the two curves, the device's individual layer characteristics and displacement as a function of actuation voltage were investigated. As shown in Figure 6.11, individual device layer thickness was calculated or derived from interferometrically measured or reported MUMPs® Run #68 [6].

Next, as shown in Figure 6.12, the actual device deflection as a function of actuation voltage was characterized. As illustrated in Figure 6.12b, interferometric measurements taken as a function of bias determined snap-down voltage as 10.13V. Also, as the device approached snap-down, the interferometric fringe patterns did not laterally shift (corresponding to tilt), thus, visually indicating piston actuation.

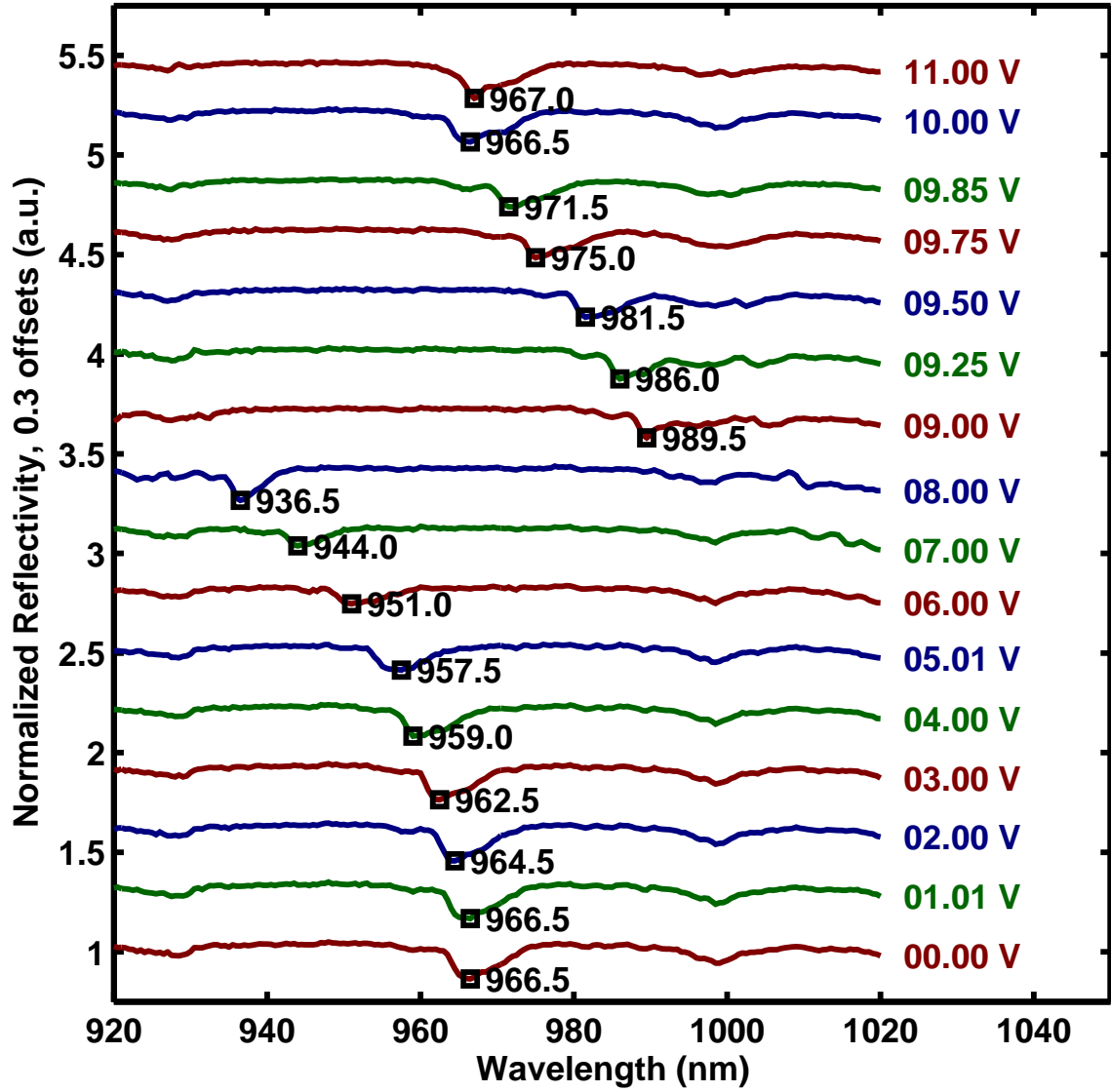


Figure 6.8: Hybrid MEM-TF: normalized measured reflectivity as a function of actuation voltage; non-catastrophic snapdown voltage was observed at 10.13 V

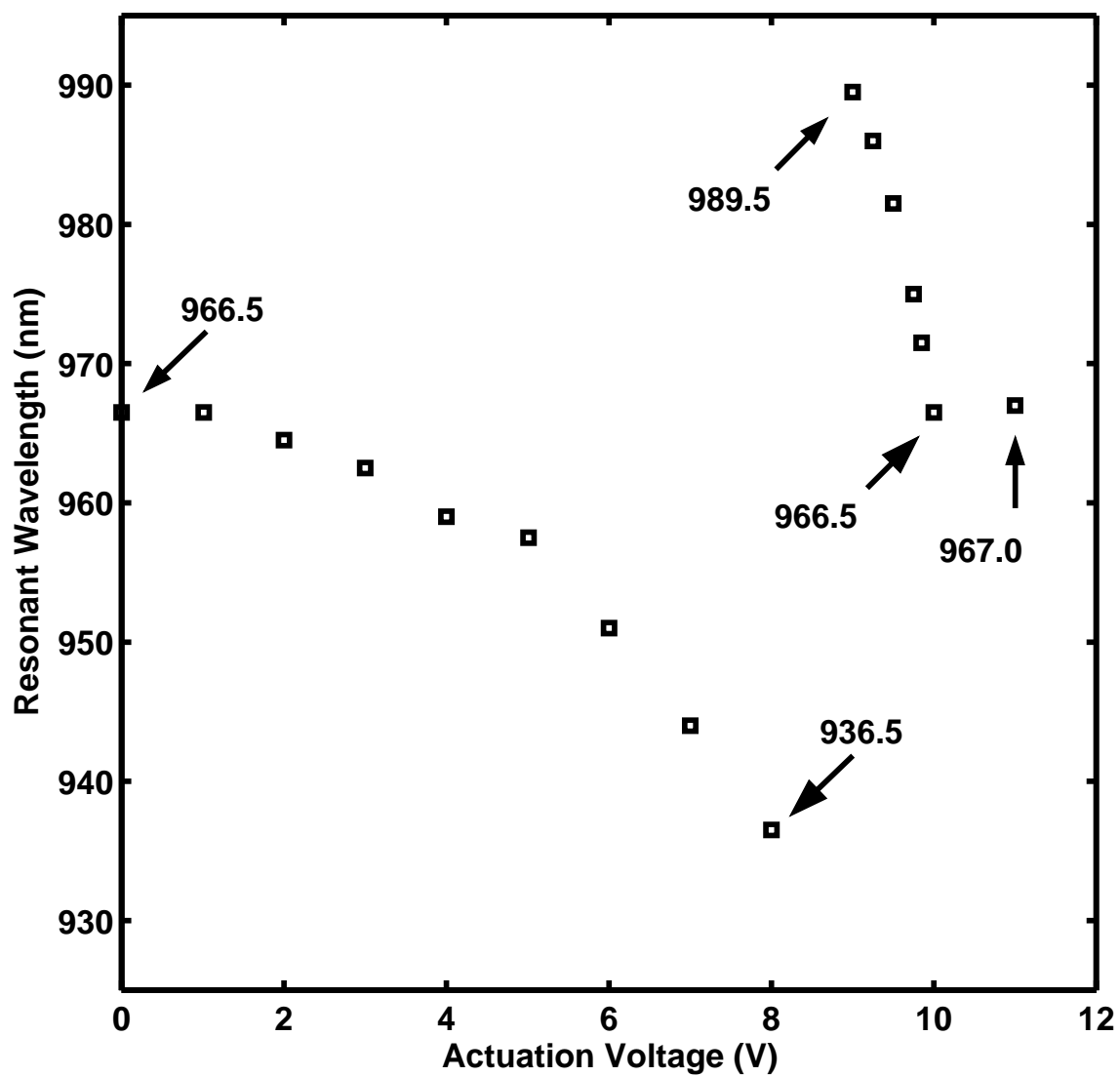


Figure 6.9: Hybrid MEM-TF: measured resonant wavelength tuning as a function of applied voltage; non-catastrophic snapdown voltage was observed at 10.13 V

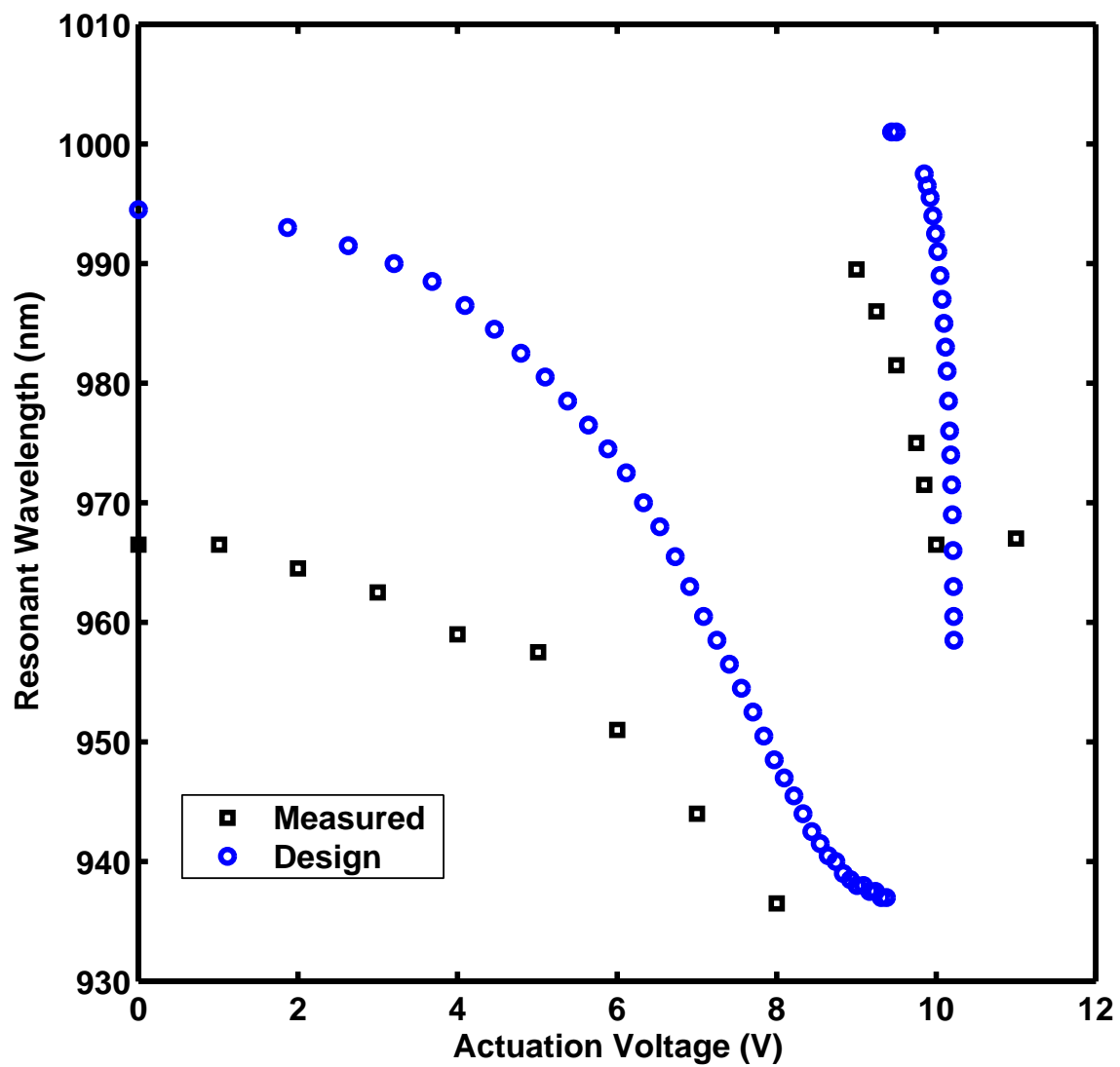


Figure 6.10: Hybrid MEM-TF: measured versus design resonant wavelength tuning as a function of applied voltage

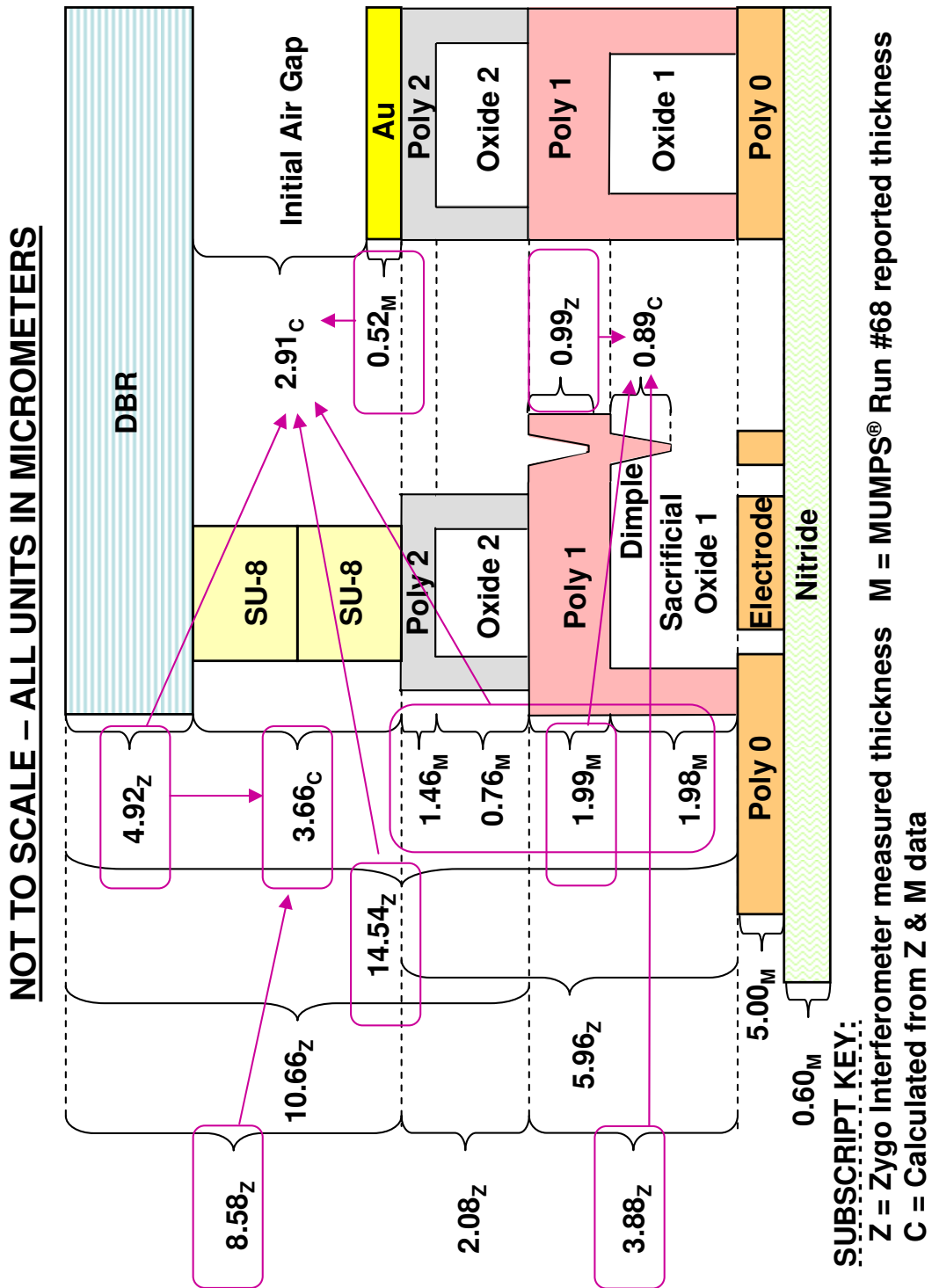
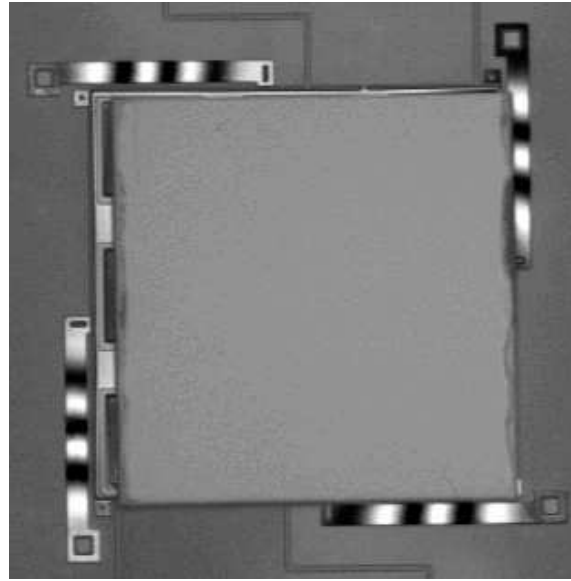
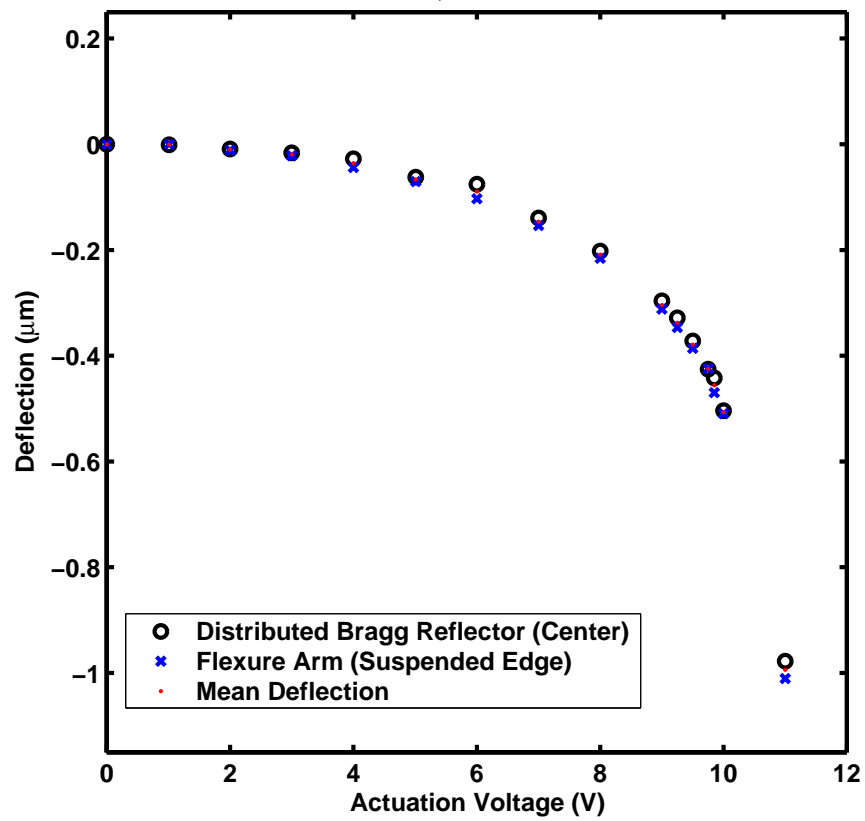


Figure 6.11: Hybrid MEM-TF: measured layer thickness data and calculations



a)



b)

Figure 6.12: Hybrid MEM-TF: a) interferometric image of device at non-catastrophic snap-down voltage of 10.13V, b) interferometrically measured vertical deflection as a function of applied electrostatic actuation voltage

As shown in Figures 6.13 and 6.14, the MT-CAD was used to simulate the hybrid MEM-TF with the as-grown DBR growth layer scale factors, measured or calculated individual layer thickness, and measured deflection as a function of applied actuation voltage. The reflectance of the measured and calculated device are plotted in Figure 6.13 for comparison purposes. In this figure, the low and high DBR stop-band minima were observed as dips in the calculated reflectance spectrum at ~ 933 and ~ 1005 nm, respectively. However, these calculated dips appeared red-shifted when compared to the measured reflectance spectrum.

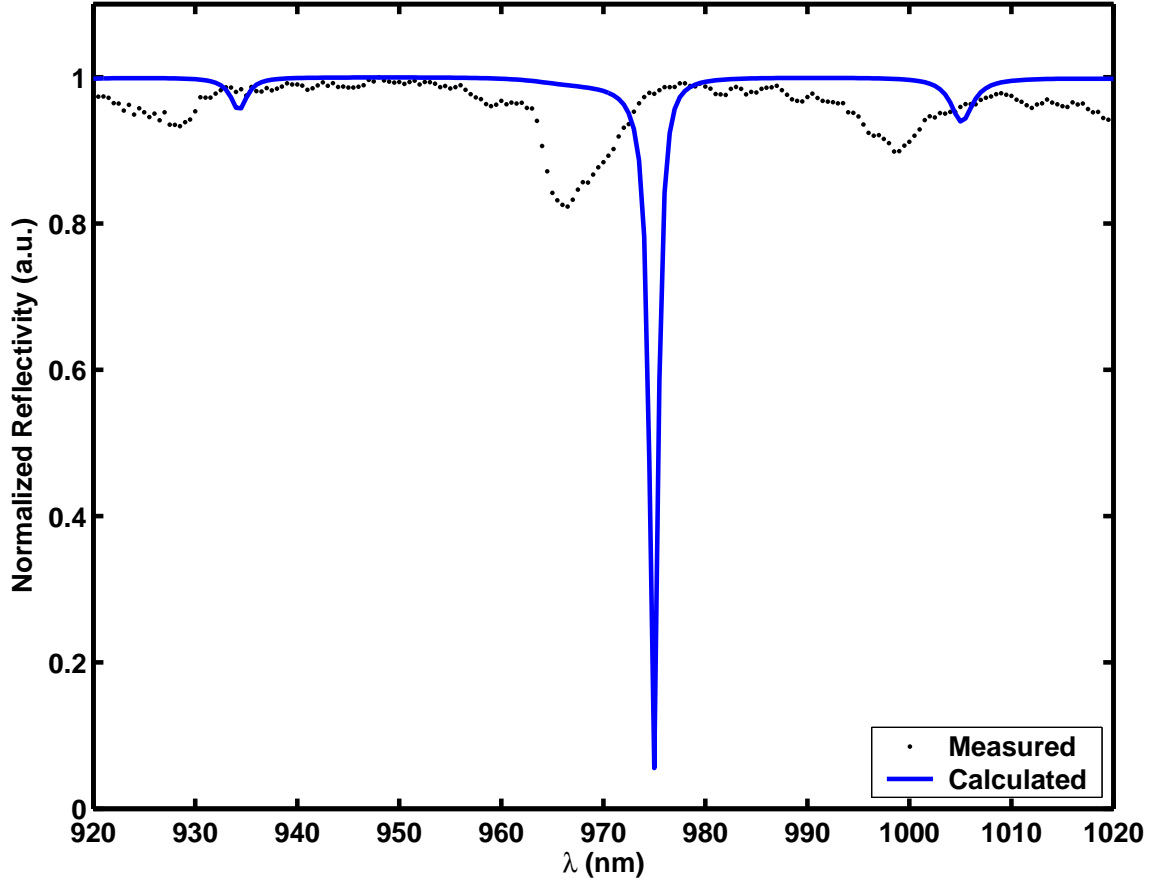


Figure 6.13: Measured versus calculated hybrid MEM-TF reflectivity as a function of wavelength; 0.0V actuation voltage, calculated via planar-planar cavity assumption

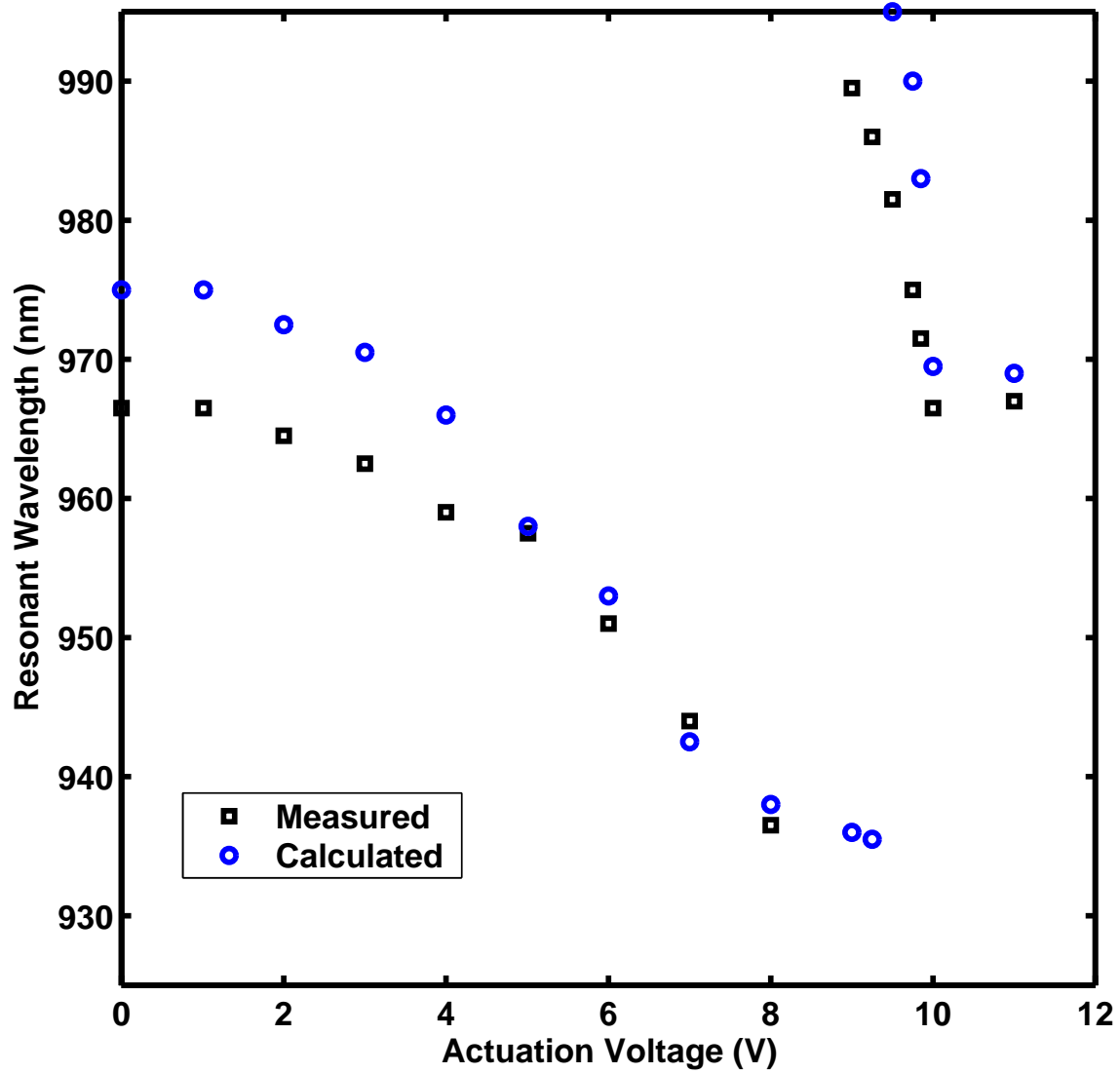


Figure 6.14: Measured versus calculated hybrid MEM-TF tuning as a function of applied actuation voltage using as-grown DBR growth layer scale factors, measured individual layer thickness, and measured deflection

Additionally, as shown in Figure 6.13, the location of the resonant wavelength dip in the measured device is blue-shifted with respect to the calculated resonant wavelength. This blue-shift may have been due to layer thickness inaccuracy due to errors in interferometric measurements of individual layer thicknesses previously illustrated in Figure 6.11. The errors may have contributed to error in the calculated initial air-gap thickness of $2.91\mu\text{m}$, leading to the discrepancy between the measured and calculated tuning curves in Figure 6.13.

6.5 Unstable Resonator Simulation versus Measurement

As shown in Figure 6.13, the reflectance curves exhibited discrepancy when comparing the width and depth of the measured and calculated results at device resonance. Thus, a ZYGO® NewView™ 5000 interferometer was used to characterize DBR surface planarity to investigate the source of these discrepancies. The interferometric image of Figure 6.15 illustrated the underlying bond-pads influence on the DBR's surface planarity and indicated surface curvature was present.

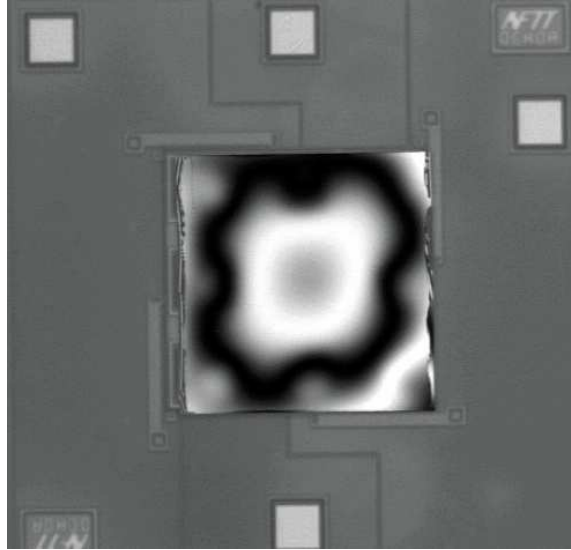


Figure 6.15: Hybrid MEM-TF: ZYGO® NewView™ 5000 interferometric image; focus was located near the surface of the flip-bonded, $250 \times 250\text{-}\mu\text{m}^2$, $\text{Al}_{0.4}\text{Ga}_{0.6}\text{As}$ -GaAs DBR

As shown in Figure 6.16, the DBR surface was slightly concave (when viewed from above the device), with a measured vertical difference of $0.4\mu\text{m}$ between the minimum near the center to the lower right DBR corner. As shown in Figures 6.16 and 6.17, the flip-bonded DBR resulted in a planar-convex cavity (when viewed from within the cavity) with a 1.19-cm radius of curvature instead of a planar-concave or planar-planar cavity, which led to diverging instead of parallel light. The curved DBR surface may have been due to an as-grown stress mismatch between adjacent $\text{Al}_{0.4}\text{Ga}_{0.6}\text{As}$ -GaAs DBR layers, or to failure to mitigate surface tension on the unsupported and suspended DBR center during device release processing.

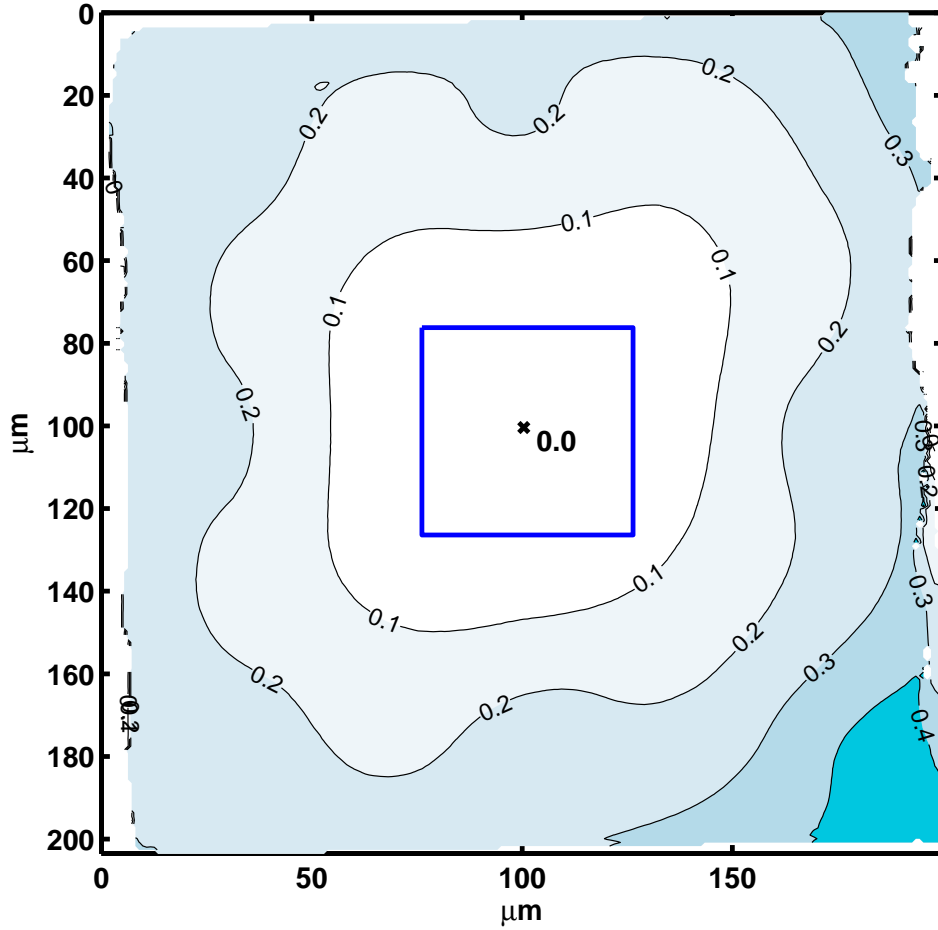


Figure 6.16: DBR surface: interferometrically measured vertical surface contours; contour level lines are in units of μm ; $50 \times 50\text{-}\mu\text{m}^2$ crop box centered on DBR minima labeled “x”

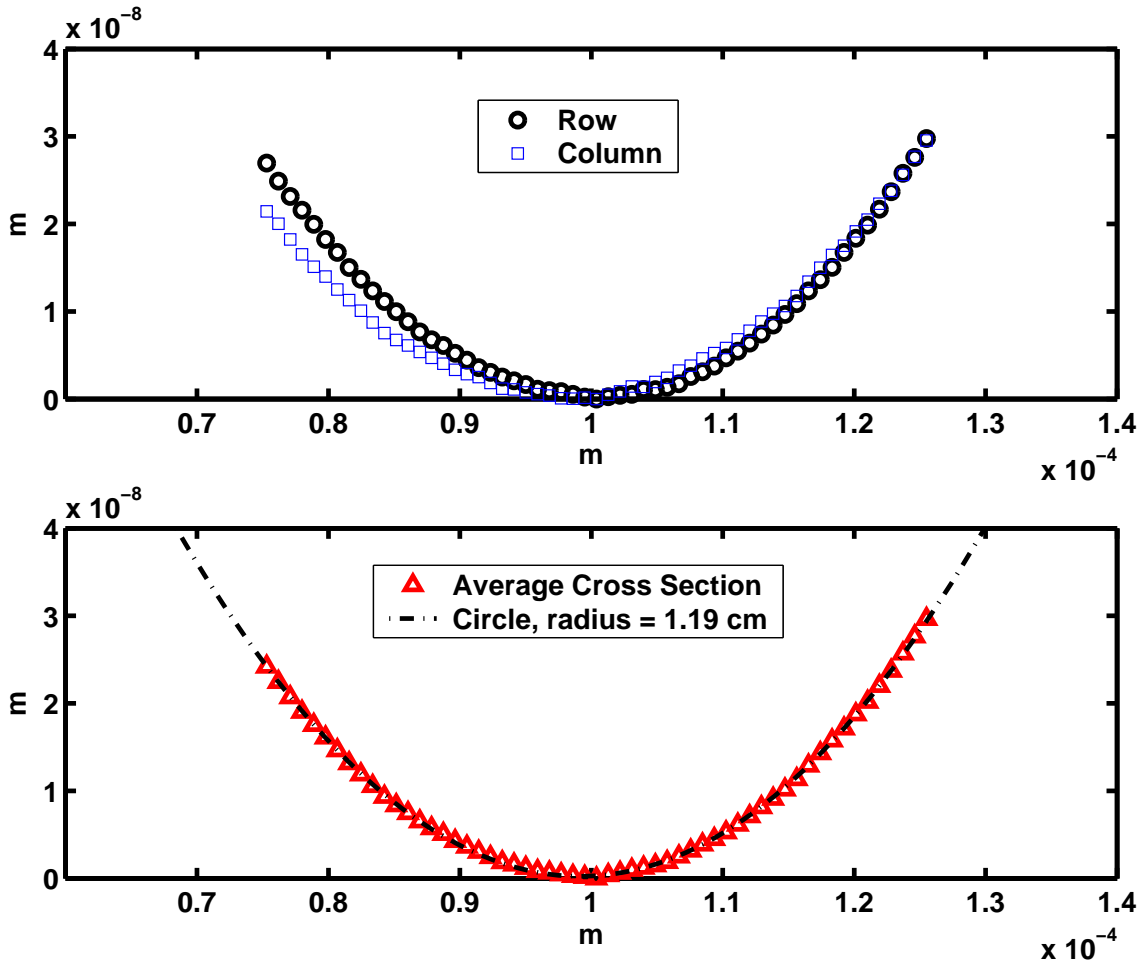


Figure 6.17: DBR interferometric data: (Top) row and column data through minimum of DBR surface; (Bottom) average cross section and calculated circle with radius of curvature = 1.19 cm

The planar-convex cavity does not satisfy the planar-planar assumption for the transfer-matrix method described in Chapter III. Since the planar-planar assumption was not met, an alternate method was required to simulate the reflectance characteristics of the unstable resonator defined here as the cavity bounded by the convex DBR mirror and planar Au mirror. The Fox-Li method [7,8] is a standard technique used to calculate optical modes in stable and unstable resonators. Thus, the Fox-Li method was implemented as a MATLAB® file [9] to calculate the reflectance of the hybrid MEM-TF.

As illustrated in Figure 6.18, the Fox-Li method begins with an initial electric field profile, E_i , incident on the DBR, then the reflected field profile, E_R , is initialized. Next, the field is transmitted through the DBR, and is propagated through the cavity to the Au mirror. The field is reflected by the Au mirror, and is propagated back to the DBR. At this step, the field is both transmitted and reflected by the DBR. The field transmitted through the DBR is summed with E_R . The field reflected by the DBR is propagated back through the cavity to the Au mirror. This processes is repeated until E_R converges.

The main loop of the Fox-Li method is incident field (from inside the cavity) reflection by the DBR, propagation of the DBR reflected field to the Au mirror, field reflection by the Au mirror, then propagation back to the DBR. Reflection at the mirrors is calculated in the spatial domain (described later), and propagation is accomplished in the frequency domain via the Fourier transform method described next.

6.5.1 Fourier Transform Field Propagation. Using the formulation presented by Goodman [10], if the complex field on the transverse (x, y) plane traveling with component of propagation in the positive z direction with $y = 0$ is defined to be $U(x, 0, 0)$, the resulting field that appears at a distance, $z = L$, is $U(x, 0, L)$. If $y = 0$, then across the $z = 0$ plane, U has a one-dimensional Fourier transform given by

$$A(f_X x, 0; 0) = \int_{-\infty}^{\infty} U(x, 0, 0) \exp[-j2\pi(f_X x)] dx \quad (6.1)$$

where U is the inverse Fourier transform of angular spectrum, A , given by

$$U(x, 0; 0) = \int_{-\infty}^{\infty} A(f_X x, 0) \exp[j2\pi(f_X x)] df_X \quad (6.2)$$

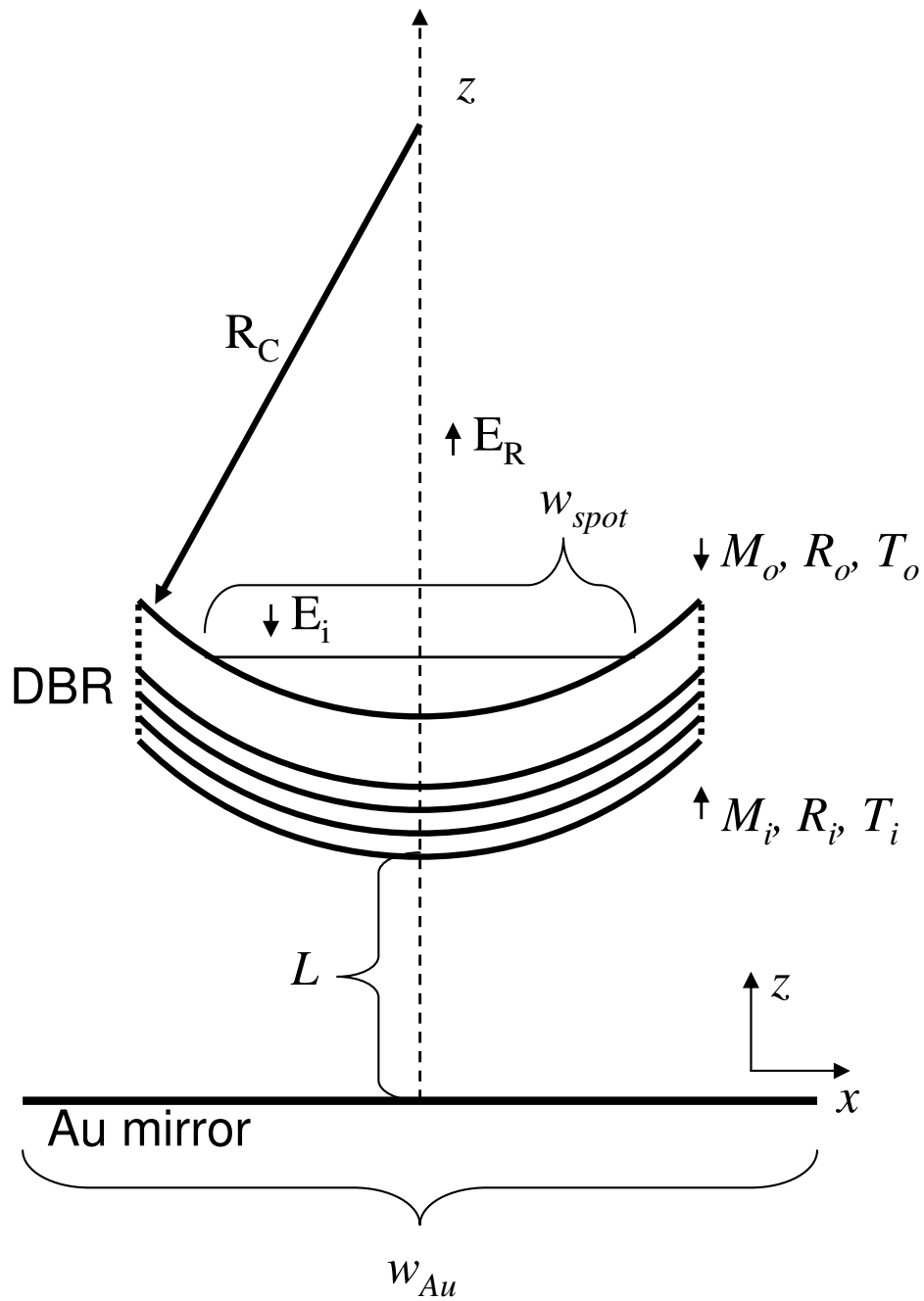


Figure 6.18: Optical microcavity bounded by a convex DBR and planar Au mirror

Goodman [10] defined the form of a simple field propagating with wave vector, \vec{k} , where \vec{k} has magnitude, $2\pi/\lambda$, with direction cosines (α, β, γ) to have a complex representation of the form

$$p(x, y, z; t) = \exp[j(\vec{k} \cdot \vec{r} - 2\pi\nu t)] \quad (6.3)$$

where $\vec{r} = x\hat{x} + y\hat{y} + z\hat{z}$ is a position vector with unit vectors $(\hat{x}, \hat{y}, \hat{z})$, and $\vec{k} = \frac{2\pi}{\lambda}(\alpha\hat{x} + \beta\hat{y} + \gamma\hat{z})$. If time dependence is dropped, the complex phasor amplitude of the plane wave across a constant z -plane is given by Goodman [10] as

$$P(x, y, z; t) = \exp(j\vec{k} \cdot \vec{r}) = e^{j\frac{2\pi}{\lambda}(\alpha x + \beta y)} e^{j\frac{2\pi}{\lambda}\gamma z} \quad (6.4)$$

where the direction cosines are interrelated through

$$\gamma = \sqrt{1 - \alpha^2 - \beta^2} \quad (6.5)$$

Thus, for $y = 0$ and across the plane, $z = 0$, the complex-exponential function, $\exp[j2\pi(f_X x)]$, may be regarded as representing a field propagating with direction cosines

$$\alpha = \lambda f_X, \beta = 0, \gamma = \sqrt{1 - (\lambda f_X)^2} \quad (6.6)$$

where the complex amplitude of the plane-wave component with spatial frequencies (f_X, f_Y) is $A(f_X, f_Y; 0)df_Xdf_Y$, evaluated at $(f_X = \alpha/\lambda, f_Y = \beta/\lambda)$. If $y = 0$ and using Goodman's [10] nomenclature, the function

$$A\left(\frac{\alpha}{\lambda}, 0; 0\right) = \int_{-\infty}^{\infty} U(x, 0, 0) \exp\left[-j2\pi\left(\frac{\alpha}{\lambda}x\right)\right] dx \quad (6.7)$$

is the *angular spectrum* of the disturbance, $U(x, 0, 0)$. Finally, as Goodman [10] has shown, and if $y = 0$, the propagation of the angular spectrum of $U(x, 0, 0)$ over a distance, $z = L$, is given by

$$A(f_X, 0; L) = A(f_X, 0; 0)K(f_X, 0; L) \quad (6.8)$$

where the *angular spectrum propagation kernel*, K , is given by

$$K(f_X, 0; L) = \exp\left(j\frac{2\pi}{\lambda}L\sqrt{1 - (\lambda f_X)^2}\right) \quad (6.9)$$

and f_X is the “angular frequency” or “spatial frequency” of a plane wave propagating with direction cosine angle, α , corresponding to a sine wave of frequency, α/λ , in the x direction [11].

6.5.2 Field Reflection and Transmission. As the field within the cavity impinges on the Au mirror, the field is reflected and scaled by the Au mirror operator, M_{Au} , given by

$$M_{Au}(x, w_{Au}, m) = R_{Au} SG(x, w_{Au}, m) \quad (6.10)$$

where the super-Gaussian operator, SG , used to aperture the Au mirror (and minimize Gibbs phenomena [11]) is given by

$$SG(x, w, m) = \exp\left[-\left(\frac{x^2}{w^2}\right)^m\right] \quad (6.11)$$

and w_{Au} is half the length of the Au mirror in the x direction, m is the order of SG , and R_{Au} is the Au mirror reflectivity. Since the Au mirror is not subject to release and is in direct contact with planar material, the Au mirror is assumed planar in

this simulation. Thus, R_{Au} was calculated via the transfer-matrix method described in Chapter III.

However, due to the DBR mirror curvature, the optical field impinging on the DBR from *outside* the cavity is spatially modified by

$$M_i(x, 0, z, w_{spot}, m) = R_i C_{DBR}(x, 0, z) SG(x, w_{spot}, m) \quad (6.12)$$

and the optical field impinging on the DBR from *inside* the cavity is spatially modified by

$$M_o(x, 0, z, w_{spot}, m) = R_o C_{DBR}(x, 0, z) SG(x, w_{spot}, m) \quad (6.13)$$

where, as defined by Klein and Furtak [12], the field wavefront curvature operator, C_{DBR} (applied when the wavefront is reflected from a spherical mirror), represented by the lens transmission function (ignoring the finite extent of the lens [12]) is given by

$$C_{DBR}(x, 0, z) = \exp \left[j(\text{sign}(z)) \frac{2\pi}{\lambda} \frac{x^2}{R_C} \right] \quad (6.14)$$

where the DBR is the lens in this simulation, the DBR radius of curvature, R_C , is negative when viewed from inside the cavity, w_{spot} is half the length (in the x direction) of the assumed spot impinging onto the curved DBR mirror (assuming the spatial extent of the spot generated by the reflectance measurement system is less than the effective spatial extent of R_C), R_i is the conjugate (to account for the the opposite orientation of the z axis in the R_i calculation via the transfer-matrix method) of the DBR mirror reflectivity when viewed from inside the cavity, R_o is DBR mirror reflectivity when viewed from outside the cavity, and $\text{sign}(z)$ is negative for DBR reflection from inside the cavity (to indicate propagation of the reflected field wavefront [12] toward the Au mirror).

Finally, the transmission of the field through the DBR from *outside* the cavity is spatially modified by

$$T_o = |T_o| \exp [j \angle(R_o)] \quad (6.15)$$

where $\angle(R_o)$ is the argument of complex R_o , and the transmission of the field through the DBR from *inside* the cavity is spatially modified by

$$T_i = -|T_o| \exp [j \angle(R_i)] \quad (6.16)$$

where $\angle(R_i)$ is the argument of complex R_i , and the finite extent of the DBR is ignored by setting the transmission operators equal in magnitude with opposite sign, and the transmission phase is the reflectivity phase corresponding to the incident view of the DBR mirror [11].

6.5.3 Calculated versus Measured Results. As shown in Figures 6.19-6.21, for this device, the planar-convex simulation via the Fox-Li method was superior to the planar-planar transmission-matrix method previously illustrated in Figures 6.13 and 6.14. Specifically, the Fox-Li simulation addressed the following discrepancies between the transmission-matrix simulation and the measured reflectance:

- **Resonant dip width:** The Fox-Li simulation indicated the increase in resonant dip width was influenced by surface curvature
- **Resonant dip depth:** The Fox-Li simulation indicated the reduction in resonant dip depth was influenced by surface curvature
- **Resonant dip blue-shift:** The Fox-Li simulation indicated the blue-shift in resonant dip location was influenced by surface curvature

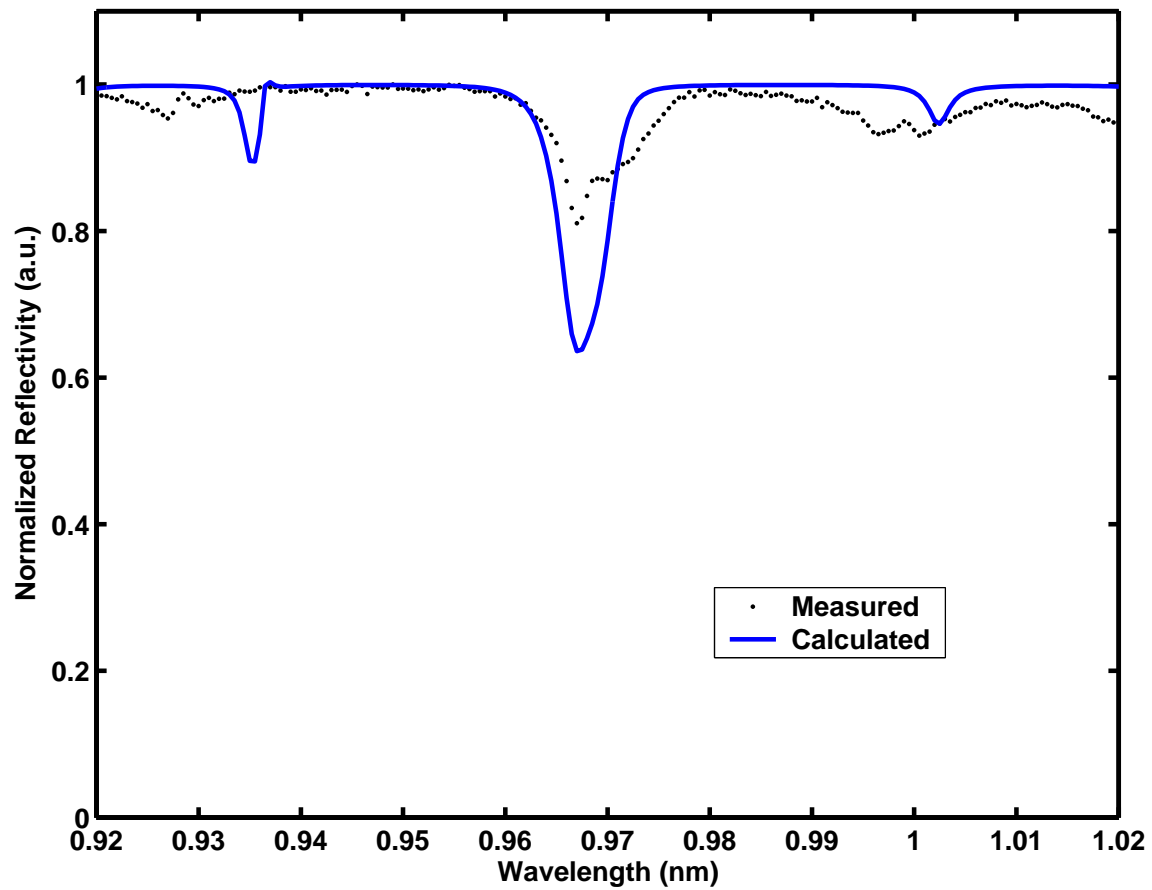


Figure 6.19: Measured versus calculated hybrid MEM-TF reflectivity as a function of wavelength; 0.0V actuation voltage, calculated via planar-convex cavity assumption

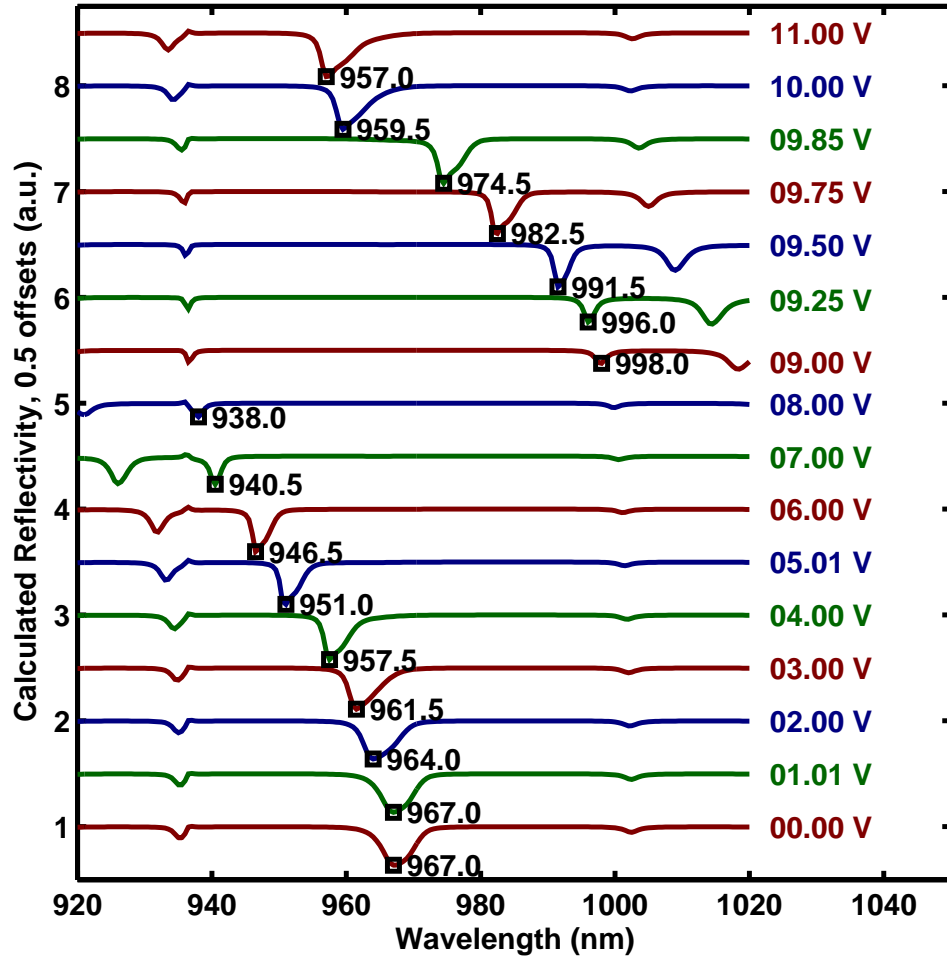


Figure 6.20: Calculated hybrid MEM-TF reflectivity as a function of wavelength

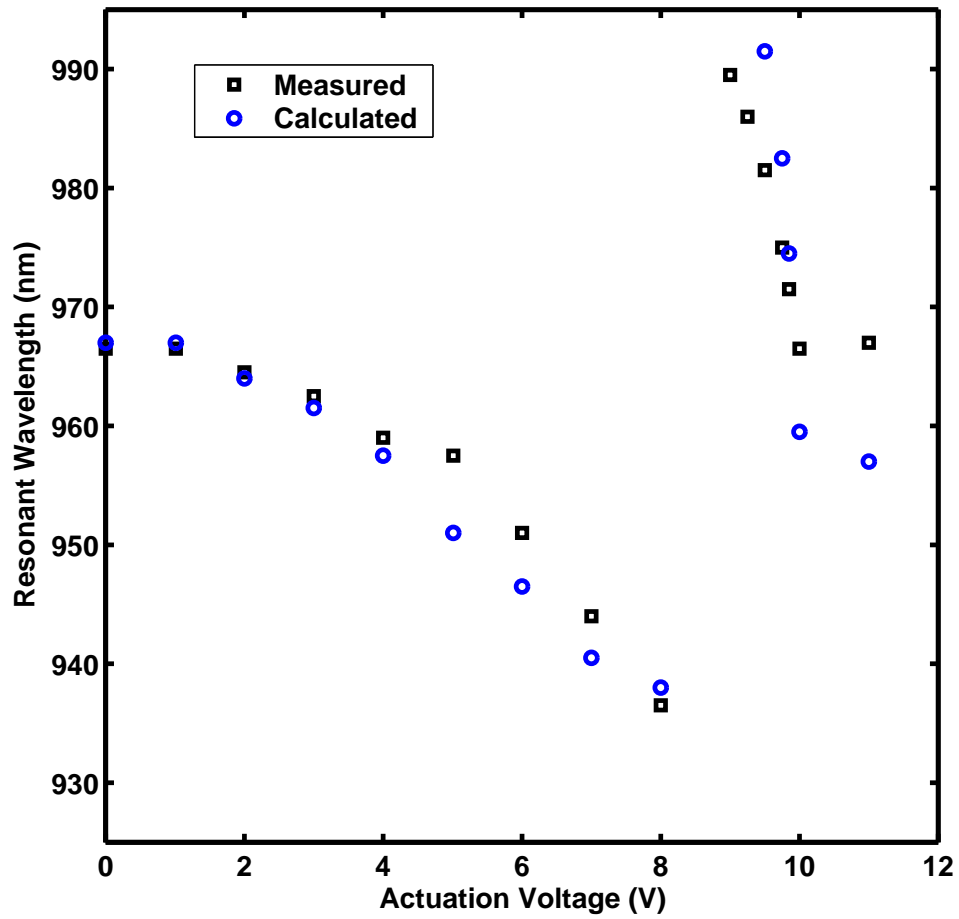


Figure 6.21: Measured versus calculated hybrid MEM-TF tuning as a function of applied actuation voltage

Additionally, the Fox-Li simulation indicated this hybrid MEM-TF may also be considered a hybrid MEM-tunable unstable resonator due to the unintended DBR surface curvature. Although this result was not anticipated, the measured data and Fox-Li simulation confirm this device demonstrated reflectance characteristics consistent with those of a tunable (planar-convex) unstable resonator.

6.6 Discussion

The device resonant-wavelength dip width was not narrow or deep over all device actuation voltages. The flip-bonded DBR resulted in a planar-convex cavity instead of a planar-concave or planar-planar cavity, which led to diverging, instead of parallel, light. The Fox-Li simulation indicated the increase in resonant dip width, reduction in resonant dip depth, and the blue-shift in resonant dip location was due to surface curvature in the flip-bonded DBR.

The curved DBR surface may have been due to an as-grown stress mismatch between adjacent $\text{Al}_{0.4}\text{Ga}_{0.6}\text{As}$ -GaAs DBR layers, or to failure to mitigate surface tension on the unsupported and suspended DBR center during device release processing which may have led to residual internal stress [13]. Additionally, the finite size of the underlying $64\text{-}\mu\text{m}^2$ Au mirror may have contributed to edge overfilling by the nominally $45\text{-}\mu\text{m}$ spot.

In addition to wide resonant dip width, shallow dip depth, and dip blue-shift (due to surface curvature), the device tuning range was limited by two primary DBR mirror design factors. First, if the DBR design had included more $\text{Al}_{0.4}\text{Ga}_{0.6}\text{As}$ -GaAs periods, the DBR would have a higher reflectivity within the stop band leading to a more narrow and deep resonant frequency dip. Additionally, the $1\text{-}\mu\text{m}$ GaAs cap layer may be replaced by additional periods to increase reflectivity; however, because mechanical strength may have been provided by this layer, removal may lead to cracks, as previously reported [3]. Second, if the DBR materials also had a stronger index contrast, the stop band would have been wider, leading to an extended tuning

range. Index contrast may be increased by investigating other material combinations compatible with the device's fabrication and release processes.

6.7 Chapter Summary

This research demonstrated a first-generation electrostatically actuated hybrid MEM-TF with $\text{Al}_x\text{Ga}_{1-x}\text{As}$ -polySi composition. This design led to a device with flip-bonded $\text{Al}_x\text{Ga}_{1-x}\text{As}$ distributed Bragg reflector and Au reflector. Key advantages included enabling the use of polySi dimples to reduce stiction and eliminate catastrophic pull-in failure, independent design and optimization of mechanical and optical elements, and the use of identical mechanical actuators for custom (design wavelength) tunable optoelectronic applications.

Bibliography

1. E. M. Ochoa, T. R. Nelson, O. Blum-Spahn, and J. A. Lott, "Computer-Aided Design Comparisons of Monolithic and Hybrid MEM-Tunable VCSELs," in *Physics and Simulation of Optoelectronic Devices XI, Proceedings of SPIE*, vol. 4986, San Jose, CA, Jan 2003, pp. 293–303.
2. E. Ochoa, L. Starman, W. Cowan, T. Nelson, O. Blum-Spahn, and J. Lott, "Polysilicon Prototypes for Flip-bonded Hybrid MEM-tunable Filters and VCSELs," in *Technical Proceedings of the 2002 International Conference on Modeling and Simulation of Microsystems*, San Juan, Puerto Rico, Apr 2002.
3. M. Harvey, E. Ochoa, J. Lott, and T. R. Nelson, "Toward the Development of Hybrid MEMS Tunable Optical Filters and Lasers," in *Proceedings of the 2004 International Conference on Compound Semiconductor Manufacturing Technology*, Miami Beach, FL, May 2004.
4. W. D. Cowan, "Foundry Microfabrication of Deformable Mirrors for Adaptive Optics," Ph.D. dissertation, Air Force Institute of Technology, Department of Electrical and Computer Engineering, Wright Patterson AFB, OH, 1998, AFIT/DS/ENG/98-07.
5. L. Torcheux, A. Mayeux, and M. Chemla, "Electrochemical Coupling Effects on the Corrosion of Silicon Samples in HF Solutions," *Journal of the Electrochemical Society*, vol. 142, pp. 2037–2046, June 1995.
6. Cronos Integrated Microsystems, "MUMPs® #68 run data," Internet, 2007, www.memscap.com/mumps/documents/PolyMUMPs.rundata.xls.
7. A. G. Fox and T. Li, "Modes in a Maser Interferometer with Curved Mirrors," pp. 1263–1270, 1964.
8. H. Kogelnik and T. Li, "Laser Beams and Resonators," *Applied Optics*, vol. 5, no. 10, pp. 1550–1567, Oct 1966.
9. R. Bedford and E. M. Ochoa, "FoxLiHMTF.m," Unpublished, Apr 2007.
10. J. Goodman, *Introduction to Fourier Optics*, 2nd ed. New York: McGraw-Hill, 1996.
11. R. Bedford, "Personal interviews," Unpublished, Jan-Apr 2007, Electro-Optical Team Member, Air Force Research Laboratory, Sensors Directorate, Wright-Patterson AFB, OH.
12. M. V. Klein and T. E. Furtak, *Optics*, 2nd ed. John Wiley and Sons, 1986.

13. C.-C. Lin, W. A. Martin, and J. S. Harris, “Optomechanical Model of Surface Micromachined Tunable Optoelectronic Devices,” *IEEE Journal on Selected Topics in Quantum Electronics*, vol. 8, no. 1, pp. 80–87, January/February 2002.

VII. Conclusions, Contributions, and Future Work

7.1 Contribution and Significance

The primary contribution of this research was demonstration of a first-generation MEMS electrostatically tunable Fabry-Perot optical filter with $\text{Al}_x\text{Ga}_{1-x}\text{As}$ -polySi composition. Significant advantages of this methodology included the following:

- Enabled the use of polySi dimples to reduce catastrophic failure due to device stiction and pull-in [1]
- Enabled independent design and optimization of mechanical and optical elements [1–4]
- Enabled ability to pre-screen optical elements prior to full device assembly [1]
- Enabled reduction in device tuning sensitivity to variations in growth of optical elements [2]
- Enabled linear tuning as a function of actuation voltage by designing mechanical actuation independent of initial air-gap between the optical reflector and optical element [1, 3]
- Enabled use of identical polySi mechanical actuators with different AlGaAs material growths [1, 4]

7.2 Accomplishments

This research demonstrated the following theoretical and/or experimental accomplishments:

- **Theoretical and Experimental Accomplishment:** Implemented and validated the electrostatic piston deflection calculation with polySi prototypes [3]

- **Theoretical Accomplishment:** Designed, implemented, and distributed *oeng775tools* (used by AFIT Photonics students for over four years), a MATLAB[®] modeling toolkit used to design, simulate, and visualize multi-layer thin-film characteristics such as power reflectance, absorption, transmission, reflectivity phase, and E-field intensity [5]
- **Theoretical Accomplishment:** Designed, implemented, and demonstrated MT-CAD, a MATLAB[®] modeling toolkit used to design, simulate, and visualize monolithic or hybrid MT-VCSEL or MEM-TF tuning as a function of applied actuation voltage [2, 6]
- **Theoretical Accomplishment:** Discovered a novel design trade-space via MT-CAD which may enable linear voltage tuning of hybrid MEM-TVCSEL [3]
- **Experimental Accomplishment:** Developed and characterized fabrication techniques to enable flip-bonding intact and crack-free $250 \times 250\text{-}\mu\text{m}^2$ DBRs to actuatable polySi MUMPs[®] devices [1, 4, 7]
- **Experimental Accomplishment:** First report of fabrication and characterization of a hybrid (polySi-AlGaAs) MEM-TF, a first step toward hybrid MEM-TVCSELs [1]
- **Experimental Accomplishment:** Fabrication of a hybrid MEM mirror; as a serendipitous spin-off of this work, this research also demonstrated the feasibility of bonding custom-fabricated, highly reflective (over multiple wavelengths) DBR material to existing MEM actuator designs, adding a new material set to the existing MEM-mirror design space [1]

Additionally, experimental MEM and VCSEL CAD tools were developed, acquired, and integrated to design, simulate, analyze, and optimize III-V and III-IV-V MEM-TF, MT-VCSEL, and MEM-tunable unstable optical resonators. PolySi mechanical structure prototypes successfully validated mechanical simulations. This research contributed toward the development of hybrid MT-VCSEL and, as serendip-

itous contributions, toward the development of hybrid MEM mirrors and hybrid MEM-tunable unstable optical resonators.

7.3 Recommendations for Future Work

There are several new and exciting areas of research that could be performed in the future. Several potential research areas which may leverage the research developed and demonstrated in this dissertation include the following:

- Investigate procedural refinement and optimization of the processing methods developed in this research to increase device yield of arrays of flip-bonded DBR to polySi MEMS actuators. In order to make this proposed methodology viable and more cost effective, yield must significantly improve, and fabrication trades should be further investigated. In particular, the long etch times and manually-intensive fabrication, assembly, and test methods developed in this research may not be optimal for mass-manufacturing efforts.
- Investigate In-In flip-bonding or other conductive bond-pad material candidates to enable demonstration of the hybrid MT-VCSEL devices proposed and simulated in Chapter III. If the hybrid MT-VCSEL is considered for future research, additional challenges may need to be closely considered. In particular, one should consider the potentially negative thermal effects on VCSEL performance if an active optoelectronic device is suspended and surrounded by a thermally non-conductive insulator such as air. Also, the processing methods developed in this research to flip-bond a DBR to a polySi actuator, and then release the DBR from the donor GaAs substrate required significant process development. This was the most challenging impediment to demonstrating a hybrid MEM-TF, and may likely be the most challenging impediment to demonstrating a hybrid MEM-TVCSEL.
- Investigate alternate DBR material compositions to minimize DBR curvature or purposely enable fabrication of a half-symmetric cavity hybrid MEM-TF

- Investigate flip-bonding custom (wavelength-optimized) DBR material to arrays of individually-addressable, MEM piston or tilt actuators to enable $\sim 100\%$ reflectivity at custom-designed wavelengths, and leverage the momentum and experience of the existing and future MEMS community
- Investigate thermal tolerance of flip-bonded DBR materials flip-bonded to MEM actuators to enable high-temperature device operation
- Investigate design and fabrication of individually-addressable, monolithic or hybrid, MEM-tunable, unstable resonator arrays for high-energy, semiconductor-based laser or LED devices to enable wavelength tuning of the cavity mode with the (temperature-dependent) gain peak so both peaks *converge* and remain aligned over a broad wavelength range while device operating temperature increases

7.4 Author's Publication List

1. J.A. Lott, M.J. Noble, E.M. Ochoa, L.A. Starman, and W.D. Cowan, *Tunable Red Vertical Cavity Surface Emitting Lasers using Flexible Micro-Electro-Mechanical Top Mirrors*, Optical MEMS, August 2000
2. Lott, J. A., E.M. Ochoa, W.J. Siskaninetz, and M.J. Noble, *Tunable Red Vertical Cavity Surface Emitting Lasers Using Electrostatic Actuation*, Conference on Optoelectronic and Microelectronic Materials and Devices, December 6, 2000
3. L.A. Starman, E.M. Ochoa, J.A. Lott, M.S. Amer, W.D. Cowan, and J.D. Busbee, *Residual stress characterization in MEMS microbridges using micro-Raman spectroscopy*, MSM 2002, April 2002
4. E.M. Ochoa, L.A. Starman, W.D. Cowan, T.R. Nelson, O. Blum-Spahn, and J.A. Lott, *Polysilicon prototypes for flip-bonded hybrid MEM-tunable filters and VCSELs*, MSM 2002, April 2002

5. J. Johnson, G. Grossetete, O. Blum-Spahn, C. Tigges, E. Ochoa, F. Gass, T. Bakke, and C. Sullivan, *Fabrication and Characterization of GaAs-based Waveguide MOEMS*, 38th Annual Symposium NM Chapter of AVS , May 14-15 2002
6. G. Grossetete, J. Johnson, O. Blum-Spahn, C. Tigges, E. Ochoa, F. Gass, T. Bakke, and C. Sullivan, *Fabrication and Characterization of GaAs-based Waveguide MOEMS*, 38th Annual Symposium NM Chapter of AVS , May 14-15 2002
7. O. Blum-Spahn, T. Bakke, C. P. Tigges, J. Johnson, G. Grossetete, F. R. Gass, E.M. Ochoa, J. L. Reno, J. F. Klem, G. M. Peake, C. T. Sullivan, *GaAs-Based Waveguide MOEMS*, Hilton Head 2002, June 2002
8. L.A. Starman, E.M. Ochoa, J.A. Lott, W.D. Cowan, M.S. Amer, J.D. Busbee, *MEMS Stress Characterization via Raman Spectroscopy*, Journal of Applied Physics, submitted July 2002
9. E. M. Ochoa, J. A. Lott, T. R. Nelson Jr., M. C. Harvey, J. A. Raley, A. Stintz, and K. J. Malloy. *Monolithic III-V and Hybrid Polysilicon-III-V Microelectromechanical Tunable Multilayer Filters and Vertical Cavity Surface Emitting Lasers*, Proceedings of SPIE, 5116:465-472 (April 2003)
10. M.C. Harvey, E.M. Ochoa, J.A. Lott, and T. R. Nelson. *Toward the Development of Hybrid MEMS Tunable Optical Filters and Lasers*. In *Proceedings of the 2004 International Conference on Compound Semiconductor Manufacturing Technology*, Miami Beach, FL, May 2004.
11. Edward Ochoa, Thomas Nelson, Robert Bedford, James Ehret, LaVern Starman, Michael Harvey, Travis Anderson, and Fan Ren, *Demonstration of Hybrid $Al_xGa_{1-x}As$ -Polysilicon Microelectromechanical Tunable Filter*, IEEE Phot. Tech. Let., vol. 19, no. 6, pp. 381-383, Mar 2007.

12. Edward Ochoa, LaVern Starman, Robert Bedford, Thomas Nelson, James Ehret, Michael Harvey, Travis Anderson, and Fan Ren, *Flip-bonding with SU-8 for Hybrid $Al_xGa_{1-x}As$ -Polysilicon MEMS-Tunable Filter*, J. Micro/Nanolith. MEMS MOEMS, vol. 6, no. 3, Jul-Sep 2007.

Bibliography

1. E. Ochoa, T. Nelson, R. Bedford, J. Ehret, L. Starman, M. Harvey, T. Anderson, and F. Ren, "Demonstration of Hybrid $\text{Al}_x\text{Ga}_{1-x}\text{As}$ -Polysilicon Microelectromechanical Tunable Filter," *IEEE Photon. Technol. Lett.*, vol. 19, no. 6, pp. 381–383, Mar. 2007.
2. E. M. Ochoa, T. R. Nelson, O. Blum-Spahn, and J. A. Lott, "Computer-Aided Design Comparisons of Monolithic and Hybrid MEM-Tunable VCSELs," in *Physics and Simulation of Optoelectronic Devices XI, Proceedings of SPIE*, vol. 4986, San Jose, CA, Jan 2003, pp. 293–303.
3. E. Ochoa, L. Starman, W. Cowan, T. Nelson, O. Blum-Spahn, and J. Lott, "Polysilicon Prototypes for Flip-bonded Hybrid MEM-tunable Filters and VCSELs," in *Technical Proceedings of the 2002 International Conference on Modeling and Simulation of Microsystems*, San Juan, Puerto Rico, Apr 2002.
4. M. Harvey, E. Ochoa, J. Lott, and T. R. Nelson, "Toward the Development of Hybrid MEMS Tunable Optical Filters and Lasers," in *Proceedings of the 2004 International Conference on Compound Semiconductor Manufacturing Technology*, Miami Beach, FL, May 2004.
5. E. M. Ochoa, "oeng775tools: A MATLAB[®] toolbox," AFIT/ENG, Wright-Patterson AFB, OH, unpublished, February 2001.
6. E. M. Ochoa, J. A. Lott, T. R. N. Jr., M. C. Harvey, J. A. Raley, A. Stintz, and K. J. Malloy, "Monolithic III-V and Hybrid Polysilicon-III-V Microelectromechanical Tunable Multilayer Filters and Vertical Cavity Surface Emitting Lasers," in *Proceedings of SPIE*, vol. 5116, April 2003, pp. 465–472.
7. E. Ochoa, L. Starman, R. Bedford, T. Nelson, J. Ehret, M. Harvey, T. Anderson, and F. Ren, "Flip bonding with SU-8 for hybrid $\text{Al}_x\text{Ga}_{1-x}\text{As}$ -polysilicon MEMS-tunable filter," *J. Micro/Nanolith. MEMS MOEMS*, vol. 6, no. 3, Jul-Sep 2007.

Appendix A. Process Flow and Equipment Checklists

The following process flow and equipment checklist time estimates assume 100 % equipment availability. However, all systems are shared on a first-come, first-served basis. In some cases, only 3-day-ahead sign-up is possible.

Table A.1: Quad Level Mask Process Flow (Est. 8-hr)

	PMGI SF6: 5k r/min 30 sec, 120 deg 2-min, 250 deg 5-min
	AZ4330: 4k r/min 30 sec, 90 deg 90 sec, 90 sec edgebead Soft/ST, AZ400K 1:4 90 sec, Oven 170 deg 1-hr
	SiN Dep: Run 'Dayclean', 10-min conditioning 'trisin', 10-min with GaAs mechanical, Measure mechanical, 30-min dep with GaAs witness, Measure witness
	AZ4110: HMDS 33-min, 5k r/min 30 sec, 90 deg 90 sec, 90 sec edgebead ST/Soft, AZ400K 1:4 90 sec, 5.8 sec HP and Vacuum, AZ400k 1:4 40 sec or until done, LFE Descum 5W 4-min
	SiN Etch: Clean1 if necessary, 10-min conditioning 'si3n4', etch 25-min with witness piece, then check witness, Run clean1
	HBPR etch (batch mode): Clean if necessary, 10-min conditioning run using 'hbpretech' program, Etch 20 percent over via interferometer, get approximately 19 peaks then flatline rises, about 3:30 total time
	ICP etch (manual mode): Clean if necessary, 10-min conditioning run and setup interferometer, Etch using interferometer or timed etch, DI dip just after remove from platen
	Inspect etch depth
	Quad Level removal: 90 deg NMP 1-hr, AMI rinse, N2 dry
	PR removal (if necessary): LFE 10-min 100W

Table A.2: GaAs Etch Process Flow (Est. 2-hr)

	Measure dry chemicals: Citric Acid .961 g, Tripotassium Citrate 1.62 g; Cover dish
	O2 Plasma LFE: 12-min, 200 W
	While die in LFE, add: 20mL DI water, 3mL Hydrogen Peroxide, Agitate then mix and crush crystals until all completely dissolved, Set on hot plate 25 deg
	Remove oxide just prior to etch: 1:8 BOE dip, DI rinse, N2 dry
	Place sample in etch; Measure and record pH
	Cover with foil
	Stop etch with DI or 2 Methanol rinses if release is objective

Table A.3: Metal Lift-off Process Flow (Est. 6.5-hr)

	Clean/prep: AMI, HMDS 33-min
	PMGI SF11 30 sec 4krpm, bake 120 deg 2-min, bake 250 deg 5-min
	5214 30 sec 5krpm, bake 110 deg 90 sec, Edge bead mask 75 sec, Develop MIF312 1:1.4 45 sec, Pattern mask 10 sec, Develop MIF312 1:1.4 90 sec
	DUV fusion expose 90 sec, Develop MF319 1-min
	LFE descum 5 W 5-min
	Perform Metal Deposition (see Temescal checklist)
	Metal lift-off: 1-hr acetone soak, acetone spray
	NMP 1-hr at 90 deg

Table A.4: Mesa Wet Etch Process Flow (Est. 2.5-hr)

	AMI, HMDS 33-min
	4330 4krpm 30 sec, bake 90 deg 90 sec
	Edgebead soft-contact 90 sec, Develop MF319 2-min
	Mesa mask 6.5 sec, Develop MF319 2-min
	Mesa etch: 1:1:10 = H2SO4:H2O2:H2O = 20 ml: 20 ml: 200 ml, Note - slowly add H2SO4 last, wait 15 min for pH to settle (to approximately 1)

Table A.5: Loomis Scribe Cleaver Checklist (Est. 30-min)

	Set vacuum toggle off
	Master switch to left
	Toggle pressure
	Insert part to dice, use tape to mask vacuum holes if necessary
	Set vacuum toggle on (to left)
	Scribe

Table A.6: Sublimation Dryer Checklist (Est. 1.5-hr)

	Run H2O
	Turn on Nitrogen (20psi)
	Turn on Thermocouple
	Insert Cyclohexane-soaked die
	Dry for 1hr
	Turn off thermocouple
	Turn off Nitrogen
	Turn off H2O

Table A.7: PlasmaTherm Downstream Stripper Checklist (Est. 30-min)

	Utilities, Vent
	Load sample with tweezers
	Utilities, Pump down until reaches 100 mTorr
	Process, Edit, Load DEN.PRC
	READY mode
	RUN
	Use tuning stub to ignite the plasma (light, lower, increase to under 10)
	When run complete, vent using pump option under Utilities

Table A.8: LFE Checklist (Est. 20-min)

	Vacuum release
	Red light flashes, count to 20
	Load then set time
	Set RF guage
	Cycle start - pumps down
	Set RF power via lower guage
	Red light flashes when done

Table A.9: Ellipsometer Checklist (Est. 5-min)

	Calibrate
	Place sample
	Loosen with hex to focus (pulled out and flip top to left)
	Push in
	Use front knob to unlock
	Use left and right knobs to center
	RUN, 10, prints
	Compare printout to calibration label

Table A.10: Nanospec Checklist (Est. 5-min)

	New Test
	Calibrate (press and hold)
	No
	2, Enter
	1, Enter (10x objective)
	Yes
	Focus on Si wafer until hexagon shaped object in focus
	Measure (scrolls through different wavelengths)
	Place your sample and slide objective over to it
	Focus again
	No, Enter
	Enter, 1.9, Enter
	Measure 3 times

Table A.11: HMDS Checklist (Est. 33-min)

	Observe pressure gauge 628 good
	Observe timer=0
	Check rubber seal in place
	Check cleanliness inside
	Call out for HMDS in case others plan/want to participate in your run
	Set timer 33-min
	Press black button to start
	Turn off alarm(s) if done

Table A.12: 790 PECVD Checklist (Est. 2-hr)

	System in idle mode
	Check two pumps colored green
	Check heat exchanger, should read 60 deg
	If logged off, enter 790dep as operator and csrl as password
	Indicator lights for ON and either STANDBY or READY must be lit
	Utilities, Vent to open chamber
	Inspect chamber walls, if excessive deposits you must clean chamber before processing
	Place sample in lower electrode using tweezers
	Make sure chamber o-ring and sealing surface clean. Wipe with Iso-propanol if necessary
	Utilities, Pump chamber and hold lid down firmly
	Wait until 100mTorr before proceed
	Process, Load process you want to run
	Click READY button since you must be in ready mode
	To start click RUN
	Enter time in dialog box that appears
	After dep step begins, record process parameters
	Will hold under vacuum when finished
	Unload using Utilities, Vent
	Pump down via Utilities, Pump
	When leave system, run Dayclean (20-min) or Nitclean if last to use. Stay at system until plasma clean started and all readings stabilized

Table A.13: 790 RIE Checklist (Est. 2-hr)

	System in idle mode
	Check two pumps green
	Check heat exchanger
	If logged off, enter 790etch as operator and csrl as password
	Indicator lights for ON and either STANDBY or READY must be lit
	Utilities, Vent to open chamber
	Inspect chamber walls, if excessive deposits you must clean chamber before processing
	Make sure chamber o-ring and sealing surface clean. Wipe with Iso-propanol if necessary
	Utilities, Pump chamber and hold lid down firmly
	Wait until 100mTorr before proceed
	Process, Load process you want to run
	Click READY button since you must be in ready mode
	To start click RUN
	Enter time in dialog box that appears
	After etch step begins, record process parameters
	Will hold under vacuum when finished
	Unload using Utilities, Vent
	Pump down via Utilities, Pump
	When leave system, run clean1. Stay at system until plasma clean started and all readings stabilized

Table A.14: Temescal Checklist (Est. 3-hr)

	Prep sample(s): To remove native oxide, $\text{NH}_4\text{OH}:\text{H}_2\text{O}=1:20$ 30 sec soak, N_2 dry, Mount in stage assembly
	Begin log book entry; Turn filament off; To vent chamber, press AUTO STOP button
	Open/prepare chamber: Inspect, vacuum, remove foil from ION gun, Remove metal shield, Remove screws perpendicular to filament, Pull out assembly, Set on an insulated structure, Insulation Tester 1000V, 0-500 Mohms, push/turn on, Check rim-rim is short, rim-grid is open, rim-filament is open, Replace assembly
	Inspect sources (Cr, Au) sufficient, set shutter and source control back to AUTO
	Verify/record sensor 1 lifetime (400-500); to change hold sides of mount while dislodging assembly, use plastic tool, insert, slightly twist to remove sensor cover, Remove then insert new sensor with contacts visible, Replace cover, Hold sides while replacing assembly, Note/record new sensor values
	Insert stage with "A" to left; Set rod to vertical with motor speed control
	Put "IN USE" sign on drum; Close drum; Turn on motor speed control and listen to confirm OK, then turn off; To evacuate chamber, press AUTO START button. Goal is low $10\text{e-}6$; After crossover reached ($\text{TC}2=70$), turn filament on
	ION MILL: Turn on argon gas; Adjust needle valve to set chamber pressure = $5\text{e-}5$ Torr; turn on motor speed control; check shutter and source control are on AUTO; Turn on ION source power supply; 10 sec to self test; Put in MANUAL mode; To turn on neutralizer, press SOURCE switch and allow 1-min to warm; Ensure Discharge voltage is 55V, Beam voltage is 500V, Accelerator voltage is 250V ; To begin sputtering, press BEAM switch; START timer now (Goal is 5min); If needed, adjust discharge current to .3-.36 mA for 20mA Beam current; Accelerator current no more than 10 percent of BEAM current, Neutralizer is 110-125 percent of beam current. Use 22-25mA; Turn off ION beam and neutralizer by pressing BEAM and SOURCE switches, press POWER switch to turn off power supply; STOP timer; Turn off the argon gas; Allow to pump down. Goal is low $10\text{e-}6$. Turn filament on.
	Insert floppy then Load program ED.CRAU_.isc; Inspect and update program material and process directories (tooling, Cr-Au dep rates and thickness); Cr: 2 Ang/sec, Power 8, 500 Ang total; Au: 5K Ang total by depositing at 3 Ang/sec, 5 Ang/sec start at 500 Ang with 15 sec ramp time, 7 Ang/sec start at 1500 Ang with 15 sec ramp time; Est of total deposition time: 26-min
	Log book base pressure before and 'Xtal Bfr' and Ensure motor speed control on
	Turn High Voltage Switch on; Check/ensure shutter and turret switches in AUTO position; Turn key on then press START; During run, check/adjust sweep, verify LAT and LONG freq=3, (Au pos/sweeps: 0,3,4,0); When done, will read IDLE and timer starts automatically
	Turn key off; Turn HIGH Voltage Switch off; Turn motor speed control off; Turn filament off; Wait 10min to convectively cool; To vent chamber, press AUTO STOP button; Remove 'IN USE' sign; Remove assembly; Replace aluminum foil cap on ION gun; To evacuate chamber, press AUTO START button; Complete log book entry

Table A.15: Flip Chip Aligner Bonder (FCAB) Checklist (Est. 1-2-hr)

	Prepare/verify set-up of FCAB: check water level, Ensure all panels secure; Turn on: On first screen, press any key to continue; On second screen, press UP/VAC, On third screen, press F VERT
	Load parts: Open upper chuck, Move pressure sensor wire is away from chuck, check vacuum hold-down patterns are down, down, up, up, down; iso-wetted wipe chucks; Place parts, then UP VAC and LO VAC keys; use vacuum hole to remove backside dust; Close upper chuck, CLAMP key
	Obtain video image: Verify/adjust clearance between upper/lower parts and camera probe; LO/AL to move camera probe into position; Upper illumination via LAMP; CAMERA until CAMERA: UP/; Joystick button until JOYST: CAM SCAN, locate upper die; FOCUS until JOYST: UP FOCUS, focus upper part; Joystick button until JOYST: CAM SCAN; locate coarse alignment features; Store locations MEM A() then # key. Return to stored locations via GO TO and #; CAMERA until CAMERA: /LO; Joystick button until JOYST: LO SCAN, locate lower die; LAMP for lower illumination; Use Lower Focus Control to focus lower part
	Align parts: Combine images CAMERA until CAMRA: UP/LO; Joystick fire button until JOYST: CAM SCAN; GO TO alignment feature on upper part; Move to matching feature on lower part; Use GO TO to return and note direction image moved; Joystick fire button until JOYST: LO SCAN, move lower die in this direction until upper/lower features overlap; repeat; Planarity alignment by moving location to center of parts; Press IL/COL key until COLLIM:; Display changes to set of bright crosses; P/ROLL key until JOYST: P/ROLL; Overlap cross patterns; Exit using IL/COL key, check/adjust since crosses move; repeat above for FINE ALIGNMENT; Toggle joystick to CAM SCAN to prevent accidental misalignment; LO/AL key to move camera probe to load position
	Program/Transfer bonding procedure: Press PROG key, then UP VAC to store initial alignment, then AUTO key; Scroll to last menu 5; Select (5) to receive from PC; In m8Talk, select Transfer to M8, click OK; Review program, then use asterisk key to exit programming mode
	Bond parts: Set Riser Stop Micrometer to 5; RISER key; Riser Stop Micrometer to set parts separation to about 1 mm; To zero out pressure reading, RISER key once to lower, then RISER again to bring parts separation back to 1mm; Turn off illumination for upper and lower camera via LAMP; To start bonding, press AUTO
	Remove parts: Wait until 'BONDING COMPLETE, PRESS ANY KEY' displayed; Press any key, then RISER key and wait until RISER: DOWN; CLAMP key, open upper chuck; Turn off upper/lower vacuum using UP/LO VAC key; Remove parts (slide, then lift); Close upper chuck and don't clamp
	Shut down: Shut-off main power switch; Close m8Talk.exe, log-off PC, then turn off monitor; Emergency shutdown: Abort a move or program by pressing any key; If aborted program, may have to release vacuum and be sure to lower riser and leave camera probe in load position and set temp on first program page to ambient

Table A.16: Dual Chamber ECR-ICP Checklist (Est. 2-hr)

	Log in to both PCs: Manual mode login on system; Load Monoetch and FileMaker on monitor PC; Excel spreadsheet, read last TEMP for chiller
	Turn on chilled water: Pull up Emergency button; Press START button; Flip switches up: Pump, Refrig; Set TEMP using SP2 and RUN button (25deg)
	In FileMaker: Mode, Duplicate Record
	Utilities, Select Active Chamber, Right Chamber; STANDBY should be selected; If were running in Auto mode, READY should be selected
	Select platen and note ID#, Make sure using blackened Al plate
	Mount conditioning run piece on platen; Want sample that has many interfaces for Monoetch trace; Turn etch monitor on
	Utilities, Load Lock, Pump; If Alarm: Click off alarm (silence), turn LED 'on' via screwdriver, if Hold on, turn off
	ELECTRODE DOWN BEFORE MOVING SAMPLE: Service, Manual Mode, Yes; Set Electrode Position to 0 (means down); Exit
	Service, Maintenance, Wafer Handling, Wafer Transfer, Load, then observe; If Alarm repeat above; Exit
	Service, Manual Mode, Yes; Use Excel spreadsheet to set Temp, Pressure, He, BCl ₃ , RF1 DCV 250, RF2 PWR 750 (1.5 * 500 W, 1.5 offset tweak), Lower Magnet = 1.0 (anything but 0), Set Electrode = 115, Set Time = 10-min (for conditioning run)
	Turn on (button switches to 'off'): Gas (fast rise), Skip Purge, Helium (if necessary, click up/down arrow to converge), Pressure, Magnets (dummy click since no magnets), RF - starts timer, if problems ALL OFF then turn on again
	FileMaker Log: RF1 power and ref, Position (Mode, Duplicate Record), etch time, mask material, parent wafer ID
	Line up interferometer: move spot to sample
	Monoetch: set to positive polarity
	Switch box to ICP
	Wait until time complete, or ALL OFF to interrupt, Set Electrode to 0, Exit;
	Service, Maintenance, Wafer Handling: Unload, Exit
	Utilities, Load Lock, Vent: Remove platen with sample; Log Excel entry
	To clean: Load isopropyl-wiped platen; Utilities, Load Lock, Pump; If Alarm repeat above; Process, Batch, File, load 'icpclean'; READY button should be illuminated; Set cooler to 25 deg (SP4 and RUN); Wait until temp set; RUN; If Alarm repeat above; Excel entry; ICP clean, 20-min, set clean time to 0, platen #; Monitor clean

Table A.17: JEOL SEM 6400 Checklist (Est. 1-2-hr)

	Monitor on: reboot VISION
	Mount specimen: ONLY use MUNG II!; Vent Load-lock: Carefully unhook latch; Load SEM; Evacuate load-lock, wait until LED off
	Check stage settings: $(X, Y, Z) = (50, 60, 15)$ mm, $Tilt = 000$ degrees; Load specimen onto stage; Check and RECORD gun, int, and spec vac pressures; Open gate valve.; Load specimen; holder should slide into the V-bracket and click; Close gate valve; OK to REMOVE GLOVES
	Initial Operation: On EOS page TWO screen, set X and Y IMAGE SHIFT to 0, On EOS page ONE screen, set accelerating voltage to 1 kV, On EOS page TWO screen, ensure auto emission is set to CNST, Wait until chamber vacuum is 1.5×10^{-6} Torr or less before proceeding; After vacuum achieved, press ACCEL VOLTAGE on button to begin auto ramping of emission current to 8 uA. RECORD value of final extraction voltage in daily operations log.
	Increase BRIGHTNESS until cursor appears, Set accelerating voltage on EOS page ONE screen, use break and esc key to turn on labels
	Column calibration: Check SEI button lit, EOS page ONE screen, adjust PROBE CURRENT knob to "6"; locate feature to use for column calibration at 40Kx mag, VERIFY working dist =15 mm, Reduce magnification to 30, adjust Z position downward at six half-turns; Stage rotation 180 degrees via red buttons located on left-most panel of right-most portion of console; Scan rotation (flip on) then turn dial to level image; Adjust FOCUS and X Y STIGMATOR controls for sharpest image; WOBBLER: If object stationary and jumps in/out of focus, no further adjustment needed; Gun alignment: Reduce PROBE CURRENT knob setting until object barely visible, adjust GUN ALIGNMENT x and y controls to move object back to where appeared at higher current setting and Repeat until object no longer shifts.
	Click FIS. Click SLOW to store image; Save via IMAGING, RECEIVE; storage via FIXED, FLOPPY; when done click EXIT
	Shutdown: Clear via FREZ, zoom to max mag, Turn off legends ESC BRK, Reduce accelerating voltage to 1, Turn off accelerating voltage off, Reduce BRIGHTNESS until both monitors dark, Return sample tilt angle to 000 (zero), Return (X, Y, Z) to $(50, 60, 15)$ mm, Return scan rotation to 0, then off; Return stage rotation to INITIAL SET position by pressing red button marked START on left-most panel of right most portion of control console
	Unload specimen: Press red button twice (90 sec) and check V5 and V6 LEDs lit; Open gate valve, push rod and unload; Close gate valve; Press red button to vent; NEW GLOVES. Remove sample; Press red button to pump down; Turn off monitor

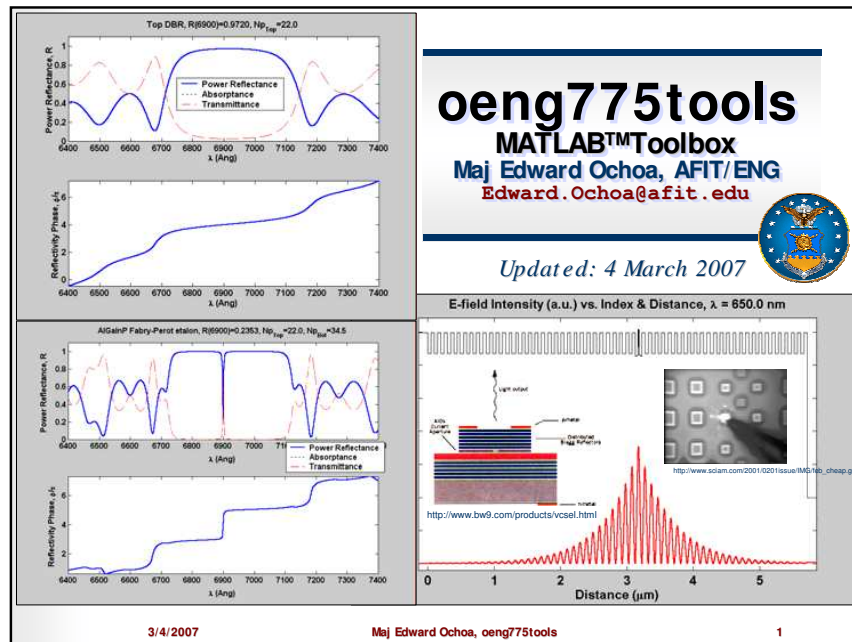
Table A.18: WYKO Interferometer Checklist (Est. 30-min)

	Check/ensure both monitors were off, 10x in home position, silver rails aligned
	Turn both monitors on; Login as wyko_user; move stage
	Start Vision32, File>Open Config>no Autofocus TAP (defaults to 2mm VSI mode with 3 averages); Use '*' button to open the intensity window
	Software: Note - for PSI (160nm roughness) measurements take 3 and set 3-4 fringe lines 45 deg across device
	Place your parts
	Use arrow or page up/down keys to increase/decrease brightness
	Focus: Rotate knob and press button to move 10x objective (Fast focus) down to about 7 mm. Clockwise moves up. Release button for fine focus; If screen red, decrease intensity
	Intensity: Hardware, Turret: Objective Choices
	Use Tip/Tilt Button to spread fringe lines and to rotate them. For VSI mode want thick bands; For PSI thin bands
	Bring down intensity so red barely disappears; Now ready to take data and scan.
	Software: SCAN (New Page icon), Scans device; Save data
	Software: Use Mask Editor icon to flatten measurement; Select 2D analysis icon for measurements; Save data
	Shut Down: Raise turret, Turn intensity to zero, set 10x objective active, remove your parts, exit program, center stage under objectives, log off computer, complete log Book, turn both monitors off, return equipment borrowed for testing

Appendix B. oeng775tools

In the course of this research, *oeng775tools* was developed. This custom MATLAB® “toolbox” is a set of functions to design, simulate, and visualize multi-layer thin-film characteristics such as power reflectance, absorption, transmission, reflectivity phase, and E-field intensity. The *oeng775tools* MATLAB® toolbox is available to members of AFRL, and has been used for several years by AFIT to support the OENG 775, Introduction to Photonics Devices course. This MATLAB® toolkit is compatible with student and professional versions of MATLAB®.

The introductory slide set for *oeng775tools* is included in this section to provide the user instruction for installation and use of the MATLAB® toolbox functions. The toolkit consists of 42 MATLAB® m-files which may be obtained for AFIT or AFRL use directly from the author.




Overview


- ◆ Description
- ◆ Assumptions
- ◆ Installation
- ◆ Tools
- ◆ Examples
- ◆ Questions

3/4/2007 Maj Edward Ochoa, oeng775tools 2


Figure B.1: *oeng775tools*: overview slides 1-2




oeng775tools - Description




- ♦ **MATLAB™ M-file Toolbox for AFIT's OENG 775**
to design, simulate, & visualize multi-layer thin film characteristics:
 - **Power Reflectance**
 - **Absorption**
 - **Transmission**
 - **Reflectivity Phase**
 - **E-field intensity**
- ♦ **POC: Maj Edward Ochoa, AFIT/ENG**
 - Edward.Ochoa@earthlink.net

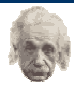


3/4/2007
Maj Edward Ochoa, oeng775tools
3




Assumptions





- ✓ You have OENG 775 handouts and notes...
- ✓ You have a working knowledge of MATLAB™
- ✓ You have MATLAB™
 - ✓ Version 5.3 (R11)
 - ✓ Version 6 (R12)
 - ✓ Student/Professional



3/4/2007
Maj Edward Ochoa, oeng775tools
4

Figure B.2: *oeng775tools*: overview slides 3-4



Installation



1. Unzip oeng775tools.zip
2. Recommend using a directory named: 'oeng775tools'
3. Add directory/contents to your MATLAB™ path; Ex:


```
>> path('c:/afit/oeng775tools',path)
```



<http://www.winzip.com/>

If install went well, should get...

3/4/2007
Maj Edward Ochoa, oeng775tools
5

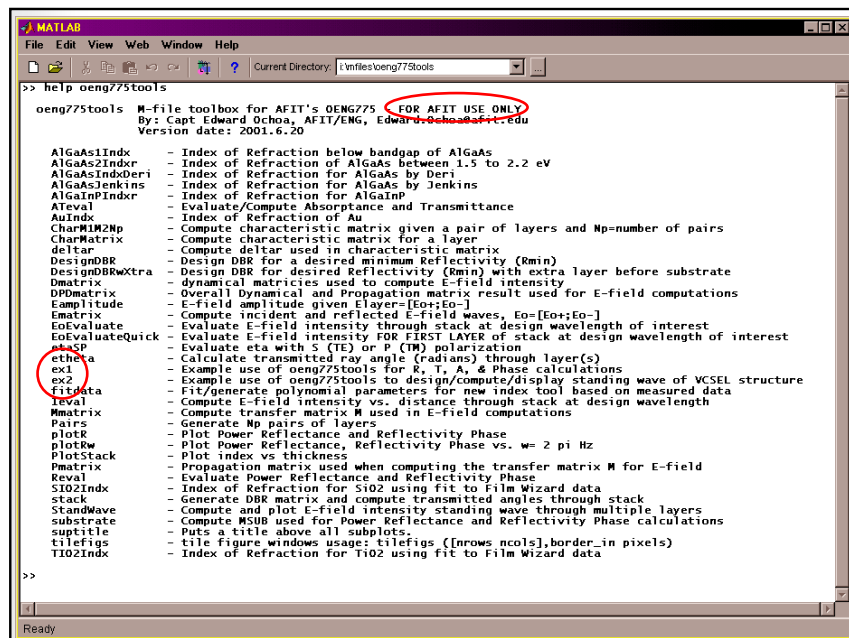



Figure B.3: oeng775tools: overview slides 5-6



Tool Categories

Primary:

1. Index of Refraction
2. R, T, A, & Phase
3. E-field, Intensity

Secondary:

- Design tools
- Plotting tools
- Utility/Timesavers

3/4/2007
Maj Edward Ochoa, oeng775tools
7

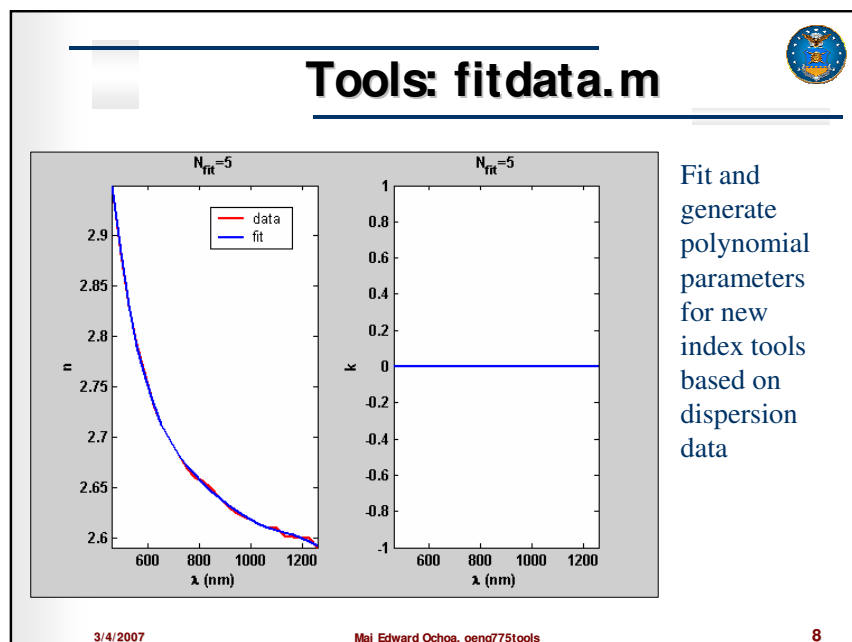


Figure B.4: *oeng775tools*: overview slides 7-8

Tools: Index of Refraction

- ◆ Input: mole fraction (x) & lambda (Angstroms)
 - **AlGaAs1Indx** - below band-gap of AlGaAs
 - **AlGaAs2Indxr** - between 1.5 to 2.2 eV
 - **AlGaAsIndxDeri** - by Deri
 - **AlGaAsJenkins** - by Jenkins
 - **AlGaInPIndxr** - for AlGaInP
 - **AuIndx** - Gold
 - **SiO2Indx** - SiO₂
 - **TiO2Indx** - TiO₂
- ◆ Output: (Complex) Index of Refraction


3/4/2007 Maj Edward Ochoa, oeng775tools 9

Tools: R, T, A, & Phase

- ◆ Input: *Use MATLAB™ 'help' on:*
 - **etheta** - angle through layer(s)
 - **deltar** - δ_r
 - **etaSP** - η_r (S or P polarization)
 - **substrate** - M_{sub}
 - **CharMatrix** - 1 layer
 - **CharM1M2Np** - Pairs of layers
 - **stack** - DBR matrix & angles
 - **pairs** - N_p pairs of layers
- ◆ Output: Characteristic Matrices


3/4/2007 Maj Edward Ochoa, oeng775tools 10

Figure B.5: *oeng775tools*: overview slides 9-10




Tools: R, T, A, & Phase ct'd...

- ◆ Input: *Use MATLAB™ 'help' on:*
 - **Reval** - Power Reflectance & Phase
 - **ATeval** - Absorptance & Transmittance
- ◆ Output:
 - Power Reflectance
 - Reflectivity Phase
 - Absorption
 - Transmission



<http://www.lucint.com/netsys/dwdm.html>

3/4/2007
Maj Edward Ochoa, oeng775tools
11



Tools: R, T, A, & Phase ct'd...

- ◆ Input: *Use MATLAB™ 'help' on:*
 - **DesignDBR** – for desired R_{\min}
 - **DesignDBRwXtra** – extra layer before substrate
 - **plotR** – Plot Power Refl. & Refl. Phase vs. λ
 - **plotRw** – Plot Power Refl. & Refl. Phase vs. ω
- ◆ Output:
 - Design Parameters for DBR
 - Plots of Power Reflectance & Reflectivity Phase

3/4/2007
Maj Edward Ochoa, oeng775tools
12

Figure B.6: *oeng775tools*: overview slides 11-12

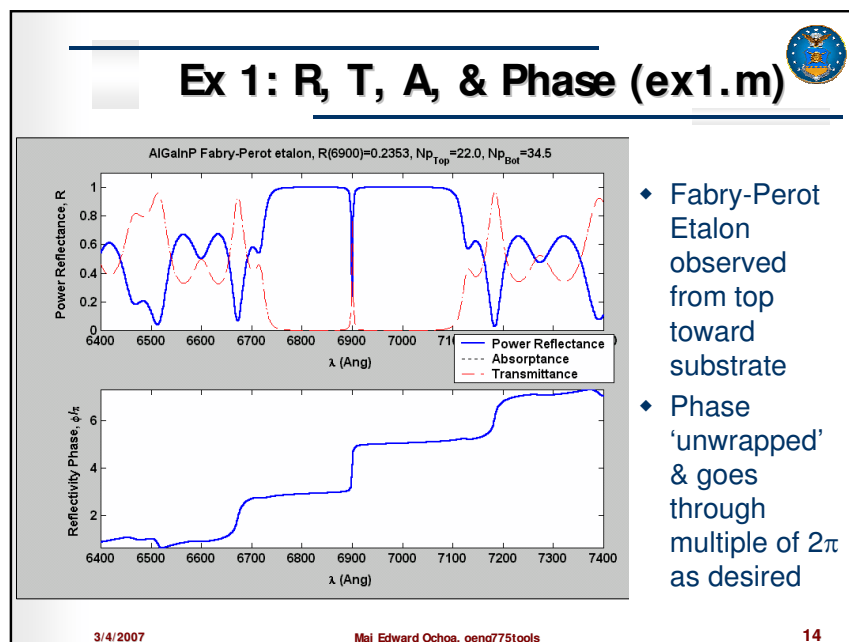
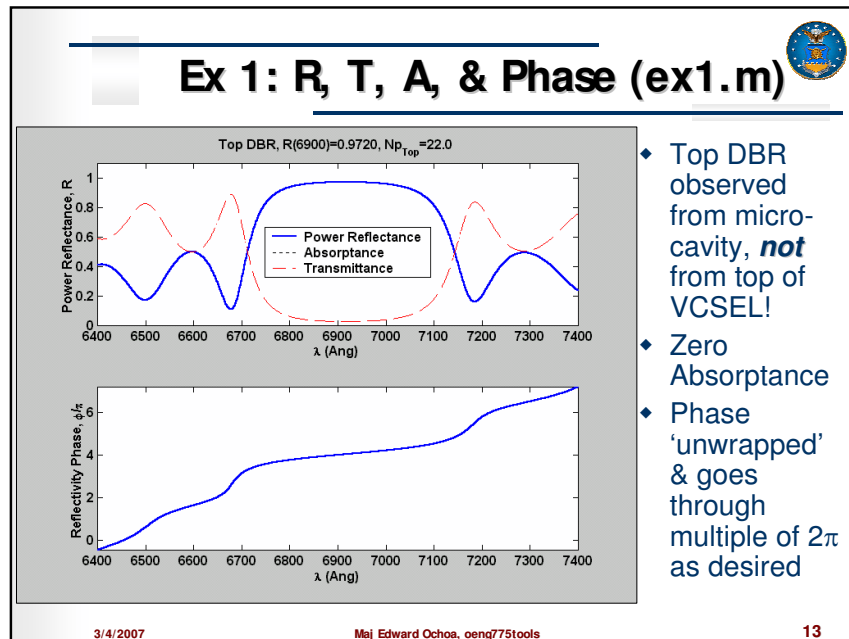



Figure B.7: oeng775tools: overview slides 13-14


Tools: E-field, Intensity



- ◆ Input: *Use MATLAB™ 'help' on:*
 - **Eamplitude** – E-field amplitude
 - **Dmatrix** – dynamical matrices
 - **Pmatrix** – Propagation matrix for E-field
 - **DPDmatrix** – Overall dynamical & prop matrix
 - **Mmatrix** – Transfer matrix used for E-field
 - **Ematrix** – Incident & Reflected E-field waves
 - **EoEvaluate** – E-field through stack
 - **EoEvaluateQuick** – E-field 1st layers of stack
 - **leval** – E-field intensity through stack
- ◆ Output: Parameters for E-field analysis

3/4/2007
Maj Edward Ochoa, oeng775tools
15

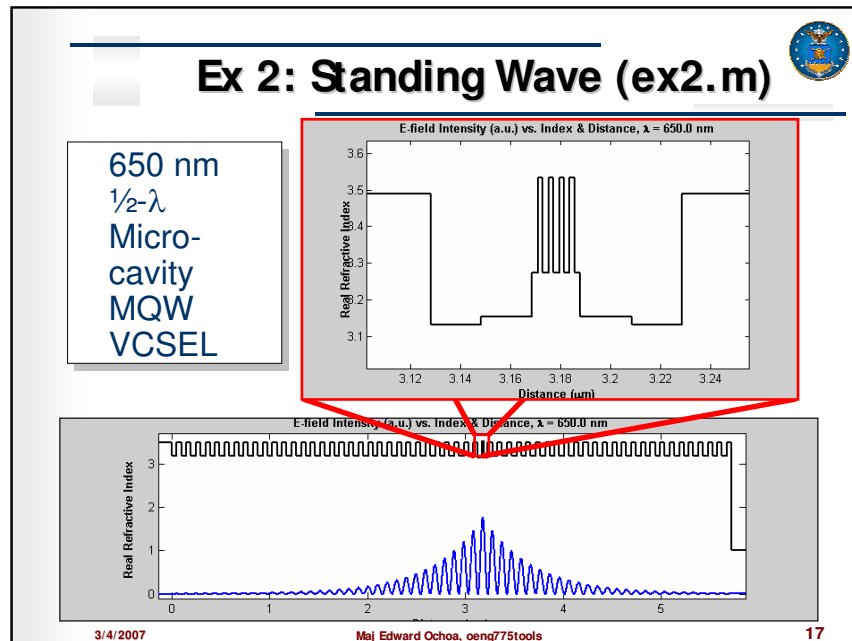
Tools: E-field, Intensity ct'd...



- ◆ Input: *Use MATLAB™ 'help' on:*
 - **PlotStack** – Plot index vs. thickness
 - **StandWave** – Compute & plot standing wave E-field intensity through multiple layers
- ◆ Output:
 - Index vs. thickness profile
 - Multi-layer E-field standing wave

3/4/2007
Maj Edward Ochoa, oeng775tools
16

Figure B.8: *oeng775tools*: overview slides 15-16



User contributed M-files

Included two additional utilities I've found extremely useful...

Source:
<ftp://ftp.mathworks.com/pub/contrib/v5/graphics/>

- ◆ Suptitle.m - Put title above all subplots
- ◆ Tilefigs.m - Tile figure windows

3/4/2007 Maj Edward Ochoa, oeng775tools 18

Figure B.9: *oeng775tools*: overview slides 17-18

Vita

Major Edward M. Ochoa graduated from Mayfield High School in Las Cruces, New Mexico. He received a Bachelor of Science degree in electrical engineering from the University of Arizona in 1992. He was commissioned through the Detachment 020 AFROTC at the University of Arizona. He received a Master of Science degree in electro-optics from the Air Force Institute of Technology in 1996.

Prior to his PhD research, he was a founding member of Qualia Computing, Inc., later CADx Systems, and then *iCAD*, Inc. He was awarded 8 patents for advanced pattern recognition algorithms and data analysis methods while developing *SecondLookTM*, *iCAD*'s mammography computer-aided breast cancer detection system. As a 15-yr active duty U.S. Air Force member, he has also developed, managed, or worked in modeling and simulation, image restoration and enhancement, algorithm optimization, signal processing, optics, microelectronics, photonics, and ground/airborne/space sensors research, development, testing, and fielding.

REPORT DOCUMENTATION PAGE					Form Approved OMB No. 0704-0188	
The public reporting burden for this collection of information is estimated to average 1 hour per response, including the time for reviewing instructions, searching existing data sources, gathering and maintaining the data needed, and completing and reviewing the collection of information. Send comments regarding this burden estimate or any other aspect of this collection of information, including suggestions for reducing the burden, to Department of Defense, Washington Headquarters Services, Directorate for Information Operations and Reports (0704-0188), 1215 Jefferson Davis Highway, Suite 1204, Arlington, VA 22202-4302. Respondents should be aware that notwithstanding any other provision of law, no person shall be subject to any penalty for failing to comply with a collection of information if it does not display a currently valid OMB control number.						
PLEASE DO NOT RETURN YOUR FORM TO THE ABOVE ADDRESS.						
1. REPORT DATE (DD-MM-YYYY) 13-09-2007		2. REPORT TYPE Doctoral Dissertation		3. DATES COVERED (From - To) Aug 1999 - Sep 2007		
4. TITLE AND SUBTITLE Hybrid Micro-Electro-Mechanical Tunable Filter				5a. CONTRACT NUMBER		
				5b. GRANT NUMBER		
				5c. PROGRAM ELEMENT NUMBER		
6. AUTHOR(S) Ochoa, Edward M., Major, USAF				5d. PROJECT NUMBER		
				5e. TASK NUMBER		
				5f. WORK UNIT NUMBER		
7. PERFORMING ORGANIZATION NAME(S) AND ADDRESS(ES) Air Force Institute of Technology Graduate School of Engineering and Management (AFIT/EN) 2950 Hobson Way, Bldg 641 WPAFB OH 45433-7765				8. PERFORMING ORGANIZATION REPORT NUMBER AFIT/DS/ENG/07-23		
9. SPONSORING/MONITORING AGENCY NAME(S) AND ADDRESS(ES) AFRL/SNDP Attn: Dr. Tom R. Nelson 2241 Avionics Circle WPAFB, OH 45433-7322 DSN: 785-1874 x3361, Thomas.Nelson@wpafb.af.mil				10. SPONSOR/MONITOR'S ACRONYM(S)		
				11. SPONSOR/MONITOR'S REPORT NUMBER(S)		
12. DISTRIBUTION/AVAILABILITY STATEMENT APPROVED FOR PUBLIC RELEASE; DISTRIBUTION UNLIMITED						
13. SUPPLEMENTARY NOTES						
14. ABSTRACT While advantages such as good thermal stability and processing-chemical compatibilities exist for common monolithic-integrated micro-electro-mechanically tunable filters (MEM-TF) and MEM-tunable vertical cavity surface emitting lasers (MT-VCSEL), they often require full processing to determine device characteristics. Alternatively, the MEM actuators and the optical parts may be fabricated separately, then subsequently bonded. This "hybrid approach" potentially increases design flexibility. Since hybrid techniques allow integration of heterogeneous material systems, "best of breed" compound optoelectronic devices may be customized to enable materials groups to be optimized for tasks they are best suited. Thus, as a first step toward a hybrid (AlGaAs-polySi) MT-VCSEL, this dissertation reports the design, fabrication, and demonstration of an electrostatically actuated hybrid MEM-TF. A 250x250-µm ² , 4.92-µm-thick, AlGaAs-GaAs distributed Bragg reflector was successfully flip-bonded to a polySi piston electrostatic actuator using SU-8 photoresist as bonding adhesive. The device demonstrated 53nm (936.5 - 989.5nm) of resonant wavelength tuning over the actuation voltage range of 0 to 10 V.						
15. SUBJECT TERMS SU-8; hybrid; microelectromechanical; tunable filter; flip bond; AlGaAs; distributed Bragg reflectors; polysilicon; hydrofluoric acid; optical tuning.						
16. SECURITY CLASSIFICATION OF:			17. LIMITATION OF ABSTRACT	18. NUMBER OF PAGES	19a. NAME OF RESPONSIBLE PERSON	
a. REPORT	b. ABSTRACT	c. THIS PAGE			Dr. Michael A. Marciniak, AFIT/ENP	
U	U	U	UU	202	19b. TELEPHONE NUMBER (Include area code) (937) 255-3636 x4529, Michael.Marciniak@afit.edu	